



HAL
open science

Hydrogen transport in tokamaks: Estimation of the ITER divertor tritium inventory and influence of helium exposure

Rémi Delaporte-Mathurin

► **To cite this version:**

Rémi Delaporte-Mathurin. Hydrogen transport in tokamaks: Estimation of the ITER divertor tritium inventory and influence of helium exposure. Chemical engineering. Université Paris-Nord - Paris XIII, 2022. English. NNT: 2022PA131054 . tel-04004369

HAL Id: tel-04004369

<https://theses.hal.science/tel-04004369v1>

Submitted on 24 Feb 2023

HAL is a multi-disciplinary open access archive for the deposit and dissemination of scientific research documents, whether they are published or not. The documents may come from teaching and research institutions in France or abroad, or from public or private research centers.

L'archive ouverte pluridisciplinaire **HAL**, est destinée au dépôt et à la diffusion de documents scientifiques de niveau recherche, publiés ou non, émanant des établissements d'enseignement et de recherche français ou étrangers, des laboratoires publics ou privés.

Hydrogen transport in tokamaks

Estimation of the ITER divertor tritium inventory and influence of helium exposure

Rémi Delaporte-Mathurin

Submitted in fulfillment of the requirements for the degree of
Doctor of Philosophy in Materials science
17th October 2022

Klaus SCHMID , Max Planck Institute for Plasma Physics	reader
Jamaa BOUHATTATE , Univ. La Rochelle	reader
Sophie BLONDEL , Univ. of Tennessee, Knoxville	committee member
Xavier BONNIN , ITER Organization	committee member
Monique GASPERINI , Univ. Sorbonne Paris Nord	committee member
Dennis WHYTE , Massachusetts Institute of Technology	committee member
Etienne HODILLE , CEA	invited member
Christian GRISOLIA , CEA	cosupervisor
Yann CHARLES , Univ. Sorbonne Paris Nord	cosupervisor
Jonathan MOUGENOT , Univ. Sorbonne Paris Nord	adviser

Abstract

English

Future fusion reactors will use a mixed fuel of deuterium and tritium. As a radioactive isotope of hydrogen, tritium can represent a nuclear safety hazard and its inventory in the reactors materials must be controlled. In ITER, the tritium in-vessel safety limit is 700 g.

The tritium inventory of the ITER divertor was numerically estimated with the FESTIM code, which was developed to simulate hydrogen transport in tungsten monoblocks. A parametric study was performed varying the exposure conditions (surface temperature and surface hydrogen concentration) and a behaviour law was extracted. This behaviour law provided a rapid way of estimating a monoblock inventory for a given exposure time and for given surface concentration and temperature. This behaviour law was then used and interfaced with output data from the edge-plasma code SOLPS-ITER in order to estimate the hydrogen inventory of the whole ITER divertor. Under conservative assumptions, the total hydrogen inventory (deuterium and tritium) was found to be well below the ITER tritium safety limit, reaching ≈ 14 g after 25 000 pulses of 400 s.

To investigate the influence of helium exposure on these results, a helium bubble growth model was developed. The results of this helium growth model were in good agreement with published numerical results and experimental observations. A parametric study was performed to investigate the influence of exposure conditions on the bubbles density and size. To investigate the influence of helium bubbles on hydrogen transport, deuterium TDS experiments of tungsten pre-damaged with helium were then reproduced. The distribution of bubbles density and size was computed using this helium bubble growth model and the results were used in FESTIM simulations. It was found that exposing tungsten to helium could potentially reduce the hydrogen inventory by saturating defects, making it impossible for hydrogen to get trapped. Moreover, the effect of helium bubbles (creation of additional traps for hydrogen) is limited to the near surface region (small compared to the monoblock's scale)

French

Les futurs réacteurs à fusion nucléaire utiliseront un combustible composé de deutérium et de tritium. En tant qu'isotope radioactif de l'hydrogène, le tritium peut représenter un risque en terme de sûreté nucléaire et son inventaire dans les matériaux des réacteurs doit être maîtrisé. Dans ITER, la limite de sécurité du tritium dans la chambre à vide est de 700 g.

L'inventaire de tritium du divertor ITER a été estimé numériquement avec le code FESTIM, qui a été développé pour simuler le transport d'hydrogène dans des monoblocs de tungstène. Une étude paramétrique a été réalisée en faisant varier les conditions d'exposition (température de surface et concentration en hydrogène de surface) et une loi de comportement a été extraite. Cette loi de comportement a permis d'estimer rapidement les inventaires monobloc pour un temps d'exposition donné et pour une concentration et une température de surface données. Elle a ensuite été utilisée et interfacée avec les données de sortie du code edge-plasma SOLPS-ITER afin d'estimer l'inventaire d'hydrogène de l'ensemble du divertor d'ITER. Avec des hypothèses conservatrices, l'inventaire total d'hydrogène (deutérium et tritium) s'est avéré bien en dessous de la limite de sécurité du tritium d'ITER, atteignant ≈ 14 g après 25 000 impulsions de 400 s.

Pour étudier l'influence de l'exposition à l'hélium sur ces résultats, un modèle de croissance de bulles d'hélium a été développé. Les résultats de ce modèle de croissance de l'hélium étaient en accord avec les résultats numériques et observations expérimentales déjà publiés. Une étude paramétrique a été réalisée pour étudier l'influence des conditions d'exposition sur la densité et la taille des bulles. Afin d'étudier l'influence des bulles d'hélium sur le transport de l'hydrogène, des expériences TDS en deutérium sur du tungstène pré-endommagé à l'hélium ont ensuite été reproduites. Les distributions de la densité et de la taille des bulles ont été calculées à l'aide de ce modèle de croissance des bulles d'hélium et les résultats ont été utilisés dans les simulations FESTIM. Il a été constaté que l'exposition du tungstène à l'hélium pouvait potentiellement réduire l'inventaire d'hydrogène en saturant les défauts, rendant impossible le piégeage de l'hydrogène. De

plus, l'effet des bulles d'hélium (création de pièges supplémentaires pour l'hydrogène) est limité au proche région de surface (petite par rapport à l'échelle du monobloc)

Introduction

"I would put my money on the sun! What a source of power! I hope we don't have to wait until oil and coal run out before we tackle that." Thomas Edison once said. The use of fossil fuels (coal, gas, oil) has allowed the modern human civilisation to reach its current standard of living. However, their intensive use led to astronomical carbon dioxide (CO₂) emissions. Since Edison died in 1931, 1500 billion tonnes of CO₂ have been emitted on Earth from burning fossil fuels and about 33 billion tonnes of CO₂ are still being released every year [1]. The consequence of these emissions is global warming and these CO₂ emissions must stop in order to limit it to an "acceptable" level - regardless of the remaining oil and coal reserves. Reducing the CO₂ emissions implies reducing the world's energy consumption while developing low-carbon sources of energy. It is very unlikely that these new sources will be able to completely replace fossil fuels. They would however act as a shock absorber in the energy crisis mankind is facing.

When looking at the Sun, Edison saw how massive and inexhaustible its energy was. The process powering the stars is called *nuclear fusion*. It does not release any greenhouse gases, it is energetically dense and its fuel is abundant on Earth. Could it be one of these new sources of energy?

Answering this question by a simple 'yes' or 'no' would be oversimplifying. Throughout the years, spectacular progress has been made. Until 2000, the performance of nuclear fusion devices doubled every 1.8 year - faster than Moore's law stating that the computational power of processor doubles every 2 years [2].

However, many other challenges lie ahead: materials development, supply-chain, systems integration, maintenance... One of these challenges is tritium, a radioactive isotope of hydrogen essential for fusion. With deuterium - another isotope of hydrogen - it will be the fuel of a fusion reactor.

The first main issue is the scarcity of tritium on Earth. Tritium decays into helium with a half-life of approximately 12 years, which means it is very rare in nature. The current reserves of tritium on Earth are a few kilograms and fusion reactors will require a lot more (around 100 kg a year for one reactor). For this reason, tritium will have to be produced inside the fusion reactor.

The second issue is due to the tritium radiotoxicity. Its ingestion - typically when present in water - is a health hazard. The quantity of tritium contained in the reactor must therefore be limited to minimise the effects of a potential accident or release to the environment.

Hydrogen retention in materials will have an impact on both these points. Due to its small size (one of the smallest elements), tritium can penetrate the materials lattices and eventually be trapped in the reactor structure. This would make the tritium fuel cycle even more challenging: how to inject tritium in the reactor if a large portion of the fuel is trapped in the materials? Moreover, as time goes by, the components of a reactor would build up an inventory of tritium, which would increase their radioactivity, making the decommissioning of a power plant more challenging. Contaminated components would indeed have to be handled as radioactive waste. Other issues like material embrittlement are also impacted by hydrogen retention.

Are we able to predict tritium retention in fusion reactors?

Will the tritium inventory remain within the safety limits over their lifespan?

What is the influence of helium impurities (present in a fusion reactor) on this retention?

These are the main questions this research aims to tackle.

Because answering these questions experimentally would prove to be very complex, a new modelling tool has been developed from scratch. FESTIM, which stands for Finite Element Simulation of Tritium In Materials, is able to simulate hydrogen transport in complex geometries encountered in tokamaks components. This PhD work focusses on the *divertor*, a component of fusion reactors made of tungsten exposed to very intense particle (hydrogen and helium) and heat fluxes. The divertor is made of multiple unit bricks called *monoblocks*. The first Chapter of this manuscript will provide a general introduction to the research and a literature review of the main phenomena at stake. A method has been developed to make use of monoblock-level FESTIM

simulations data and scale it up to divertor-level to have an estimate of the hydrogen inventory in the entire divertor. Finally, a separate model has been developed to study the behaviour of helium in tungsten. This model has then been coupled to hydrogen simulations to investigate the potential effect of helium on the previously calculated hydrogen inventory.


Contents

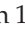



Abstract	iii
Introduction	v
Contents	vii
Notation	xv
List of Terms	xvii
1 Fusion: general introduction	1
1.1 Thermonuclear fusion	1
1.2 Tokamaks: how to bottle a star	3
1.2.1 Technology [4]	3
1.2.2 Triple product	4
1.2.3 Plasma-facing materials	6
1.2.4 Divertor	7
1.3 The tritium issue	11
1.3.1 Breeding	11
1.3.2 Safety	13
1.4 Helium and Hydrogen in metals	13
1.4.1 Particle sources	14
1.4.2 H/W & He/W interactions	15
1.4.3 He/H interactions	27
1.5 Problem definition	28
2 Model description	31
2.1 Introduction	31
2.2 H transport	31
2.2.1 Macroscopic Rate Equations model	31
2.2.2 Boundary conditions	32
2.2.3 Interface condition: conservation of chemical potential	35
2.3 Heat transfer	35
2.4 Implementation	36
2.4.1 The finite element method: FEniCS	36
2.4.2 Main features of Finite Element Simulation of Tritium in Materials (FESTIM)	39
2.5 Verification & Validation	40
2.5.1 Analytical verification	40
2.5.2 Experimental validation	45
2.5.3 Comparison with TMAP7	51
2.6 Summary	53
3 Monoblocks	55
3.1 Model description	55
3.2 Simulation simplifications	58
3.2.1 Thermal behaviour	58
3.2.2 Influence of dimensionality	59
3.2.3 Influence of interface condition	61

3.2.4	Influence of cycling	62
3.3	Monoblock behaviour law	65
3.3.1	Assumptions and simplifications	65
3.3.2	Results	66
3.3.3	Discussion	67
3.4	Summary	69
4	Divertor inventory estimation	71
4.1	Methodology	71
4.1.1	Plasma simulations	71
4.1.2	Estimation of exposure conditions	73
4.2	ITER results	74
4.3	WEST results	78
4.3.1	Influence of the input power	78
4.3.2	Influence of the puffing rate	79
4.4	Summary	83
5	Influence of helium on hydrogen transport	85
5.1	Sources of helium	85
5.1.1	Neutron induced transmutation	85
5.1.2	Tritium decay	86
5.1.3	Comparison to direct implantation	87
5.2	Bubble growth model	89
5.2.1	Helium clustering model	89
5.2.2	Grouped approach	91
5.3	Verification & Validation	95
5.3.1	Code comparison: Tendril case	95
5.3.2	Comparison with experiments	96
5.4	Bubble growth study	98
5.4.1	Half-slab case	98
5.4.2	Influence of exposure parameters on helium bubble growth	100
5.5	Influence on hydrogen transport	108
5.5.1	Experiment	108
5.5.2	Bubble growth simulation	108
5.5.3	FESTIM simulations	108
5.5.4	Results	109
5.6	Summary	113
6	Conclusion	115
APPENDIX		119
A	FESTIM verification	121
A.1	Conservation of chemical potential (MES)	121
A.2	Conservation of chemical potential (MMS)	123
A.3	Heat transfer (MMS)	124
B	Interface transient model	127
C	DEMO monoblocks	131
C.1	Methodology	131




C.2 Standard case	133
C.3 Influence of the monoblock thickness	136
Bibliography	139

List of Figures

1.1	Binding energy per nucleon [3].	1
1.2	Evolution of the potential energy of two nuclei with their relative distance. Reproduced from [4].	2
1.3	Fusion cross sections [5].	3
1.4	Magnetic field lines in a tokamak. Contribution of the toroidal and poloidal components. . . .	4
1.5	Triple product. An interactive version of this plot is available at [14].	6
1.6	Comparison of the tokamaks ITER, JET, ARC, WEST and SPARC. Data from [14].	7
1.7	Sketch of the tokamak divertor configuration (source: EFDA-JET).	8
1.8	Heat flux, particle flux and particle energy along the ITER divertor computed by the edge-plasma simulation code SOLPS (shot #122399) [26].	9
1.9	Structure of the ITER divertor. (images: ITER Organization, [32]).	10
1.10	Thermal response of ITER-like monoblocks.	10
1.11	DEMO model showing HCLL blankets  , plasma  , magnets  , and structural steel  . Reproduced from [39].	11
1.12	Evolution of the maximum fusion power on the grid for different doubling times.	12
1.13	Interactions of solute species in tungsten.	14
1.14	Cross section of the ${}^3\text{He}(n, T)\text{H}$ reaction [69].	15
1.15	Simplified potential energy diagram showing two different types of defects.	16
1.16	Example of the trajectory of a He_2 cluster in tungsten. Reproduced from [82].	17
1.17	Diffusivity values for tungsten, copper and CuCrZr. Data from [96].	18
1.18	H TDS spectrum of pre-damaged W. Reproduced from [97].	19
1.19	Detrapping energy of a hydrogen atom in several defects in tungsten: vacancies, impurities, self-interstitial atoms (SIA), grain boundaries (GB), in tungsten depending on the number of trapped hydrogen atoms. Reproduced from [105].	20
1.20	Solubility values for tungsten, copper and CuCrZr. Data from [96].	21
1.21	Transmission electron microscopy image of tungsten irradiated with He ions at different fluxes (Low Flux (LF) = $2.9 \times 10^{20} \text{ m}^{-2} \text{ s}^{-1}$ and High Flux (HF) = $2.3 \times 10^{22} \text{ m}^{-2} \text{ s}^{-1}$) showing the presence of He bubbles. Reproduced from [97].	23
1.22	Scanning Electron Microscopy images of the surface of W samples exposed to 50 eV H plasma at 573 K and 1273 K. Reproduced from [133].	24
1.23	Molecular dynamics simulation of He bubble bursting in W. Reproduced from [139].	25
1.24	W fuzz observed in Alcator C-Mod. Reproduced from [142].	26
1.25	Fuzzy W scanning/transmission electron microscopy images showing the presence of He bubbles in tendrils. Reproduced from [151].	27
2.1	100 eV deuterium implantation profile in tungsten computed from Stopping Range of Ions in Matter (SRIM). Reproduced from [174].	33
2.2	Concentration profile with recombination flux and volumetric source term at $x = R_p$. Dashed lines correspond to the time evolution.	34
2.3	Representation of the mathematical problem.	37
2.4	1D example of an approximated solution u (exact in blue, approximated in orange) with basis function ϕ_i for linear finite elements with 2 nodes.	38
2.5	Example of a complex 3D geometry (here a breeding blanket section) mesh readable by FESTIM [70].	40
2.6	Temporal evolution of the outward particle flux φ at $x = l$ (Case 1).	41
2.7	Evolution of the L2 error on φ as a function of the stepsize and element length (Case 1).	43

2.8	Evolution of the L2 norm of the error as function of element size h for the 1D H transport case (Case 2a).	45
2.9	Comparison of the computed concentrations with the exact solution (Case 2b).	46
2.10	Evolution of the L2 error on c_m (left) and c_t (right) showing the convergence rates for the 2D H transport case (Case 2b).	46
2.11	Diagram of the parametric optimisation routine.	47
2.12	Normalised cost function $\hat{f} = (f - \min f)/(\max f - \min f)$ as function of E_1 (eV) and n_1 (at fr) with global minimum located at (0.86 eV, 1.2×10^{-3} at fr).	48
2.13	Number of cost function evaluations required to converge towards the global minimum with 100 different initial guesses sorted by distance to the global minimum for several minimisation algorithms. Each cost function evaluation takes 20 s to compute. White stripes correspond to initial guesses for which the algorithm did not converge to the global minimum.	49
2.14	Fitting TDS spectrum performed on Tungsten by Ogorodnikova <i>et al</i> [106]. Dots correspond to experimental data.	50
2.15	TDS spectrum reproduced with several sets of parameters showing the existence of several solutions to a single optimisation problem.	50
2.16	TMAP7 - FESTIM comparison 1D geometry showing W  , Cu  , CuCrZr 	51
2.17	Temperature profile simulated by FESTIM for comparison case with TMAP7.	52
2.18	Comparison of results provided by FESTIM and TMAP7.	53
3.1	ITER monoblock geometry showing W armour  , Cu interlayer  , CuCrZr alloy cooling pipe  . The monoblock thickness is 12 mm.	56
3.2	Material properties used in the simulations [93, 101, 200–202].	57
3.3	Thermal behaviour of the monoblock.	59
3.4	Meshes used for the monoblock simulations.	60
3.5	Representation of the 2D and 1D approximations on a monoblock geometry. The arrows represent geometry independencies.	60
3.6	Comparison of monoblock inventories for the 1D, 2D approximations and the 3D case.	61
3.7	Influence of continuity of chemical potential on the monoblock hydrogen inventory. The bottom plot shows the contribution of the trapped hydrogen in W, Cu and CuCrZr as well as the total mobile hydrogen for the case with continuity of chemical potential.	62
3.8	Influence of interface conditions on concentration fields at $t = 2 \times 10^7$ s, $\varphi_{\text{heat}} = 7 \text{ MW m}^{-2}$	63
3.9	Influence of interface conditions on retention fields at $t = 6.1 \times 10^4$ s.	63
3.10	ITER plasma cycle. Evolution of heat flux and implanted particle flux.	64
3.11	Evolution of the monoblock inventory as a function of the implanted fluence for cycled (solid) and continuous (dashed) exposure on a 1D case.	64
3.12	Evolution of the monoblock inventory during the sixth cycle for the high flux case.	65
3.13	Evolution of the concentrations of traps 1 and 2 as a function of temperature for a local mobile hydrogen concentration of $1 \times 10^{22} \text{ m}^{-3}$ and error associated with neglecting trap 2.	66
3.14	Example retention fields in m^{-3} after a 10^7 s exposure.	67
3.15	Evolution of the inventory after a 10^7 s exposure as a function of T_{surface} and c_{surface} alongside with simulation points (grey crosses). The simulations points were fitted with a Gaussian regression process [208] providing the standard deviation σ	68
4.1	Poloidal cross section of Tungsten Environment Steady state Tokamak (WEST) and International Thermonuclear Experimental Reactor (ITER) showing the divertors in red.	72
4.2	Method of WEST divertor hydrogen (H) inventory estimation based on the surface concentration, the surface temperature and the behaviour law obtained in Chapter 3.	73
4.3	Evolution of the implantation range and the reflection coefficient as a function of incident energy E and angle of incidence.	74

4.4	Distribution of exposure conditions (heat flux, particle flux and particle incident energy) along the ITER divertor for several divertor neutral pressures [26].	75
4.5	Surface temperature, surface concentration and inventory per unit thickness along the ITER divertor with neutral pressures varying from 2 Pa to 11 Pa. The area corresponds to the 95% confidence interval.	75
4.6	Hydrogen inventory in the ITER divertor as a function of neutral pressure after 10^7 s of exposure (approximately 25 000 discharges).	76
4.7	H retention at the strike points (defined as maximum temperature) as a function of the divertor neutral pressure.	77
4.8	Evolution of the H inventory of the ITER divertor with the number of 400 s discharges.	78
4.9	Distribution of surface temperature T_{surface} , surface concentration c_{surface} and inventory per unit thickness along the WEST divertor with input powers varying from 0.49 MW to 2.0 MW with a puffing rate of 2.5×10^{21} molecule s^{-1}	79
4.10	H inventory at the inner and outer strike points (Inner Strike Point (ISP) and Outer Strike Point (OSP)) and in the private flux region as a function of the input power with a puffing rate of 2.5×10^{21} molecule s^{-1}	80
4.11	Evolution of the WEST divertor inventory as a function of input power for several puffing rates.	81
4.12	Temporal evolution of Plasma Facing Unit (PFU) inventories for different values of puffing rate (left) and input power (right).	81
4.13	Distribution of surface temperature T_{surface} , surface concentration c_{surface} and inventory per unit thickness along the WEST divertor with a puffing rate varying from 4.4×10^{20} s^{-1} to 4.7×10^{21} s^{-1} with 0.45 MW of input power.	81
4.14	Evolution of the WEST divertor inventory as a function of puffing rate.	82
4.15	H retention at the strike points and in the private flux region as a function of puffing rate with 0.45 MW of input power.	82
5.1	Muir neutron energy spectrum corresponding to a DT reaction sampled with 5000 particles.	86
5.2	Helium generation via transmutation in a monoblock (only tungsten is shown).	88
5.3	Steady state helium generation from tritium decay in a monoblock.	88
5.4	Comparison of the three sources of helium in a monoblock. The source from direct implantation was computed for an incident flux of 5×10^{25} m^{-2} s^{-1} with a gaussian distribution (mean of 1 nm and standard deviation of 1.5 nm).	89
5.5	Representation of helium (He) clustering in solids. Dissociation is omitted for simplification purposes. The thickness of the grey arrows represents the magnitude of the reaction rate between mobile He_1 and other clusters at the same distance.	90
5.6	Validity of the sum approximation in the computation of the bubble radius assuming c_i has a gaussian distribution centered on μ and with a standard deviation σ	94
5.7	He clusters concentration profiles in the tendrils at 500 K, 1000 K and 1500 K under 100 eV He exposure at 1×10^{22} m^{-2} s^{-1} at a fluence of 5×10^{25} m^{-2} . Comparison between the current implementation (solid) and Faney's results [89] (dashed).	95
5.8	Helium clusters concentration profiles on the tendrils case with dissociation energies varying from -0.5 eV (dash-point) to +0.5 eV (dash).	97
5.9	Transmission Electron Microscopy (TEM) images of W after exposure to 75 eV He at 2.3×10^{22} m^{-2} s^{-1} and 1053 K for 13 s showing bubbles that have burst, large size bubbles at the near surface and small size bubbles in the bulk.	98
5.10	Comparison of experimental results with simulations for W implanted with 75 eV He at 2.3×10^{22} m^{-2} s^{-1} and 1053 K for 13 s. Error bars correspond to the lowest and highest radius in the TEM image.	98
5.11	Concentration profiles of He_1 (left) and bubbles (right) in W exposed to 100 eV He at 10^{22} m^{-2} s^{-1} and 1000 K.	99

5.12	Profile of mean bubble radius $\langle r_b \rangle$ as a function of depth x in tungsten (W) exposed to 100 eV He at $10^{22} \text{ m}^{-2} \text{ s}^{-1}$ and 1000 K.	100
5.13	Average helium content $\langle i \rangle$ and average radius $\langle r \rangle$ in all clusters (mobile and bubbles) in W exposed to 100 eV He at $10^{22} \text{ m}^{-2} \text{ s}^{-1}$ and 1000 K.	101
5.14	Comparison of several quantities of interest for several values of N in W exposed to 100 eV He at $10^{20} \text{ m}^{-2} \text{ s}^{-1}$ and 1000 K.	102
5.15	Evolution of quantities as a function of the implanted flux and temperature after 1 h of 100 eV He exposure. Grey crosses correspond to simulations points.	103
5.16	Temporal evolution of quantities in W exposed to 100 eV He at $10^{22} \text{ m}^{-2} \text{ s}^{-1}$ and 1000 K for temperatures varying from 120 K to 1200 K and implanted fluxes varying from $10^{17} \text{ m}^{-2} \text{ s}^{-1}$ to $10^{21} \text{ m}^{-2} \text{ s}^{-1}$. Each line corresponds to a simulation point (grey crosses on Figure 5.15a and points on Figure 5.16d). The lines are coloured according to the parameter $c_{\text{He}_1, \text{ideal}} = \varphi_{\text{imp}} R_p / D(T)$ with $R_p = 1.5 \text{ nm}$ and D the diffusion coefficient of He ₁ in W.	104
5.17	Temporal evolution of $\langle \bar{i}_b \rangle$, I_{bubbles} and I in W exposed to 100 eV He at $1.59 \times 10^{18} \text{ m}^{-2} \text{ s}^{-1}$ and 1020 K. The dashed grey vertical line represents the transition from nucleation regime to bubble growth regime.	105
5.18	Evolution of $\langle \bar{i}_b \rangle$, \hat{I}_{bubbles} and \hat{I} as a function of \hat{t} for several $c_{\text{He}_1, \text{ideal}}$ values. The blue curves correspond to the fitted evolutions.	107
5.19	Spatial distribution of the bubbles density and the equivalent trap density (assuming $f = 3 \times 10^{18} \text{ m}^{-2}$).	109
5.20	Results of the Thermo-Desorption Spectroscopy (TDS) fitting procedure.	110
5.21	Evolution of the trap densities between the second and fifth TDS.	111
5.22	Schematic interpretation of the simulation results showing the several stages of the experiment (from He implantation to TDS cycles).	112
A.1	Concentration profiles simulated by FESTIM against analytical solutions.	121
A.2	Comparison of concentration fields simulated by FESTIM with manufactured solutions.	124
A.3	Verification of the heat transfer module in FESTIM.	125
A.4	Evolution of the L2 error on T showing the convergence rates for the 2D heat transfer case.	126
B.1	Idealised potential energy diagram describing the interactions of H at the interface between two materials. In this case, $E_{S,1} > E_{S,2}$ (consistent with a W/Cu interface Table 3.1).	127
B.2	(a) Evolution of the ratio c_2/c_1 with normalised time t/τ_i for different values of $E_{i \rightarrow 2}/k_B T$. (b) Evolution of the ratio $\theta_i/\theta_i^{\text{eq}}$ with normalised time t/τ_i (independent of $E_{i \rightarrow 2}/k_B T$). (c) Evolution of the time to reach 95% of the steady-state concentration, τ_1 and τ_2 as a function of $E_{i \rightarrow 2}/k_B T$. (d) Evolution of θ_i^{eq} as a function of $E_{i \rightarrow 2}/k_B T$. The temperature in the simulation is 475 K, the concentration in the material 1 (W) is $c_1 = 10^{18} \text{ m}^{-3}$ and the concentration of trapping site at the interface is $n_i = 10^{19} \text{ m}^{-2}$	130
C.1	3D geometry of the DEMO monoblock used for the simulations showing W armour  , Cu interlayer  , CuCrZr alloy cooling pipe 	132
C.2	Temperature field of the 3D DEMO monoblock.	133
C.3	Retention fields of the DEMO monoblock with (left) or without (right) recombination on the poloidal gaps (standard case). Note the colour bars are different.	134
C.4	Temporal evolution of the monoblock inventory (standard case).	135
C.5	Temporal evolution of outgassing fluxes for the standard case with desorption from the poloidal gaps. Blue lines correspond to the fluxes towards the vacuum vessel, the orange line is the flux towards the coolant.	135
C.6	Evolution of the inventory with or without recombination at the poloidal gap for several monoblock thicknesses at $t = 1 \times 10^6 \text{ s}$	136

C.7	Evolution of the permeation flux to the coolant with or without recombination at the poloidal gap for several monoblock thicknesses at $t = 1 \times 10^6$ s.	137
C.8	Evolution of the permeation flux with or without recombination at the poloidal gap for several monoblock thicknesses without CuCrZr extrusion at $t = 1 \times 10^6$ s.	138

List of Tables

1.1	Comparison of some hydrogen transport modelling tools.	29
2.1	Parameters used for the analytical verification (Case 1).	42
2.2	Traps properties used in the comparison with TMAP7.	51
3.1	Materials properties used in the simulations. Thermal properties are fitted from ANSYS. T is the temperature in K.	58
3.2	Traps properties used in the simulations [193, 203].	58
4.1	Setup parameters used in the SOLEDGE3X simulations.	72
5.1	Pure He clusters properties in W. Diffusion properties are taken from Faney et al. [89] and binding energies are taken from Becquart et al. [238].	95
5.2	Trap properties used to fit the TDS spectra. The density distribution n_b as well as detrapping energies E_p are assumed constant across TDS experiments.	109
5.3	Results of the fitting procedure. Detrapping energies E_p are given in eV, trap densities in at fr and f in m^{-2}	110
C.1	Traps properties used in the 3D DEMO monoblocks simulations.	132

Notation

The next list describes several symbols that will be later used within the body of the document.

λ	Thermal conductivity	$\text{W m}^{-1} \text{K}^{-1}$
λ_{decay}	Radioactive decay constant	s
$\langle i_b \rangle$	Average helium content in c_b	
$\langle r_b \rangle$	Average radius in c_b	m
Ω	Geometrical domain	
$\partial\Omega$	Boundary of a geometrical domain	
ρ	Volumetric density	kg m^{-3}
$\tau_{1/2}$	Radioactive half-life	s

φ_{heat}	Heat flux per unit surface	W m^{-2}
φ_{imp}	Implanted particle flux per unit surface	$\text{m}^{-2} \text{s}^{-1}$
$\varphi_{\text{incident}}$	Incident particle flux per unit surface	$\text{m}^{-2} \text{s}^{-1}$
c_{m}	mobile concentration of hydrogen	m^{-3}
$c_{\text{t},i}$	concentration of trapped hydrogen in trap i	m^{-3}
c_{b}	Total concentration of helium clusters above a given threshold	m^{-3}
C_p	Heat capacity	W K^{-1}
D	Diffusion coefficient	$\text{m}^2 \text{s}^{-1}$
D_0	Diffusivity pre-exponential factor	$\text{m}^2 \text{s}^{-1}$
E_D	Diffusivity activation energy	eV
$E_{k,i}$	Trapping rate of trap i activation energy	eV
$E_{p,i}$	Detrapping rate of trap i activation energy	eV
E_S	Solubility activation energy	eV
h	Convective heat transfer coefficient per unit surface	$\text{W m}^{-2} \text{K}^{-1}$
k_B	Boltzmann constant	eV K^{-1}
k_i	Trapping rate of trap i	$\text{m}^3 \text{s}^{-1}$
K_r	Recombination coefficient	$\text{m}^4 \text{s}^{-1}$
$k_{0,i}$	Trapping rate of trap i pre-exponential factor	$\text{m}^3 \text{s}^{-1}$
n_i	Density of trap i	m^{-3}
p_i	Detrapping rate of trap i	s^{-1}
$p_{0,i}$	Detrapping rate of trap i pre-exponential factor	s^{-1}
Q	Plasma amplification factor. The ratio of the fusion power generated by the power absorbed by the plasma.	
r	Particle reflection coefficient	
r_A	Capture radius of species A	m
R_p	Implantation range	m
S	Solubility	$\text{m}^{-3} \text{Pa}^{-0.5}$
S_0	Solubility pre-exponential factor	$\text{m}^{-3} \text{Pa}^{-0.5}$
T	Temperature	K

t	Time	s
T_{coolant}	Coolant temperature	K
u	An arbitrary solution	
v	A test function	

List of Terms

A

ACHLYS Hydrogen transport code developed by UKAEA. 28, 29

advection Transport of particles (or heat) via motion of the medium (as opposed to diffusion where the medium can be immobile). 21, 22

ARC Affordable Robust Compact. 6

ASDEX Axially Symmetric Divertor Experiment. 8

B

bcc body-centered cubic. Type of metallic lattice. 22

Be beryllium. 7, 12, 83

blistering Formation of blisters: plastic deformation (swelling) of the metal near the surface due to high pressure in bubbles. 24

breeding blanket Components of a fusion reactor responsible for producing tritium from the neutrons of the fusion reactions. 11–13, 15, 116

bursting Explosion of a gas bubble near the metal surface. 25

C

CANDU CANada Deuterium Uranium reactor. 11

CFC Carbon fiber composite. 7

CG Conjugate Gradient. 47

CRDS Coupled Reaction Diffusion System. 29

D

D deuterium. 2, 27, 28, 111

DCLL Dual-Coolant-Lithium-Lead. 12

DEMO DEMOnstration power plant. 6, 8, 83

detrapping Opposite to trapping. 17, 18

DFT Density Functional Theory. 16, 18, 19, 22, 91

diffusion For particles: process resulting from the random motion of particles from high concentration regions to regions of low concentrations. For heat: transport of thermal energy from high temperature regions to low temperature regions. 15, 16, 22, 78, 99

dislocation loop Defects formed by agglomerations of point-defects into planes. 17, 23

divertor Component of a tokamak diverting the magnetic field lines creating one or several X-points. The divertor is responsible for exhausting heat and particle from the plasma. The targets of the divertor is where the plasma is directed to absorb heat and particle fluxes. xii, xiii, 7, 8, 14, 15, 24, 25, 28, 29, 71–73, 75–83, 85, 86, 115

E

EELS Electron Energy Loss Spectroscopy. 23

ENDF Evaluated Nuclear Data File. 85

F

FDM Finite Difference Method. 28

FEM Finite Element Method. 28

FEniCS Open-source finite element solving library. 36, 39, 40, 53, 95

FESTIM Finite Element Simulation of Tritium in Materials. vii, viii, xi, 29, 31, 36, 39–41, 46, 53, 83, 86, 108, 110, 113, 115, 116

FIB Focused Ion Beam. 96

first wall Cover of the inner surface of the vacuum vessel in front of the plasma. 14, 83, 116

fluence Total quantity of particles a sample has been exposed to over a given period of time. Product of the particle flux by the exposure time. 26, 99, 104, 108

FPY full power year. 15

Frenkel pair A self-interstitial atom and a vacancy. 22

fuel recycling Phenomenon occurring when particles from the plasma are neutralised at the walls and ionised again. 14

fuzz Porous, nanostructure sometimes observed on tungsten under helium irradiation. 25–27

H

H hydrogen. xii, xiii, 13, 16, 18, 21, 22, 28, 71, 73, 74, 78, 83, 109, 110

HCLL Helium-Cooled-Liquid-Lead. 12

HCPB Helium-Cooled-Pebble-Bed. 12

He helium. xiii–xv, 13, 16–18, 22, 23, 25–28, 89–93, 95, 98–104, 108–112

HIIPC Hydrogen Isotope Inventory Processes Code. 29

HIT Hydrogen Isotope Transport code. 28, 29

I

ICRF Ion Cyclotron Range of Frequencies. 71

IMAS Integrated Modelling Analysis Suite. 72

inventory Total quantity of particles in a domain (sample, component, reactor...). It can be obtained by integrating the retention over the domain. xii, xiii, 12, 13, 25, 28, 29, 71, 73–83, 104

isotope Member of a family of elements sharing the same number of protons but different numbers of neutrons. 2, 11, 13, 28

ISP Inner Strike Point. xiii, 8, 80, 82

ITER International Thermonuclear Experimental Reactor. xi–xiii, 6–11, 13, 24, 29, 71–73, 75–78, 83, 85, 115, 116

IVT Inner Vertical Target. 8, 75, 76

J

JET Joint European Torus. 6, 8

L

lattice Three-dimensional crystalline structure of metals. The lattice is how the atoms are ordered within a metal. 14, 22, 23, 25

Li lithium. 11

loop punching Helium bubble growth mechanism leading to the formation of a dislocation loop. 23–25, 28

M

MAST-U Mega Amp Spherical Tokamak Upgrade. 8

MD Molecular Dynamics. 16, 23, 91, 93, 96

MES Method of Exact Solutions. 41

MHIMS Migration of Hydrogen Isotopes in Materials. 29

MMS Method of Manufactured Solutions. 41–44

monoblock A unit brick made of a tungsten armour with a CuCrZr cooling pipe and a copper interlayer. xiii, 8, 29, 71, 73, 74, 76, 78, 83, 85–89

MRE Macroscopic Rate Equations. 31

N

NIF National Ignition Facility. 5

O

OpenMC Open-source neutronics code. 85, 86

OSP Outer Strike Point. xiii, 8, 80, 82

OVT Outer Vertical Target. 8, 75, 76

P

P1 Lagrange finite element of order 1, also called piecewise linear elements. 42, 125

P2 Lagrange finite element of order 2. 125

P3 Lagrange finite element of order 3. 125

Paramak Code for generating parametric tokamak geometries. 85, 116

permeation Transport of particles through a material membrane. 12, 13, 116

PFM Plasma Facing Material. 6, 7, 15

PFU Plasma Facing Unit. xiii, 8, 78, 81

plasma Ionised gas. Sometimes referred as the fourth state of matter. 3–8, 11, 14, 25–29, 71, 78, 86

private flux region WEST divertor region located between the strike points. xiii, 72, 78–80, 82

R

retention Local concentration of soluted species (hydrogen or helium) including the mobile and trapped species. xiii, 15, 25, 27–29, 78, 79, 82, 83

S

self-interstitial An atom initially in the lattice located at interstitial sites. 17, 23, 94

self-trapping See trap mutation entry. 22, 91

separatrix Last closed flux surface, intersects the X-point. 8

SOLEEDGE3X Plasma boundary code. xv, 71–74

SOLPS-ITER Primary plasma boundary code used at ITER. 71–74

Soret effect Diffusion assisted by thermal gradients. 16

SPARC Soonest Private-funded Affordable Robust Compact. 6, 8

SRIM Stopping Range of Ions in Matter. xi, 33, 74, 95, 108, 109

startup inventory Tritium inventory required by new reactors to account for the initial tritium losses (processing time, trapping in components...). 12, 13

stellarator Toroidal fusion reactor using magnetic fields to confine the plasma. The difference with the tokamak is the twisted magnetic coils and the absence of a central solenoid inducing a current in the plasma. 4, 5

STEP Spherical Tokamak for Electricity Production. 6

strike point Location on the divertor where the separatrix crosses the solid target. It is where the highest heat and particle fluxes are observed. xiii, 8, 72, 75–80, 82

T

T tritium. 2

TBR tritium breeding ratio. 12, 13

TDS Thermo-Desorption Spectroscopy. xiv, xv, 17, 28, 46–48, 108–111, 113

TEM Transmission Electron Microscopy. xiii, 96, 98

tendril Nanometre-thick columns forming the fuzz. xiii, 25, 95, 96

TESSIM Tritium Extraction System SIMulator. 29

thermophoresis See Soret effect. 16

TMAP7 Tritium Migration Analysis Program, Version 7. 29

TNC Truncated Newton method. 47, 48

tokamak Toroidal fusion reactor using magnetic fields to confine the plasma. Acronym for "TOroidalnaia KAmera s MAgnitnymi Katouchkami", which means "Toroidal chamber with magnetic coils". 4–7, 25, 26, 28, 71, 85

transmutation Conversion of a chemical element into another chemical element by changing the number of neutrons or protons in the nucleus. 85

transmutation gas Gas produced by transmutation (typically helium or hydrogen). 15

trap mutation Process where over-pressurised helium clusters eject a metal lattice atom creating a Frenkel pair. 22, 89, 91, 93, 94, 99

trapping Process involving a particle being retained in a potential energy well. 7, 12, 17

U

UKAEA United-Kingdom Atomic Energy Authority. 6

V

V&V Verification and Validation. 40

vacancy Defect in the lattice where a metal atom is missing. 17, 18, 22, 23, 91, 93

W

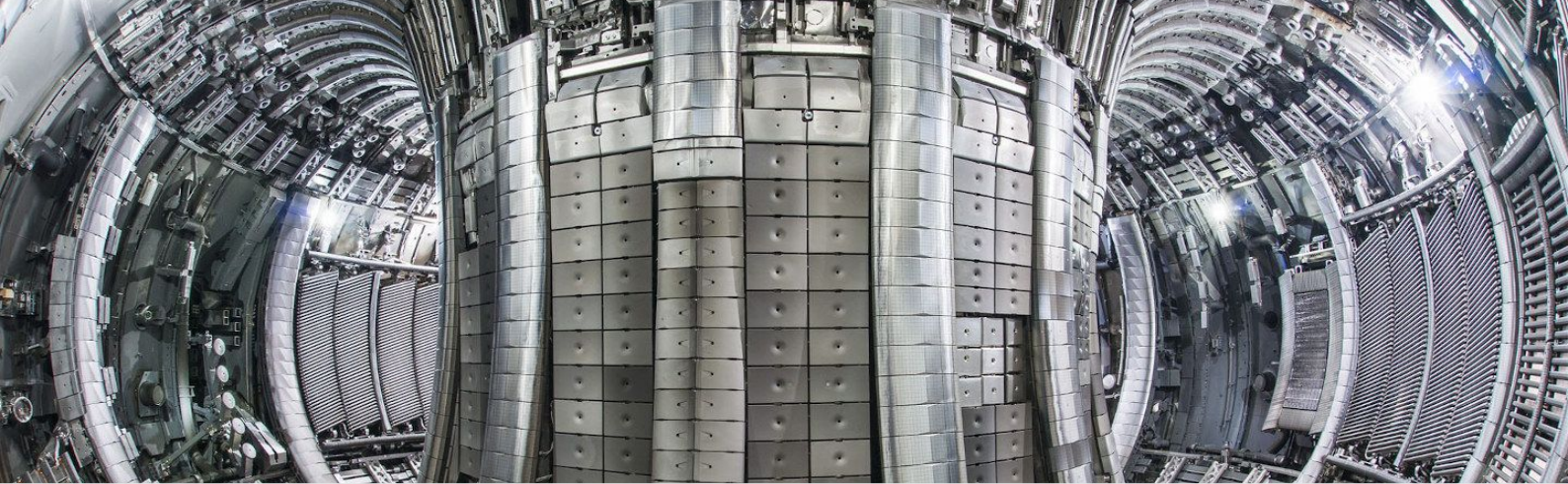
W tungsten. xiv, xv, 7, 8, 16, 17, 22–28, 55, 95, 98, 100, 101, 108

WCLL Water-Cooled-Lithium-Lead. 12

WEST Tungsten Environment Steady state Tokamak. xii, xiii, 8, 71–73, 78, 79, 81–83

X

X-point Point in space where the poloidal field has zero magnitude. 8, 71



1 Fusion: general introduction

1.1 Thermonuclear fusion

The fundamental principle of nuclear fusion is to fuse two light nuclei into a heavier nucleus. The mass difference between the products and the reactants is released in the form of energy (see Equation 1.1).

$$E = \Delta mc^2 \quad (1.1)$$

where Δm is the mass difference, c is the speed of light in vacuum. This process is the opposite process of nuclear fission, powering the current nuclear plants.

When looking at the different binding energies per nucleon of the elements (see Figure 1.1), it becomes clear that light elements release energy from fusion and heavy elements release energy from fission.

- 1.1 Thermonuclear fusion 1
- 1.2 Tokamaks: how to bottle a star 3
- 1.3 The tritium issue 11
- 1.4 Helium and Hydrogen in metals 13
- 1.5 Problem definition . . 28

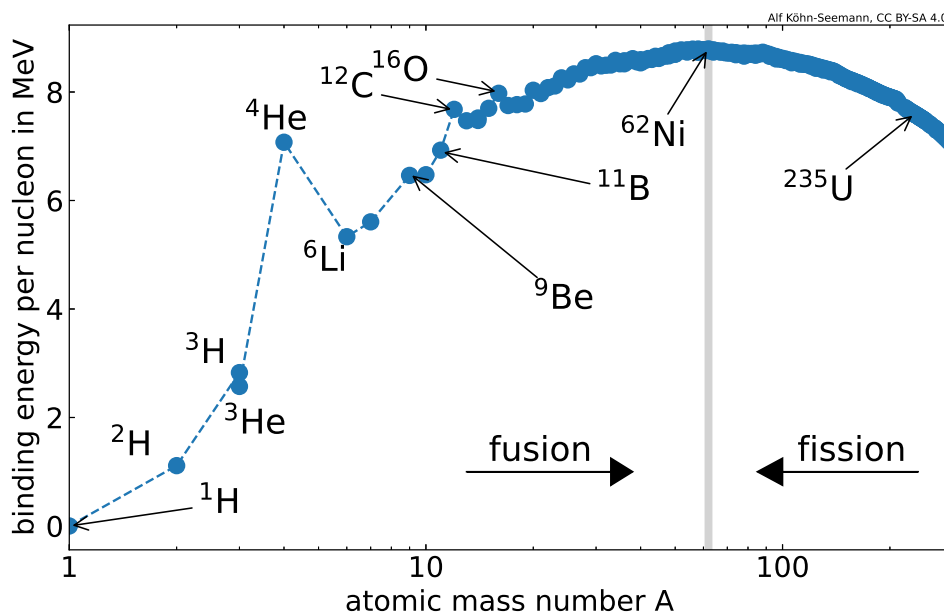


Figure 1.1: Binding energy per nucleon [3].

Nuclei are positively charged. To be able to fuse, they must overcome the Coulomb barrier induced by the electromagnetic repulsion (see Figure 1.2). This Coulomb barrier increases with the charge of the nuclei (i.e. the number of protons). This means that

the nuclei must collide with a high enough velocity. At the atomistic scale, the velocity v_{th} is a function of temperature (see Equation 1.2). This is one of the reasons why the probability of a fusion reaction is temperature dependent.

$$v_{\text{th}} = \sqrt{\frac{k_B T}{m}} \quad (1.2)$$

where $k_B = 1.3806 \times 10^{-23} \text{ m}^2 \text{ s}^{-2} \text{ kg K}^{-1}$ is the Boltzmann constant, T is the nucleus temperature in K and m is the nucleus mass in kg.

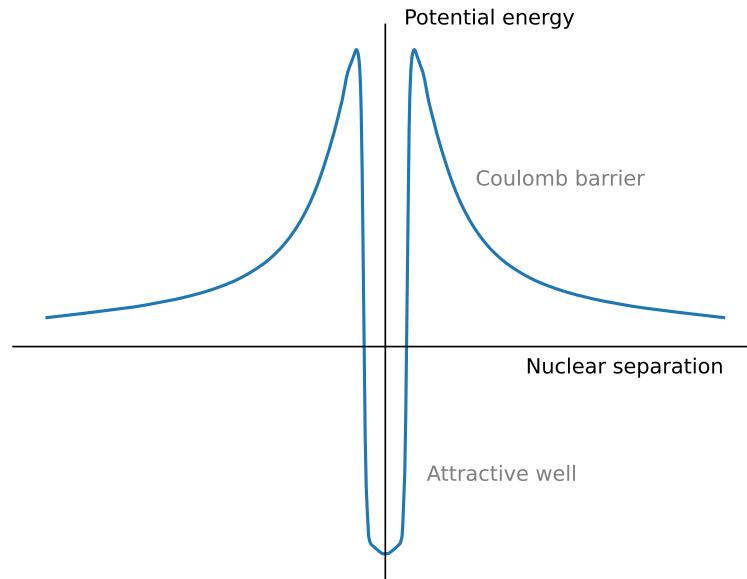
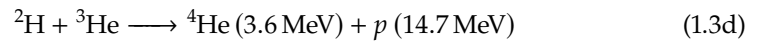
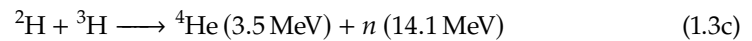
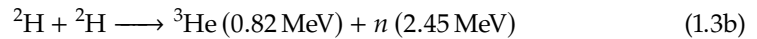
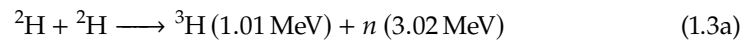


Figure 1.2: Evolution of the potential energy of two nuclei with their relative distance. Reproduced from [4].

Hydrogen, as the lightest element, has the lowest fusion temperature. It is also the most abundant element on Earth (although bound to other elements). Depending on which hydrogen isotope is used, different fusion reactions are possible (see Equation 1.3) [5].

[5] Forrest et al. (2012)



Each of these reactions has a different cross-section (measure of the reaction probability). The deuterium (D)-tritium (T) reaction is the one with the highest cross-section at 'low' temperature (see Figure 1.3). This is the reason why this reaction has been the focus of nuclear fusion for decades. More recently, private companies have started experimenting with more exotic reactions like proton-boron (TAE Technologies) or D- ${}^3\text{He}$ (Helion Energy).

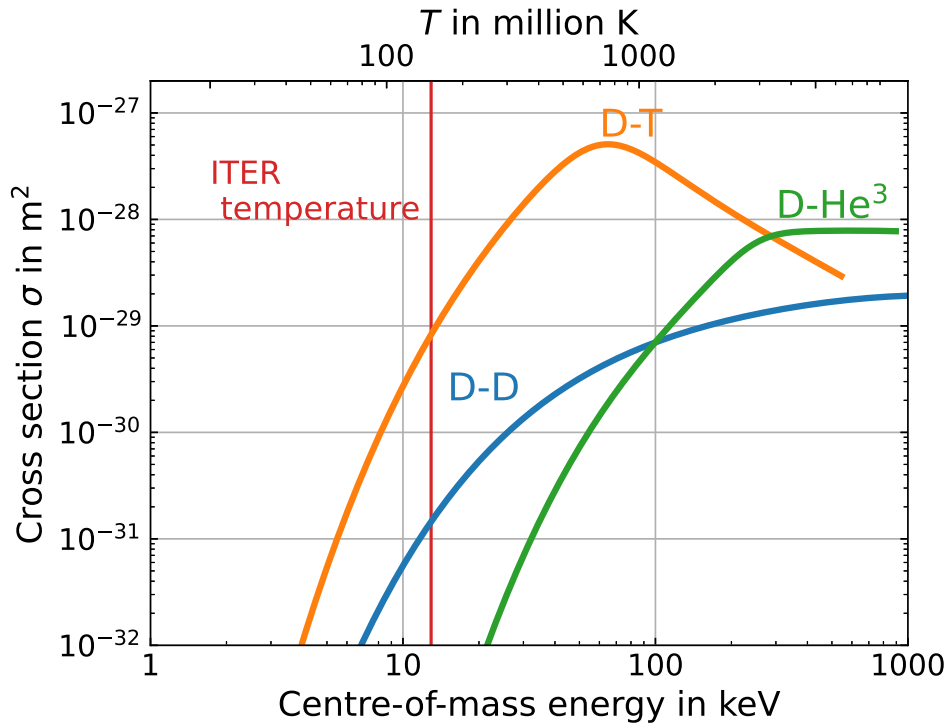


Figure 1.3: Fusion cross sections [5].

1.2 Tokamaks: how to bottle a star

1.2.1 Technology [4]

As explained above, for fusion to occur, the fuel must be heated up to millions of degrees. At these temperatures, the DT gas becomes a plasma where electrons are torn out from the nuclei. The principle of magnetic confinement reactors is to trap the electrically charged particles in a magnetic cage. The electrons and ions then gyrate around the magnetic field lines and the Larmor radius of the gyration is given by:

$$R = \frac{\sqrt{2mT}}{eB} \quad (1.4)$$

where m is the mass of the particle, T its temperature, e its charge and B the magnetic field. In a hot plasma (10 keV) with a strong magnetic field of 3 T, the Larmor radius of ions is ≈ 1 mm, which is much smaller compared to the size of a reactor. The Larmor radius of an electron is orders of magnitude smaller due to its lower mass. Straight magnetic lines can therefore confine charged particles in the direction perpendicular to the field lines. However, the particles are not confined in the parallel direction.

This issue can be solved by closing the field lines, forming a torus-shaped magnetic field. However, this configuration poses another problem: bending the field lines creates a magnetic field gradient in the radial direction. This magnetic field gradient and the centrifugal force cause the particles to drift upwards (or downwards depending on their charge). Due to this drift, the particles end up escaping the magnetic confinement until they touch the walls of the chamber and neutralise (making it impossible for them to fuse).

Two options exist to compensate this drift. The first is to add a poloidal component to the magnetic field and twist the magnetic lines. This is done by inducing a current in the plasma thanks to a central solenoid (see Figure 1.4). This configuration is called

Tokamak which stands for ‘toroidalnaia kamera s magnitnymi katouchkami’ (toroidal chamber with magnetic coils).

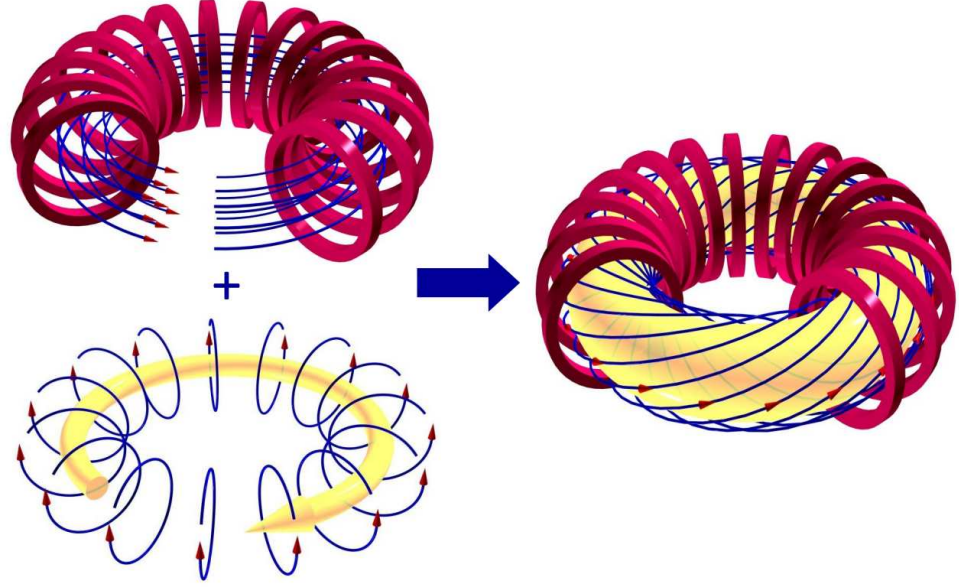


Figure 1.4: Magnetic field lines in a tokamak. Contribution of the toroidal and poloidal components.

The second option is to twist the magnetic field by twisting the toroidal coils themselves. This configuration is called a stellarator and has the advantage of not having an induced current and is therefore inherently steady-state. The tokamak, on the other hand, is a pulsed device. This is because the central solenoid has a limited capacity. The main drawback of the stellarator is the complexity of the coils. Since each coil has a unique shape, the cost of manufacturing such a reactor is higher than tokamaks for which coils can be manufactured in series.

1.2.2 Triple product

The power balance in a fusion reactor is given by [4]:

$$\frac{\partial W}{\partial t} = P_{\text{fusion}} + P_{\text{heating}} - P_{\text{losses}} \quad (1.5)$$

W is the thermal energy density stored in the plasma and can be expressed in J m^{-3} by:

$$W = 3nT \quad (1.6)$$

where n is the plasma density in m^{-3} and T is the plasma temperature in J. P_{fusion} , expressed in W m^{-3} , is the power density generated from fusion reactions themselves and can be expressed by:

$$P_{\text{fusion}} = n_D n_T \langle \sigma \rangle E \quad (1.7)$$

where n_D and n_T are the densities in m^{-3} of deuterium and tritium respectively, $\langle \sigma \rangle$ is the DT reactivity in $\text{m}^3 \text{s}^{-1}$ and E is the energy of the fusion reaction in J. Because the neutrons have little interaction with the plasma, $E \approx E_\alpha = 3.56 \text{ MeV}$. Moreover, assuming a 50%-50% mixture of deuterium and tritium, $n_D = n_T = \frac{1}{2}n$. The fusion power can therefore be written as:

$$P_{\text{fusion}} = \frac{1}{4}n^2 \langle \sigma \rangle E_\alpha \quad (1.8)$$

The amplification factor Q defines the ratio of the fusion power by the heating power. The heating power P_{heating} is therefore written as:

$$P_{\text{heating}} = \frac{P_{\text{fusion}}}{Q} \quad (1.9)$$

Finally, P_{losses} is the rate at which the plasma loses energy, either by losing mass (particles escaping the magnetic cage) or by radiation. It is characterised by an energy confinement time τ_E and can be expressed as:

$$P_{\text{losses}} = \frac{W}{\tau_E} = \frac{3nT}{\tau_E} \quad (1.10)$$

Assuming energy equilibrium (i.e. $\frac{\partial W}{\partial t} = 0$), Equation 1.5 can therefore be written as:

$$P_{\text{losses}} = P_{\text{fusion}} + P_{\text{heating}} \quad (1.11)$$

$$\Leftrightarrow \frac{3nT}{\tau_E} = \frac{1}{4}n^2 \langle \sigma \rangle E_\alpha + \frac{P_{\text{fusion}}}{Q} \quad (1.12)$$

Re-arranging the terms, one can obtain:

$$nT\tau_E = \frac{12T^2}{\langle \sigma \rangle E_\alpha} \cdot \frac{1}{1 + \frac{1}{Q}} \quad (1.13)$$

$nT\tau_E$ is known as the *triple product*, a figure of merit describing the performance of a fusion reactor. Equation 1.13 gives the triple-product required to achieve a given amplification factor Q at a given temperature T .

When P_{heating} approaches zero (i.e. the auxiliary heating systems are shut down), the amplification factor Q approaches ∞ . Therefore:

$$nT\tau_E \rightarrow \frac{12T^2}{\langle \sigma \rangle E_\alpha} \quad (1.14)$$

The quantity $T^2/\langle \sigma \rangle$ has a minimum around $T = 14$ keV. Furthermore, when $10 \text{ keV} < T < 20 \text{ keV}$, the DT reactivity can be approximated by $\langle \sigma \rangle \approx 1.1 \times 10^{-24} T^2$.

Equation 1.14 can therefore be written as:

$$nT\tau_E \geq 3 \times 10^{21} \text{ keV s m}^{-3} \quad (1.15)$$

This is known as the Lawson criterion, which needs to be satisfied in order to reach *ignition* ($Q = \infty$).

Fusion devices can therefore be classified into three categories. Stars like our Sun have very high confinement times and densities while remaining at relatively low temperatures (the sun core is at 1.2 keV). Magnetic confinement devices (tokamaks, stellarators, etc.) exhibit temperatures orders of magnitude higher than stars but have confinement times of the order of ~ 1 s. A third way of achieving fusion is to heat and compress a target of fuel with either lasers (NIF [6], Laser Mega Joule [7]), pistons (General Fusion) or by smashing it at high speed with a projectile (First Light Fusion). These devices, known as *inertial fusion devices*, exhibit extremely high densities ($\sim 10^{31} \text{ m}^{-3}$) but short confinement times ($\sim 10^{-11}$ s).

[6] Zylstra et al. (2022)

[7] Miquel et al. (2016)

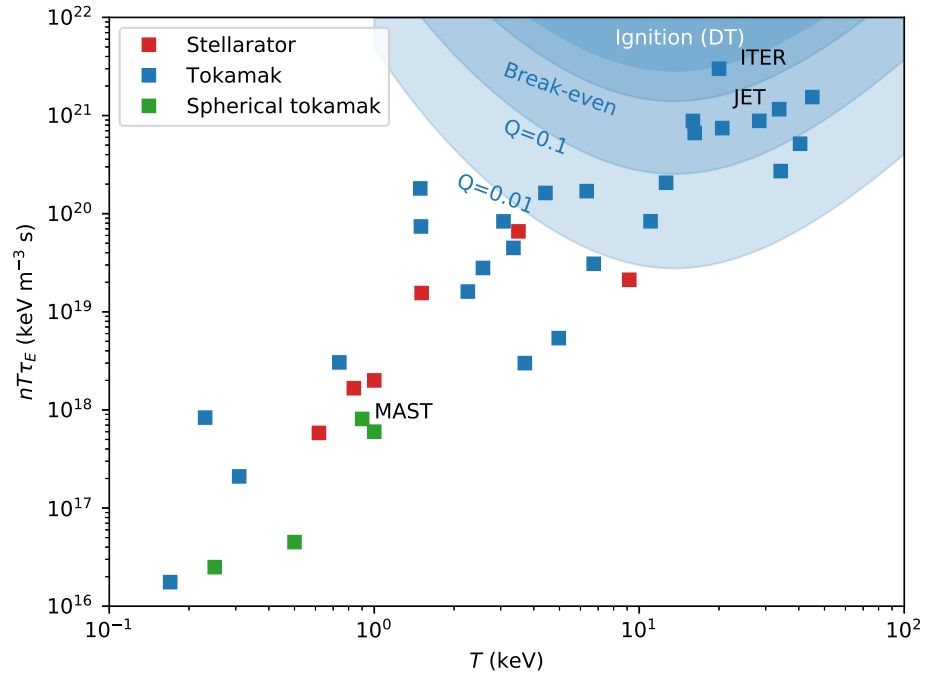


Figure 1.5: Triple product. An interactive version of this plot is available at [14].

So far, no fusion device has been able to even reach *break-even* ($Q = 1$) (see Figure 1.5). The record of $Q = 0.68$ by the European tokamak Joint European Torus (JET) and was performed in 1997 [8]. The objective of the International Thermonuclear Experimental Reactor (ITER) tokamak, currently under construction in France, is to demonstrate an amplification factor of $Q = 10$ over 400 s [9]. Note that ITER will not produce any electricity as this will be the role of a future fusion reactor: DEMOnstration power plant (DEMO) [10]. Other designs aim at demonstrating plasma gain (i.e. $Q > 1$) sooner than ITER and at a smaller scale (see Figure 1.6). This is the case of SPARC and ARC developed by Commonwealth Fusion Systems and MIT [11, 12] or STEP designed by the United-Kingdom Atomic Energy Authority (UKAEA) [13].

[8] Mailloux et al. (2022)

[9] Casper et al. (2013)

[10] Federici et al. (2014)

[11] Sorbom et al. (2015)

[12] Creely et al. (2020)

[13] Wilson et al. (2020)

1.2.3 Plasma-facing materials

The walls of a fusion reactor are exposed to intense heat and particle fluxes. The choice of Plasma Facing Materials (PFMs) is therefore crucial.

An appropriate PFM must have good thermal properties to withstand the extreme heat fluxes. To minimise electric arcs, the materials must have a high electrical conductivity. A high thermal conductivity is required as well as a very high melting point to enhance heat exhaust but also minimise the impact of arcing (material release from erosion) [15, 16]. The material must also resist to thermal shock encountered during short plasma discharges or transient events in the plasma [17].

[15] Ivanova (2012)

[16] McCracken (1980)

[17] Van den Kerkhof et al. (2021)

In order to maximise the components' lifespan, PFMs must resist erosion. This is even more important when the eroded particle reduce plasma performances by making it radiate and cool down.

The choice of a PFM is also critical from the nuclear safety point of view. First, the quantity of tritium retained in the materials need to be minimised (this point will be detailed in Section 1.3). Second, neutron activation of the material can increase the quantity of radioactive waste and must be minimised.

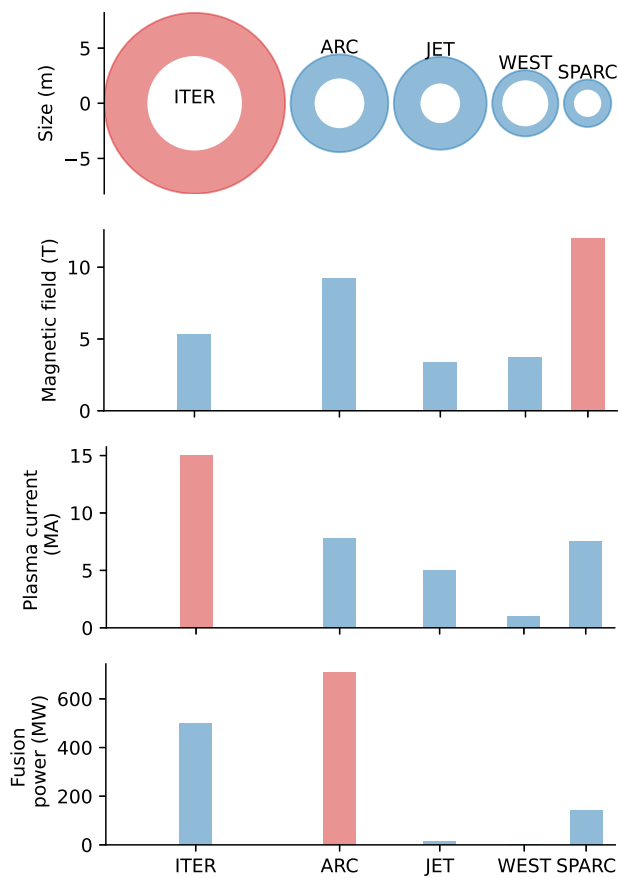


Figure 1.6: Comparison of the tokamaks ITER, JET, ARC, WEST and SPARC. Data from [14].

One of the first PFM was Carbon fiber composite (CFC) [18]. CFC had the great advantage of not melting and withstand very high heat fluxes. Using CFC also increased the plasma performances greatly [19]. Unfortunately, graphite being porous, hydrogen (and therefore tritium) retention was high [20]. Plus carbon can react with plasma particles forming methane. Methane is then deposited on locations hard to access in the reactor trapping tritium even more. For these two safety reasons, CFC was replaced with Tungsten (W) or beryllium (Be) (or both). The advantage of Be is that it creates a stable oxide. The formation of this oxide layer consumes oxygen and reduces the oxygen impurity level in the plasma.

W has a very high melting point (3422 °C) and retains less tritium [21]. However, W being a high-Z element, eroded W will make the plasma radiate and cool it down. For this reason, the ITER divertor will be made of W but the first wall (which has a large surface area) will be made of Be.

1.2.4 Divertor

In a fusion reactor, heat and particles (fusion ashes) need to be extracted. In most tokamaks, the escaping plasma is diverted towards a dedicated component that is heat-resistant. Such a configuration is called a *divertor* configuration. The divertor

[18] Linke et al. (2019)

[19] Federici et al. (2001)

[20] Sugiyama et al. (2004)

[21] Pajuste et al. (2021)

allows the creation of a X-point and a separatrix decoupling the plasma edge from the walls. The X-divertor is a common configuration (used in ASDEX, WEST, JET, ITER) but more advanced configurations exist such as the Super-X divertor (MAST-U) [22], X-Point Target (SPARC) [23, 24] or the Snowflake configurations [25].

[22] Havlíčková et al. (2015)

[23] Rodriguez-Fernandez et al. (2022)

[24] Kuang et al. (2020)

[25] Ryutov et al. (2015)

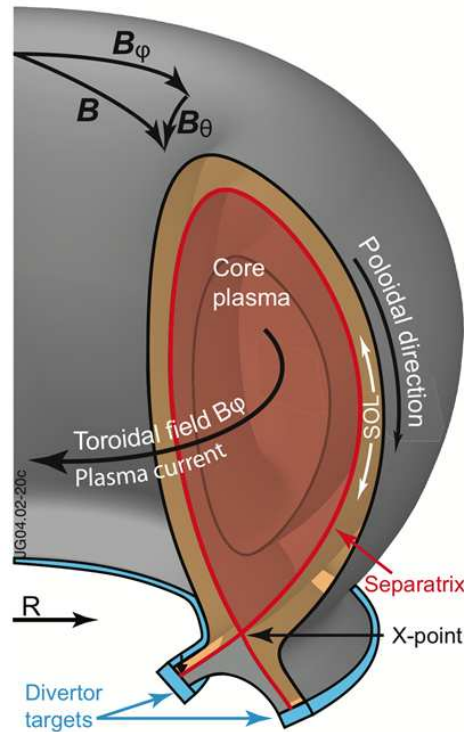


Figure 1.7: Sketch of the tokamak divertor configuration (source: EFDA-JET).

In a divertor configuration, the intersection between the magnetic field lines and the targets are called *strike points*. The X-divertor has two strike points on the inner and outer targets (see Figure 1.7). At these strike points, the targets will experience very intense heat and particle fluxes (see Figure 1.8).

The ITER divertor will be composed of 54 cassettes (see Figure 1.9). Each cassette is made of two targets - the Inner Vertical Target (IVT) and Outer Vertical Target (OVT) -, a dome and two reflector plates. The inner and outer strike points (respectively ISP and OSP) will be located on the IVT and the OVT. These elements are themselves made of rows, called Plasma Facing Units (PFUs), of small unit bricks of a few dozens of millimetres called monoblocks. In ITER, the IVT has 16 PFUs and the OVT has 22 PFUs. Monoblocks are typically made of a W substrate with a cooling pipe running through. This cooling channel is necessary to keep the component's temperature below its operating limit and exhaust heat.

[27] Vizvary et al. (2020)

[28] Huang et al. (2016)

[29] Hirai et al. (2016)

[30] Domptail et al. (2020)

[31] You et al. (2018)

[33] Durif et al. (2019)

[34] Durif (2019)

[35] Visca et al. (2018)

Several monoblock designs are currently studied for DEMO with varying dimensions, different materials for the cooling pipe or the interlayer, etc. [27–30]. The main candidate is the ITER-like design, the type of monoblock that will be used in ITER [29]. This design has a W substrate with a CuCrZr cooling pipe and a Cu interlayer for compliance. In ITER, monoblocks will be 12 mm-thick whereas they will be thinner (4 mm) in DEMO [31].

Studies on ITER-like monoblocks have demonstrated the resistance of the monoblock design to high heat loads while investigating the effect of W recrystallisation [33–35] (see Figure 1.10).

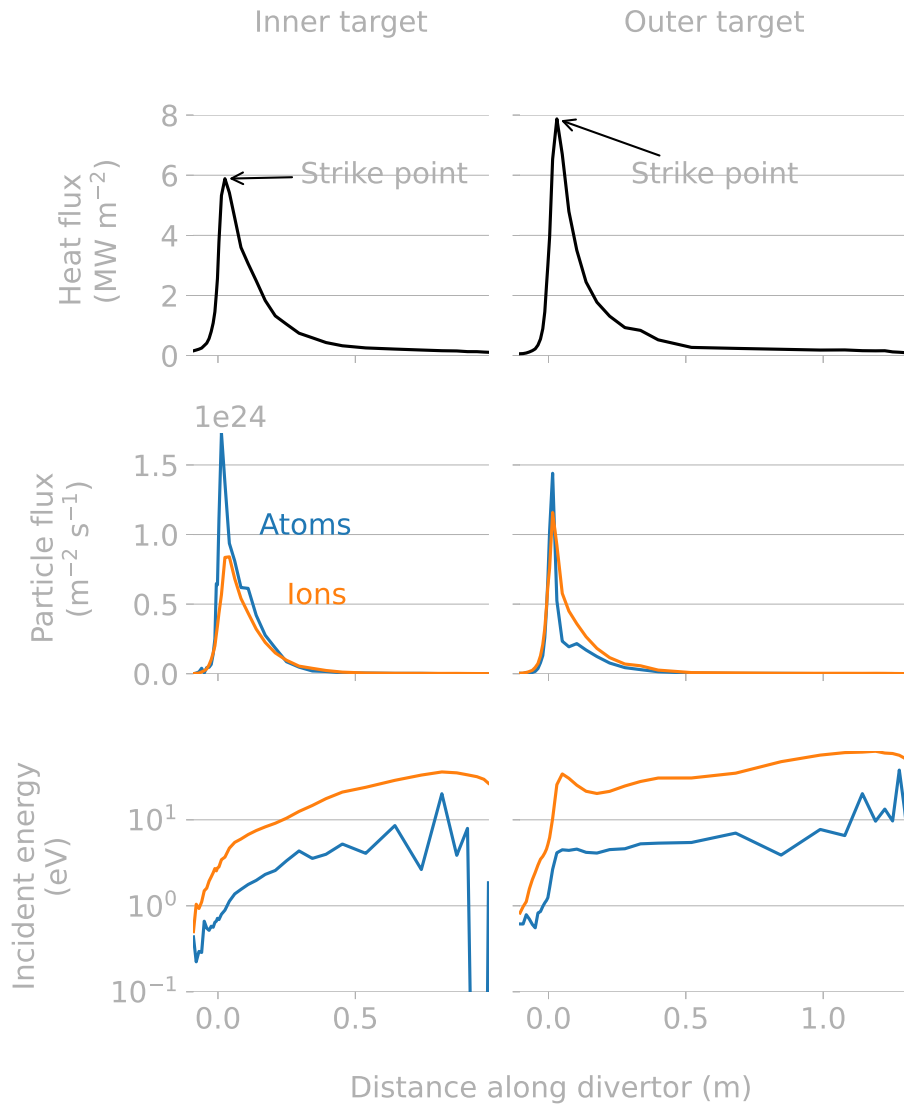


Figure 1.8: Heat flux, particle flux and particle energy along the ITER divertor computed by the edge-plasma simulation code SOLPS (shot #122399) [26].

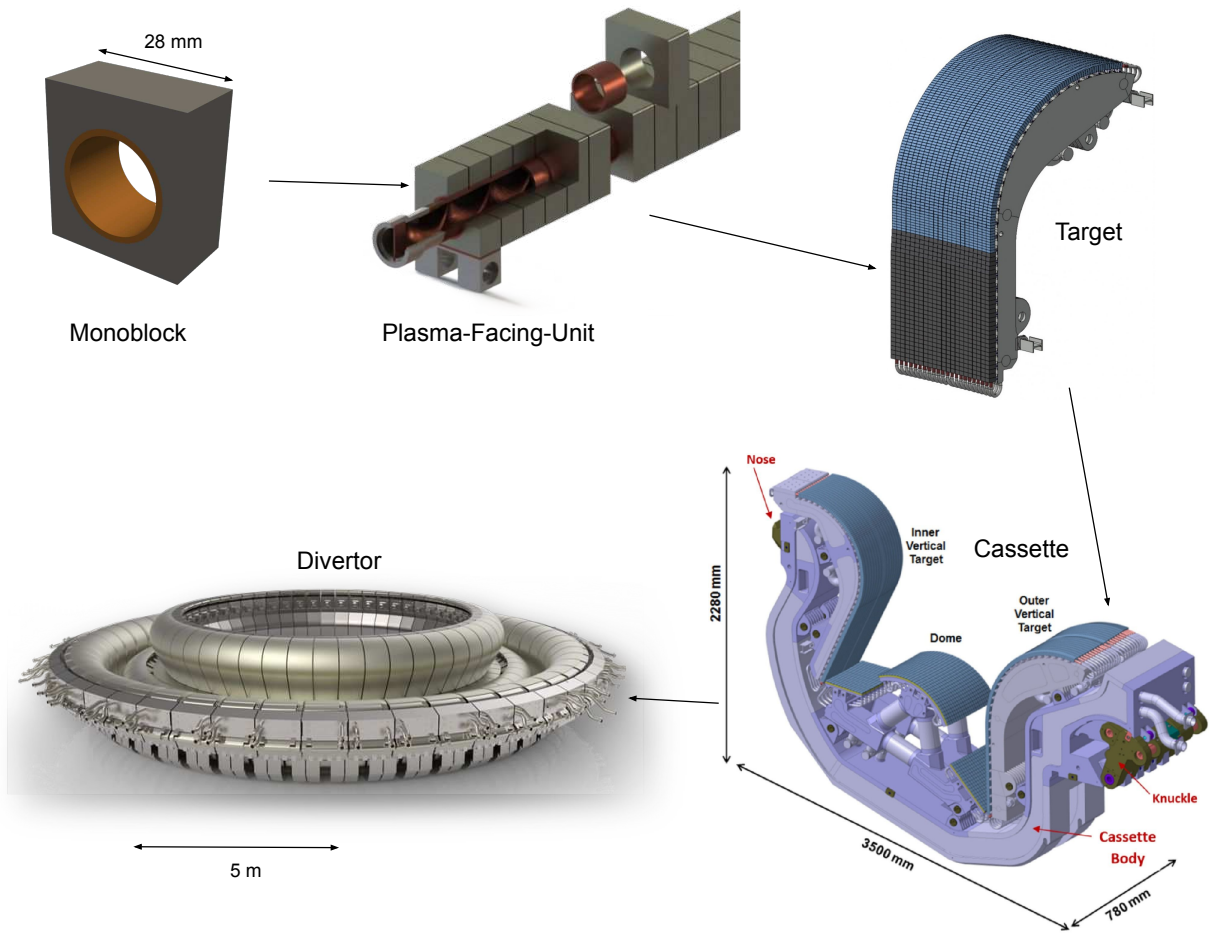
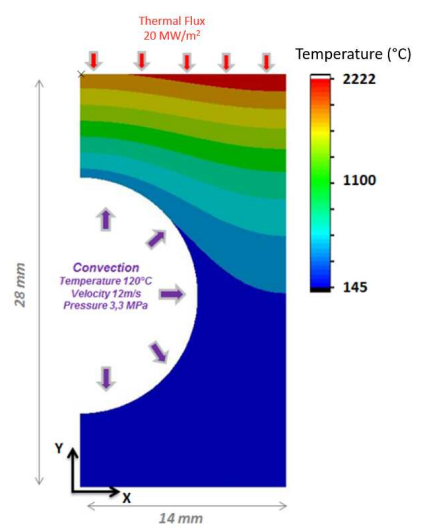
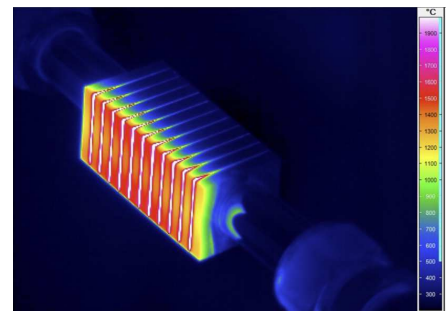


Figure 1.9: Structure of the ITER divertor. (images: ITER Organization, [32]).



(a) Simulated temperature field in a monoblock at 20 MW m^{-2} heat loading, water cooling at 120°C . Reproduced from [34].



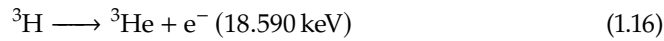
(b) Experimental measurement of monoblocks thermal response at 20 MW m^{-2} heat loading, water cooling at 130°C . Reproduced from [35].

Figure 1.10: Thermal response of ITER-like monoblocks.

1.3 The tritium issue

Tritium is a radioactive isotope of hydrogen with a half-life is 12.32 years [36]. It decays into ^3He emitting a beta particle (see Equation 1.16).

[36] Jordan et al. (1967)



This is an issue for both the fuel supply chain and nuclear safety.

1.3.1 Breeding

Due to its radioactive nature, tritium is very rare on Earth. The current reserve of tritium in the world is a few dozens of kilograms. It is naturally produced by interaction of cosmic rays with the nitrogen in the atmosphere (0.2 kg per year). Tritium is however produced in larger quantities in fission CANada Deuterium Uranium reactors (CANDUs) as a by-product (130 g per year per CANDU reactor [37]).

[37] Ni et al. (2013)

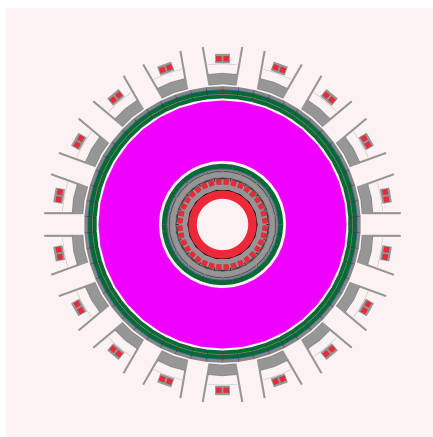
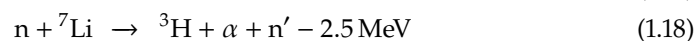
ITER itself will consume around 18 kg of tritium over the duration of its operation [38], which represent a yearly consumption of 0.9 kg for a 20-year lifetime. A 800 MWe DEMO-type commercial fusion reactor would burn around 300 g of tritium per day (≈ 100 kg a year).

[38] Glugla et al. (2007)

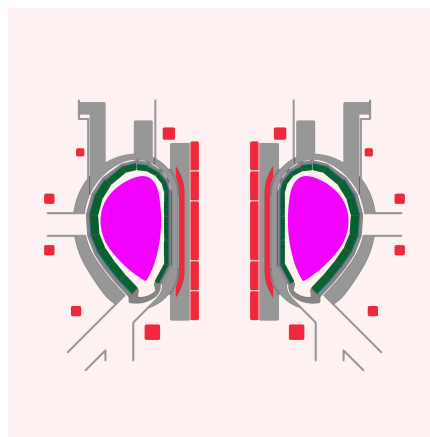
For all these reasons, tritium must be produced on-site in large quantities for a fusion economy to be possible.

To this end, the neutrons of the DT fusion reactions will be harnessed in a component containing lithium (Li) surrounding the plasma called the *breeding blanket* (see Figure 1.11).

Depending on the Li isotope, two reactions can occur:



(a) View from above.



(b) Side view.

Figure 1.11: DEMO model showing HCLL blankets ■, plasma ■, magnets ■, and structural steel ■. Reproduced from [39].

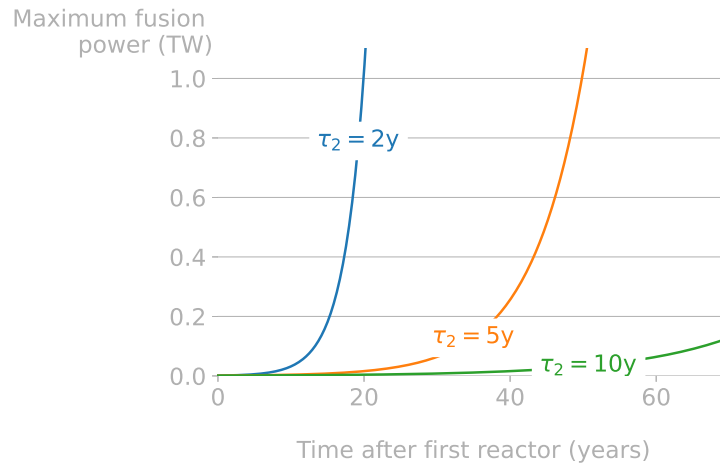


Figure 1.12: Evolution of the maximum fusion power on the grid for different doubling times.

Several breeding blankets designs have been proposed and divided in three main categories: ceramic concepts, liquid metal concepts, and molten-salts concepts. All designs differ in the choice of tritium breeder, coolant and geometry.

The European candidates for breeding blankets in DEMO are the Water-Cooled-Lithium-Lead (WCLL) [40, 41], the Helium-Cooled-Pebble-Bed (HCPB) [42–44], the Helium-Cooled-Liquid-Lead (HCLL) [45, 46] and the Dual-Coolant-Lithium-Lead (DCLL) [47, 48] [49].

The tritium breeding ratio (TBR) is defined as the number of tritium atoms produced per generated neutrons. In order to ensure tritium self-sufficiency, the TBR of the blanket must be greater than or equal to one [50]. A TBR greater than one can only be obtained by neutron multiplication with lead or Be.

Moreover, the TBR must account for:

- ▶ losses via permeation, trapping, radioactive decay (5% per year)
- ▶ safety reserve in case of interruption of the fuel cycle
- ▶ supply of new reactors, also called the *startup inventory*

The TBR target in conventional power plants is around 1.05 [39]. Though this would achieve self-sufficiency, it is not enough to sustain the development of a fusion energy market.

The evolution of the maximum fusion power on the grid P_{\max} can be expressed as:

$$P_{\max} = P_{\text{plant}} \times 2^{t/\tau_2} \quad (1.19)$$

where τ_2 is the doubling time (i.e. the time after which a plant has doubled its initial tritium inventory), t is the time, and P_{plant} is the power of a single plant. This expression assumes the only source of tritium is the reactors currently under operation.

Assuming $P_{\text{plant}} = 1 \text{ GW}$, with a doubling time $\tau_2 = 2 \text{ years}$, it will take 20 years to produce 1 TW of fusion electricity on the grid (see Figure 1.12). This time reaches 50 years with a doubling time of 5 years.

For fusion power plants to achieve a doubling time $\tau_2 \leq 3 \text{ years}$ (doubling times in power industry are typically 5 years), the TBR must be greater than 1.15 [51]. Other key parameters influence the required TBR (for a given doubling time) like the tritium burn-up fraction, the fueling efficiency, the plant availability factor...

[40] Aubert et al. (2020)

[41] Del Nevo et al. (2019)

[42] Hernández et al. (2018)

[43] Hernández et al. (2017)

[44] Pereslavtsev et al. (2017)

[45] Aubert et al. (2018)

[46] Jaboulay et al. (2017)

[47] Urgorri et al. (2017)

[48] Palermo et al. (2015)

[49] Federici et al. (2019)

[50] Abdou et al. (2015)

[39] Shimwell et al. (2019)

[51] Abdou et al. (2020)

Tritium transport in breeding blankets is crucial as trapped tritium in solid parts would increase the startup inventory. For a given doubling time, a higher startup inventory means a higher TBR requirement. The blanket inventory in the solid parts can be reduced by (1) reducing the amount of solid components (this will also increase the TBR [39]) (2) designing permeation barriers [52].

[52] Utili et al. (2022)

1.3.2 Safety

Tritium is also an issue in terms of nuclear safety. As a radioactive isotope, its ingestion - in the form of tritiated water HTO - is a health hazard. Its biological half-life (i.e. once ingested by humans) is around 10 days - which can be considered as low toxicity [53, 54]. Tritium's half-life once incorporated in organic compounds increases to 40 days and is associated with a higher toxicity [53]. To put tritium toxicity in perspective, it has been estimated that drinking 2 L of water with the highest permissible level of tritium contamination ($10\,000\text{ Bq L}^{-1}$) each day for a year results in a total radiation dose of 0.1 mSv, which is equivalent to two weeks natural radioactivity exposure [55].

[53] Bridges et al. (2007)

[54] Janssens (2007)

[55] Hyatt (2021)

[56] Honda et al. (2000)

[57] Roth et al. (2008)

[58] De Temmerman et al. (2017)

To limit the potential environmental releases due to a loss of vacuum accident, its inventory in fusion reactors must be limited [56]. In ITER for instance, the in-vessel inventory of tritium is limited to 1 kg including 120 g retained in cryo-pumps and 180 g of measurement uncertainties [57, 58]. This limit has been determined to avoid evacuation of population around the reactor in the event of a loss of vacuum accident.

[59] Arredondo et al. (2021)

[60] Shimada et al. (2018)

Moreover, as tritium can migrate in materials, components that have been in contact with it are considered as tritiated waste and must be handled. Tritium migration through complete material layers (permeation) to the cooling tubes [59, 60] can lead to contamination of coolants and must be taken into account in the detritiation process. Tritium permeation to the atmosphere must also be controlled.

[61] Liger (2018)

[62] Lefebvre et al. (2012)

Detritiation techniques are being developed to reduce the volume of tritiated waste in future fusion reactors [61]. These techniques mainly consist in heating the tritiated samples and recovering the tritiated gas [62] that can be reused as fuel. Tritium minimisation techniques such as Laser Induced Desorption or *baking* are also being developed to reduce the tritium inventory during operations [58].

[58] De Temmerman et al. (2017)

[52] Utili et al. (2022)

[63] Causey et al. (2012)

Permeation barriers are being studied to greatly reduce the permeation of tritium to the cooling fluids [52, 63, 64]. The idea is to coat inner and/or outer surfaces of cooling pipes with alumina-based coatings or ceramics (e.g. Al_2O_3 , Cr_2O_3 , Er_2O_3). Natural oxides are also considered for permeation barriers. These coatings can also act as an anti-corrosion barrier. The use of these permeation barriers - by definition minimising permeation - could potentially increase materials inventories.

[64] Utili et al. (2021)

1.4 Helium and Hydrogen in metals

This Section summarises the main processes at stake (see Figure 1.13) when helium (He) and hydrogen (H) particles interact with metals and with each other.

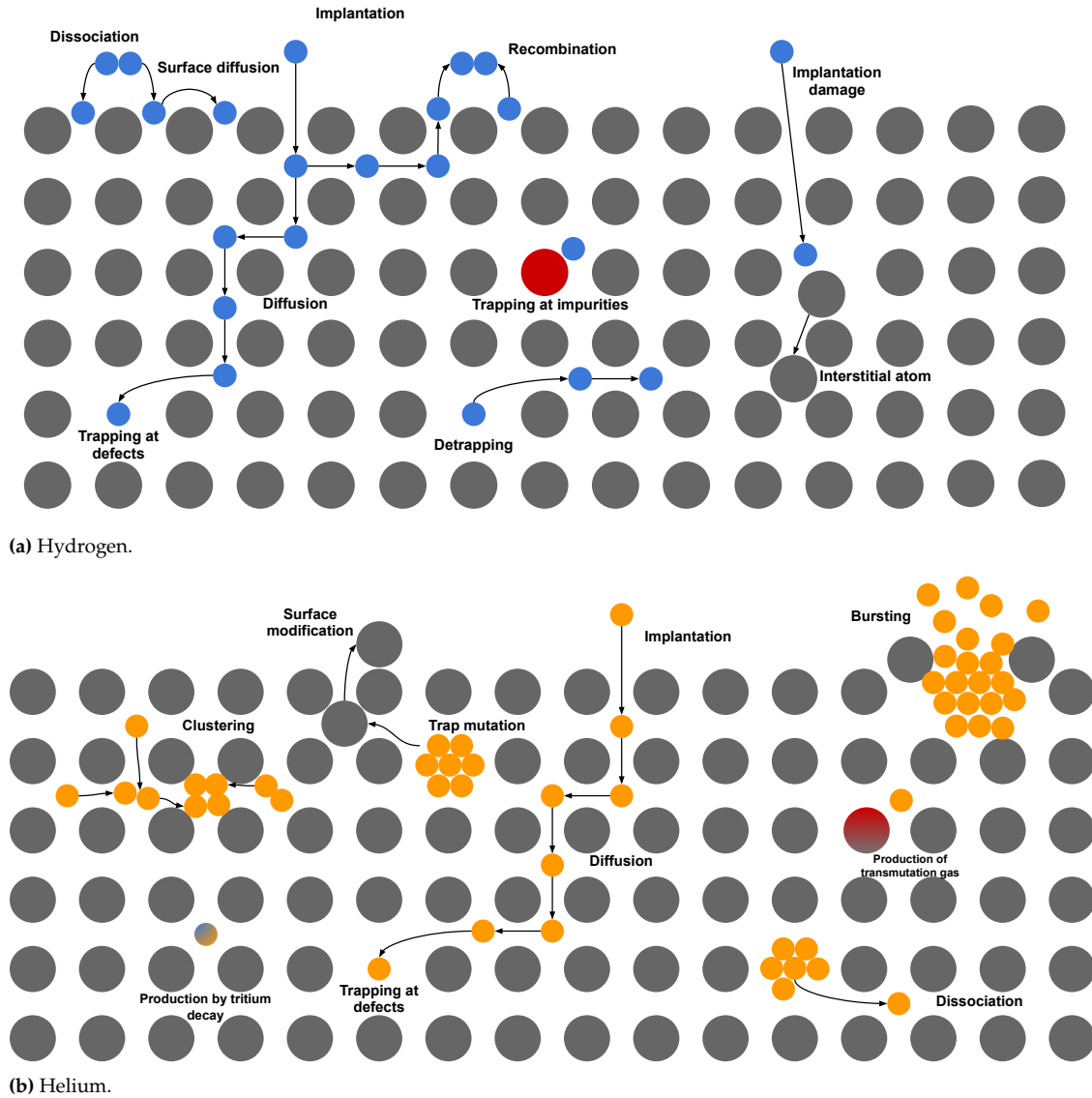


Figure 1.13: Interactions of solute species in tungsten.

1.4.1 Particle sources

Hydrogen

Deuterium and tritium being the fuel of fusion reactors, the primary source of hydrogen in the divertor is the plasma itself. The wall of a fusion reactor (first wall and divertor) is bombarded with high energy hydrogen ions. Due to their small size, these ions can penetrate the metal lattice and be implanted in the material.

Components are also exposed to neutral hydrogen particles either in the atomic or molecular form. This is also the case for the divertor region where fuel recycling can occur [65, 66].

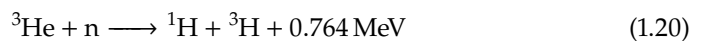
[65] Denis et al. (2019)

[66] Causey (2002)

[67] Shimada et al. (2017)

Tritium can also be produced by the neutron capture of helium-3 [67, 68] (see Equation 1.20 and Figure 1.14).

[68] Knoll (1989)



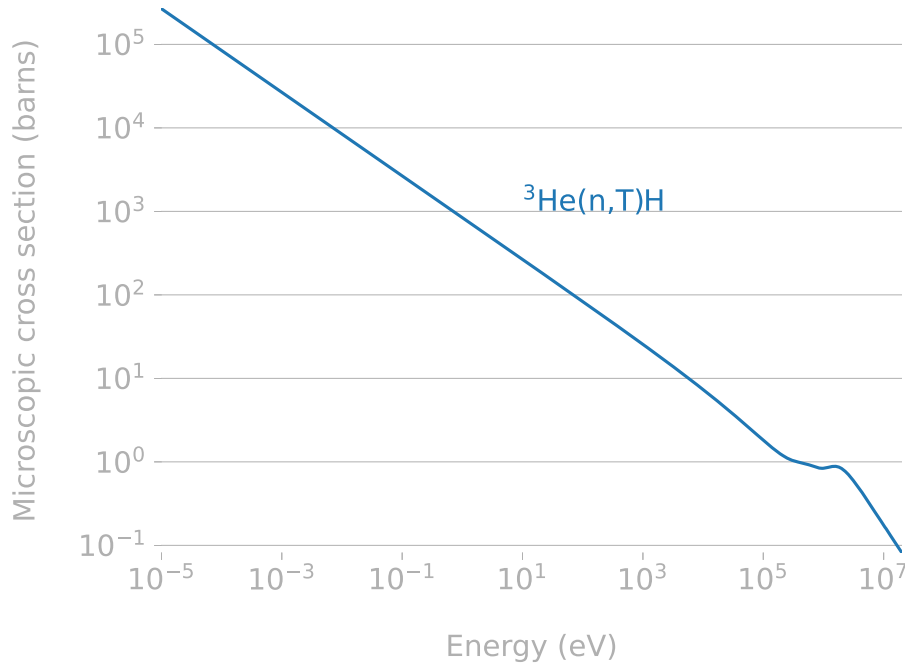


Figure 1.14: Cross section of the $^3\text{He}(n,T)\text{H}$ reaction [69].

Finally, interactions of lithium with neutrons represent a major source of tritium in tritium breeding blankets [70].

[70] Dark et al. (2021)

Helium

Helium is the product of the fusion reaction (see Equation 1.3). Therefore, the wall of a fusion reactor is also bombarded with helium ions. This is the primary source of helium in PFMs.

Helium can also be produced in materials indirectly. Since tritium decays into helium-3 (see Equation 1.16), regions with high tritium retention are expected to act as a source of helium over time [67]. Moreover, interactions of neutrons (from the fusion reactions) with metallic elements (e.g. tungsten or iron) can produce helium via transmutation [71]. This *transmutation gas* production has been estimated using well-established neutronics simulations (Monte-Carlo simulations modelling the path of neutrons in matter) [72, 73]. Depending on the position in the DEMO divertor, cumulative helium production over the course of three full power years (FPYs) could reach more than 400 appm.

[71] Watanabe et al. (2011)

[72] Gilbert et al. (2013)

[73] Gilbert et al. (2012)

1.4.2 H/W & He/W interactions

Diffusion

The repulsion of metal atoms with solute species creates wells of potential energy located at interstitial sites (see Figure 1.15). The solute atoms in metals can then jump from interstitial site to another thanks to thermal vibration. This process is called *diffusion*. The 'height' of the potential energy wells is called the *diffusion activation*

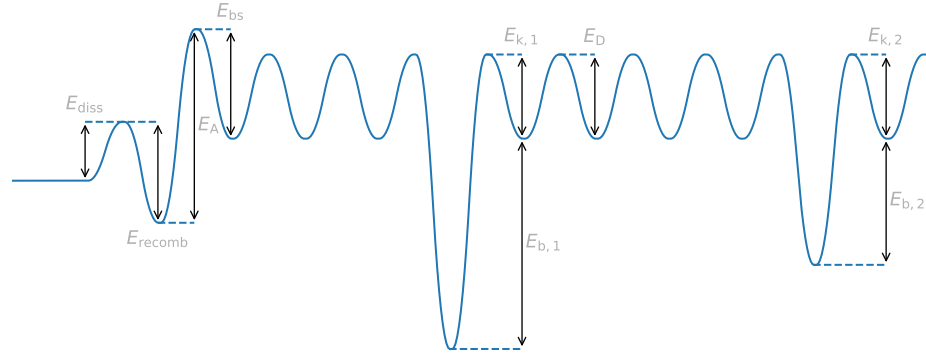


Figure 1.15: Simplified potential energy diagram showing two different types of defects.

energy or energy barrier E_D . Diffusion is therefore a thermally activated process governed by a diffusion coefficient D expressed in $\text{m}^2 \text{s}^{-1}$, which follows an Arrhenius law:

$$D = D_0 \exp(-E_D/k_B T) \quad (1.21)$$

where E_D is expressed in eV, T is the temperature in K, $k_B = 8.617 \times 10^{-5} \text{ eV K}^{-1}$ is the Boltzmann constant.

[74] Martínez et al. (2021)

[75] Hodille et al. (2017)

[76] Longhurst (1985)

[77] Benannoune et al. (2020)

[78] Boisse et al. (2014)

[79] Boisse et al. (2014)

[80] Lam et al. (2021)

[81] Behler (2015)

[84] Wang et al. (2020)

[85] Zhou et al. (2016)

[86] Kato et al. (2015)

[87] Liu et al. (2014)

[82] Faney (2013)

[88] Faney et al. (2014)

[89] Faney et al. (2015)

[90] Sefta (2013)

[91] Perez et al. (2017)

Diffusion can also be assisted by temperature gradients (called the *Soret effect* or *thermophoresis*) [74–76] or hydrostatic pressure gradients. The tungsten property to simulate the Soret effect (Soret coefficient or heat of transport) is currently missing from literature (for hydrogen). Hodille et al. used the properties of steel as an approximation [75]. Benannoune and coworkers performed hydrogen transport studies with hydrostatic pressure gradients showing it could have an impact of around 10% in steel components [77].

Diffusion coefficients (also called diffusivities) can be computed by Molecular Dynamics (MD) and Density Functional Theory (DFT). The principle of MD is to calculate the trajectory of atoms in a simulation box (see Figure 1.16). The trajectory of a particle i in a system of N particles can be computed from Newton's second law of motion:

$$m_i \vec{a}_i = \sum_{j=1, j \neq i}^N \vec{F}_{i,j} \quad (1.22)$$

where m_i is the mass of the particle, \vec{a}_i is its acceleration, $\vec{F}_{i,j}$ is the force applied to the particle due to its interaction with particle j . The forces between atoms is only a function of the interatomic potentials. These potentials can be found in literature or can be estimated from *ab initio* computations (DFT) [78, 79] or from methods based on machine learning [80, 81].

By measuring the trajectory of a diffusing species from MD simulations for a long time, its diffusion coefficient D can be estimated from Einstein equation [83]:

$$\lim_{t \rightarrow \infty} \frac{\langle R^2(t) \rangle}{6t} = D \quad (1.23)$$

where $\langle R^2(t) \rangle$ is the mean squared displacement of the species.

This modelling technique was used to estimate the diffusion coefficient of H in W [84–87] and for He in W [82, 88–91].

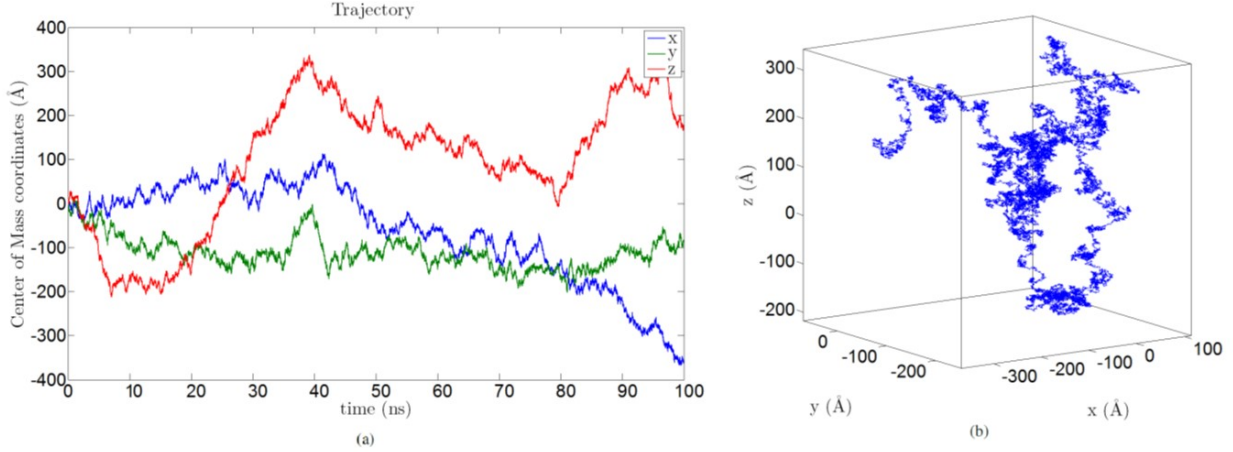


Figure 1.16: Example of the trajectory of a He₂ cluster in tungsten. Reproduced from [82].

Diffusivity of hydrogen has also been measured experimentally in W [92–94], copper and copper alloys (CuCrZr) [95] and other metals. Note that the diffusion coefficients measured experimentally are usually effective coefficients accounting for trapping effects (detailed below). Because He tends to cluster (as explained below), measuring its diffusivity experimentally is extremely complicated and therefore most estimations of He diffusion coefficients are numerical. Figure 1.17 is a collection of diffusivity values found in literature (measured experimentally or computed) for tungsten, copper and CuCrZr.

[92] Holzner et al. (2020)

[93] Frauenfelder (1969)

[94] Anderl et al. (1990)

[95] Anderl et al. (1992)

Trapping at defects

Due to the repulsion between solute species and the surrounding metal atoms, defects can act as wells of potential energy for solute species (see Figure 1.15). Once in that attractive well, species can escape it only if their kinetic energy (i.e. the temperature) is high enough. Species can be trapped at vacancies, dislocation loops, self-interstitial atoms (in the case of hydrogen in tungsten), impurities, etc.

The trapping process can be described as:



where H is the particle in an interstitial site (i.e. mobile), [] is the defect and [H] represents the particle trapped in the defect. The trapping rate and detrapping rate can be respectively expressed as:

$$k = k_0 \exp \frac{-E_k}{k_B T} \quad (1.25)$$

$$p = p_0 \exp \frac{-(E_b + E_k)}{k_B T} = p_0 \exp \frac{-E_p}{k_B T} \quad (1.26)$$

where E_k is the trapping energy in eV, k_B is the Boltzmann constant in eV K⁻¹, T is the temperature in K, E_b is the binding energy of the particle with the defect and $E_p = E_b + E_k$ is the detrapping energy. A common assumption is that $E_k = E_D$.

Each rate therefore has two parameters: the pre-exponential factor and the activation energy. These parameters can be identified from fitting Thermo-Desorption Spectroscopy (TDS) experiments. TDS experiments consist in loading a metal sample with the studied

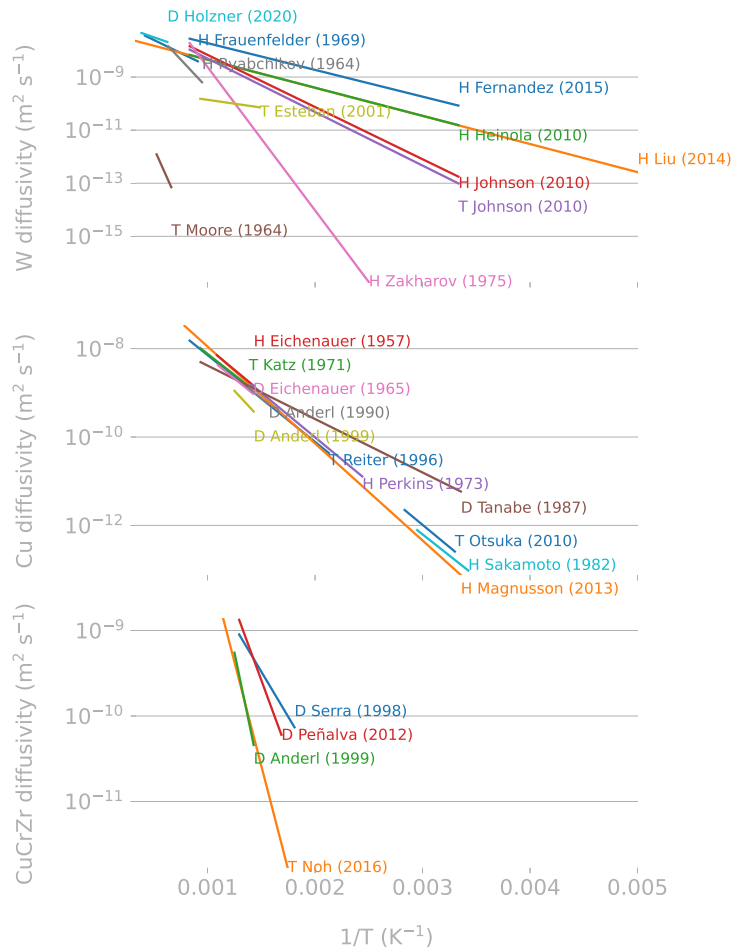


Figure 1.17: Diffusivity values for tungsten, copper and CuCrZr. Data from [96].

species (e.g. H or He) and heat it at different temperatures with a well controlled temperature ramp (e.g. 1 K s^{-1} , 10 K s^{-1} ...) while measuring the desorption flux. This results in a spectrum which typically has one or several desorption peaks corresponding to different traps (see Figure 1.18). Peaks appearing at high temperatures correspond to “deep” traps with a high detrapping energy E_p .

These parameters can also be obtained from DFT calculations [98–104].

Some defects can trap several hydrogen/helium atoms. For instance, up to approximately seven helium atoms can be trapped in a mono-vacancy at room temperature [89]. DFT calculations also show that defects like mono-vacancies, dislocations or grain boundaries can retain multiple hydrogen atoms (see Figure 1.19). As the number of trapped particles (helium or hydrogen) increases, the binding energy of a particle with the defect usually decreases. In other words, the more particles are trapped in a defect the easier it is for a hydrogen atom to escape. For instance, the binding energy of a helium atom in an empty mono-vacancy is around 4 eV and around 2.5 eV if the vacancy already retains four helium atoms [89]. Similarly, the binding energy of a hydrogen atom in a mono-vacancy varies from 0.5 eV (with six hydrogen atoms trapped) to 1.3 eV (empty vacancy) (see Figure 1.19).

Defects can either be pre-existent in the material (sometimes called *intrinsic* defects): impurities, grain boundaries, etc. They can also be caused by external factors (*extrinsic* defects) like particle bombardment (ions, neutrons) [106] or mechanical stress [77].

- [98] Hou et al. (2019)
- [99] Backer et al. (2017)
- [100] Backer et al. (2017)
- [101] Fernandez et al. (2015)
- [102] Lu et al. (2014)
- [103] Heinola et al. (2010)
- [104] Zhou et al. (2010)
- [89] Faney et al. (2015)
- [106] Ogorodnikova et al. (2003)
- [77] Benannoune et al. (2020)

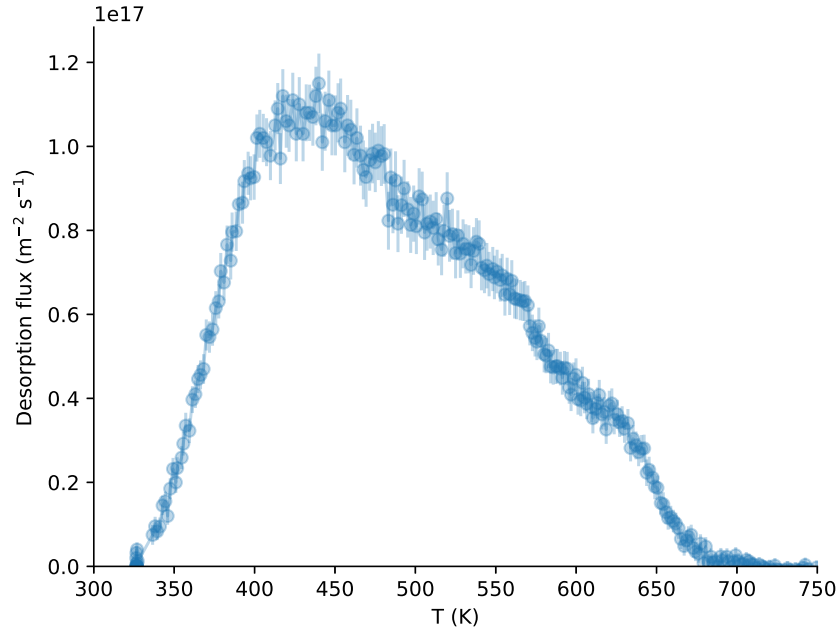


Figure 1.18: H TDS spectrum of pre-damaged W. Reproduced from [97].

Surface dissolution

When a surface is in contact with a gas, molecular species (e.g. H_2 , T_2 , $HD\dots$) can dissociate into mono-atomic species. After their dissociation, the atomic particles can be adsorbed on the surface (on adsorption sites) [107]. This dissociation is described by a sticking probability usually associated with an Arrhenius law $s = s_0 \exp(-E_s/k_B T)$. DFT calculations can calculate energy barriers for adsorption and migration of solute species on surfaces [108]. Studies have however shown that this process is not thermally activated (i.e. $E_s = 0$) [109, 110] but rather depends on the ratio of the surface concentration of the species (hydrogen or helium) by the concentration of adsorption sites. This quantity is called the *surface coverage* θ . When $\theta = 1$, the surface is fully saturated and when $\theta = 0$ all the adsorption sites are available. Moreover, the presence of impurities occupying adsorption sites can decrease the sticking probability of a species [111, 112].

Adsorbed particles can then be *absorbed* in the bulk (see Figure 1.15). This thermally activated process is associated with an absorption coefficient following an Arrhenius law $A = A_0 \exp(-E_A/k_B T)$. The absorption process is modelled using DFT and absorption activation energies E_A can be determined for different surface orientations [113–115].

All these processes (dissociation, adsorption and absorption) can be described by an absorption flux:

$$\varphi_{\text{abs}} = nK_{\text{abs}}P \quad (1.27)$$

where n is the absorption order, K_{abs} is the absorption coefficient expressed in $\text{m}^{-2} \text{s}^{-1} \text{Pa}^{-1}$ and P is the partial pressure of hydrogen in Pa.

Desorption of solute species at the surface is expressed by a desorption flux:

$$\varphi_{\text{des}} = K_{\text{des}}c_{\text{surface}}^n \quad (1.28)$$

[107] Hodille et al. (2021)

[108] Heinola et al. (2010)

[109] Alnot et al. (1989)

[110] Tamm et al. (1970)

[111] Dunand et al. (2022)

[112] Whitten et al. (1998)

[113] Johnson et al. (2010)

[114] Nojima et al. (2007)

[115] Ajmalghan et al. (2019)

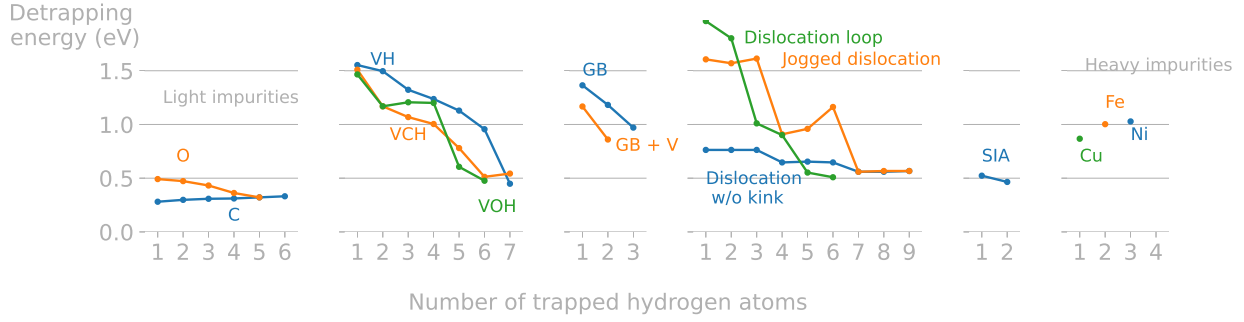


Figure 1.19: Detrapping energy of a hydrogen atom in several defects in tungsten: vacancies, impurities, self-interstitial atoms (SIA), grain boundaries (GB), in tungsten depending on the number of trapped hydrogen atoms. Reproduced from [105].

where K_{des} is the desorption coefficient expressed in $\text{m}^{-2+3n} \text{s}^{-1}$, c_{surface} is the surface concentration in m^{-3} , and n is the order of the desorption.

When the equilibrium between absorption and desorption is reached, $\varphi_{\text{abs}} = \varphi_{\text{des}}$, which gives:

$$nK_{\text{abs}}P = K_{\text{des}}c_{\text{surface}}^n \quad (1.29)$$

By rearranging Equation 1.29:

$$c_{\text{surface}} = \sqrt[n]{n \frac{K_{\text{abs}}}{K_{\text{des}}} \sqrt[n]{P}} \quad (1.30)$$

When the absorption/desorption order is $n = 1$ (monoatomic absorption):

$$c_{\text{surface}} = SP \quad (1.31)$$

This relationship is known as Henry's law of solubility and $S = K_{\text{abs}}/K_{\text{des}}$ is the material solubility expressed in $\text{m}^{-3} \text{Pa}^{-1}$.

When the absorption/desorption order is $n = 2$ (diatomic absorption):

$$c_{\text{surface}} = S\sqrt{P} \quad (1.32)$$

This equilibrium is known as Sievert's law of solubility and $S = \sqrt{2K_{\text{abs}}/K_{\text{des}}}$ is the material solubility expressed in $\text{m}^{-3} \text{Pa}^{-0.5}$. The solubility of tungsten, copper and CuCrZr are described in Figure 1.20.

The product of the solubility and diffusivity is called *permeability*.

Interface between materials

[116] Krom et al. (2000)

At the interface between two materials, the continuity of chemical potential has to be ensured [116]. The continuity of chemical potential is conveyed by the continuity of P , the local partial pressure of hydrogen at equilibrium. In a metal, P can be expressed from Sievert's law of solubility (see Equation 1.32):

$$P = (c_{\text{m}}^-/S^-)^2 \quad (1.33)$$

with c_{m} the concentration of mobile species in the material, S the solubility in the materials expressed in $\text{m}^{-3} \text{Pa}^{-0.5}$. At the interface between two metallic surfaces, the

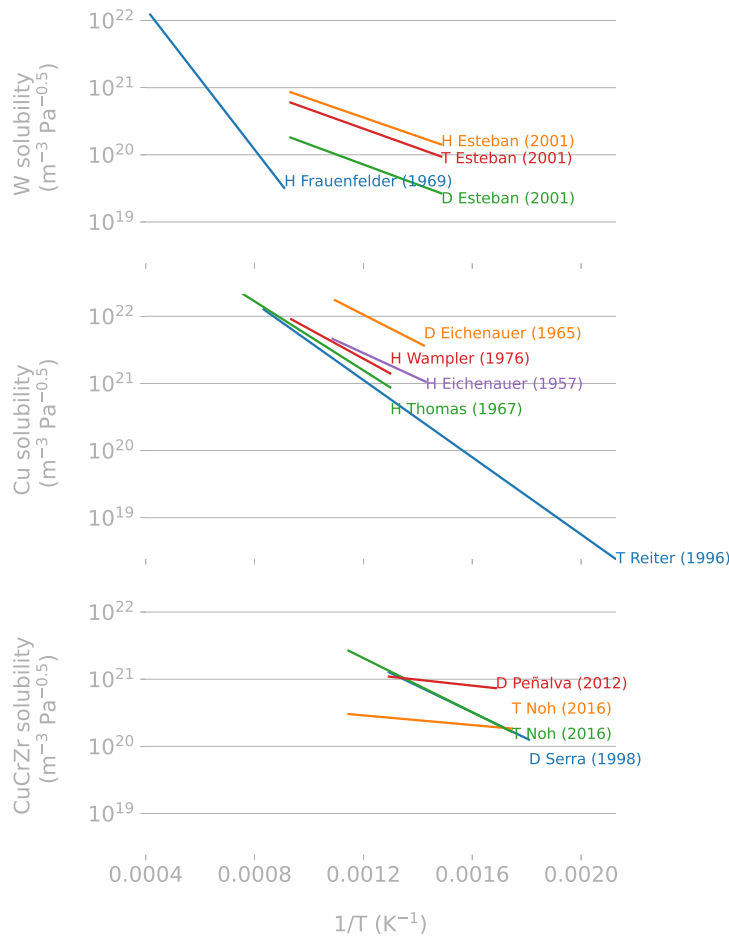


Figure 1.20: Solubility values for tungsten, copper and CuCrZr. Data from [96].

chemical potential continuity is therefore conveyed by the continuity of the quantity c_m/S :

$$(c_m^-/S^-)^2 = (c_m^+/S^+)^2 \quad (1.34)$$

In the case of a metal in contact with a non-metallic liquid behaving according to Henry's law (e.g. a molten salt):

$$(c_m^-/S^-)^2 = c_m^+/S^+ \quad (1.35)$$

with S the solubility of H in the materials expressed in $\text{m}^{-3} \text{Pa}^{-0.5}$ or $\text{m}^{-3} \text{Pa}^{-1}$.

A jump in concentration will therefore occur at the interface between two materials with different solubilities.

Advection in liquids

Advection occurs when a mobile species is in a liquid (molten salts, water, coolants...) and depends on the liquid velocity. This advective transport adds up to the diffusive transport.

Depending on the liquid velocity and the species diffusivity in this liquid, the mass transport can be predominated by one of the two phenomena. The Péclet number Pe is a dimensionless number employed to estimate this dominance.

$$\text{Pe} = \frac{\text{advective transport rate}}{\text{diffusive transport rate}} = \frac{Lu}{D} \quad (1.36)$$

where L is a characteristic length, u is the fluid velocity and D is the species diffusivity in this fluid.

When $\text{Pe} \gg 1$, advection is the dominant transport phenomena. When $\text{Pe} \ll 1$, diffusion dominates and advection can be neglected.

For hydrogen diffusing in liquid LiPb (typically in a WCLL breeding blanket with a characteristic length $L \approx 1$ m), with $D \approx 1 \times 10^{-9} \text{ m}^2 \text{ s}^{-1}$ and $u \approx 1 \times 10^{-4} \text{ m s}^{-1}$ [70], $\text{Pe} \approx 10^5$, which means that advection dominates the mass transport and cannot be neglected.

[70] Dark et al. (2021)

Clustering

Single He atoms implanted into the material diffuse rapidly due to the high W-He repulsion. This high repulsive W-He interaction is such that interstitial He atoms preferably rearrange into groups of atoms in order to minimise the number of repulsive interactions [117, 118]. This phenomenon, called *clustering*, was highlighted by DFT studies [119, 120] and MD simulations [121]. Small clusters are themselves mobile as long as all the He atoms within the cluster are occupying interstitial position in the solid lattice. The activation energy for interstitial He atoms and clusters in W ranges from 0.15 to 0.45 eV according to Perez et al. [91]. He clusters will eventually grow by interacting with either interstitial He atoms or other clusters.

[117] Hamid et al. (2019)

[118] Hammond et al. (2018)

[91] Perez et al. (2017)

Clustering of H atoms is less clear and Henriksson et al. showed that H atoms do not form bonds with other H atoms in body-centered cubic (bcc) W [122].

[122] Henriksson et al. (2005)

Bubble nucleation

If its size is big enough, the cluster pressure is sufficient to knock off a W atom from the lattice, creating a W vacancy and an interstitial W atom (a Frenkel pair). This process is called trap mutation or *self-trapping* and the trapped clusters act as nuclei for bubble formation.

Trap mutation has been modelled in W using DFT [78] and Monte Carlo computations [123]. It has been shown that this phenomenon depends not only on the number of He atoms in the cluster but also on temperature, position of the cluster to the free surface or even the crystal orientation [124–126]. At this point, the trapped cluster occupies the newly created W vacancy position. It is considered immobile since it would require either diffusion of another vacancy next to it, or recombination of the Frenkel pair in order to diffuse [127].

[78] Boisse et al. (2014)

[123] De Backer et al. (2015)

[124] Blondel et al. (2017)

[125] Hu et al. (2014)

[126] Hu et al. (2014)

[127] Morishita (2007)

Bubble growth

Once a bubble nucleus is created via trap mutation, it can continue to grow by absorbing other clusters. Two or more bubbles can also coalesce and form a bigger bubble. Condon and Schober [128] reviewed the key mechanisms of bubble growth in metals.

[128] Condon et al. (1993)

Each of these mechanisms can become dominant over another depending on the implantation and the metal conditions. Bubbles can continue to grow by absorbing interstitial He atoms or mobile He clusters (i.e. that have not self trapped). Considering

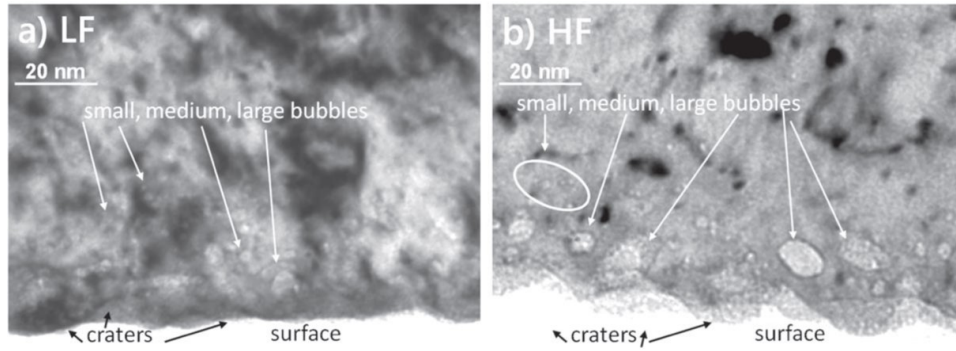


Figure 1.21: Transmission electron microscopy image of tungsten irradiated with He ions at different fluxes (Low Flux (LF) = $2.9 \times 10^{20} \text{ m}^{-2} \text{ s}^{-1}$ and High Flux (HF) = $2.3 \times 10^{22} \text{ m}^{-2} \text{ s}^{-1}$) showing the presence of He bubbles. Reproduced from [97].

that vacancies are mobile in the solid, the volume of a bubble could also increase if a vacancy or a vacancy cluster interacts with a He bubble. The same is true for He-vacancies or H-vacancies clusters.

There is no experimental evidence of He clustering with self-interstitial W atoms [88].

During the growth of a He bubble by absorbing He atoms, if the pressure increases until reaching a critical value, dislocation loop punching can occur. During the punching event, a whole facet of W atoms is pushed, and the vacant lattice sites are absorbed by the bubble allowing the bubble to expand and reducing the pressure in it [90]. The produced self-interstitial W atoms will likely be attracted by *image forces* at the surface and will contribute to the roughening of the surface and/or formation of surface structures.

Dislocation loops happen at very high pressure and if the number of vacancies in the lattice is low compared to the amount of He atoms. This is the case when a high He flux is applied and the He ions energy is low so that no displacement damaged is produced [90]. If vacancies were created via He ions implantation, they could interact with existing He bubbles which would have the effect of increasing the volume and thus decreasing the pressure (assuming no change in temperature and no other implantation mechanism).

Coalescence of He bubbles has been observed in MD simulations [117, 129, 130] and would tend to increase the bubble size decreasing the bubble density at the same time. This may not have an impact on He concentration on the macroscopic scale but might influence bubble bursting.

The pressure inside the bubble and the bubble radius are two parameters of interest and are correlated. Sefta [90] proposed to use the Wolfer equation of state in order to determine the number of He atoms contained in a He bubble based on its pressure, the latter being calculated from its radius and its surface tension. One must be aware that if radii and pressure of bubbles computation is quite straightforward using MD [130] or cluster dynamics [89] simulations it will be more complex to estimate these metrics considering a continuum model that does not keep track of every type of clusters but only a few of them. The only information *a priori* available in this case is indeed the local helium concentration and an equivalence could be found by either having a high density of small bubbles or a low density of big bubbles. An effort has been made by Ialovega to measure the pressure inside helium bubbles using Electron Energy Loss Spectroscopy (EELS) [131]. This technique, consisting in analysing the electron energy loss as they interact with matter [132], showed evidence that the observed cavities (see Figure 1.21) were filled with helium.

Ultimately, a bubble can form blisters, increase its size via loop punching or even burst.

[88] Faney et al. (2014)

[90] Sefta (2013)

[117] Hamid et al. (2019)

[129] Hammond et al. (2019)

[130] Zhang et al. (2019)

[90] Sefta (2013)

[130] Zhang et al. (2019)

[89] Faney et al. (2015)

[131] Ialovega (2021)

[132] Pyper et al. (2017)

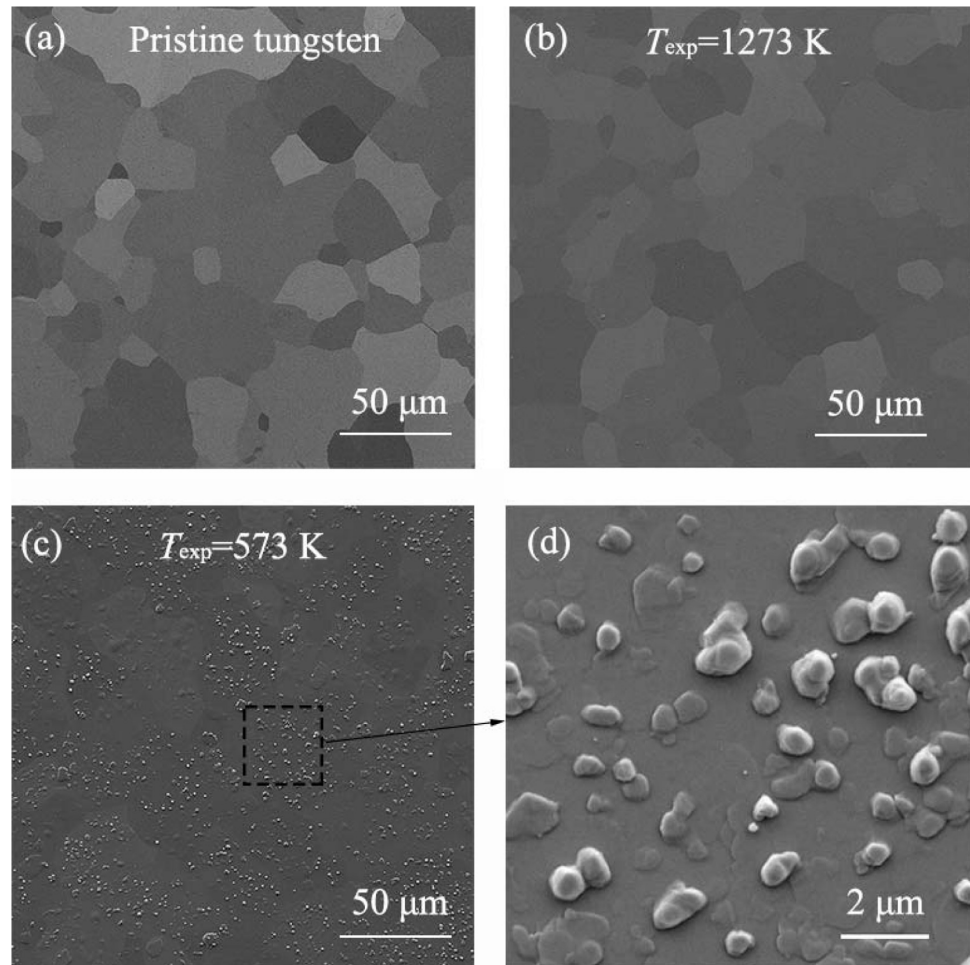


Figure 1.22: Scanning Electron Microscopy images of the surface of W samples exposed to 50 eV H plasma at 573 K and 1273 K. Reproduced from [133].

Blistering

During helium or hydrogen implantation, *blistering* can be observed under certain conditions. Blisters are plastic deformation (swelling) of the metal near the surface due to high pressure in bubbles (see Figure 1.22). This phenomenon is separated from loop punching even though loop punching can be considered as a plastic deformation. Blistering usually happens at low temperatures because only then the growth rate of the bubble is greater than the dissolution in the bulk (which depends on the thermally activated diffusion coefficient and solubility). Eventually, if the rate of incoming atoms is greater than the rate of re-dissolution in the bulk, blisters can rupture. Similarly, if the rate of incoming atoms is less than the rate of re-dissolution in the bulk, the blister will collapse.

Helium blistering has been observed in W at low temperature (< 1000 K) [134]. Hydrogen blistering was also observed in W [135]. Causey et al. also reviewed a wide range of studies showing H exposure leads to blistering [66]. Blistering was found to lead to local hardening in W due to the production of dislocations [133]. It can also form cracks depending on the alloying elements in W and the microstructure [136].

Hydrogen blistering was observed under high energy irradiation (typically from a few keV to MeV). These energies are orders of magnitudes higher than the ones expected in the ITER divertor (see Figure 1.8).

It was also found that hydrogen blister formation was avoided in tungsten at temperatures above 600 K [137, 138].

[134] Baldwin et al. (2010)

[135] Haasz et al. (1999)

[66] Causey (2002)

[133] Chen et al. (2019)

[136] Ueda et al. (2005)

[137] Wang et al. (2001)

[138] Shimada et al. (2003)

Bursting

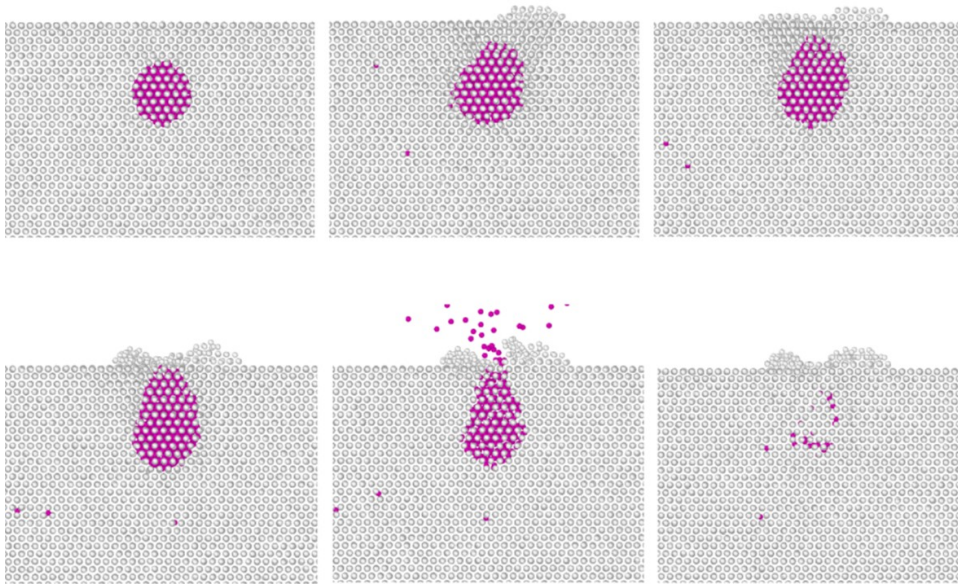


Figure 1.23: Molecular dynamics simulation of He bubble bursting in W. Reproduced from [139].

When a bubble grows near the surface and is over-pressurised, bursting can occur (see Figure 1.23). As the bubble size increases via loop punching, the W lattice is deformed and the ligament thickness decreases. The latter can rupture which would make all the He atoms contained in the bubble to be released to the vacuum. This is why He bursting is characterised by sharp drops in the He inventory [129].

Sefta and co-workers observed that bursting is more likely to happen at high temperatures. This phenomenon contributes to surface roughening and could be the beginning of the formation of fuzz [140]. Indeed, a bursting event could either form a crater on the W surface or an empty cavity due to self-healing. In the last case, called a *pinhole* bursting event, the cavity can be repressurised with He atoms. Blondel et al. proposed to model bursting as a stochastic function of depth in the material rather than a calculation of the bubble pressure. They have also shown that simulation parameters have an impact on the retention [141]. They have shown that the size of the reaction network size (using cluster dynamics) does not seem to have an influence (between 250 and 200) as the first bursting events happen with clusters of size He₈₀.

If bursting is not included in continuum simulations, the volume fraction of He present in W could become very large and the dilute limit approximation could no longer be valid [90]. The correct metric for estimating bursting probabilities must therefore be chosen with care.

W tendrils or “nano-fuzz”

In 2012, Wright et al. [142] observed the formation of nanostructures on the surfaces of the W divertor of the reactor Alcator C-mod. These nanostructures are made of W tendrils (see Figure 1.24). These structures are called W fuzz, nano-fuzz or even fuzzy W. Because a small portion of the divertor grew W fuzz, no conclusion was made regarding its influence on the plasma operation. However, if these structures were to be removed during plasma operation via erosion, W atoms could be fed into the plasma, affecting the tokamak performances. Moreover, this phenomenon could increase the W dust formation in the reactor and lead to contamination and safety

[129] Hammond et al. (2019)

[140] Sefta et al. (2013)

[141] Blondel et al. (2018)

[90] Sefta (2013)

[142] Wright et al. (2012)

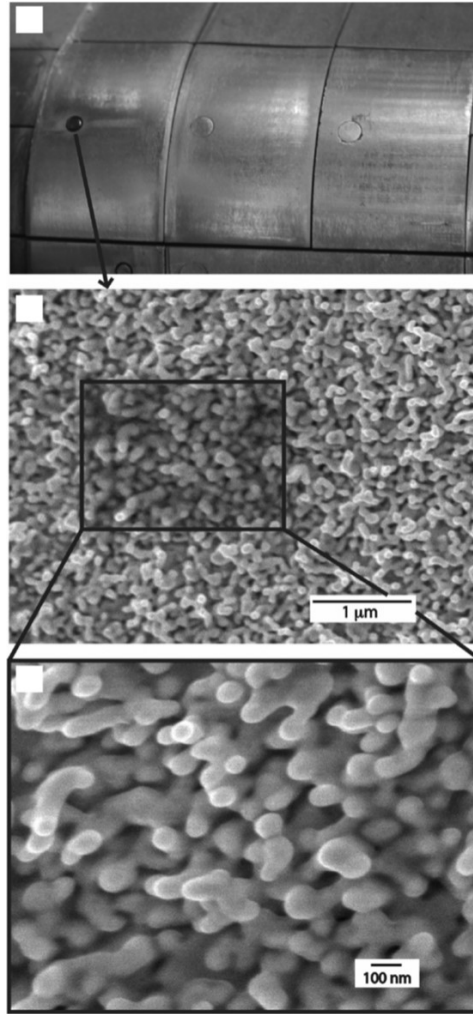


Figure 1.24: W fuzz observed in Alcator C-Mod. Reproduced from [142].

[143] Grisolia et al. (2015)

[134] Baldwin et al. (2010)

[144] Nishijima et al. (2011)

[145] Baldwin et al. (2009)

[146] Baldwin et al. (2008)

[147] Woller et al. (2015)

[148] Hammond (2017)

[149] Wirtz et al. (2016)

[134] Baldwin et al. (2010)

[150] Takamura et al. (2006)

issues since the dust particles can be radioactive [143]. The formation of W fuzz also increases the specific surface area and therefore the potential intake of hydrogen.

W fuzz has been observed at high temperature ($>1000\text{K}$), high flux ($>1 \times 10^{21} \text{He}^+ \text{m}^{-2} \text{s}^{-1}$) and long exposure ($t > 1 \times 10^2 \text{s}$) [134, 144].

The reason of the fuzz formation is still unclear but could be due to bursting events and/or accumulation of self interstitial W atoms at the surface [145–148]. Thermal properties of the media are also impacted by the formation of W fuzz [149] which could have a severe impact during ELM-like events. After 1h of plasma implantation, nanostructuring can be found deep in the bulk (up to several hundred of μm). According to Baldwin and Doerner [134], heavy alloying helps reduce the formation of He-induced fuzz.

Takamura et al. showed fuzz could be grown under relevant tokamak conditions (high-flux He plasma irradiation and surface temperature greater than 1250 K) [150]. Baldwin et al. showed the fuzz thickness evolved as a square root of the fluence [145].

McCarthy et al. studied the formation of W fuzz (see Figure 1.25) at helium fluences ranging from $4 \times 10^{23} \text{m}^{-2}$ to 10^{25}m^{-2} , temperatures ranging from 1050 K to 1150 K and He ion energies from 80 eV to 100 eV. They identified different fuzz growth regimes depending on the He fluence due to the change in porosity of the fuzzy layer during the growth process. The rate of growth was found to be dependent on the temperature and the state (ion or atom) of the incident He particles.

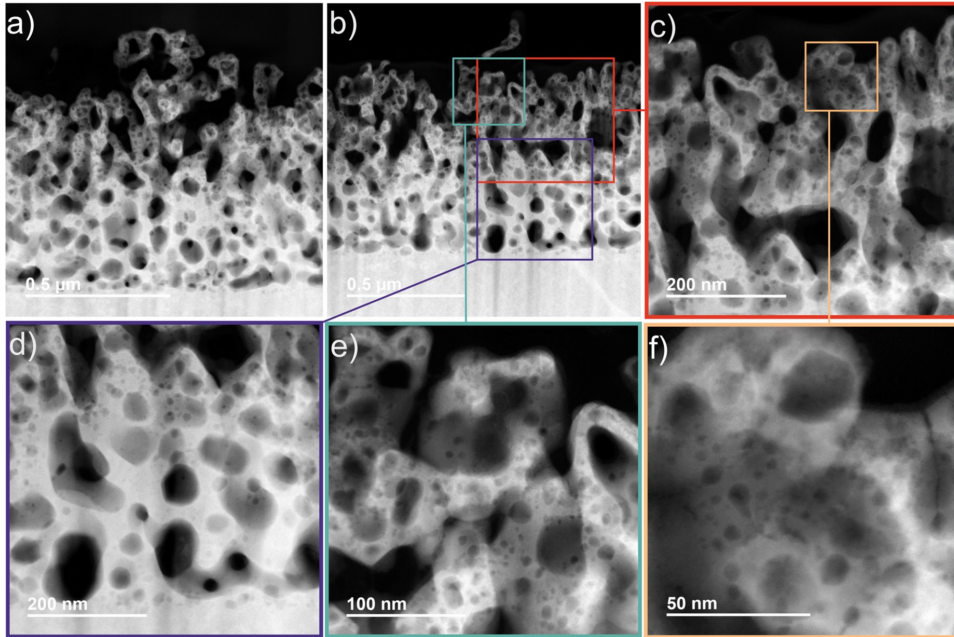


Figure 1.25: Fuzzy W scanning/transmission electron microscopy images showing the presence of He bubbles in tendrils. Reproduced from [151].

Recent modelling work also showed temperature could significantly affect the bursting of He bubbles and therefore the growth of W fuzz [152].

[152] Niu et al. (2021)

De Temmerman et al. concluded that temperature was the most critical parameter controlling W fuzz growth [153].

[153] De Temmerman et al. (2012)

Cracks

The role of He implantation in cracks formation is still unclear since cracks have also been observed during pure thermal shock on W PFC [149]. Under some specific conditions, cracks can close due to thermal expansion which induce frictional loads on the structure. The formation of W nano-fuzz could also bridge those cracks as observed by Lemahieu et al. [154].

[149] Wirtz et al. (2016)

[154] Lemahieu et al. (2016)

Reduction of thermal performances

Several of the above phenomena can have an impact on plasma facing materials thermal performances [155, 156]. First, having a network of bubbles will lead to a reduction of local apparent conductivity as thermal constriction will occur between the bubbles. Therefore, for a given heat load of the surface of a PFC, temperature will likely increase. Then, development of surface structures will be accompanied by surface roughening therefore modifying the reflectivity and emissivity [157]. For a given incident flux, the net radiative flux to which the surface of the component is exposed will then increase. This could lead to reduction of the PFC heat exhaust capacity and furthermore local melting [149].

[155] Cui et al. (2017)

[156] Buzi et al. (2017)

[157] Tokunaga et al. (2004)

[149] Wirtz et al. (2016)

1.4.3 He/H interactions

Lee et al. studied the influence of He implantation on D retention. They showed with Elastic Recoil Detection depth profiles (up to 40 nm) that D is trapped where He is trapped and proposed that He bubbles produce secondary defects around them which

[158] Lee et al. (2007)

can trap D [158]. These defects can be interstitial loops produced by loop punching or even vacancies created by stress field induced by overpressurised bubbles. Lee et al. also suggested that no evidence had been found on trapping of D by chemisorption on the inner surface of a He bubble nor by molecular interaction with the He cluster. The privileged mechanism is therefore the trapping of D in the defects made by the stress field induced by the He bubble to the crystalline structure of the W. Bergstrom et al. however showed hydrogen can be located at the surface of He bubbles [159].

[159] Bergstrom et al. (2017)

[160] Ueda et al. (2009)

It has been shown by Ueda et al. that He implantation (even in small amounts) greatly affects H blistering in W [160]. With only 0.1% of He in the ion beam one can observe that H blistering is completely suppressed for temperature greater than 653 K. At lower temperature, H blistering occurs but is significantly reduced. This phenomenon is due to the fact that H migration to the bulk and accumulation at grain boundaries is avoided by He bubbles at the near surface which act as a diffusion plug for H. The same phenomenon has been observed by Miyamoto et al. [161] which contributes to reducing H retention. Markelj et al. [162] showed however that He implantation can increase D retention in the He clustering zone. This suggests that observed reduction or increase of D retention in mixed H-He plasma experiment depend on the implantation depth.

[161] Miyamoto et al. (2011)

[162] Markelj et al. (2017)

Ialovega et al. performed sequential H implantation/desorption cycles on W samples pre-damaged with He [97]. He bubbles were found in the near surface region (see Figure 1.21) and significantly different TDS spectra were observed after several H implantations/desorptions (see Figure 1.18). This works gives evidence of an interaction between He and H in W.

[97] Ialovega et al. (2020)

1.5 Problem definition

The main focus of this PhD work is the estimation of H isotopes retention and permeation in tokamaks. We will try to answer the following questions:

- ▶ How does the tritium inventory evolve over the lifespan of the fusion reactor?
- ▶ Does it remain within the safety limits?
- ▶ What is the impact of the presence of helium?

Due to the time scales at play and the complexity of the components, answering these questions experimentally is complex. Numerical models can however be used to simulate components over long time scales and with complex geometries. However, the tools currently available did not meet the requirements of either dimensionality, physics, performance or availability.

Numerous simulation tools have been developed throughout the years (see Table 1.1). Most of these codes are not able to run multimaterial and/or multidimensional simulations. These features are however essential to fully simulate monoblocks (see Section 1.2.4). Many of them rely on the Finite Difference Method (FDM) whereas HIT [163], Abaqus [77] and ACHLYS [164] rely on the Finite Element Method (FEM). Moreover, some do not have an integrated heat transfer solver - essential for an accurate estimation of temperature fields and therefore thermally activated processes. Some of these codes rely on proprietary software like Abaqus or COMSOL for HIT - limiting their accessibility and scalability (parallel computing). The code ACHLYS meets all these requirements and is the only one available open-source but was only released in mid 2021. Finally, good computing performances were required in order to simulate the full divertor. This ruled out the use of Abaqus in its current state as it was initially designed for thermo-mechanical simulations.

[163] Candido et al. (2020)

[77] Benannoune et al. (2020)

[164] Dixon (2021)

For all these reasons, the FESTIM code was developed and used to conduct this PhD research.

Table 1.1: Comparison of some hydrogen transport modelling tools.

	1D	2D	3D	Multimaterial	Heat transfer	Open-source	Programming language
TMAP7 [165]	✓			✓			Fortran
HIIPC [166]	✓				✓		Fortran
CRDS [167]	✓						Mathematica
MHIMS [105]	✓						Fortran
TESSIM [168]	✓			✓			
HIT [163]	✓	✓	✓	✓	✓		COMSOL interface
Abaqus [77]	✓	✓	✓	✓	✓		Fortran user subroutines
ACHLYS [164]	✓	✓	✓	✓	✓	✓	C++

► **Chapter 2**

The first part of this work was to develop a model and a simulation tool - FESTIM - capable of solving hydrogen transport problem in 2D/3D. This Chapter will describe the mathematical models used in FESTIM as well as the global numerical implementation. Finally, it will detail the analytical verification and experimental validation strategy. This last point includes a code comparison with the reference code TMAP7.

► **Chapter 3**

This Chapter will focus on estimating the tritium retention in monoblocks. To this end, a FESTIM model of ITER-like monoblock will be developed. A behaviour law linking the monoblock inventory to exposure conditions (surface concentration and surface temperature) will be obtained.

► **Chapter 4**

The next stage is to scale up from a monoblock model to a full divertor model. The behaviour law obtained in Chapter 3 will be coupled to plasma simulations (providing distributions of exposure conditions). The inventory of the ITER and WEST divertors will be computed for several plasma scenarios.

► **Chapter 5**

Finally, the influence of helium exposure and the presence of helium bubbles was studied. To this end, a finite element solver was first developed to simulate helium transport and clustering in tungsten. This code was compared to the Xolotl code [141]. This helium transport code was then coupled to FESTIM to estimate the potential impact of helium on the tritium inventory estimations.

[141] Blondel et al. (2018)

2 Model description

2.1 Introduction

This Chapter describes the mathematical models used to simulate H transport in tokamaks plasma facing components. The numerical scheme to solve these equations and an introduction to the finite element method alongside with its implementation in the Finite Element Simulation of Tritium in Materials (FESTIM) code are also presented. Finally, the verification & validation of FESTIM is performed to guaranty its reliability.

2.1	Introduction	31
2.2	H transport	31
2.3	Heat transfer	35
2.4	Implementation	36
2.5	Verification & Validation	40
2.6	Summary	53

2.2 H transport

2.2.1 Macroscopic Rate Equations model

The Macroscopic Rate Equations (MRE) model will be employed. The principle is to split the hydrogen isotopes into several populations: the mobile hydrogen particles and the hydrogen particles trapped in the i -th trap. Their concentration in H m^{-3} are respectively c_m and $c_{t,i}$. They can be expressed in atomic fraction (at.fr.) by normalising them to the atomic density of the material.

Fick's first law of diffusion states that the particle flux is driven by the concentration gradient. The particle flux J is therefore expressed by:

$$J = -D\nabla c_m \quad (2.1)$$

where D is the diffusion coefficient in $\text{m}^2 \text{s}^{-1}$. The Soret effect and the effect of hydrostatic pressure are here neglected due to a lack of data.

The spatio-temporal evolution of these concentrations is commonly described by the following reaction-diffusion system [169]:

$$\frac{\partial c_m}{\partial t} = \nabla \cdot J + \Gamma - \sum \frac{\partial c_{t,i}}{\partial t} \quad (2.2)$$

$$\frac{\partial c_{t,i}}{\partial t} = k_i \cdot c_m \cdot (n_i - c_{t,i}) - p_i \cdot c_{t,i} \quad (2.3)$$

[169] McNabb et al. (1963)

In Equation 2.2, Γ is the volumetric source term of particles in $\text{m}^{-3} \text{s}^{-1}$, which can be used to simulate any process producing H in the bulk. This is the case for plasma implantation and nuclear reactions producing H.

In Equation 2.3, k_i and p_i are the trapping and detrapping rates expressed in $\text{m}^3 \text{s}^{-1}$ and s^{-1} respectively and n_i is the trap density in m^{-3} .

At steady state (i.e. $\frac{\partial c_m}{\partial t} = 0$ and $\frac{\partial c_{t,i}}{\partial t} = 0$), the mobile H concentration is independent of $c_{t,i}$. Equation 2.3 can be rewritten as:

$$c_{t,i} = n_i \frac{1}{\frac{p_i}{k_i c_m} + 1} \quad (2.4)$$

The quantity $(p_i/(k_i c_m) + 1)^{-1}$ determines the trap occupancy. As it approaches one (high mobile concentration, low detrapping rate or high trapping rate), the trapped concentration approaches the trap density. As it approaches zero (high detrapping rate, low mobile concentration or low trapping rate), the trapped concentration approaches zero.

2.2.2 Boundary conditions

Several boundary conditions will be employed in order to constrain either the concentration (Dirichlet boundary condition) or the concentration gradient (Neumann, Robin boundary condition) at the domain's boundaries.

Dissociation and recombination fluxes

The concentration gradient can be constrained on the boundaries (see Equation 2.5).

$$-D(T)\nabla c_m \cdot \mathbf{n} = f(x, t) \quad \text{on } \partial\Omega \quad (2.5)$$

where $D(T) = D_0 \exp(\frac{-E_D}{k_B T})$ is the diffusion coefficient in $\text{m}^2 \text{s}^{-1}$, \mathbf{n} is the boundary normal vector and $\partial\Omega$ is the domain boundary.

f can be expressed as a molecular recombination flux:

$$-D(T)\nabla c_m \cdot \mathbf{n} = K_r(T)c_m^n \quad \text{on } \partial\Omega \quad (2.6)$$

where $K_r(T) = K_{r0} \exp(\frac{-E_{K_r}}{k_B T})$ is the recombination coefficient expressed in $\text{m}^{3n-2} \text{s}^{-1}$, $n \in \{1, 2\}$ is the order of the recombination. This is the Waelbroeck model [170]. This model may not be valid for all cases [171] and a more extended and more complex model from Pick-Sonnenberg [172] could be more generic. In a metal, $n = 2$ and in a non-metallic liquid, $n = 1$. Recombination occurs when hydrogen particles located at the surface of the material combine with other particles (which can be other hydrogen particles) and are no longer bonded with the metal surface. It can happen both in presence of a vacuum or when the metal is in contact with a fluid (gas or liquid).

Similarly, a dissociation flux can be applied when a surface is in contact with a gas atmosphere of H₂:

$$-D(T)\nabla c_m \cdot \mathbf{n} = K_d(T)P \quad \text{on } \partial\Omega \quad (2.7)$$

where $K_d(T) = K_{d0} \exp(\frac{-E_{K_d}}{k_B T})$ is the dissociation coefficient expressed in $\text{m}^{-3} \text{Pa}^{-1}$. Dissociation is the opposite process of recombination and occurs when particles in the surrounding atmosphere or fluid reach the metal surface and are adsorbed. These particles can then reach the bulk and diffuse in the metal.

[170] Waelbroeck et al. (1984)

[171] Schmid et al. (2021)

[172] Pick et al. (1985)

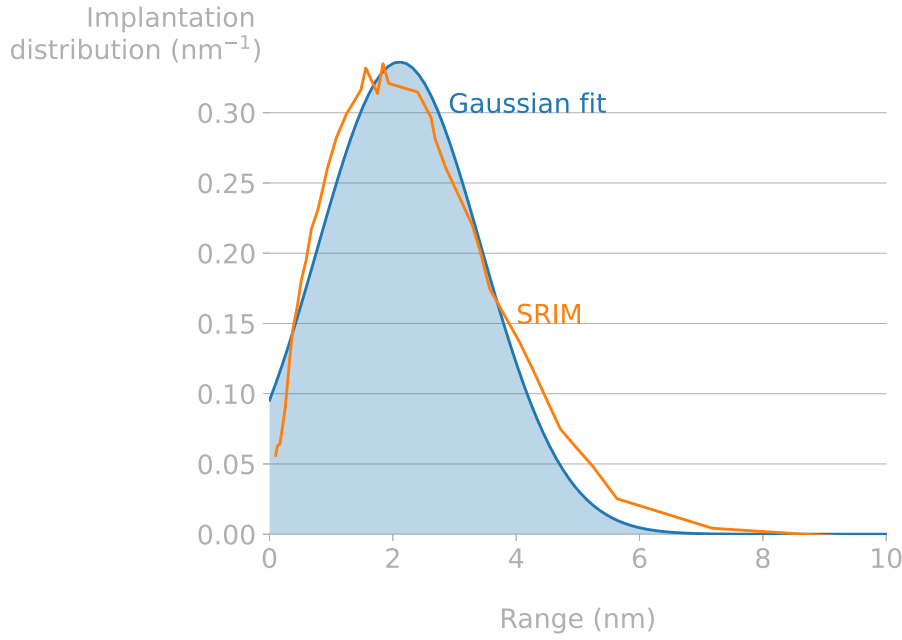


Figure 2.1: 100 eV deuterium implantation profile in tungsten computed from SRIM. Reproduced from [174].

With $n = 2$, a steady-state approximation of the flux balance between recombination and dissociation fluxes is the Sievert's law (see Equation 2.8).

$$c_m = S(T)\sqrt{P} \quad \text{on } \partial\Omega \quad (2.8)$$

where P is the partial pressure of hydrogen at the boundary in Pa, $S(T) = S_0 \exp(\frac{-E_s}{k_B T})$ is the material solubility in $\text{m}^{-3} \text{Pa}^{-1/2}$ and T is the local temperature in K. This law of equilibrium is a steady-state approximation of a more complex model which takes into account flux exchanges between adsorbed and mobile concentrations at the boundary. It is therefore valid when applied to cases where the kinetics are fast enough for the system to remain at equilibrium.

Analytical simplification for an implanted source of H

Plasma implantation of hydrogen particles can be modelled with a volumetric source. Typically, the depth of the implantation profile R_p is a few nanometres depending on the incident particles energy and incident angle. These profiles can be simulated by Monte Carlo codes like Stopping Range of Ions in Matter (SRIM) [173] and have a gaussian-like shape (see Figure 2.1). This volumetric source term can be simplified into a Dirichlet boundary condition (i.e. enforcing the mobile particle concentration at the exposed surface).

[173] Ziegler et al. (2010)

Let us consider a volumetric source term of hydrogen $\Gamma = \varphi_{\text{imp}} f(x)$ where f is a narrow Gaussian distribution. The concentration profile of mobile particles can be approximated by a triangular shape [175] (see Figure 2.2).

[175] Schmid (2016)

The concentration profile is therefore maximum at $x = R_p$. The expression of maximum concentration value c_{max} can be obtained by expressing the flux balance at equilibrium:

$$\varphi_{\text{imp}} = \varphi_{\text{recomb}} + \varphi_{\text{bulk}} \quad (2.9)$$

where φ_{recomb} is the recombination flux and φ_{bulk} is the migration flux.

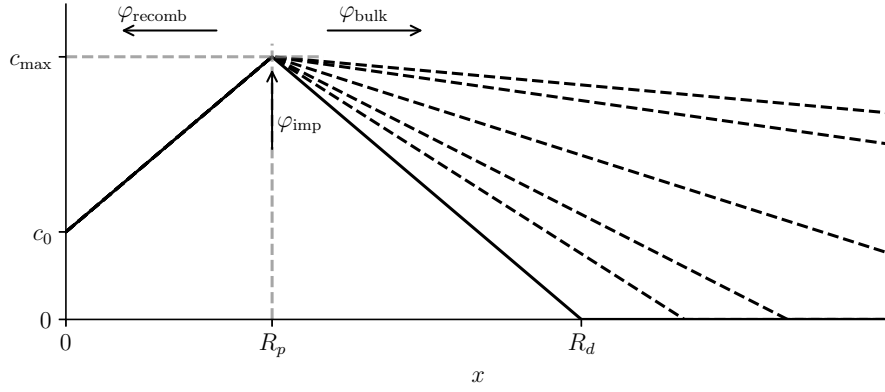


Figure 2.2: Concentration profile with recombination flux and volumetric source term at $x = R_p$. Dashed lines correspond to the time evolution.

φ_{bulk} can be expressed as:

$$\varphi_{\text{bulk}} = D \cdot \frac{c_{\text{max}}}{R_d(t) - R_p} \quad (2.10)$$

with R_d the diffusion depth.

When $R_d \gg R_p$, $\varphi_{\text{bulk}} \rightarrow 0$. Equation 2.9 can therefore be written as:

$$\varphi_{\text{recomb}} \approx \varphi_{\text{imp}} \quad (2.11)$$

Moreover, according to Fick's law, φ_{recomb} can be expressed as:

$$\varphi_{\text{recomb}} = D \cdot \frac{c_{\text{max}} - c_0}{R_p} = \varphi_{\text{imp}} \quad (2.12)$$

$$\Leftrightarrow c_{\text{max}} = \frac{\varphi_{\text{imp}} R_p}{D} + c_0 \quad (2.13)$$

Assuming second order recombination, φ_{recomb} can also be expressed as a function of the recombination coefficient K_r :

$$\varphi_{\text{recomb}} = K_r c_0^2 = \varphi_{\text{imp}} \quad (2.14)$$

$$\Leftrightarrow c_0 = \sqrt{\frac{\varphi_{\text{imp}}}{K_r}} \quad (2.15)$$

By replacing Equation 2.15 in Equation 2.13 one can obtain:

$$c_{\text{max}} = \frac{\varphi_{\text{imp}} R_p}{D} + \sqrt{\frac{\varphi_{\text{imp}}}{K_r}} \quad (2.16)$$

As the recombination process becomes fast (i.e. $K_r \rightarrow \infty$), $c_0 \rightarrow 0$ and $c_{\text{max}} \rightarrow \frac{\varphi_{\text{imp}} R_p}{D}$.

Since the main driver for the diffusion is the value c_{max} , when R_p is negligible compared to the dimension of the simulation domain, one can simply impose this value at the surface.

A transient solution based on trap properties can be derived [105]:

$$c_{\max}(t) = \left(\frac{R_p \varphi_{\text{imp}}}{D} + \sqrt{\frac{\varphi_{\text{imp}}}{K_r}} \right) \cdot \frac{\tau}{t} \cdot \left(\sqrt{1 + \frac{t}{\tau}} - 1 \right)^2 \quad (2.17)$$

where τ is a characteristic time expressed by:

$$\tau = \frac{R_p \sum R_i n_i}{8\varphi_{\text{imp}}} \quad (2.18)$$

In this expression, $R_i = (p_i/(k_i c_{\max}) + 1)^{-1}$ represents the maximum filling ratio of the trap i and n_i is the trap density. When $t \gg \tau$, $c_{\max}(t) \approx \frac{R_p \varphi_{\text{imp}}}{D} + \sqrt{\frac{\varphi_{\text{imp}}}{K_r}}$

2.2.3 Interface condition: conservation of chemical potential

The continuity of chemical potential can be ensured by performing a change of variable in Fick's second law of diffusion with $\phi = c_m/S$ (in the case of a metal) [176] when internal conditions cannot be set. Neglecting the trapping and generation terms, Equation 2.2 therefore reads:

[176] Smith (2009)

$$\begin{aligned} \frac{\partial \phi S}{\partial t} &= \nabla \cdot (D \nabla \phi S) + f \\ &= \nabla \cdot (D S \nabla \phi + D \phi \nabla S) + f \end{aligned} \quad (2.19)$$

where f is some source term.

Equation 2.3 reads:

$$\frac{\partial c_{t,i}}{\partial t} = k_i \phi S (n_i - c_{t,i}) - p_i c_{t,i} \quad (2.20)$$

After solving Equation 2.19 for ϕ , c_m can be retrieved by multiplying the solution by S .

2.3 Heat transfer

Due to the numerous processes that are thermally activated, it is essential to have an accurate temperature field. Moreover, most tokamak plasma facing components are exposed to intense heat fluxes and are actively cooled, exhibiting high temperature gradients. The temperature fields are even more complex when dealing with non-trivial geometries like monoblocks or breeding blankets. For these reasons, heat transfers need to be modelled.

The equation describing heat conduction in solids is described as follows:

$$\rho \cdot C_p \frac{\partial T}{\partial t} = \nabla \cdot (\lambda \nabla T) \quad (2.21)$$

where ρ is the density of the material in kg m^{-3} , C_p its specific heat capacity expressed in $\text{J kg}^{-1} \text{K}^{-1}$ and λ the thermal conductivity expressed in $\text{W m}^{-1} \text{K}^{-1}$.

The thermal properties C_p , ρ and λ are usually temperature dependent.

For heat transfer problems, three types of boundary conditions can be imposed.

First, the temperature can be fixed on the boundary with a Dirichlet boundary condition (see Equation 2.22).

$$T = T(x, y, z, t) \quad \text{on } \partial\Omega \quad (2.22)$$

where $\partial\Omega$ is the domain boundary.

On the other hand, a heat flux can also be imposed by enforcing the temperature gradient (see Equation 2.23). This condition is called a Neumann condition.

$$-\lambda \nabla T \cdot \mathbf{n} = f(x, y, z, t) \quad \text{on } \partial\Omega \quad (2.23)$$

where λ is the thermal conductivity in $\text{W m}^{-1} \text{K}^{-1}$.

Finally, to model a convective heat flux when the surface is in contact with a fluid (e.g. cooling pipes, natural convection...), a Robin boundary condition needs to be employed (see Equation 2.24).

$$-\lambda \nabla T \cdot \mathbf{n} = h(T - T_{\text{ext}}) \quad \text{on } \partial\Omega \quad (2.24)$$

where h is the heat transfer coefficient in $\text{W m}^{-2} \text{K}^{-1}$, T_{ext} is the fluid temperature in K. The heat transfer coefficient can be dependent on the temperature and the flow characteristics. It is obtained by computing the Nusselt number from correlations linking it to the Reynolds number of the flow and the Prandtl number of the fluid [177] (e.g. Dittus-Boetler, Sieder-State, Gnielinski...). Once the Nusselt number is known, the heat transfer coefficient h reads:

$$h = \frac{\lambda Nu}{L} \quad (2.25)$$

with Nu the Nusselt number and L the characteristic length in m.

2.4 Implementation

The models described in the previous sections can be hard to solve analytically for complex problems (complex geometries, transients, combined boundary conditions, coupling, etc.). The code FESTIM [178] was therefore developed in order to numerically solve these coupled equations.

2.4.1 The finite element method: FEniCS

FESTIM is based on the Finite Element Method to solve this set of differential equations and boundary conditions. Several finite element libraries are available open-source (deal.II [179], MFEM [180], MOOSE [181], FreeFEM++ [182]...). The open-source python/C++ package FEniCS [183] was employed for it provides a user-friendly python interface. The finite element method is a versatile tool that can solve any partial differential equation on an arbitrary geometry in 1D, 2D or 3D. The main advantage of this method compared to the finite difference method is the simplicity of its application to complex geometries and unstructured meshes. Indeed, implementing a finite difference scheme for such a problem would be tedious and extra care must be taken for mistakes in the implementation could result in losses in efficiency and accuracy of the numerical solution.

This section illustrates the finite element method applied to Poisson's equation [184].

The mathematical problem can be described by Equation 2.26 where u is the unknown to be solved governed by Poisson's equation. The problem is constrained by boundary

[177] Poirier et al. (2016)

[178] Delaporte-Mathurin et al. (2019)

[179] Arndt et al. (2021)

[180] Kolev et al. (2010)

[181] Permann et al. (2020)

[182] Hecht (2012)

[183] Alnæs et al. (2015)

[184] Logg et al. (2012)

conditions defined on $\partial\Omega$, the boundary of the domain Ω . The value of u is prescribed on the subset Γ_D (Dirichlet boundary condition) whereas the value of the normal derivative of u is prescribed on the remaining boundary Γ_N (Neumann boundary condition) (see Figure 2.3).

$$-\nabla^2 u = f \quad \text{on } \Omega \quad (2.26a)$$

$$u = u_0 \quad \text{on } \Gamma_D \subset \delta\Omega \quad (2.26b)$$

$$-\frac{\partial u}{\partial n} = g \quad \text{on } \Gamma_N \subset \delta\Omega \quad (2.26c)$$

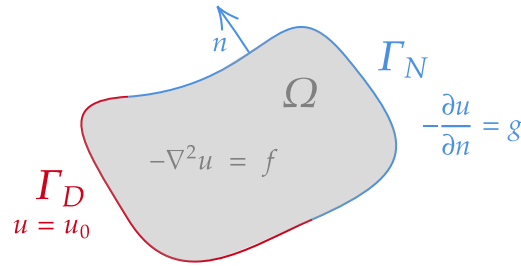


Figure 2.3: Representation of the mathematical problem.

The first step of the finite element method is to build a variational formulation (also called *weak form*) of the governing Equation 2.26 (called the *strong form*). To do so, the equation is multiplied by a function v (called the *test function*) and integrated over the domain Ω . The following expression is obtained:

$$\int_{\Omega} -\nabla^2 u v \, dx = \int_{\Omega} f v \, dx \quad \forall v \in \hat{V} \quad (2.27)$$

The function space \hat{V} is defined as:

$$\hat{V} = \{v \in H^1(\Omega) : v = 0 \text{ on } \Gamma_D\} \quad (2.28)$$

Equation 2.27 needs now to be rewritten in order to only have first order derivatives. To do so, Gauss-Green's lemma is employed:

$$\int_{\Omega} -\nabla^2 u v \, dx = \int_{\Omega} \nabla u \cdot \nabla v \, dx - \int_{\partial\Omega} \frac{\partial u}{\partial n} v \, ds \quad (2.29)$$

Since the test function v vanishes on Γ_D , the following variational problem is obtained: find $u \in V$ such that

$$\int_{\Omega} \nabla u \cdot \nabla v \, dx = \int_{\Omega} f v \, dx - \int_{\Gamma_N} g v \, ds \quad \forall v \in \hat{V} \quad (2.30)$$

The function space V is defined as:

$$V = \{v \in H^1(\Omega) : v = u_0 \text{ on } \Gamma_D\} \quad (2.31)$$

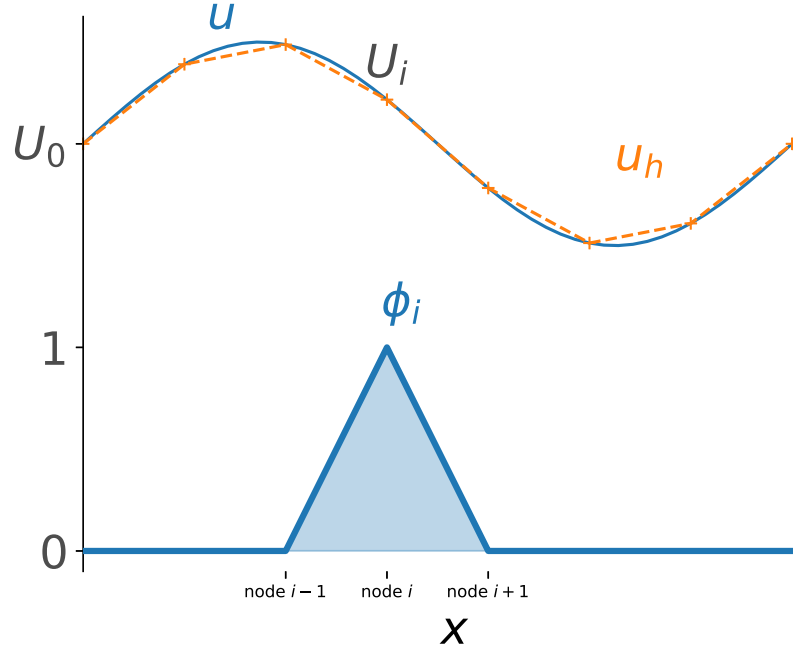


Figure 2.4: 1D example of an approximated solution u (exact in blue, approximated in orange) with basis function ϕ_i for linear finite elements with 2 nodes.

Poisson's equation can now be discretised by restricting the variational problem Equation 2.30 to discrete function spaces V_h and \hat{V}_h : find $u_h \in V_h \subset V$

$$\int_{\Omega} \nabla u_h \cdot \nabla v \, dx = \int_{\Omega} f v \, dx - \int_{\Gamma_N} g v \, ds \quad \forall v \in \hat{V}_h \subset \hat{V} \quad (2.32)$$

To solve Equation 2.32, a suitable pair of discrete function spaces V_h and \hat{V}_h must be constructed. Piecewise polynomial basis functions $\{\phi_i\}_{i=1}^N$ are defined for V_h and $\{\hat{\phi}_j\}_{j=1}^N$ for \hat{V}_h .

The approximated solution u_h therefore reads (see Figure 2.4):

$$u_h(x) = \sum_{i=1}^N U_i \phi_i(x) \quad (2.33)$$

where U_i are the coefficient to be determined on each node (called degrees of freedom). N is the number of nodes used to discretise the domain.

By replacing u_h in Equation 2.32 with Equation 2.33 and varying the basis functions $\hat{\phi}_j$:

$$\sum_{i=1}^N U_i \int_{\Omega} \nabla \phi_i \cdot \nabla \hat{\phi}_j \, dx = \int_{\Omega} f \hat{\phi}_j \, dx - \int_{\Gamma_N} g \hat{\phi}_j \, ds, \quad j = 1, 2, \dots, N \quad (2.34)$$

This can be written in a matrix form:

$$AU = b \quad (2.35)$$

where

$$A_{ji} = \int_{\Omega} \nabla \phi_i \cdot \nabla \hat{\phi}_j \, dx \quad (2.36a)$$

$$b_j = \int_{\Omega} f \hat{\phi}_j \, dx - \int_{\Gamma_N} g \hat{\phi}_j \, ds \quad (2.36b)$$

The integral terms in Equation 2.36 are computed with Gauss-Legendre quadrature.

After solving Equation 2.35, the U_i coefficients are known and the approximated solution u_h can be computed. Non-linear problems are solved similarly where the solution is approached using Newton's method.

The weak formulation of the steady state McNabb & Foster equation is:

$$\int_{\Omega} \nabla c_m \cdot \nabla v_m \, dx = \int_{\Omega} (k c_m (n - c_t) - p c_t) v_t \, dx \quad \forall (v_m, v_t) \in \hat{V} \quad (2.37)$$

where \hat{V} is a suitable vector-functionspace.

The transient formulation can be obtained by adding transient terms to Equation 2.37 $\int_{\Omega} \frac{c_m - c_{m,old}}{\Delta t} v_m \, dx$ and $\int_{\Omega} \frac{c_t - c_{t,old}}{\Delta t} v_t \, dx$ (forward Euler time discretisation). $c_{m,old}$ and $c_{t,old}$ are the previous solutions for the mobile concentration and trapped concentration respectively and Δt is the timestep.

2.4.2 Main features of FESTIM

FESTIM provides an even higher level of abstraction than FEniCS by providing a user-friendly interface dedicated to H transport and heat transfer problems. Users only have to provide inputs such as material properties, traps properties, geometry, solving parameters, without having to dive into the finite element implementation. In other words, users do not need to be finite element experts to run a FESTIM simulation (though knowledge and experience in finite elements will help in solving numerical problems).

Multidimensional multi-material transient simulations coupled with heat transfer can therefore be run fairly easily without finite element knowledge. Nevertheless, since FESTIM is object-oriented, advanced users will always be able to turn FESTIM inside-out to adapt the code to their specific needs (specific boundary conditions, slight changes in the governing equations...). Since FESTIM is written in python - which is a fairly easy-to-learn programming language - no advanced level of coding is required.

As mentioned above, FESTIM simulates hydrogen transport (diffusion and trapping) and additional physics can be incorporated, such as the Soret effect (even though not used in this work) and conservation of chemical potential at interfaces... The hydrogen transport equations can be coupled to the heat equation (weak coupling). Various types of boundary conditions are available for both the H transport (imposed concentration, recombination flux, dissociation flux, implanted source approximation...) and the heat transfer problems (imposed temperature, imposed flux, convective flux...). Traps densities in FESTIM can also be time-dependent allowing the users to simulate extrinsic traps (e.g. irradiation induced traps, stress induced traps...).

Thanks to the finite element method, geometries used in FESTIM can be complex (see Figure 2.5). The meshing capability of FESTIM is limited to 1D meshes, and it was

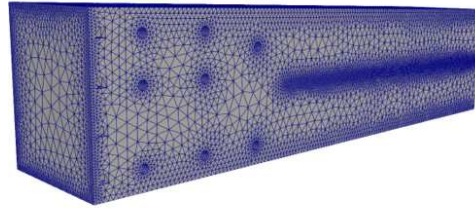


Figure 2.5: Example of a complex 3D geometry (here a breeding blanket section) mesh readable by FESTIM [70].

decided to instead make FESTIM accept (with the XDMF format) complex meshes from third-party applications dedicated to meshing such as SALOME or GMSH. These third-party applications can for instance be useful to run CAD-based simulations. Users can also decide to use the FEniCS built-in meshing tool.

Similarly, FESTIM (FEniCS) visualisation functions are limited. FESTIM is not a graphical application, but the files generated by FESTIM (XDMF, CSV, TXT) can easily be read and post-processed by specialised tools such as Paraview [185], matplotlib [186], NumPy [187], etc.

[185] Ahrens et al. (2005)

[186] Hunter (2007)

[187] Harris et al. (2020)

Regarding the default finite elements used in FESTIM are first order piecewise elements (called P1, Lagrange or also Continuous Galerkin 1). Using these finite elements for trapped concentration exhibiting discontinuities (at the interface between two materials for instance) can cause performance issues and loss of accuracies. Therefore, it can be switched to discontinuous elements (DG1) when needed to avoid under- or over-shoots in the concentration fields. Many different finite elements are available in FEniCS [188] and their description is outside the scope of this work.

When dealing with transient problems, FESTIM provides an adaptive stepsize allowing the stepsize to increase (by a user-defined factor) when the convergence criterion is easily reached by the solver. This greatly improves the performance of the code since less timesteps are needed.

2.5 Verification & Validation

Before using the FESTIM code for analysis, it has to be verified and validated. The Verification and Validation (V&V) has two goals: (1) to prove that the governing equations are correctly solved and that the code is error free and (2) to demonstrate that the governing equations actually reproduce processes observed experimentally. In other words, verification is answering the question “*Are we building the code right?*” and validation is answering the question “*Are we building the right code?*”.

This Section details the V&V of FESTIM.

2.5.1 Analytical verification

Verification is the process of ensuring the governing equations are correctly solved in FESTIM. This is an integral part of every simulation code for it guarantees the code is error free. It is generally hard to simply substitute this process by code comparison (cross-checks between two different codes) because often the codes are implemented differently. Moreover, if the code we are comparing with is not verified, then obtaining

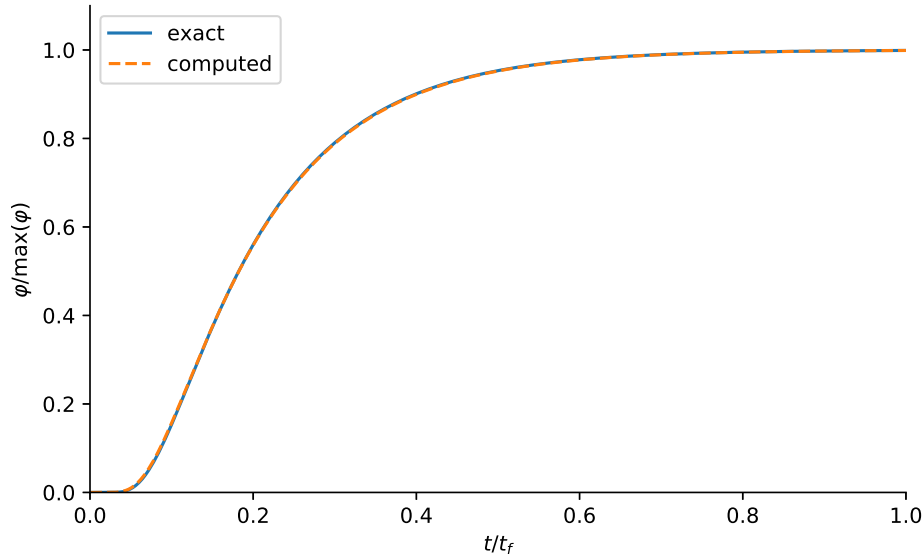


Figure 2.6: Temporal evolution of the outward particle flux φ at $x = l$ (Case 1).

similar results does not give any guarantee on the code accuracy as two different codes can have the same bug.

Several methods can be used to verify a code but the Method of Exact Solutions (MES) and the Method of Manufactured Solutions (MMS) are employed here.

Both methods consist in comparing a computed solution with an exact solution and measuring the error. The exact solution in the MES is obtained by solving the governing equations analytically. When using the MMS, the problem is reversed: an arbitrary exact solution (called *manufactured solution*) is chosen and injected in the governing equations. It is then possible to determine source terms and boundary conditions. These are then fed into the code and the computed solution is compared to the manufactured (exact) solution.

This MMS is often used to unravel the complexity of governing equations [189, 190]. This is particularly useful when dealing with complex geometries or to exercise non-trivial material properties.

[189] Dudson et al. (2016)

[190] Roache (2002)

This section describes two verification cases of FESTIM. The first one uses the MES and the second one the MMS. More complex and thorough verification cases are shown in Appendix A.

Case 1: H transport (MES)

For this verification case, a 1D slab is considered with a thickness l . The concentration of mobile particles was set to c_0 on one side of the slab and set to zero on the other side. Only one trap is considered in this case and its density n is homogeneously distributed.

The trapping parameter ζ is defined in [191] as follows:

[191] Longhurst et al. (2005)

$$\zeta = \frac{p}{k n} + \frac{c_m}{n} \quad (2.38)$$

In our case, we choose the trapping and detrapping rates k and p , the concentration c_0 and the temperature T so that $\zeta \gg \frac{c_m}{n}$. This condition is equivalent to having the trap

Table 2.1: Parameters used for the analytical verification (Case 1).

Parameter	Units	Value
D_0	$\text{m}^2 \text{s}^{-1}$	2.0
k_0	$\text{m}^3 \text{s}^{-1}$	0.01
p_0	s^{-1}	1.0
E_D	eV	0.2
E_k	eV	0.1
E_p	eV	0.1
c_0	m^{-3}	2.0
n	m^{-3}	2.0
l	m	1.5
T	K	300
t_f	s	2000

filling ratio $(p/(k c_m) + 1)^{-1} \ll 1$. This is known as the *effective diffusivity regime* where the diffusion is almost identical to the case where there are no traps. In this regime, the governing equations are identical as a pure diffusion regime and are therefore easy to solve analytically.

The coefficient D is then replaced by an effective diffusion coefficient:

$$D_{\text{eff}} = \frac{D}{1 + \frac{1}{\zeta}} \quad (2.39)$$

The particle flux at the background surface ($x = l$) is expressed in $\text{H m}^{-2} \text{s}^{-1}$ and finally defined in [191] by:

$$\varphi(t) = \frac{c_0 D}{l} \left[1 + 2 \sum_{m=1}^{\infty} (-1)^m \exp \left(-m^2 \frac{\pi^2 D_{\text{eff}} t}{l^2} \right) \right] \quad (2.40)$$

In Equation 2.40, the infinite sum has been truncated at $m = 10000$.

All the parameters used in this verification case are defined in Table 2.1. These parameters have been chosen for the sake of verification and do not necessarily represent realistic conditions as verification is a mathematical exercise. One can notice on Figure 2.6 that the numerical results are in good agreement with the analytical solution. The relative L2 error between analytical and numerical solutions was found to be $\approx 1\%$ with 1000 piecewise linear elements (P1) and a stepsize of 1 s. This value decreases with the stepsize and with the element size (see Figure 2.7).

Since this test case is very similar to a pure diffusion case, it does not exercise all terms of the governing equations. To do so, the governing equations would have to be solved for a generic case which proves to be complex. This is why the MMS will be used instead.

Case 2: H transport (MMS)

Principle The MMS is often used to unravel the complexity of governing equations [189, 190]. This is particularly useful when dealing with complex geometries or to exercise non-trivial material properties.

[189] Dudson et al. (2016)

[190] Roache (2002)

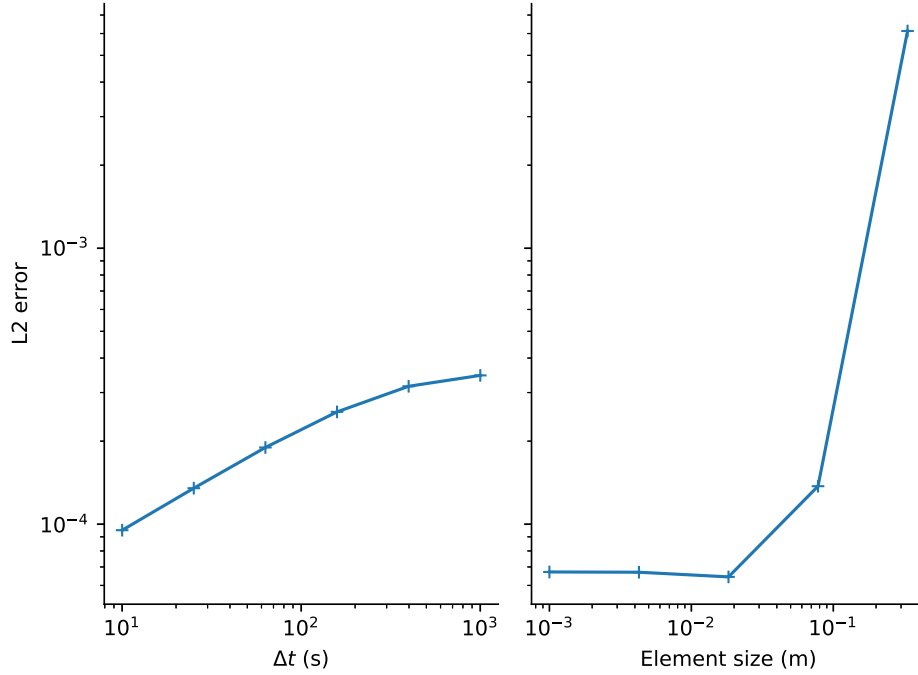


Figure 2.7: Evolution of the L2 error on φ as a function of the stepsize and element length (Case 1).

The principle of the MMS is to manufacture an exact solution. Again, physical realism is not a concern here as verification is a mathematical exercise. This manufactured solution needs to be non-trivial in order to test the robustness of the implementation. It is then passed through the governing equations (either the heat equation or the hydrogen transport equations) and source terms are obtained.

Let us take a simple example with the Poisson equation defined on a 1D domain $[x_1, x_2]$:

$$\frac{\partial u}{\partial t} = \frac{\partial^2 u}{\partial x^2} + q \quad (2.41)$$

where u is the unknown, q is the source term.

The manufactured solution is arbitrarily defined as:

$$U(t, x) = A + \sin(x + Bt) \quad (2.42)$$

where A and B are real numbers, t is the time, and x is the spatial coordinate. By replacing u by $U(t, x)$ in Equation 2.41, we can identify the source term q that would produce the solution $U(t, x)$:

$$Q(t, x) = B \cos(x + Bt) + \sin(x + Bt) \quad (2.43)$$

Several boundary conditions can be used to produce $U(t, x)$. We can for instance set a Dirichlet boundary condition on the boundaries $x = x_1$ and $x = x_2$:

$$u(t, x_1) = U(t, x_1) \quad (2.44)$$

$$u(t, x_2) = U(t, x_2) \quad (2.45)$$

or Neumann boundary conditions:

$$\left. \frac{\partial u(t, x)}{\partial x} \right|_{x=x_1} = \left. \frac{\partial U(t, x)}{\partial x} \right|_{x=x_1} \quad (2.46)$$

$$\left. \frac{\partial u(t, x)}{\partial x} \right|_{x=x_2} = \left. \frac{\partial U(t, x)}{\partial x} \right|_{x=x_2} \quad (2.47)$$

or even a combination of Dirichlet and Neumann boundary conditions.

By solving Equation 2.41 with $q = Q(t, x)$ and initial condition $u = U(0, x)$, we can obtain the computed solution u_{computed} . The error between the computed solution u_{computed} and the exact solution $U(t, x)$ can be calculated to assess the code accuracy.

Case 2a: Application to 1D hydrogen transport Let us apply the MMS to the hydrogen transport model on a 1D domain Ω . In order to exercise all terms in Equation 2.2 and Equation 2.3, the following manufactured solutions are chosen:

$$\begin{cases} c_{mD} = 1 + x^2 + \sin(t) \\ c_{t,1D} = 1 + x^2 + \cos(t) \end{cases} \quad (2.48)$$

By combining Equation 2.2, Equation 2.3 and Equation 2.48, one can obtain the following source terms:

$$\begin{cases} f = \cos(t) - \sin(t) - 2D \\ g_1 = p_1 c_{t,1D} - k_1 c_{mD} (n_1 - c_{t,1D}) - \sin(t) \end{cases} \quad (2.49)$$

f is the source term of the mobile concentration equation and g_1 is the source term of the trapped concentration equation.

where g_1 is an additional source term in Equation 2.3. The Dirichlet boundary conditions for c_m and $c_{t,1}$ are:

$$\begin{cases} c_m = 1 + x^2 + \sin(t) & \text{on } \partial\Omega \\ c_{t,1} = 1 + x^2 + \cos(t) & \text{on } \partial\Omega \end{cases} \quad (2.50)$$

where $\partial\Omega$ is the boundary of the domain. Finally, initial values for c_m and $c_{t,i}$ are:

$$\begin{cases} c_m(t=0) = 1 + x^2 \\ c_{t,1}(t=0) = 2 + x^2 \end{cases} \quad (2.51)$$

Once all these parameters are fed into FESTIM, one can easily compare the computed solution with the exact solution in Equation 2.48. The L2-norm E_{c_m} can then be calculated as follows:

$$E_{c_m} = \sqrt{\int_{\Omega} (c_{mD} - c_m)^2 dx} \quad (2.52)$$

The evolution of E_{c_m} as function of the element size h is shown on Figure 2.8. One can notice that E_{c_m} increases as $A \cdot h^k$. This is known as the *asymptotic regime* and the coefficient k is called the convergence rate. k typically approaches $N + 1$ as h approaches zero, N being the order of the finite elements. In this case, $k \approx 2$ as expected since first order finite elements have been used.

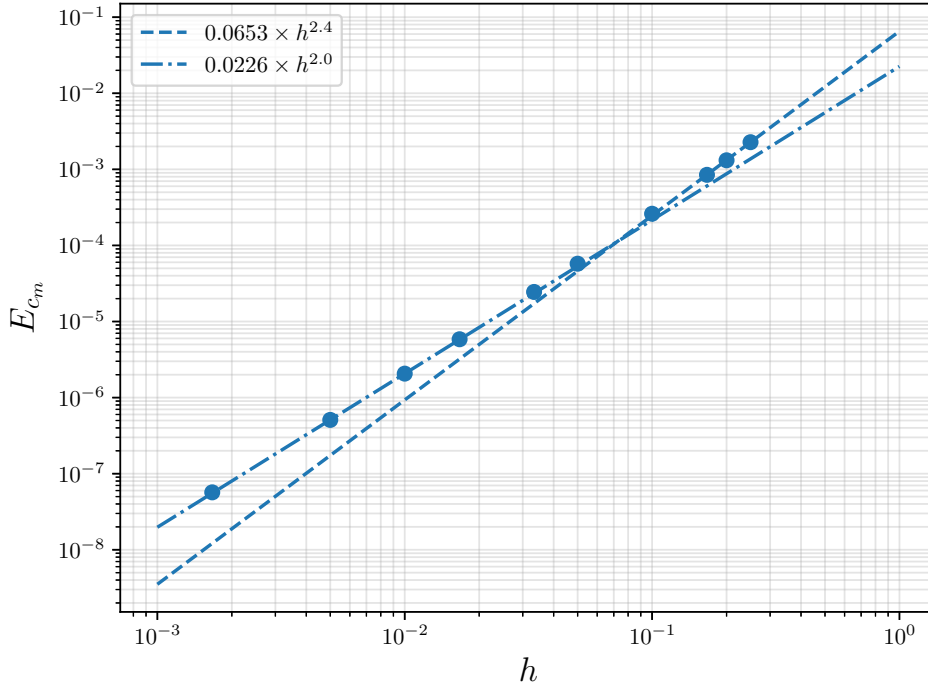


Figure 2.8: Evolution of the L2 norm of the error as function of element size h for the 1D H transport case (Case 2a).

Case 2b: Application to 2D hydrogen transport The same method can be applied to a 2D case. Let us choose the following steady state test problem on a domain $\Omega = [0, 1] \times [0, 1]$ with the manufactured solution $c_D(x, y) = \sin(\omega\pi x) \sin(\omega\pi y)$.

$$\nabla \cdot D \nabla c_m = -f_1 \quad (2.53)$$

$$k c_m (n - c_t) - p c_t = -f_2 \quad (2.54)$$

$$c_m = c_t = c_D \text{ on } \partial\Omega \quad (2.55)$$

$$D = 2 \quad (2.56)$$

$$p = 3 \quad (2.57)$$

$$k = 2 \quad (2.58)$$

$$(2.59)$$

The source terms f_1 and f_2 and the boundary conditions can be obtained in a similar fashion by replacing c_m and c_t in the governing equations.

It was shown that the computed solutions was similar to the exact solutions (see Figure 2.9). Moreover, the convergence rates confirm the mesh dependency of the computed solutions' accuracy (see Figure 2.10).

2.5.2 Experimental validation

Now that the code has been verified (i.e. it solves the governing equations correctly), experimental validation is still required to check that these equations actually represent experimentally observed processes. TDS experiments are a very good example of experiments that can be reproduced for experimental validation of the hydrogen transport model.

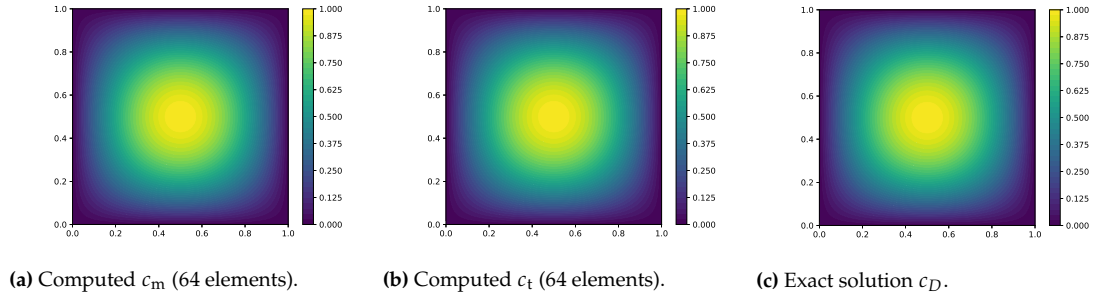


Figure 2.9: Comparison of the computed concentrations with the exact solution (Case 2b).

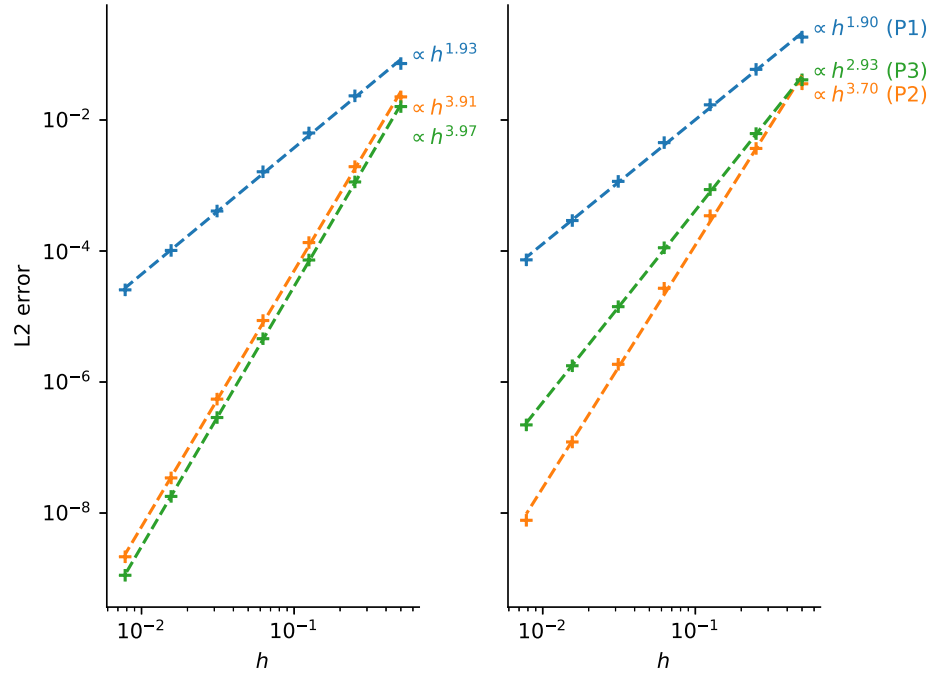


Figure 2.10: Evolution of the L2 error on c_m (left) and c_t (right) showing the convergence rates for the 2D H transport case (Case 2b).

Methodology

[192] Yu et al. (2019)

[193] Hodille et al. (2015)

Fitting experimental data by manually tweaking parameters as in [192, 193] can be really time-consuming, sometimes days in some cases. Moreover, some possible solutions in the parameter space might be missed by the user. This process has been automated by embedding FESTIM in a minimisation algorithm.

As in manual fitting, the parametric optimisation problem is solved by minimising a function representing the residual between simulated results and some reference data. This function f is called *cost function*. Considering fitting one or several TDS spectra (in order to identify for instance trapping parameters or diffusion coefficients), f can simply be the mean absolute error described in Equation 2.60 representing the residual between the simulated spectrum and the experimental reference:

$$f(\mathbf{x}) = \frac{\sum_{i=0}^N \alpha_i(T_i) |d_i - d_{\text{sim}}|}{\sum_{i=0}^N \alpha_i(T_i)} \quad (2.60)$$

where \mathbf{x} is the set of parameters used for the simulation, d_{sim} are the values of the simulated spectrum, N is the number of experimental points (T_i, d_i). In Equation 2.60,

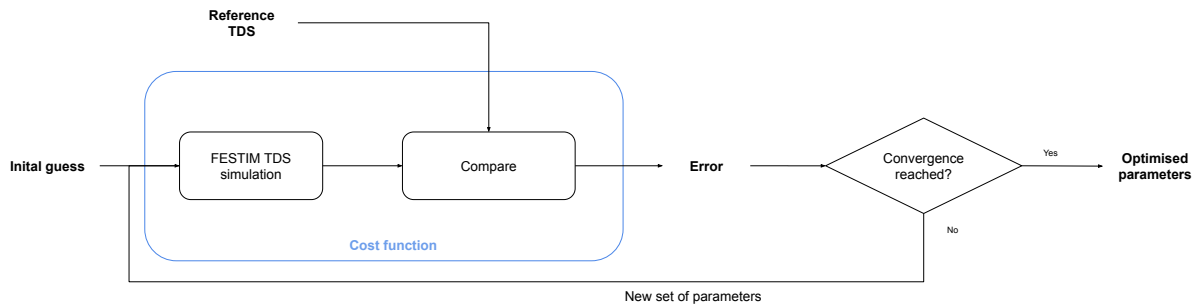


Figure 2.11: Diagram of the parametric optimisation routine.

$f(\mathbf{x})$ can be weighted by coefficients α_i in order to have a better fit on specific regions of the spectrum.

The parametric optimisation problem can now be solved by finding the minimum of the cost function f . A comparative study of the several optimisation algorithms which can be employed has been performed. These algorithms require the user to give an initial set of parameters called *initial guess* and evaluate the cost function with several parameters sets until the convergence criterion is reached (see Figure 2.11). As in [194], the Python package SciPy [195] will be employed.

Four minimisation algorithms have been benchmarked against a test case. In the following example an experimental TDS spectrum from Ogorodnikova et al. [106] will be fitted and materials properties such as trap density and detrapping energy will be identified. For this example case, two intrinsic traps and one extrinsic trap are set. The only free parameters are E_1 and n_1 , respectively the detrapping energy and density of trap 1. The other parameters are constrained and described in [178]. The cost function f has been plotted on Figure 2.12 as function of E_1 and n_1 .

In this case, when only two free parameters are set the cost function has only one minimum (it is not necessarily the case for higher dimension optimisation problems). However, if one fixes the trap density n_1 above $\approx 2 \times 10^{-3}$ at fr, the cost function has two local minima which can lead the optimisation routine to converged to a non-global minimum. Moreover, f is smooth and quadratic around its minimum located at $(E_1, n_1) = (0.86 \text{ eV}, 1.2 \times 10^{-3} \text{ at fr})$. For detrapping energies below 0.6 eV and/or densities below 0.5×10^{-3} at fr, the cost function is constant. This is because for these values, the contribution of this trapping site to the TDS spectrum is zero either because the density is close to zero, or because the energy is too low for these traps to be filled at the implantation temperature of 300 K. Variations in these regions do not modify the simulated spectrum and thus do not modify the cost function value.

Four different optimisation algorithms are being compared: Nelder-Mead (also called the simplex method), Powell, Truncated Newton method (TNC) and Conjugate Gradient (CG). Thorough descriptions of these algorithms would be beyond the scope of this research but can be found in [196]. The performances of these algorithms have been compared with 100 different initial guesses randomly distributed on the (E_1, n_1) plane and are shown on Figure 2.13. It appears that the CG algorithm is less robust since for some cases it didn't converge towards the global minimum (see white bands on Figure 2.13). The Nelder-Mead algorithm appears to be the most efficient with initial guesses both close and far from the global minimum since the number of cost function evaluations ranges from 50 to 100 whereas other algorithms require more than 100. This can be explained by the fact that Nelder-Mead is a derivative-free algorithm whereas the TNC and CG algorithms need to compute first order derivatives thus

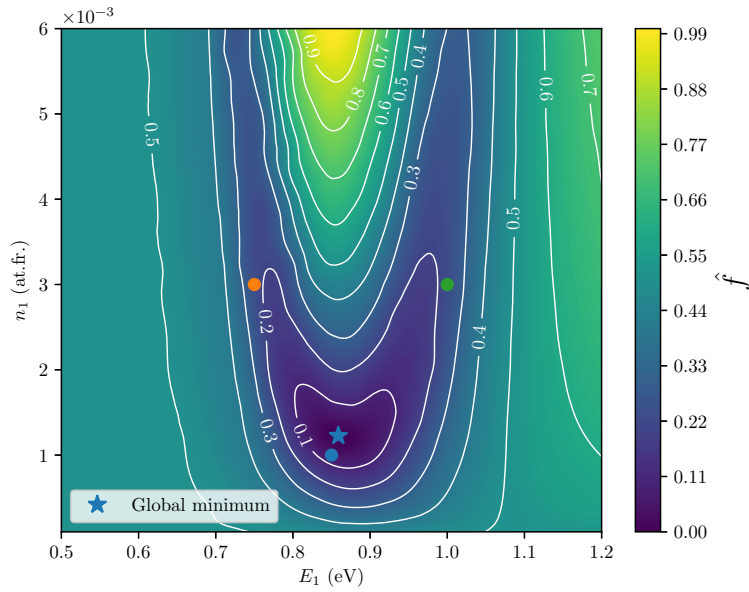
[194] Drexler et al. (2019)

[195] Virtanen et al. (2020)

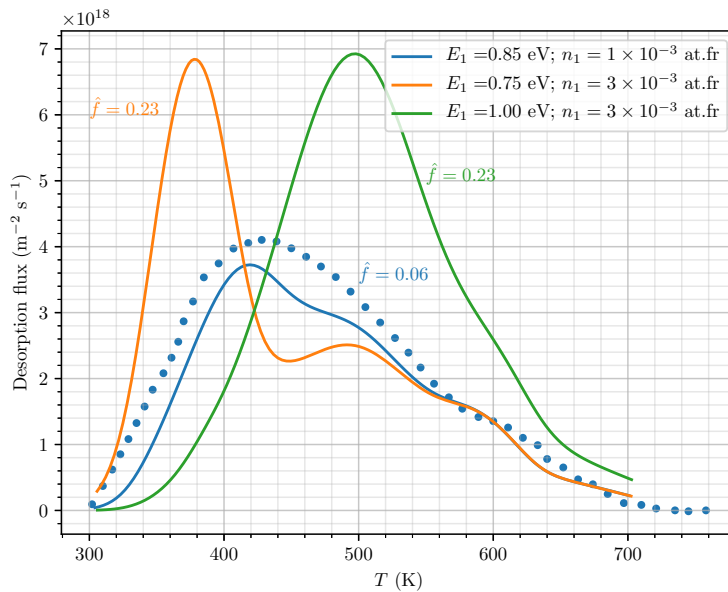
[106] Ogorodnikova et al. (2003)

[178] Delaporte-Mathurin et al. (2019)

[196] Nocedal et al. (2006)



(a) Normalised cost function.



(b) Corresponding simulated TDS spectra.

Figure 2.12: Normalised cost function $\hat{f} = (f - \min f) / (\max f - \min f)$ as function of E_1 (eV) and n_1 (at fr) with global minimum located at $(0.86 \text{ eV}, 1.2 \times 10^{-3} \text{ at fr})$.

increasing the number of function evaluations. This will be even more true when increasing the number of free parameters since the derivative will become more costly to compute.

It is worth noting that the Nelder-Mead algorithm is an unconstrained method. If constraints or bounds are needed, TNC might be a more suitable choice.

Though in the following, the Nelder-Mead algorithm will be employed in the following cases.

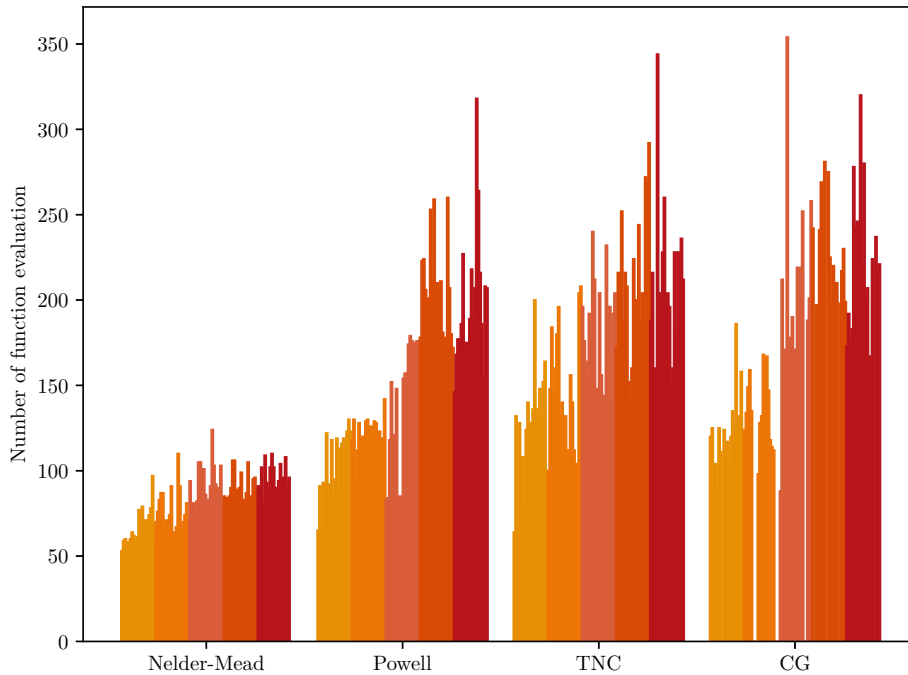


Figure 2.13: Number of cost function evaluations required to converge towards the global minimum with 100 different initial guesses sorted by distance to the global minimum for several minimisation algorithms. Each cost function evaluation takes 20 s to compute. White stripes correspond to initial guesses for which the algorithm did not converge to the global minimum.

Validation on tungsten

The TDS spectrum measured by Ogorodnikova et al. [106] has been reproduced by setting all traps parameters as free parameters. The fitting procedure has been run for several numbers of traps as shown on Figure 2.14a. It is clear that setting only one trap is not sufficient to reproduce the experimental data. The two traps case shows better results but also has a discrepancy near 600 K. This discrepancy is removed when setting a third extrinsic trap to the simulation.

For this last case, the five free parameters are the detrapping energies $E_{p,1}$, $E_{p,2}$, $E_{p,3}$ and densities n_1 , n_2 (the third trapping site being created during the implantation, for which the creation parameters are not part of the free parameters and taken from [106] or [193]). This optimisation case is therefore a 5D optimisation problem. Every other parameter is taken from [193]. The resulting fit is shown on Figure 2.14b alongside with the contribution of each trap to the total spectrum. An interesting feature of this spectrum is the negative area of the contribution of the second trap around 400 K. Because not all of these traps are saturated, when trap 1 is emptying, some hydrogen particles are nearly instantly trapped in the second trap which has a higher detrapping energy.

The identified parameters are similar to the ones found by Hodille et al. in [193]. The total fitting procedure took a few hundred of cost function evaluations. One single cost function evaluation ‘costing’ less than 20 s to compute (for that specific case), the total procedure lasted less than 3 h.

Limitations

Even though an automated technique is proposed, the user still has some choices to make in order to ensure the credibility of the fitted spectrum. Weighting the cost function near regions of interest will result in a better fit in these regions. Users should also be aware of the number of traps the data is being fitted with. As shown on Figure

[106] Ogorodnikova et al. (2003)

[193] Hodille et al. (2015)

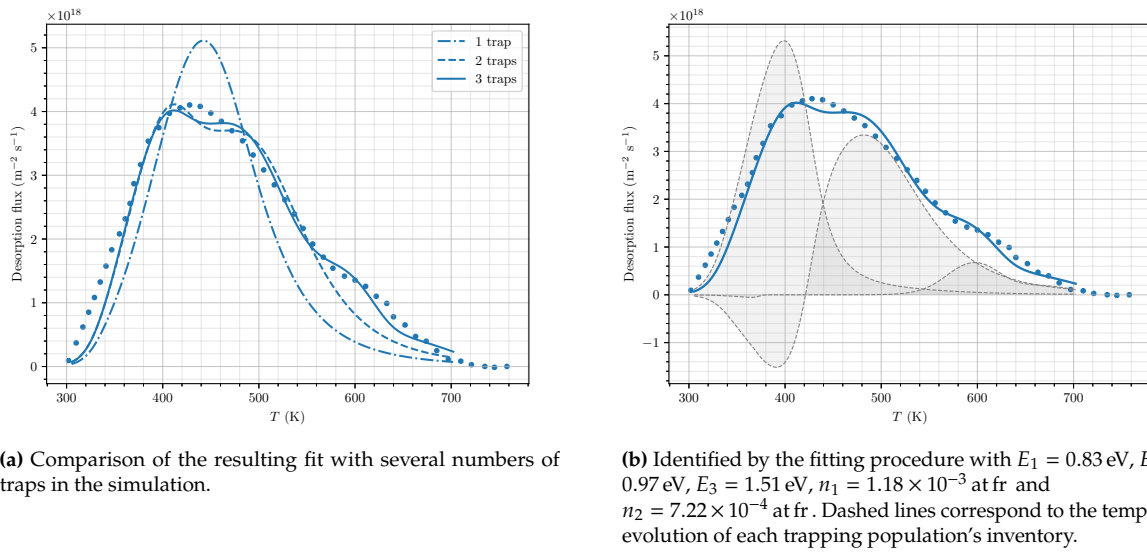


Figure 2.14: Fitting TDS spectrum performed on Tungsten by Ogorodnikova *et al* [106]. Dots correspond to experimental data.

2.14a too few traps in the simulation will not result in a satisfactory fit (even though the optimisation routine will converge to an optimised solution). Moreover, as shown on Figure 2.15, one single TDS spectrum can be reproduced with several traps of different energies and densities. This means that the cost function with several traps as free parameters can have several local minima of very similar values. Adding traps to an optimisation problem can also help to have a better fit of the experimental data in some cases. But artificially adding more and more traps is not necessarily realistic and could lead to misinterpretation of the results.

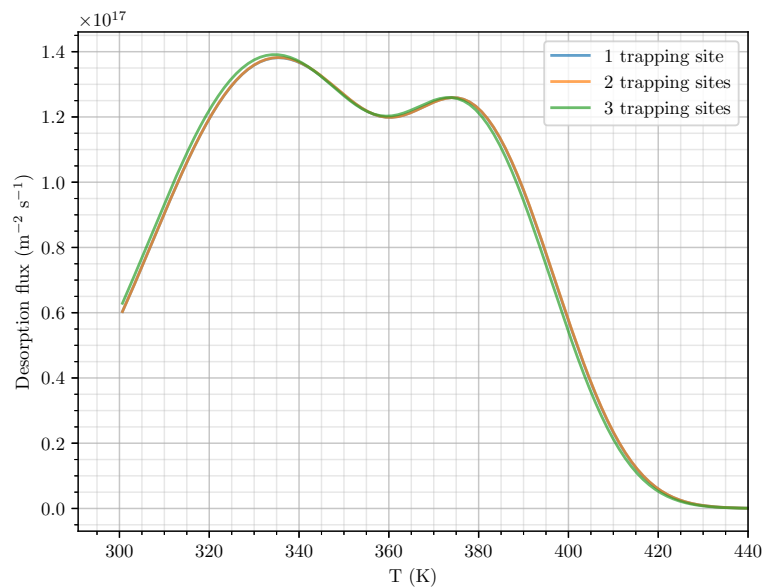


Figure 2.15: TDS spectrum reproduced with several sets of parameters showing the existence of several solutions to a single optimisation problem.

[197] Hurley *et al.* (2015)

In the first case with only one trapping site, as described by Hurley *et al.* in [197], the binding energy is 0.55 eV and the trap density is $2.08 \times 10^{24} \text{ m}^{-3}$. The appearance of two peaks is due to the desorption on different sides of the sample as explained in [197]. In the second case, the curve as been reproduced with two trapping sites

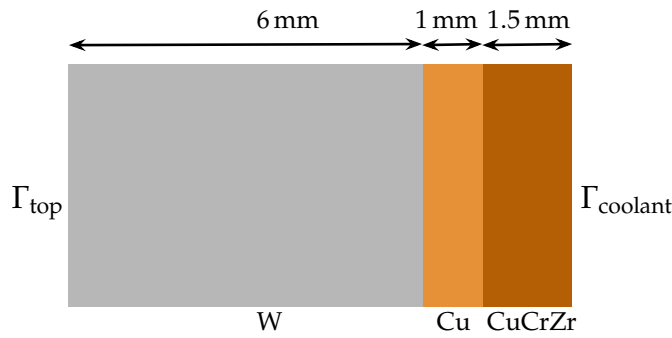


Figure 2.16: TMAP7 - FESTIM comparison 1D geometry showing W , Cu , CuCrZr .

Table 2.2: Traps properties used in the comparison with TMAP7.

	Material	$k_0(\text{m}^3 \text{s}^{-1})$	$E_k(\text{eV})$	$p_0(\text{s}^{-1})$	$E_p(\text{eV})$	$n_i(\text{at fr})$
Trap 1	W	3.8×10^{-17}	0.39	8.4×10^{12}	1.20	5.0×10^{-4}
Trap 2	W	3.8×10^{-17}	0.39	8.4×10^{12}	1.40	5.0×10^{-3}
Trap 3	Cu	6.0×10^{-17}	0.39	8.0×10^{13}	0.50	5.0×10^{-5}
Trap 4	CuCrZr	1.2×10^{-16}	0.42	8.0×10^{13}	0.50	5.0×10^{-5}
Trap 5	CuCrZr	1.2×10^{-16}	0.42	8.0×10^{13}	0.83	4.0×10^{-2}

which energies and densities are respectively 0.51 eV and 0.57 eV and $2.02 \times 10^{24} \text{ m}^{-3}$ and $2.12 \times 10^{24} \text{ m}^{-3}$. In the third case, it has been reproduced with three trapping sites which energies and densities are respectively 0.55 eV, 0.38 eV and 0.51 eV and $2.12 \times 10^{24} \text{ m}^{-3}$, $2.26 \times 10^{24} \text{ m}^{-3}$ and $2.13 \times 10^{24} \text{ m}^{-3}$.

This example illustrates how a single spectrum can be simulated with several sets of parameters by varying the number of traps in the simulation. One way to avoid this from happening is to have a set of experiments with varying parameters such as the implantation temperature, the heating ramp, the fluence, dwelling time before TDS, etc.

[165] Longhurst (2008)

2.5.3 Comparison with TMAP7

The FESTIM code was compared to TMAP7 [165] on a 1D case.

The 1D simulation case is a 8.5 mm-thick composite slab made of W, Cu and CuCrZr (see Figure 2.16). The plasma facing surface Γ_{top} is located at $x = 0 \text{ mm}$ and the surface cooled by water Γ_{coolant} is located at $x = 8.5 \text{ mm}$. The trapping parameters are detailed in Table 2.2. The boundary conditions are detailed in Equation 2.61.

$$T = 1200 \text{ K} \quad \text{on } \Gamma_{\text{top}} \quad (2.61a)$$

$$c_m = \frac{\varphi_{\text{imp}} \cdot R_p}{D} \quad \text{on } \Gamma_{\text{top}} \quad (2.61b)$$

$$T = 373 \text{ K} \quad \text{on } \Gamma_{\text{coolant}} \quad (2.61c)$$

$$-D\nabla c_m \cdot \mathbf{n} = K_{\text{CuCrZr}} \cdot c_m^2 \quad \text{on } \Gamma_{\text{coolant}} \quad (2.61d)$$

with $K_{r,\text{CuCrZr}} = 2.9 \times 10^{-14} \cdot \exp(-1.92/(k_B \cdot T))$ the recombination coefficient of the CuCrZr (in vacuum) expressed in $\text{m}^4 \text{s}^{-1}$ [198].

[198] Anderl et al. (1999)

The Dirichlet boundary condition on Γ_{top} for the hydrogen transport corresponds to a flux balance between the implanted flux and the flux that is retro-desorbed at the surface (see Section 2.2.2). The temperature profile in TMAP7 was fixed on the temperature profile produced by FESTIM (see Figure 2.17).

TMAP7 and FESTIM were found to be in very good agreement (see Figure 2.18).

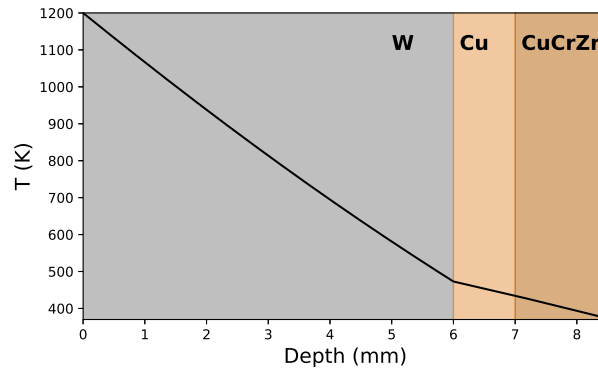


Figure 2.17: Temperature profile simulated by FESTIM for comparison case with TMAP7.

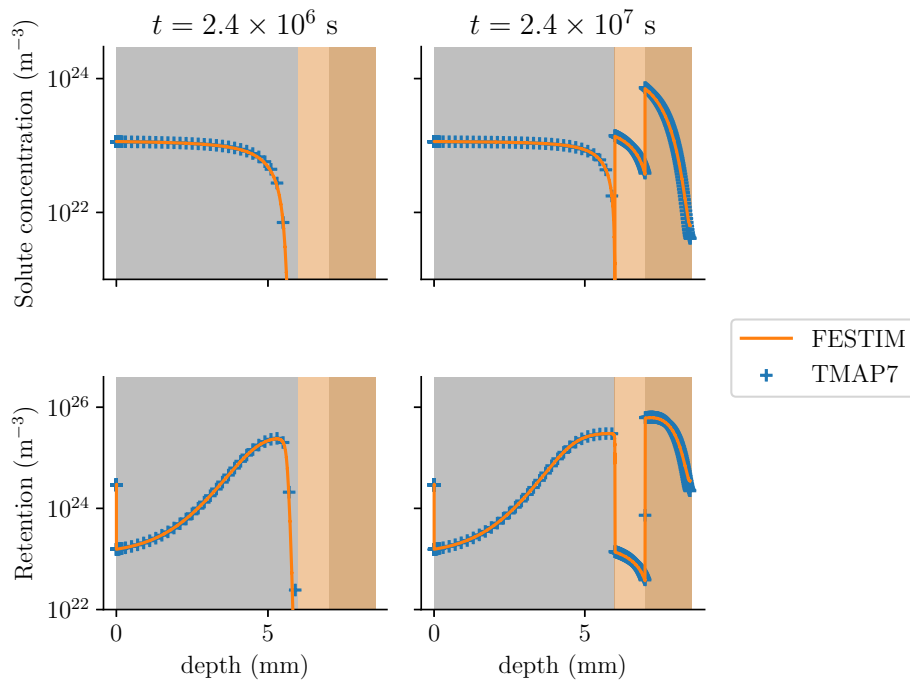


Figure 2.18: Comparison of results provided by FESTIM and TMAP7.

2.6 Summary

The macroscopic rate equations model describing the transport (diffusion and trapping) of H in solids was presented alongside with additional models such as the conservation of chemical potential at interfaces. Due to the presence of thermally activated processes (diffusion, trapping, detrapping, surface processes...), the heat transfer equation has to be solved numerically. All these equations are solved with the newly developed finite element code FESTIM, which heavily relies on FEniCS.

FESTIM has been verified using methods such as the Method of Exact Solutions and the Method of Manufactured Solutions. On the other hand, it was shown that FESTIM could be employed to reproduce experiments (TDS experiments) performed on tungsten. This validation process could be extended by reproducing other types of experiments such as permeation experiments and profilometry. However, this set of equation (shared amongst H transport codes) has already proven to be capable of reproducing these experiments. This has been done, for instance, during the validation of TMAP7 [165].

Thanks to this verification & validation process, it was shown that (1) the hydrogen transport governing equations were correctly solved and (2) these equations can represent processes observed experimentally.

The FESTIM code can then be safely employed to perform analysis on tokamak components.

[165] Longhurst (2008)



3 Monoblocks

In order to assess the behaviour of H in the divertor, component-level simulations of monoblocks are required.

This chapter will focus on simulating H transport in ITER-like monoblocks.

Section 3.1 will describe the model geometry, the boundary conditions as well as the materials and trap properties. Then, Section 3.2 will review the simplifications that can be brought to the model to reduce the computation time. Finally, with these simplifications, a parametric study will be performed and a behaviour law linking the monoblock H inventory to the exposure conditions will be determined in Section 3.3.

- 3.1 Model description . . . 55
- 3.2 Simulation simplifications 58
- 3.3 Monoblock behaviour law 65
- 3.4 Summary . . . 69

3.1 Model description

The monoblock geometry is described on Figure 3.1. The boundary conditions for the heat transfer problem are described in Equation 3.1 and those for the hydrogen transport problem are described in Equation 3.2. An instantaneous recombination is assumed on the poloidal and toroidal gaps and at the plasma facing surface. This assumption is consistent with the high recombination coefficient measured by Ogorodnikova [199] compared to Anderl’s coefficient [95].

[199] Ogorodnikova (2019)
 [95] Anderl et al. (1992)
 [193] Hodille et al. (2015)

The materials properties (diffusivity, solubility, and thermal conductivity, density and heat capacity) are described in Table 3.1 and plotted on Figure 3.2. Finally, the traps properties are described in Table 3.2. The traps for W were taken from [193] and the trap created by ion implantation is neglected for it only affects the near surface of the monoblock.

$$-\lambda \nabla T \cdot \mathbf{n} = \varphi_{\text{heat}} \quad \text{on } \Gamma_{\text{top}} \quad (3.1a)$$

$$-\lambda \nabla T \cdot \mathbf{n} = -h \cdot (T_{\text{coolant}} - T) \quad \text{on } \Gamma_{\text{coolant}} \quad (3.1b)$$

where $T_{\text{coolant}} = 323 \text{ K}$ and $h = 70\,000 \text{ W m}^{-2} \text{ K}^{-1}$.

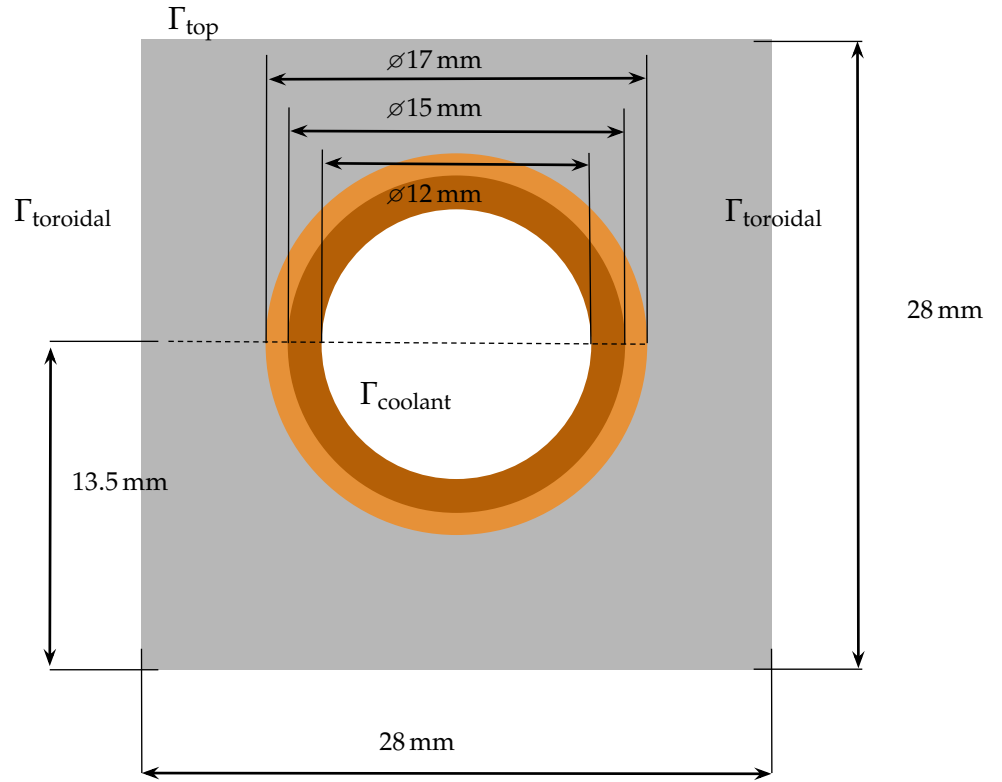


Figure 3.1: ITER monoblock geometry showing W armour \square , Cu interlayer \square , CuCrZr alloy cooling pipe \square . The monoblock thickness is 12 mm.

$$c_m = \frac{\varphi_{\text{imp}} R_p}{D} \quad \text{on } \Gamma_{\text{top}} \quad (3.2a)$$

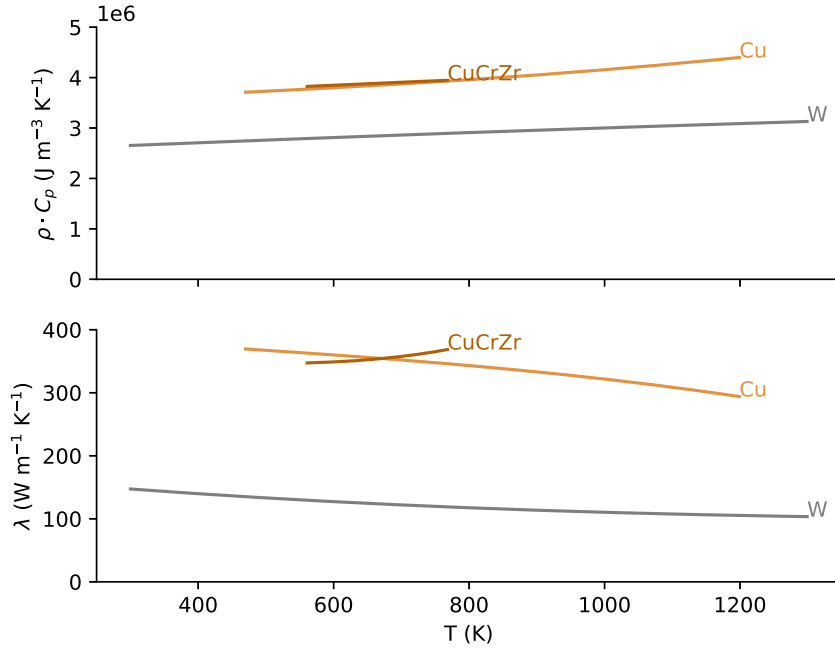
$$-D \nabla c_m \cdot \mathbf{n} = K_{r, \text{CuCrZr}} \cdot c_m^2 \quad \text{on } \Gamma_{\text{coolant}} \quad (3.2b)$$

$$c_m = 0 \quad \text{on } \Gamma_{\text{toroidal}} \text{ and } \Gamma_{\text{poloidal}} \quad (3.2c)$$

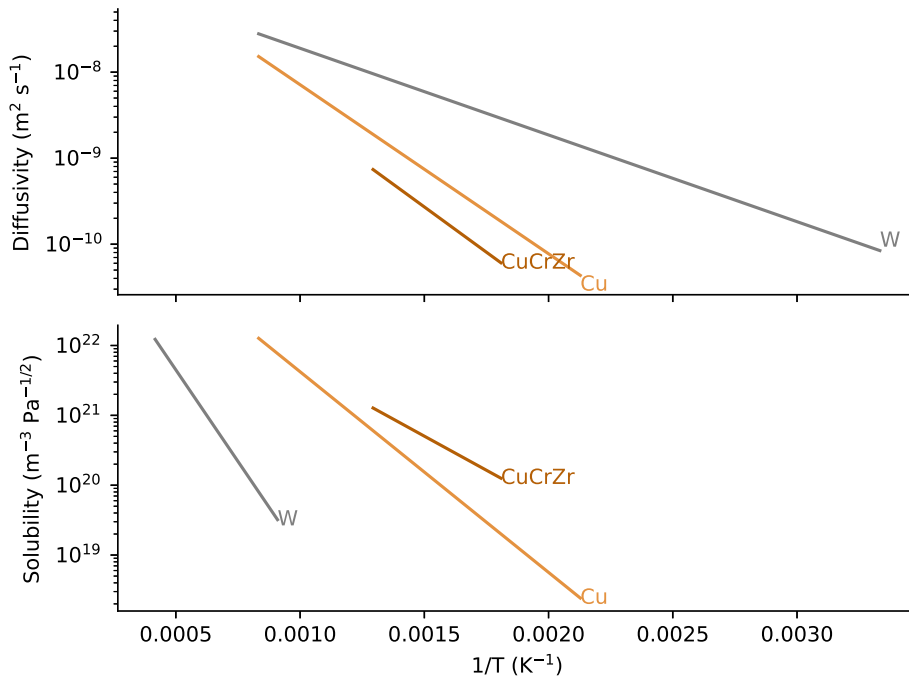
$$(3.2d)$$

where $K_{r, \text{CuCrZr}} = 2.9 \times 10^{-14} \cdot \exp(-1.92/(k_B \cdot T))$ the recombination coefficient of the copper alloy (in vacuum) expressed in $\text{m}^4 \text{s}^{-1}$ [198].

[198] Anderl et al. (1999)



(a) Thermal properties.



(b) H transport properties.

Figure 3.2: Material properties used in the simulations [93, 101, 200–202].

Table 3.1: Materials properties used in the simulations. Thermal properties are fitted from ANSYS. T is the temperature in K.

Material	Thermal properties		Hydrogen transport properties			
	$\rho \cdot C_p$ ($\text{J K}^{-1} \text{m}^{-3}$)	λ ($\text{W m}^{-1} \text{K}^{-1}$)	D_0 ($\text{m}^2 \text{s}^{-1}$)	E_D (eV)	S_0 ($\text{m}^{-3} \text{Pa}^{-0.5}$)	E_S (eV)
W [93, 101]	$5.1 \times 10^{-6} \cdot T^3$ $- 8.3 \times 10^{-2} \cdot T^2$ $+ 6.0 \times 10^2 \cdot T$ $+ 2.4 \times 10^6$	$-7.8 \times 10^{-9} \cdot T^3$ $+ 5.0 \times 10^{-5} \cdot T^2$ $- 1.1 \times 10^{-1} \cdot T$ $+ 1.8 \times 10^2$	1.9×10^{-7}	0.20	1.87×10^{24}	1.04
Cu [200]	$1.7 \times 10^{-4} \cdot T^3$ $+ 6.1 \times 10^{-2} \cdot T^2$ $+ 4.7 \times 10^2 \cdot T$ $+ 3.5 \times 10^6$	$-3.9 \times 10^{-8} \cdot T^3$ $+ 3.8 \times 10^{-5} \cdot T^2$ $- 7.9 \times 10^{-2} \cdot T$ $+ 4.0 \times 10^2$	6.6×10^{-7}	0.39	3.14×10^{24}	0.57
CuCrZr [201]	$-1.8 \times 10^{-4} \cdot T^3$ $+ 1.5 \times 10^{-1} \cdot T^2$ $+ 6.2 \times 10^2 \cdot T$ $+ 3.5 \times 10^6$	$5.3 \times 10^{-7} \cdot T^3$ $- 6.5 \times 10^{-4} \cdot T^2$ $+ 2.6 \times 10^{-1} \cdot T$ $+ 3.1 \times 10^2$	3.9×10^{-7}	0.42	4.28×10^{23}	0.39

Table 3.2: Traps properties used in the simulations [193, 203].

	Material	$k_0(\text{m}^3 \text{s}^{-1})$	$E_k(\text{eV})$	$p_0(\text{s}^{-1})$	$E_p(\text{eV})$	$n_i(\text{at fr})$
Trap 1	W	8.96×10^{-17}	0.2	1×10^{13}	0.87	1.1×10^{-3}
Trap 2	W	8.96×10^{-17}	0.2	1×10^{13}	1.00	4.0×10^{-4}
Trap 3	Cu	6.0×10^{-17}	0.39	8.0×10^{13}	0.50	5.0×10^{-5}
Trap 4	CuCrZr	1.2×10^{-16}	0.42	8.0×10^{13}	0.85	5.0×10^{-5}

3.2 Simulation simplifications

3.2.1 Thermal behaviour

Steady-state heat transfer simulations were performed with FESTIM with varying heat fluxes φ_{heat} . With $\varphi_{\text{heat}} = 1 \text{ MW m}^{-2}$, the surface temperature of the monoblock was found to be around 400 K (see Figure 3.3a) whereas with $\varphi_{\text{heat}} = 10 \text{ MW m}^{-2}$ the surface was around 1400 K (see Figure 3.3b).

The average surface temperature T_{surface} therefore increases linearly with the heat load and can be fitted by Equation 3.3 (see Figure 3.3c).

$$T_{\text{surface}} = 1.1 \times 10^{-4} \cdot \varphi_{\text{heat}} + T_{\text{coolant}} \quad (3.3)$$

[29] Hirai et al. (2016)

This was found to be in very good agreement with experimental measurements performed in [29]. Using a mean surface temperature had low influence on the hydrogen transport results compared to a non-homogeneous surface temperature that could be obtained with a heat flux condition since surface temperature gradient was low compared to the one between the top surface and the cooling surface.

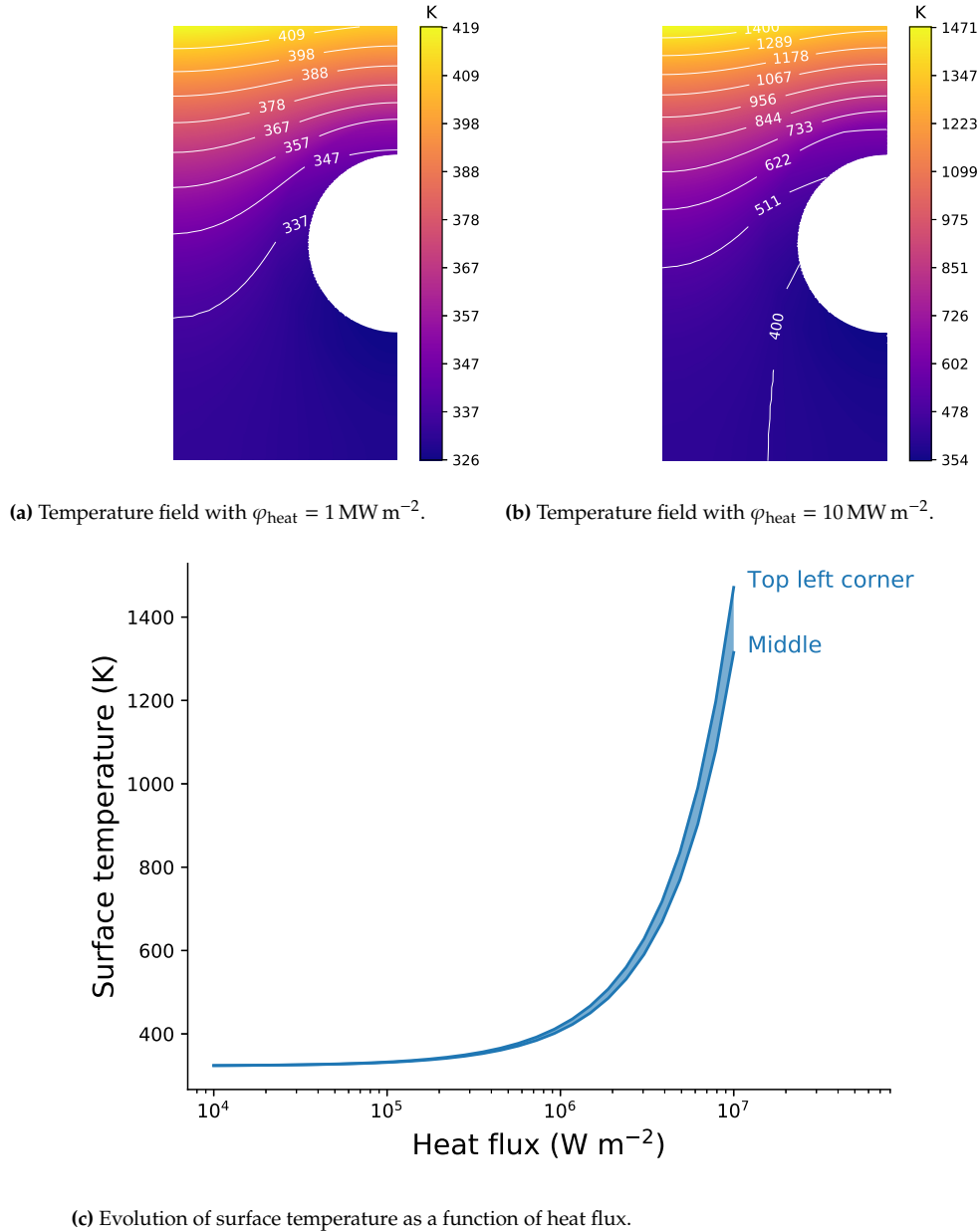


Figure 3.3: Thermal behaviour of the monoblock.

3.2.2 Influence of dimensionality

The first simplification that can be done is the dimensionality. A full 3D simulation would be the most accurate, but also the most expensive in terms of computation time (partly because more cells are required for the same spatial discretisation as seen on Figure 3.4). Conversely, 1D simulations are faster to run, but are less accurate. This is sometimes referred as the *curse of dimensionality*.

A 2D approximation assumes the solution is independent of the poloidal direction. The hydrogen inventory is obtained by:

$$\text{inv} = e \int_{\Omega} (c_m + \sum c_{t,i}) dS \quad (3.4)$$

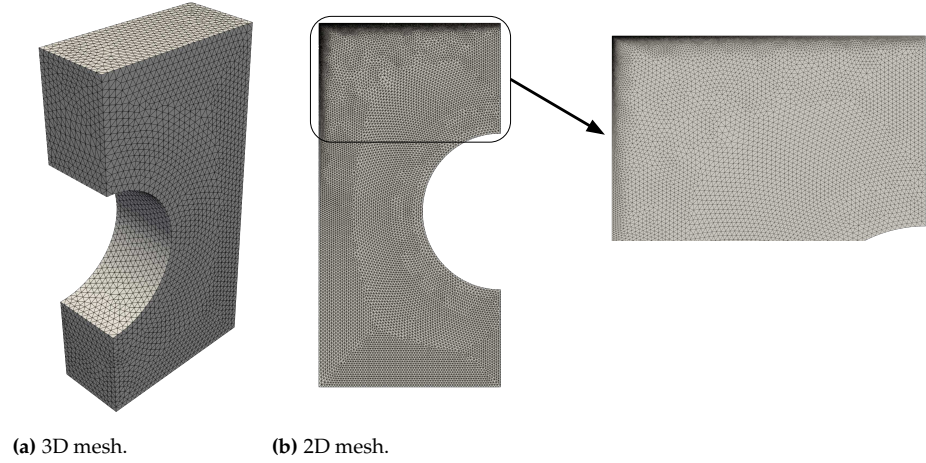


Figure 3.4: Meshes used for the monoblock simulations.

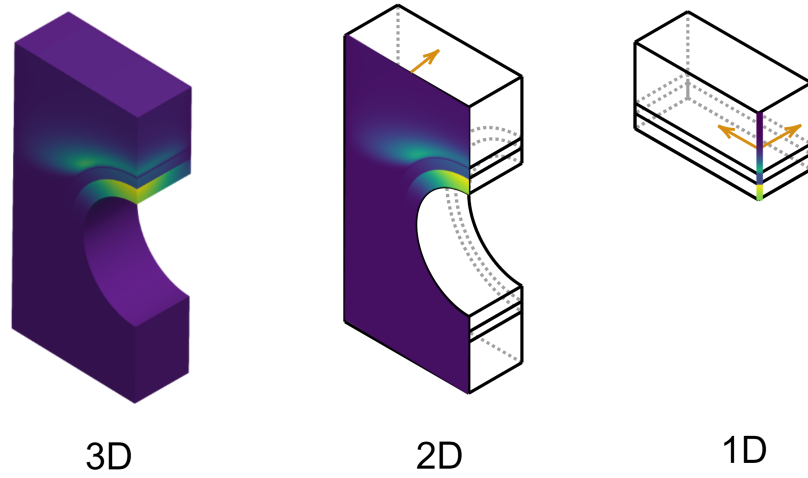


Figure 3.5: Representation of the 2D and 1D approximations on a monoblock geometry. The arrows represent geometry independencies.

where e is the monoblock thickness.

Similarly, the 1D approximation assumes the solution is independent of both the poloidal and the toroidal direction (see Figure 3.5). It also cannot capture the full geometry of the monoblock as it would assume Cu and CuCrZr slabs instead of hollow cylinders. The hydrogen inventory is obtained by:

$$\text{inv} = eL \int_{\Omega} (c_m + \sum c_{t,i}) dl \quad (3.5)$$

where L is the monoblock width.

Monoblocks simulations were run in 1D, 2D, and 3D and the inventory was computed for each case (see Figure 3.6). Both the 1D and 2D approximations overestimate the inventory compared to the 3D reference, these approximations are therefore conservative. It should however be noticed that, when neglecting the recombination on the poloidal gap (i.e. assuming hydrogen cannot desorb from this surface), the 2D approximation is strictly equivalent to the 3D reference (see C). For these reasons, the 2D approximation will be employed in the following sections as it is the best compromise between accuracy and computational time.

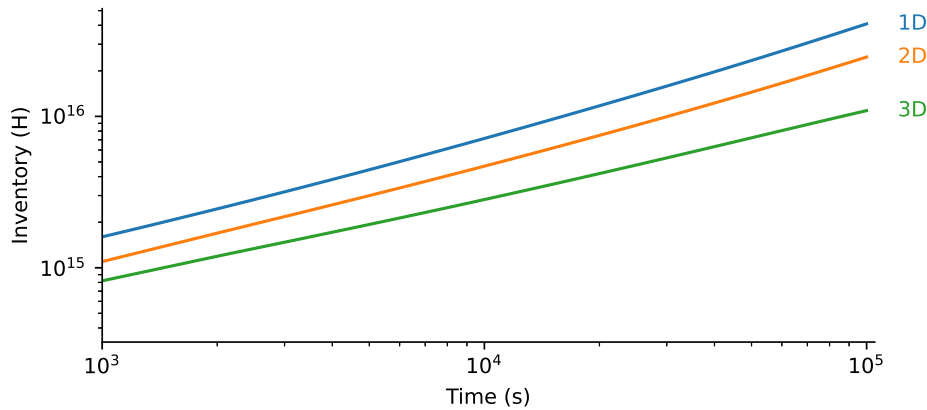


Figure 3.6: Comparison of monoblock inventories for the 1D, 2D approximations and the 3D case.

3.2.3 Influence of interface condition

As monoblocks are made of several materials (tungsten, copper and CuCrZr), the continuity of chemical potential across interfaces results in a mobile concentration jump (see Section 2.2.3). However, the problem could be simplified if, instead of ensuring the continuity of chemical potential, one ensured the continuity of mobile concentration across interfaces. Indeed, this would allow getting rid of one equation and therefore reduce the computational time. But is this simplification valid?

To verify its validity, 2D monoblock simulations are performed with chemical potential continuity (see Equation 1.34) or mobile concentration continuity and the temporal evolution of the inventory was computed. The implanted flux φ_{imp} was fixed to $1.0 \times 10^{21} \text{ m}^{-2} \text{ s}^{-1}$ and the heat flux φ_{heat} varied from 3.0 MW m^{-2} to 7.0 MW m^{-2} .

For the low flux cases (3 MW m^{-2} and 5 MW m^{-2}), no difference was found (see Figure 3.7). For the case at 6 MW m^{-2} , differences start to appear after $3 \times 10^6 \text{ s}$ ($7 \times 10^5 \text{ s}$ at 7 MW m^{-2}). After $2 \times 10^7 \text{ s}$ of continuous exposure, the absolute difference at 6 MW m^{-2} was 25 % and 55 % at 7 MW m^{-2} .

This time of appearance of differences corresponds to the time required for the hydrogen to migrate up to the W/Cu interface. This is explained by the high solubility ratio between W, Cu and CuCrZr leading to a higher concentration of mobile particles in CuCrZr (see Figure 3.8) and therefore a higher trapping rate. Since the trap density in Cu is low, the global inventory is not affected by it.

Similarly, before reaching the W/Cu interface, the retention profiles are identical regardless of the interface condition (see Figure 3.9).

The retro-desorbed flux (from the monoblock to the plasma) does not depend on the interface conditions since interfaces are far from the exposed surface. Moreover, outgassing flux through the cooling pipe greatly depends on the boundary condition imposed at the cooling surface. Therefore, in order to assess the impact of interface conditions on the outgassing flux through the cooling pipe, uncertainties must first be lifted regarding the recombination process occurring on surfaces in contact with water.

Since this work is motivated by the estimation of the divertor inventory, the concentration continuity assumption is therefore valid since only a few monoblocks are exposed to high heat fluxes and most of the divertor is at the coolant temperature (this will be explained further in Chapter 4).

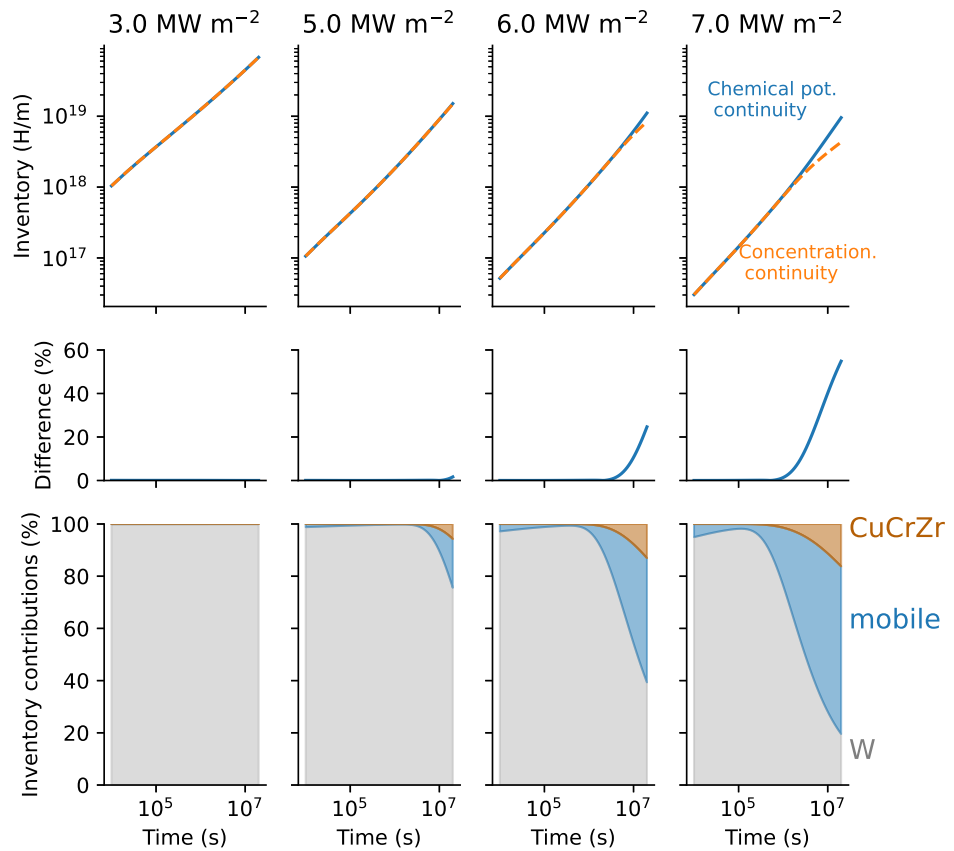


Figure 3.7: Influence of continuity of chemical potential on the monoblock hydrogen inventory. The bottom plot shows the contribution of the trapped hydrogen in W, Cu and CuCrZr as well as the total mobile hydrogen for the case with continuity of chemical potential.

3.2.4 Influence of cycling

[204] Lister et al. (2006)

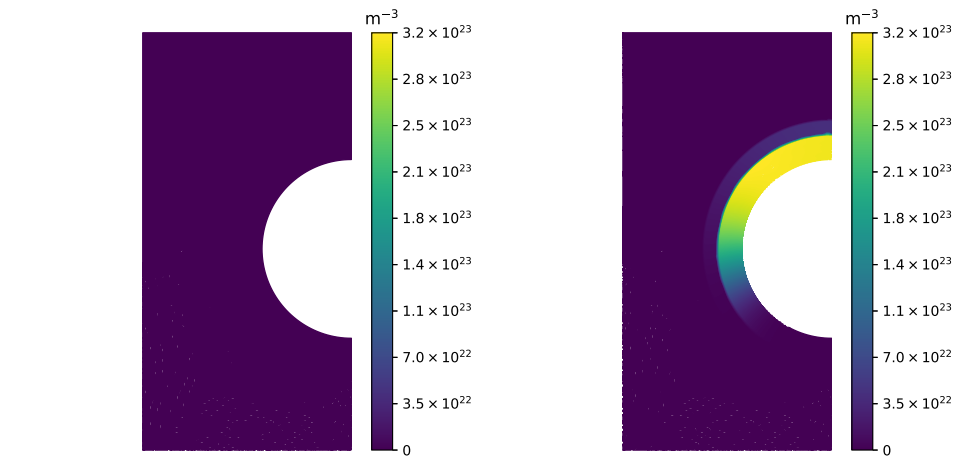
In ITER, the plasma operation will not be continuous. Instead, pulses of 600 s will be shot [204] with a ramp-up of 100 s, a plateau during 400 s, a ramp-down of 100 s and 1000 s of dwell time between pulses (see Figure 3.10). Simulating these transient cycles would require stepsizes of ≈ 10 s in order to capture the ramp-up and ramp-down phases. Simulating one cycle would therefore require more than 60 steps (excluding the resting phase).

On the other hand, FESTIM has an adaptive stepsize feature allowing the stepsize to increase (resp. decrease) when steps are solved in less (resp. more) than five Newton iterations. Therefore, if a continuous plasma exposure was simulated, the adaptive stepsize would allow the stepsize to increase up to thousands of seconds, reducing a lot the simulation time.

To verify the validity of the continuous exposure approximation, 1D simulations were run with plasma cycles or continuous exposure. For the cycled simulation, both the heat flux φ_{heat} and the particle flux φ_{imp} were varied from zero during the resting phases to their nominal values during the plateau phase (see Figure 3.10).

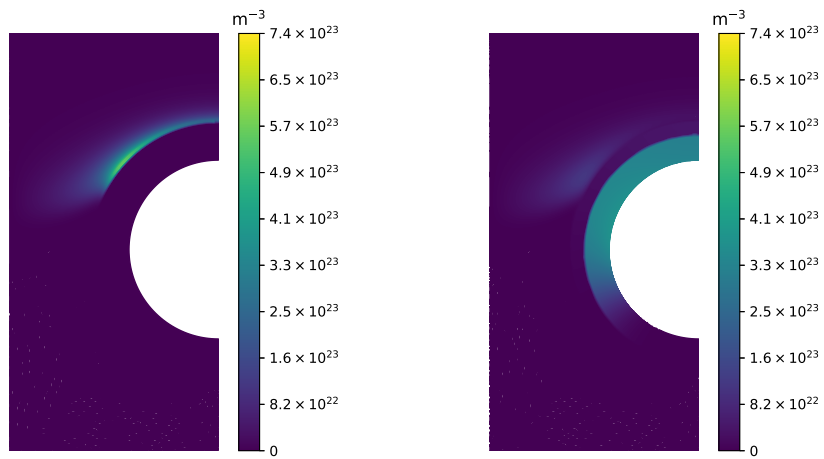
Two cases were run:

- ▶ High flux: $\varphi_{\text{heat}} = 13 \text{ MW m}^{-2}$ and $\varphi_{\text{imp}} = 1.6 \times 10^{22} \text{ m}^{-2} \text{ s}^{-1}$
- ▶ Low flux: $\varphi_{\text{heat}} = 5 \text{ MW m}^{-2}$ and $\varphi_{\text{imp}} = 5.0 \times 10^{21} \text{ m}^{-2} \text{ s}^{-1}$



(a) c_m (continuity of c_m).

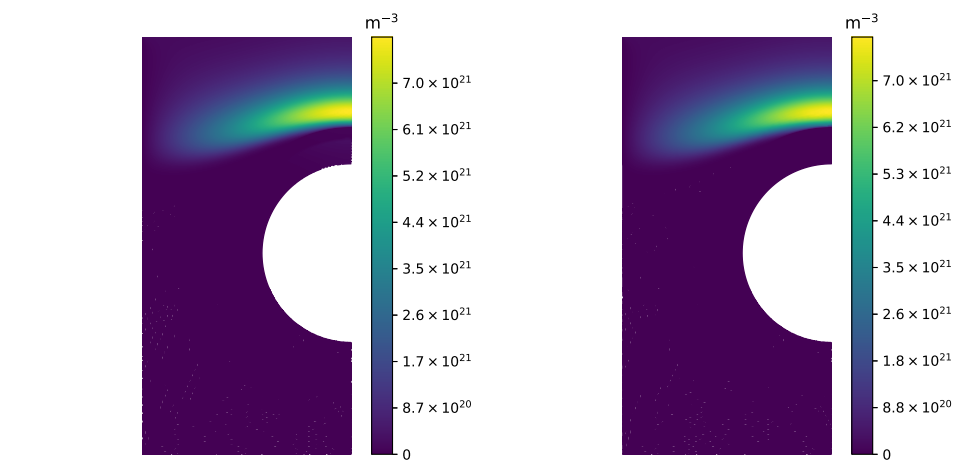
(b) c_m (continuity of chemical potential).



(c) Retention (continuity of c_m).

(d) Retention (continuity of chemical potential).

Figure 3.8: Influence of interface conditions on concentration fields at $t = 2 \times 10^7$ s, $\varphi_{\text{heat}} = 7 \text{ MW m}^{-2}$.



(a) continuity of chemical potential.

(b) continuity of mobile concentration.

Figure 3.9: Influence of interface conditions on retention fields at $t = 6.1 \times 10^4$ s.

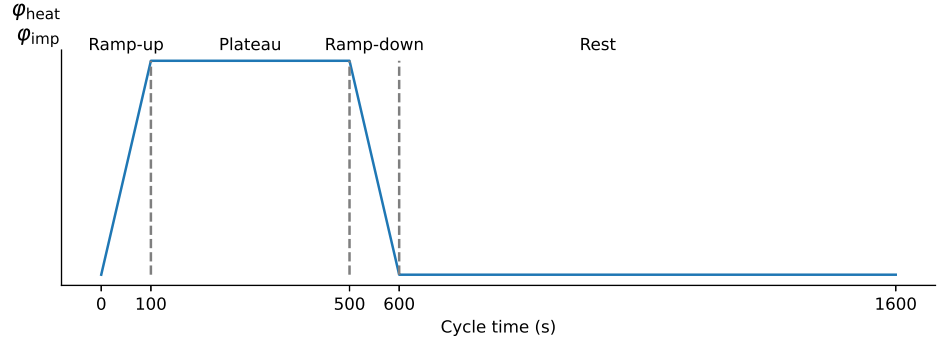


Figure 3.10: ITER plasma cycle. Evolution of heat flux and implanted particle flux.

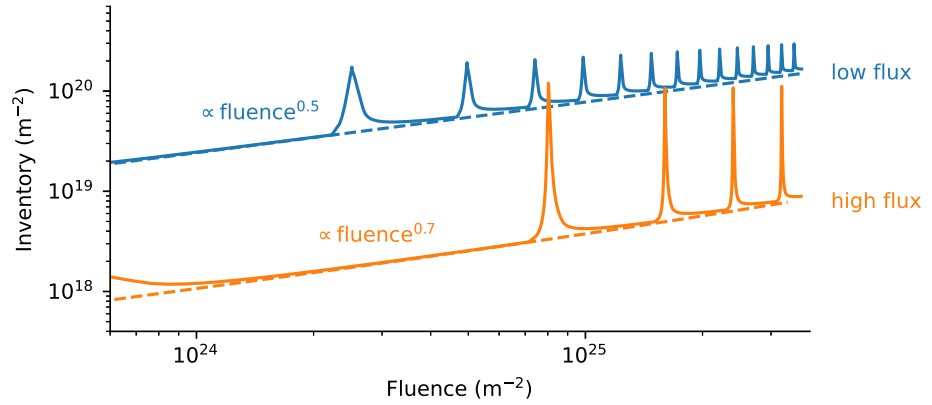


Figure 3.11: Evolution of the monoblock inventory as a function of the implanted fluence for cycled (solid) and continuous (dashed) exposure on a 1D case.

In the high flux case, the surface temperature is about 1400 K during the plateau whereas it is only ≈ 500 K for the low flux case. The evolution of the inventory for both cases was calculated with or without cycling (see Figure 3.11). To be able to compare the cases, the inventory is shown as a function of the fluence:

$$\text{fluence}(t) = \int_0^t \varphi_{\text{imp}}(t) dt \quad (3.6)$$

For the continuous cases, the inventory evolves as a power law of the fluence. For the cycled simulations, spikes appear periodically (between every cycle). These spikes correspond to ramp-down and ramp-ups during the cycles (see Figure 3.12). During the ramp-down, as the temperature decreases, the traps filling ratio increases, which results in an increase in the inventory. During the resting phase (not shown on Figure 3.11 since the flux is null), the inventory is kept constant. During the ramp-up, the temperature increases again and the hydrogen trapped close to the plasma-facing surface is desorbed and diffuses either back to the plasma, or deeper into the bulk. Finally, during the plateau phase, the inventory increases as a power law of the fluence.

These kinetics are observed for both the low flux and high flux cases. However, in the low flux case, the height of the spikes is greatly reduced. This is explained by the lower temperature difference between the resting phase and the plateau phase.

In both cases, the evolution trends are the same with or without cycling and the inventory evolution during the plateau phases match the continuous case. These results are consistent with the one observed in [205] with other trapping parameters. For a monoblock where the flux is even lower and the temperature difference is almost zero, no spikes will appear, and the cycled and continuous cases will match.

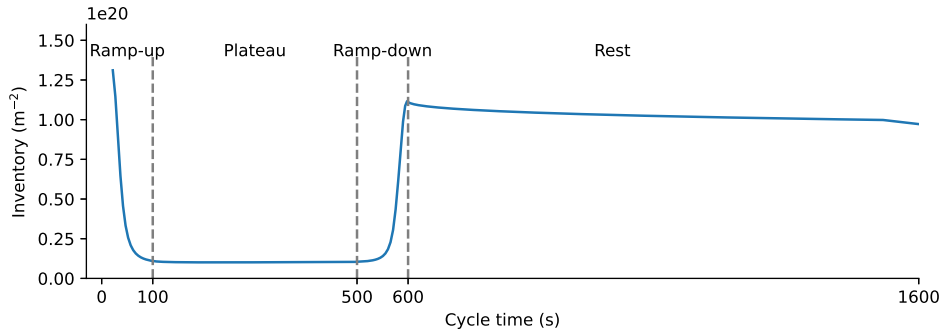


Figure 3.12: Evolution of the monoblock inventory during the sixth cycle for the high flux case.

Moreover, the “height” of these spikes is constant. This means that, after more cycles, these spikes will become negligible compared to the bulk inventory. For the high flux case, the inventory spike will be negligible (10% of the total inventory) after approximately 4000 cycles. For the low flux case, it is negligible after only 1150 cycles.

This therefore validates the continuous exposure simplification.

3.3 Monoblock behaviour law

Monoblocks in a fusion reactor will be exposed to a wide range of exposure conditions (heat and particle fluxes) and their behaviour in terms of hydrogen transport will change based on these conditions. In ITER, these fluxes can reach $\approx 10 \text{ MW m}^{-2}$ and $\approx 10^{24} \text{ H m}^{-2} \text{ s}^{-1}$ (see Figure 1.8). The distribution of these fluxes depend on many operation parameters.

One way of simulating a whole divertor would be to simulate each and every monoblock for a given scenario along one Plasma-Facing Unit. However, this method would be computationally expensive as it requires redoing the simulations for every scenario.

Another, more efficient method, is to perform a parametric study on a monoblock. The exposure parameters are varied and for each set of parameters, the quantity of interest (here the hydrogen inventory) is computed. A relationship is then produced between the exposure parameters and the quantity of interest: a *behaviour law*. This method is more robust in the sense that it does not require to run additional simulations once this relationship is obtained but simply uses this relationship to obtain the quantity of interest.

The goal of this Section is to establish this relationship between the exposure conditions of the monoblock and its hydrogen content at a given time.

3.3.1 Assumptions and simplifications

For the sake of simplicity and computational time, Trap 2 (in W) is neglected. This trap was neglected for it has the lowest density. However this will induce errors (< 80%) in the inventory computation (see Figure 3.13)

Note that this method could be applied to any set of trapping parameters. Continuity of mobile concentration at interfaces between materials is also assumed in order to save computational time (see Section 3.2.3). To remain conservative, no recombination on the gaps (toroidal and poloidal) is assumed. The 2D approximation can therefore be used (see Section 3.2.2). Moreover, cycling is neglected (see Section 3.2.4). The temperature will be imposed on Γ_{top} from the relationship obtained in Section 3.2.1.

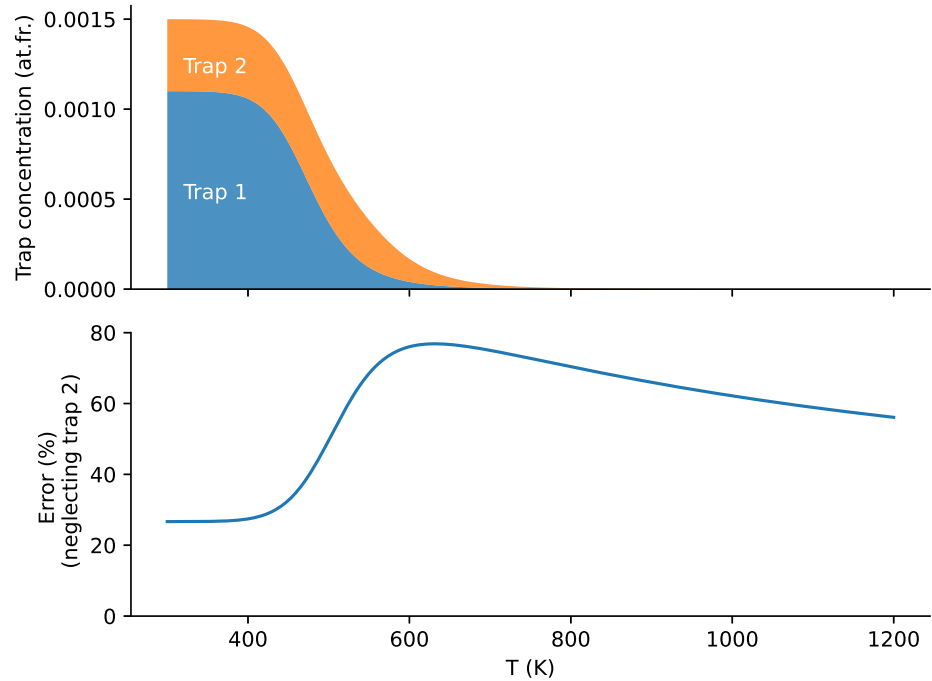


Figure 3.13: Evolution of the concentrations of traps 1 and 2 as a function of temperature for a local mobile hydrogen concentration of $1 \times 10^{22} \text{ m}^{-3}$ and error associated with neglecting trap 2.

3.3.2 Results

In this section, the total inventory of hydrogen in monoblocks has been calculated as a function of T_{surface} and c_{surface} . Temperature and mobile concentration of hydrogen were imposed with Dirichlet boundary conditions on Γ_{top} with T_{surface} varying from T_{coolant} to 1200 K and c_{surface} varying arbitrarily from 10^{20} m^{-3} to $6 \times 10^{22} \text{ m}^{-3}$. For surface temperatures below 500 K, 1D simulations were performed for the penetration depth of hydrogen remained very low (a few microns) and 1D approximation was sufficient [206]. For temperatures above 500 K for which edge effects become dominant, 2D simulations have been performed.

[206] Benannoune et al. (2019)

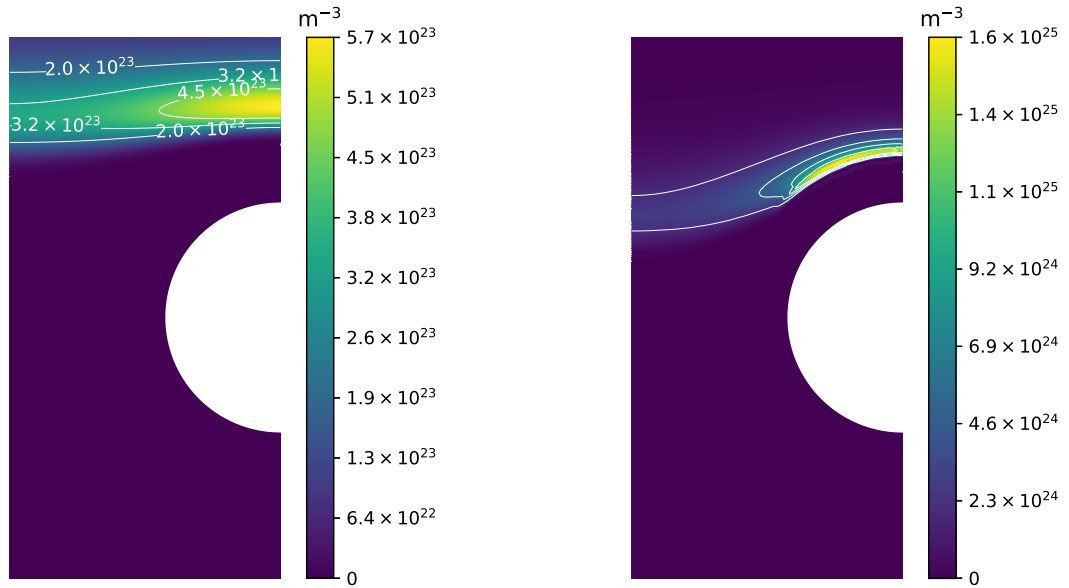
After 10^7 s a high retention zone appeared far from the exposed surface Γ_{top} (see Figure 3.14). This high retention zone is due to thermal effects. As seen in Figure 3.3a and Figure 3.3b, the temperature was found to decrease in regions close to the cooling pipe Γ_{coolant} leading to an increase in trap occupancy, creating this high retention zone. This is however not true for monoblocks where $T_{\text{surface}} \approx T_{\text{coolant}}$ since the temperature gradient in the domain is very low. Instead, trap occupancy is close to one and the retention is high in the whole region where hydrogen has penetrated and not only far from the top surface.

In order to obtain this continuous field (see Figure 3.15), more than 600 simulations randomly distributed on the parameter plane were run and analysed using a Gaussian process machine learning algorithm [207] as in [39] based on the python package inference-tools [208]. The inventory obtained by the Gaussian regression process is also given for a constant value of $c_{\text{surf}} = 2 \times 10^{21} \text{ m}^{-3}$ (top inset) and a constant temperature $T = 850 \text{ K}$ (left inset). The Gaussian regression process was particularly appropriate as it calculates a local standard deviation σ based on the localisation of the data points and the deviation of the computed inventories. The lower the density of simulation points, the higher was the value of σ (for example around 850 K on the top inset of Figure 3.15). However, despite the lack of simulation in this region, the value of σ was still acceptable (only a few percents of the inventory) ensuring the quality of the resulting interpolation.

[207] Rasmussen et al. (2006)

[39] Shimwell et al. (2019)

[208] Bowman (2020)



(a) $T_{\text{surface}} = 700 \text{ K}$ and $c_{\text{surface}} = 10^{20} \text{ m}^{-3}$.

(b) $T_{\text{surface}} = 1000 \text{ K}$ and $c_{\text{surface}} = 10^{21} \text{ m}^{-3}$.

Figure 3.14: Example retention fields in m^{-3} after a 10^7 s exposure.

As expected, inventory was found to globally increase with c_{surface} . For $T_{\text{surface}} > 550 \text{ K}$, the inventory tended to decrease with surface temperature. However, for $T_{\text{surface}} < 550 \text{ K}$, inventory increased with surface temperature. This phenomenon is due to a trade-off between an increase of the detrapping rate and an increase of the diffusion coefficient making the hydrogen particles penetrate deeper into the bulk. Above 550 K , detrapping becomes dominant and inventory decreases. This mapping of inventory as a function of T_{surface} and c_{surface} provides an easy way of estimating the inventory in monoblocks for several exposure conditions without having to run many simulations. Indeed, to estimate the inventory with different exposure conditions, one only needs to associate these conditions $(\varphi_{\text{inc}}, E)$ to a couple $(c_{\text{surf}}, T_{\text{surf}})$.

3.3.3 Discussion

Even though this methodology provides a rapid way of estimating hydrogen content in the whole divertor, some assumptions have however been made.

First, a steady state exposure was considered for simplification purposes. This result is however conservative. As seen in [75, 178], cycling effects could have an influence in regions where T_{surface} varies a lot, for example within 10 cm on both sides of the strike points. Though, since a large majority of monoblocks stay at room temperature, even during operations the thermal effect should remain low and discrepancies would rather be due to particle flux evolution along the target.

This study presents the hydrogen trapping in W monoblocks. It shows that the latter remains low but, as already pointed out by JET studies, the trapping on Be co-deposited layers is expected to be the main mechanism for tritium retention in ITER [209, 210]. Such layers could be found in the cold regions of the divertor but as soon as the strike points hit these layers, they should be sputtered away (as sputtering of Be is possible even at low energy [209, 211]). The retention where the deposited layers are not present (either sputtered or not formed anyway) would then be given by the model presented here.

[75] Hodille et al. (2017)

[178] Delaporte-Mathurin et al. (2019)

[209] Brezinsek et al. (2015)

[210] Heinola et al. (2015)

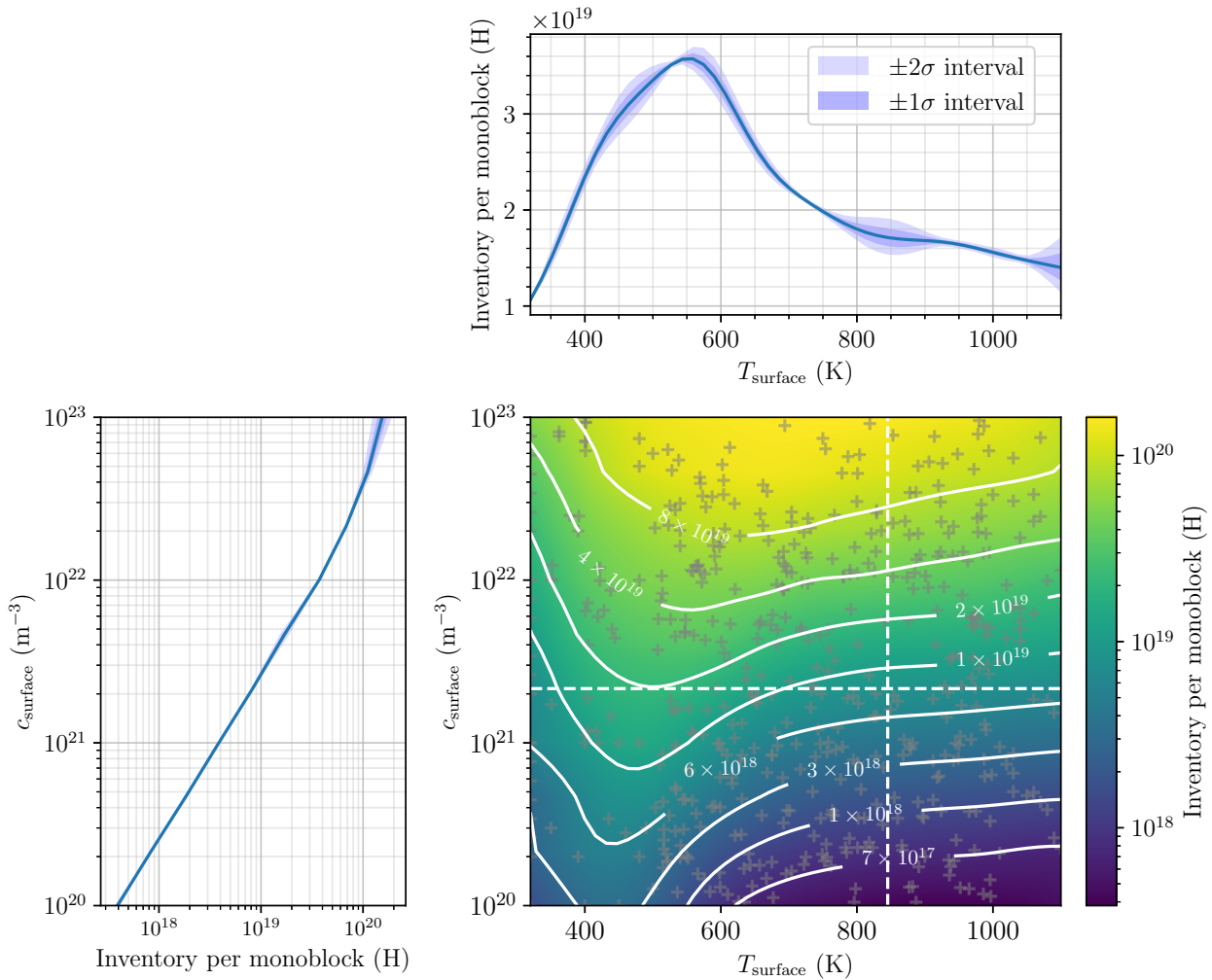


Figure 3.15: Evolution of the inventory after a 10^7 s exposure as a function of T_{surface} and c_{surface} alongside with simulation points (grey crosses). The simulations points were fitted with a Gaussian regression process [208] providing the standard deviation σ .

[198] Anderl et al. (1999)

The molecular recombination coefficient at the surface of the cooling pipe was taken from [198] and was measured in vacuum. One could argue that recombination in presence of water will be facilitated. This parameter has a very low influence on the inventory since it is dominated by retention in tungsten. This parameter will however have an influence on the permeation flux and should be studied in future work.

Similarly, the influence on molecular recombination on the sides of the monoblock was found to have a low impact on the results. By assuming an instantaneous recombination coefficient, the relative error on the monoblock inventory was found to be significant only in hot regions (i.e. within 10 cm on both sides of the strike points). The influence on the total divertor inventory is therefore low (less than 5% after a 10^7 s exposure) since it is dominated by regions where $T_{\text{surface}} \approx T_{\text{coolant}}$.

[212] Hu et al. (2015)

It should be noted that specific scenarios like edge localised modes (ELMs) were also not taken into account in this work since their timescale is very short. ELMs are transient plasma events releasing thermal energy and particles and locally increasing the heat flux at the surface of the monoblock. MRE simulations by Hu and Hassanein [212] suggest that a 400 s discharge with 1 Hz or 10 Hz ELMs significantly reduces (77%) the inventory in W materials. However, the modelling of the ELM is simulated by increasing the temperature for a very short time without changing the incident flux of particles that can also be much higher thus balancing the fuel retention reduction.

Another study by Schmid et al. [175] also simulated the effect of 1 Hz ELMs on fuel retention in W. The outcome is that 6 s of 1 Hz-ELMs does not affect significantly the fuel retention, though the temperature excursion in those simulations are smaller than for the one of Hu and Hassanein. Thus, the effect of ELMs, especially the balance between increase of heat flux, incident energy and particle flux, could either favour or disfavour trapping, diffusion and migration and therefore the overall retention.

[175] Schmid (2016)

In this study the model to link the concentration of mobile particles at the surface (implantation zone) with the exposure condition considers that the particles are implanted in the bulk and that the recombination coefficient is very high since many uncertainties concerning the recombination coefficient are yet to be lifted. However, if an exothermic process is considered as in [199], this should have low influence since recombination is very quick at a temperature close to that of the coolant.

[199] Ogorodnikova (2019)

On the other hand, experimental results [213] suggest that for ion energy below 5 eV/H, typical of detached plasma as the one treated in the previous section, the surface process can be important and limits the uptake of hydrogen, i.e. the adsorption on the surface and the further absorption from surface to bulk could be the limiting process for the growth of c_{surface} during such exposure. The evolution of c_{surface} to the exposure condition for that range of energy (and therefore the inventory) would then be different. The advantage of the presented method is that taking into account such process is relatively easy as no expensive simulations are needed. One would only need to modify the model giving c_{surface} as a function of $(E_{\text{inc}}, \varphi_{\text{inc}})$ to include the different surface processes. To this end, one can use kinetic surface models [214–217].

[213] 't Hoen et al. (2013)

Trap properties have a great impact on the inventory. In this study, a homogeneous trap distribution is assumed for simplification purposes. A more thorough study could investigate the influence on trap distribution, energy and density. Trap properties might also vary along the divertor based on exposure conditions. Moreover the impact of neutrons must be assessed as neutron-induced traps have a high detrapping energy.

[214] Hodille et al. (2017)

[215] Založnik et al. (2017)

[216] Pečovnik et al. (2019)

Finally, helium implantation in the materials and bubble formation could modify the hydrogen transport in monoblocks.

[217] Guterl et al. (2019)

3.4 Summary

H transport in ITER-like monoblocks was simulated with FESTIM.

The validity of various simplifications and assumptions was first studied. A relationship between the average surface temperature and the heat flux was obtained. It was then shown that the choice of interface conditions (continuity of chemical potential or continuity of mobile concentration) had low impact on the monoblock inventory. Moreover, the 2D approximation was found to be the best compromise between accuracy of the solution and computational time. The effect of loading cycles was also investigated. Between plasma pulses, a zone with higher retention appears near the plasma exposed surface due to the temperature variation. These modifications of the retention fields vanish as soon as the next cycle starts again and this zone is heated up again. This means that cycling has no effect on the global retention field and that cycles can safely be concatenated (continuous exposure) to simulate H transport.

A parametric study was then performed in order to assess the influence of exposure conditions (surface concentration and surface temperature). A behaviour law was obtained correlating exposure conditions to the monoblock inventory at a given exposure time. This law will be extremely useful to estimate H retention in divertors in Chapter 4 since not all monoblocks will be exposed to the same exposure.



4 Divertor inventory estimation

This Chapter focusses on the estimation of the H inventory in the divertors of WEST and ITER. This estimation relies on the monoblock behaviour law computed in Chapter 3. This behaviour law allows rapid evaluations of the monoblocks H inventory for any exposure condition. Inputs are taken from SOLEDGE3X-EIRENE [218] and SOLPS-ITER [219] plasma simulations. The influence of several control parameters is investigated: the input power (i.e. how much heating power is injected in the plasma), the gas puffing rate, and the divertor pressure of neutral particles in ITER. Gas puffing is used in most tokamaks to locally increase the plasma density [220]. One of the advantages of gas puffing is a better coupling of the Ion Cyclotron Range of Frequencies (ICRF) heating with the plasma [221].

4.1	Methodology	71
4.2	ITER results	74
4.3	WEST results	78
4.4	Summary	83

4.1 Methodology

To make use of the monoblock inventory behaviour law, distribution of surface concentrations and surface temperatures along the divertors will be required. They will be converted from plasma simulations outputs.

4.1.1 Plasma simulations

This Section describes the parameters of the plasma simulations. These simulations were run with SOLEDGE3X-EIRENE for WEST and SOLPS-ITER for ITER. In a nutshell, these codes solve, for each species (ions and electrons), the particle density, velocity and temperature. The equations at stake are comparable to the Navier-Stokes equations coupled to the heat equation and interactions with the electromagnetic fields in the plasma [222]. Subsequently, the incident particle fluxes, heat fluxes and particle energy can be calculated along the tokamak wall. For the SOLEDGE3X-EIRENE runs, the puffing rate and the input power were used as control parameters. For SOLPS-ITER calculation, the divertor neutral pressure is the control parameter.

[222] Bufferand et al. (2015)

SOLEDGE3X-EIRENE runs

The Lower-Single-Null magnetic configuration (i.e. a single X-point in the lower part of the vacuum vessel) used for the 2D simulations in SOLEDGE3X-EIRENE transport code (v588.165) are based on the experimental WEST plasma discharge #54903 at

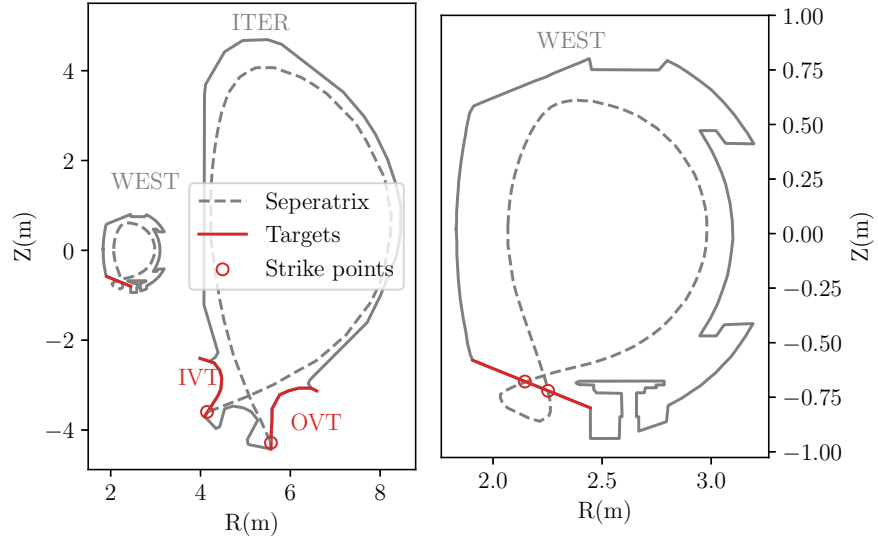


Figure 4.1: Poloidal cross section of Tungsten Environment Steady state Tokamak (WEST) and ITER showing the divertors in red.

$T_{\text{flat-top}} = 8$ s (see Figure 4.1). In order to get as many divertor conditions as possible, the puffing rate was varied from 4.5×10^{20} molecule s^{-1} to 4.72×10^{21} molecule s^{-1} and the input power from 0.449 MW to 2.5 MW. The setup parameters of the simulation are listed in Table 4.1. R_{wall} is the recycling coefficient of main chamber wall, R_{pump} is the recycling coefficient of the pump, D is the cross-field mass diffusivity perpendicular to the flux surface, ν is the momentum diffusivity, χ_e and χ_i are the energy diffusivity for electrons and ions, respectively. While the value of these coefficients is required for the sake of reproducibility, their detailed description [223] is outside the scope of this research. The gas puff position is set inside the private flux region (i.e. the region between the two strike points) and the pump position is set under the baffle.

[223] Ciraolo et al. (2019)

Table 4.1: Setup parameters used in the SOLEDGE3X simulations.

Plasma composition	Deuterium, no impurity
Recycling coefficients	$R_{\text{wall}} = 0.99$ $R_{\text{pump}} = 0.95$
SOL input power	from 0.449 MW to 2.5 MW
Gas puffing rate	from 4.5×10^{20} molecule s^{-1} to 4.72×10^{21} molecule s^{-1}
Drifts	-
Plasma transport coefficients	$D = 0.3 \text{ m}^2 \text{ s}^{-1}$ $\nu = 0.3 \text{ m}^2 \text{ s}^{-1}$ $\chi_e = \chi_i = 1.0 \text{ m}^2 \text{ s}^{-1}$

SOLPS-ITER runs

[26] Pitts et al. (2019)

[219] Kaveeva et al. (2020)

Several ITER cases were taken from [26] with divertor neutral pressures varying from 1.8 Pa to 11.2 Pa. These SOLPS-ITER [219] scenarios can be found in the ITER Integrated

Modelling Analysis Suite (IMAS) database [224, 225]. The nine simulations used in this work are labelled 122396, 122397, 122398, 122399, 122400, 122401, 122402, 122403 and 122404. These have been run in baseline detached burning plasma conditions ($Q = 10$ with 50MW of input power).

[224] Imbeaux et al. (2015)

[225] Park et al. (2020)

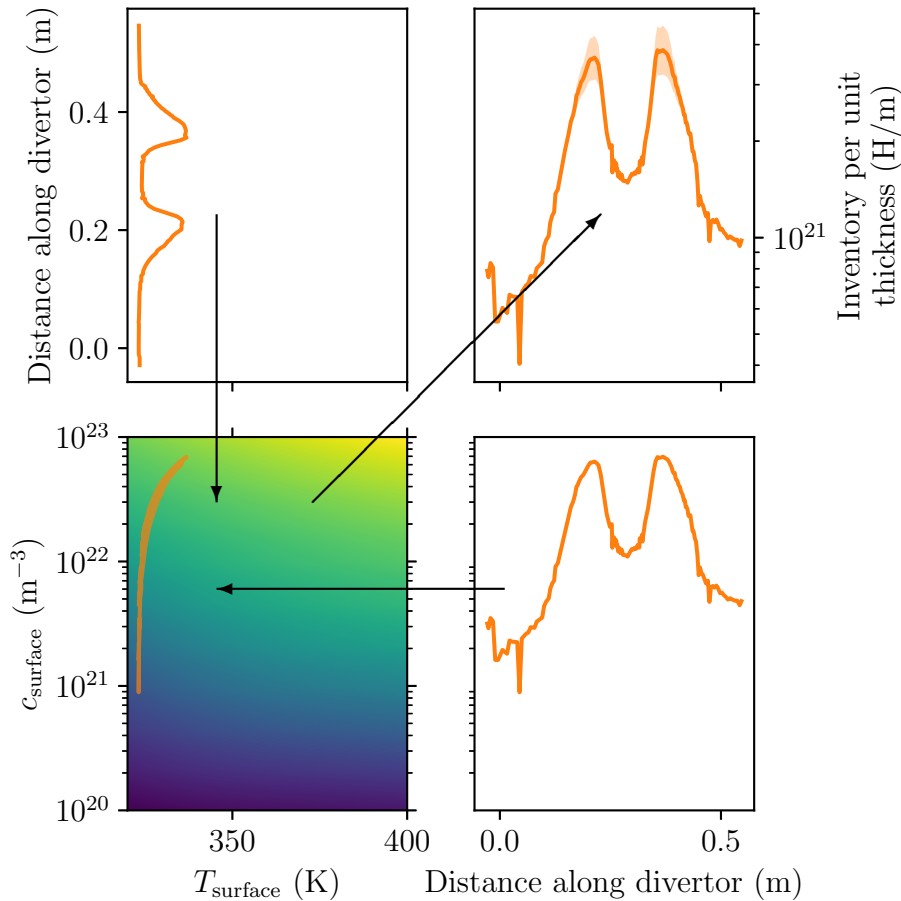


Figure 4.2: Method of WEST divertor H inventory estimation based on the surface concentration, the surface temperature and the behaviour law obtained in Chapter 3.

4.1.2 Estimation of exposure conditions

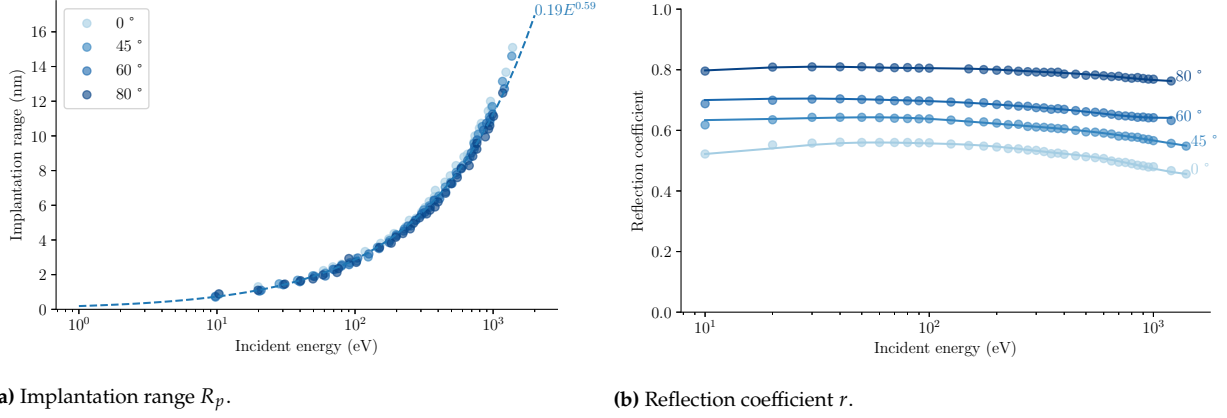
According to the behaviour law obtained in Chapter 3, the temporal evolution of the H inventory along the divertors can be estimated from the surface concentration of mobile hydrogen and surface temperature (see Figure 4.2).

The distribution of the exposure conditions (angles of incidence, particles energies, particles fluxes and heat flux) are produced by SOLEDGE3X/SOLPS-ITER along the divertors of WEST and ITER (see Figure 4.1 and Figure 4.2). These exposure conditions are converted into distributions of surface temperature T_{surface} and surface hydrogen concentration c_{surface} by Equation 3.3 and Equation 4.1.

Note: see Section 3.2.1 for more details on the monoblock thermal behaviour.

$$c_{\text{surface}} = c_{\text{surface, ions}} + c_{\text{surface, atoms}} \quad (4.1)$$

$c_{\text{surface, ions}}$ and $c_{\text{surface, atoms}}$ are the contributions of the ions and atoms to the surface

(a) Implantation range R_p .(b) Reflection coefficient r .**Figure 4.3:** Evolution of the implantation range and the reflection coefficient as a function of incident energy E and angle of incidence.

hydrogen concentration. They can be expressed as:

$$c_{\text{surface},i} = \frac{R_{p,i} \varphi_{\text{imp},i}}{D(T_{\text{surface}})} \quad (4.2)$$

where $R_{p,i}$ is the implantation depth in m, $\varphi_{\text{imp},i}$ is the implanted particles flux in $\text{m}^{-2} \text{s}^{-1}$ and D is the H diffusion coefficient in $\text{m}^2 \text{s}^{-1}$ (see Section 2.2.2).

Finally, the implanted flux can be expressed as:

$$\varphi_{\text{imp},i} = (1 - r_i) \varphi_{\text{incident } i} \quad (4.3)$$

where r_i is the reflection coefficient and, $\varphi_{\text{incident } i}$ is the incident particle flux expressed in $\text{m}^{-2} \text{s}^{-1}$.

The implantation range R_p and the reflection coefficient r depend on the incident energy and angle of incidence of particles. These relations can be obtained from SRIM [173] simulations (see Figure 4.3a). It was found that the angle of incidence had low influence on the implantation range. R_p can therefore be expressed as a function of the incident energy only:

$$R_p = 1.9 \times 10^{-10} E^{0.59} \quad (4.4)$$

where E is the incident energy in eV.

The evolution of the reflection coefficient r can also be estimated with SRIM. The reflection coefficient varies from around 0.5 at 0° to 0.8 at 80° (see Figure 4.3b). According to [225], the incident angles for ions and atoms were assumed to be 60° and 45° , respectively. It should be noted that since SRIM is based on the binary collision approximation, values around 10 eV might not be fully valid.

All of these steps have been automated and packaged into a tool called divHretention. divHretention can directly interpret SOLPS-ITER/SOLEDGE3X data and produce a distribution of monoblock inventory as in Figure 4.2.

4.2 ITER results

The exposure conditions vary with respect to the divertor neutral pressure (see Figure 4.4).

[173] Ziegler et al. (2010)

[225] Park et al. (2020)

The source-code of the tool is under version control and openly available via GitHub under a MIT licence [226]. The divHretention python package is distributed via PyPi [227]. Moreover, all the results obtained in this Chapter can be reproduced with the scripts available at <https://github.com/RemDelaporteMathurin/divHretention-Nucl.Fusion-2021>.

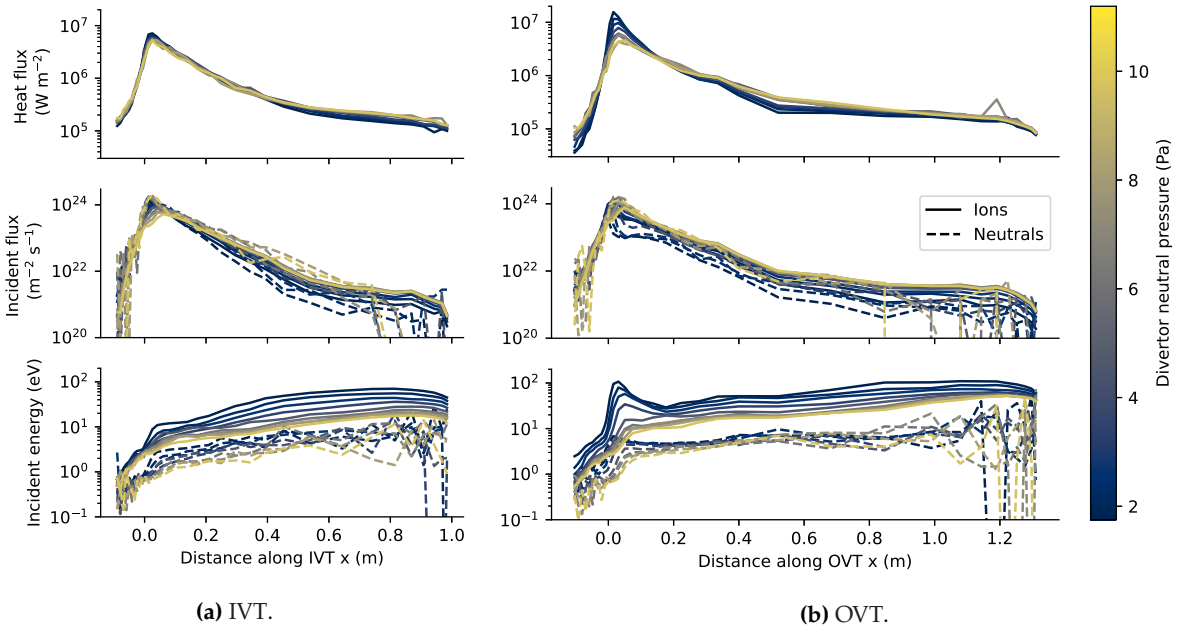


Figure 4.4: Distribution of exposure conditions (heat flux, particle flux and particle incident energy) along the ITER divertor for several divertor neutral pressures [26].

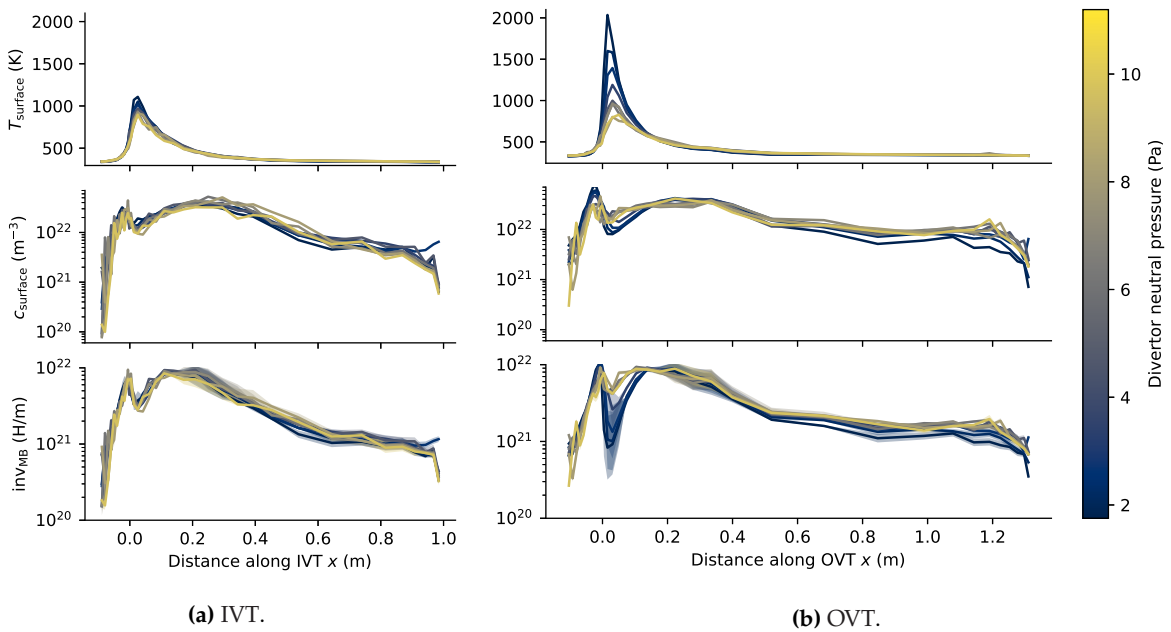


Figure 4.5: Surface temperature, surface concentration and inventory per unit thickness along the ITER divertor with neutral pressures varying from 2 Pa to 11 Pa. The area corresponds to the 95% confidence interval.

Peak temperatures at strike points increased when decreasing the divertor neutral pressure (see Figure 4.5b). The peak temperature at the outer strike point reached 2000 K at 2 Pa and more than 1000 K at the inner strike point, which is in accordance with the results obtained by Pitts et al. [26].

[26] Pitts et al. (2019)

The inventory in the whole divertor is computed as follows:

$$\text{inv}_{\text{divertor}} = N_{\text{cassettes}} \cdot (\text{inv}_{\text{IVT}} + \text{inv}_{\text{OVT}}) \quad (4.5)$$

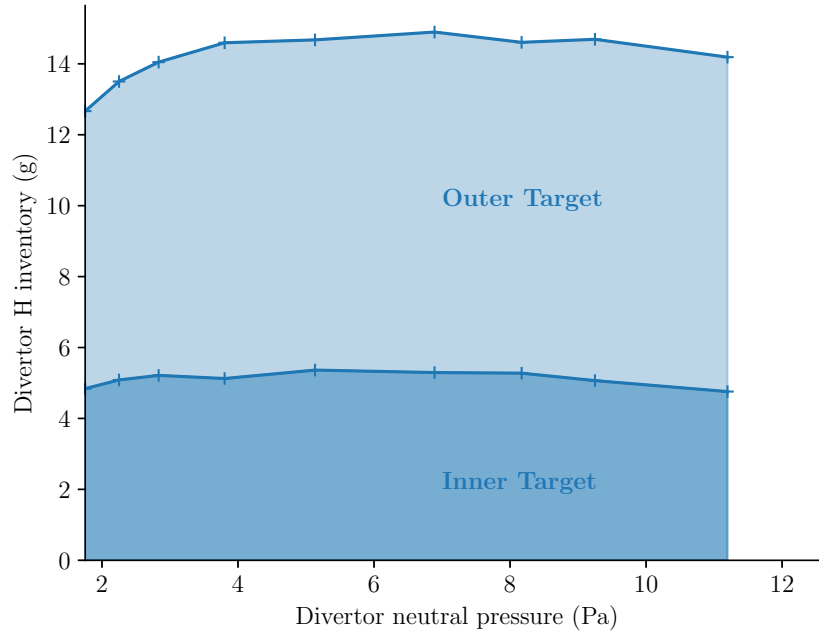


Figure 4.6: Hydrogen inventory in the ITER divertor as a function of neutral pressure after 10^7 s of exposure (approximately 25 000 discharges).

with $N_{\text{cassettes}} = 54$ the number of cassettes, inv_{IVT} and inv_{OVT} the total inventory in the IVT and OVT respectively (in one cassette).

$$\text{inv}_{\text{IVT}} = N_{\text{PFU-IVT}} \cdot \int_{\text{IVT}} \text{inv}_{\text{MB}}(x) dx \quad (4.6)$$

$$\text{inv}_{\text{OVT}} = N_{\text{PFU-OVT}} \cdot \int_{\text{OVT}} \text{inv}_{\text{MB}}(x) dx \quad (4.7)$$

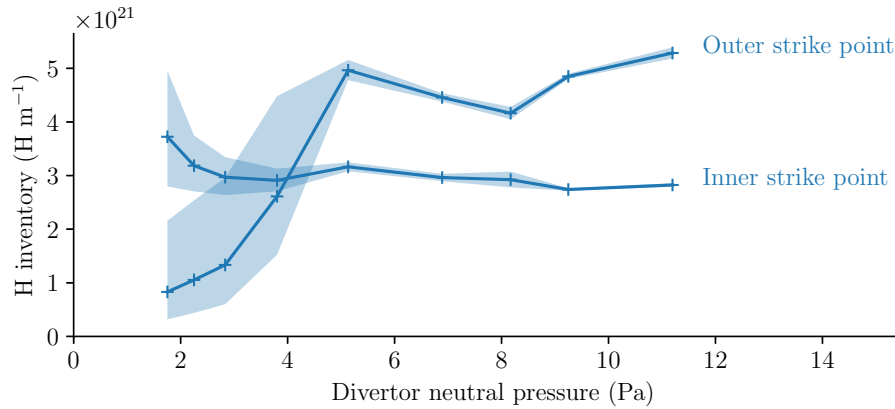
$N_{\text{PFU-IVT}} = 16$ and $N_{\text{PFU-OVT}} = 22$ the number of plasma facing units per cassette in the inner and outer targets respectively (see Section 1.2.4), inv_{MB} is the monoblock inventory per unit thickness and x the distance along the targets. Here, $\int_{\text{OVT}} \text{inv}_{\text{MB}}(x) dx$ corresponds to the area of the profile shown on Figure 4.5b.

The inventory in the outer target was found to be nearly twice that of the inner target. This is largely explained by the larger number of plasma facing units in the outer target and therefore a greater exposed surface. The global inventory increased with the divertor neutral pressure and a roll-over is observed above 7 Pa (see Figure 4.6). This roll-over is consistent with the results obtained in [26]. The inventory increase was found to be more important in the outer vertical target. This was explained by the fact that the plasma is more detached at the inner target. Therefore the surface temperature reduction is more significant in the outer vertical target and the surface concentration is increased (see Figure 4.5b).

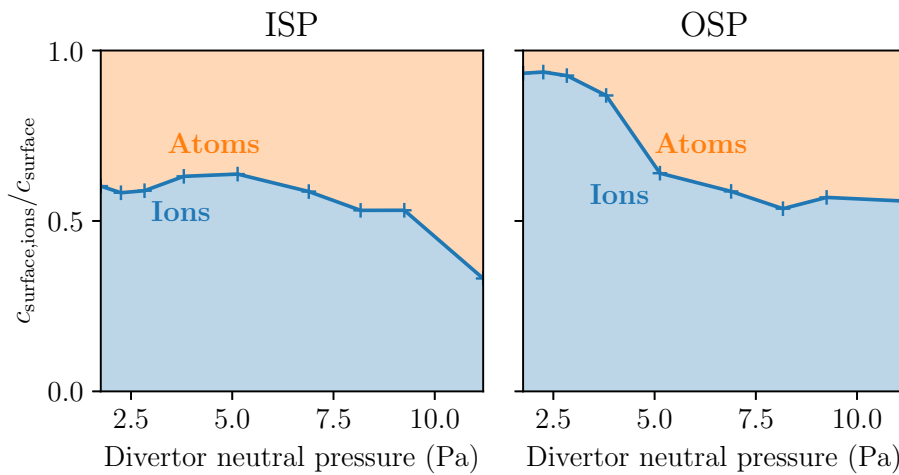
[26] Pitts et al. (2019)

The maximum inventory was found at around 7 Pa and was approximately 14 g of H, which is well below the ITER in-vessel safety limit of tritium (700 g), especially considering only half of this quantity will be tritium. This is especially true considering that this was for a very long exposure time of 10^7 s, which corresponds to 25 000 pulses of 400 s.

The inventory at the inner strike point is constant from 4 Pa whereas the inventory at the outer strike point globally increases with the divertor neutral pressure (see Figure



(a) Inventory per unit thickness after 10^7 s of exposure (approximately 25 000 discharges). Area corresponds to the 95% confidence interval.



(b) Contribution of ions to the surface concentration of H.

Figure 4.7: H retention at the strike points (defined as maximum temperature) as a function of the divertor neutral pressure.

4.7a). The contribution of ions to the surface concentration at the inner strike point is around 50 % and tends to decrease with increasing neutral pressure (see Figure 4.7b). At low divertor neutral pressure, the contribution of ions at the outer strike point is around 90 % and tends to decrease with increasing neutral pressure. This can be explained by the fact that in both inner and outer targets, the integrated flux of ions decreases with increasing neutral pressure whereas the integrated flux of atoms increases, leading to a greater proportion of neutral particles.

For all divertor neutral pressures, the temporal evolution of the divertor inventory is approximately the same (see Figure 4.8). The inventory is plotted as a function of the number of ITER discharges (see Figure 3.10). The additional inventory per 400 s discharge was found to decrease with time. Past 300 discharges, the additional inventory per discharge decreases with the number of discharges. The maximum is around 5 mg/discharge between 30 and 100 discharges.

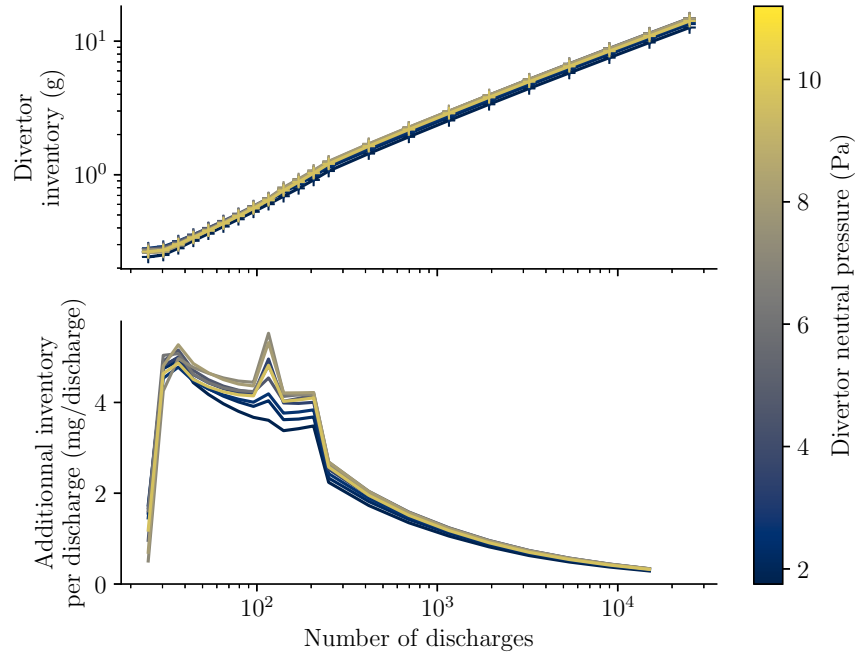


Figure 4.8: Evolution of the H inventory of the ITER divertor with the number of 400s discharges.

4.3 WEST results

All the computations have been made for very long exposure times (10^7 s) in order to better visualise trends. Even though cycling can have an effect on H outgassing at the monoblock plasma facing surface, it was shown in Section 3.2.4 that the evolution of the monoblock inventory with the fluence was not affected. Moreover, it can be shown that the divertors inventories evolve with a power law dependence of time.

4.3.1 Influence of the input power

The input power was varied between 0.49 MW and 2.0 MW. Two puffing rate values were used: 2.5×10^{21} molecule s^{-1} and 4.4×10^{21} molecule s^{-1} .

The maximum retention was found to be located at the strike points (see Figure 4.9). The retention at the outer strike point was higher than at the inner strike point. The retention at the strike points was found to increase with the input power whereas it slightly decreased in the private flux region (see Figure 4.10a). This was explained by an attachment of the plasma decreasing the particle flux in the private flux region. Since the surface temperature is constant, this leads to a decrease in the surface concentration of hydrogen as seen on Figure 4.9. On the other hand, the increasing temperature at the strike points only enhanced the diffusion process while remaining low enough so that hydrogen could get trapped.

The total inventory in the WEST divertor is computed as follows:

$$\text{inv}_{\text{divertor}} = N_{\text{PFU}} \cdot \int \text{inv}_{\text{MB}}(x) dx \quad (4.8)$$

where $N_{\text{PFU}} = 480$ is the number of PFU in WEST, inv_{MB} is the inventory per unit thickness in H m^{-1} (see Figure 4.9) and x the distance along the target in m.

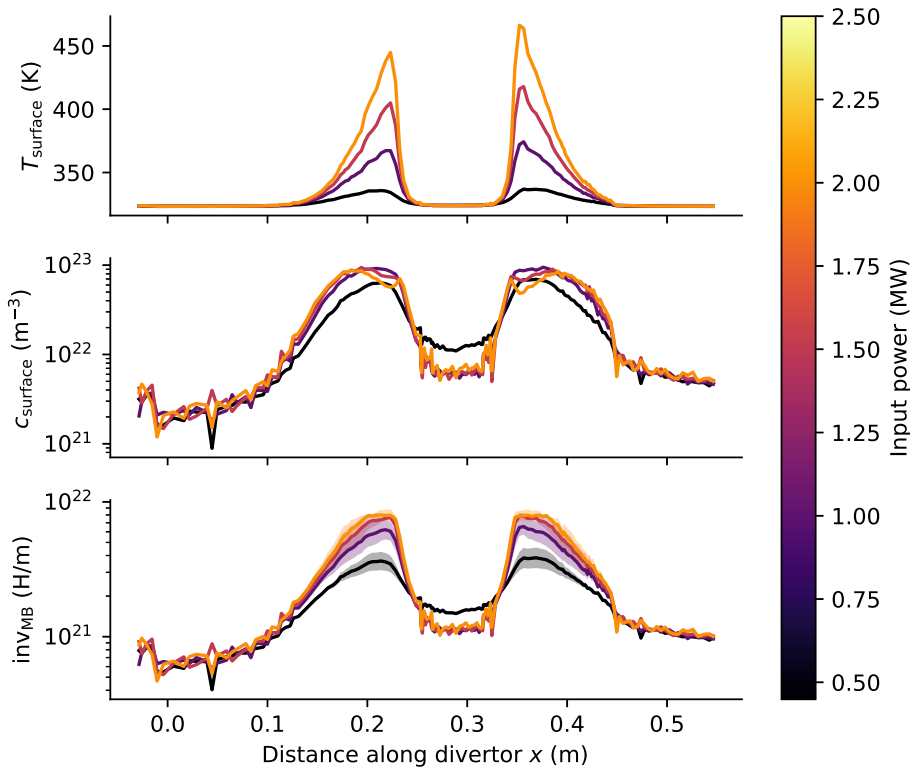


Figure 4.9: Distribution of surface temperature T_{surface} , surface concentration c_{surface} and inventory per unit thickness along the WEST divertor with input powers varying from 0.49 MW to 2.0 MW with a puffing rate of $2.5 \times 10^{21} \text{ molecule s}^{-1}$.

The divertor inventory increased with the input power (see Figure 4.11) and evolved as the power 0.3 of the input power. The maximum divertor inventory was $8.8 \times 10^{23} \text{ H}$ at 2.0 MW of input power. This value of input power is still relatively low. Increasing the puffing rate lead to an increase in the inventory. This will be explained more thoroughly in Section 4.3.2.

At the strike points, the retention is dominated by the ion flux whereas neutrals are dominant in the private flux region (see Figure 4.10b). The contribution of ions at the strike points increased with the input power but remained approximately constant in the private flux region.

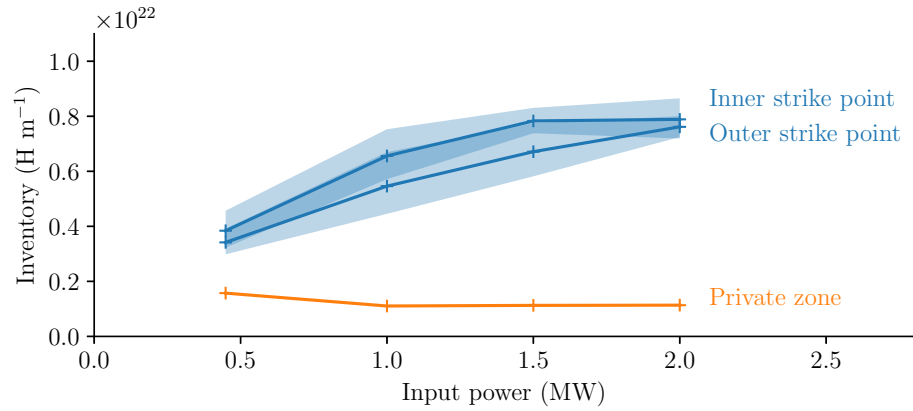
The divertor inventory was found to increase as a power law of time (see Figure 4.12).

4.3.2 Influence of the puffing rate

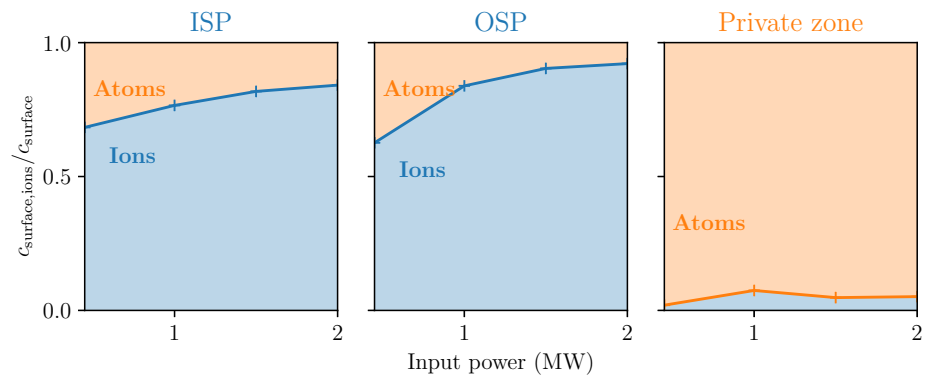
A parametric study on the puffing rate was performed. The puffing rate was varied between $4.4 \times 10^{20} \text{ molecule s}^{-1}$ and $4.7 \times 10^{21} \text{ molecule s}^{-1}$. The input power was fixed to 0.45 MW.

The maximum retention was again located at the strike points for all puffing rates values (see Figure 4.13). The inventory at the outer strike point was higher than at the inner strike point. The inventory in the private flux region was found to increase with the puffing rate whereas it was almost constant at the strike points (see Figure 4.15a). As for the power scan, the ions' contribution to the inventory is rather low in the private flux region (see Figure 4.15b). Moreover, the contribution of ions decreases rapidly at the strike points and represents only half of the surface concentration at $4 \times 10^{21} \text{ molecule s}^{-1}$.

The inventory in the whole WEST divertor is computed from Equation 4.8. As for the power scan, the divertor inventory increased as the power 0.2 of the puffing



(a) Inventory per unit thickness after 10^7 s of exposure. The area corresponds to the 95% confidence interval.



(b) Contribution of ions to the surface concentration of H.

Figure 4.10: H inventory at the inner and outer strike points (Inner Strike Point (ISP) and Outer Strike Point (OSP)) and in the private flux region as a function of the input power with a puffing rate of 2.5×10^{21} molecule s^{-1} .

rate (see Figure 4.14). The maximum inventory was found to be 5×10^{23} H at 4.7×10^{21} molecule s^{-1} .

The divertor inventory was found to increase as a power law of time.

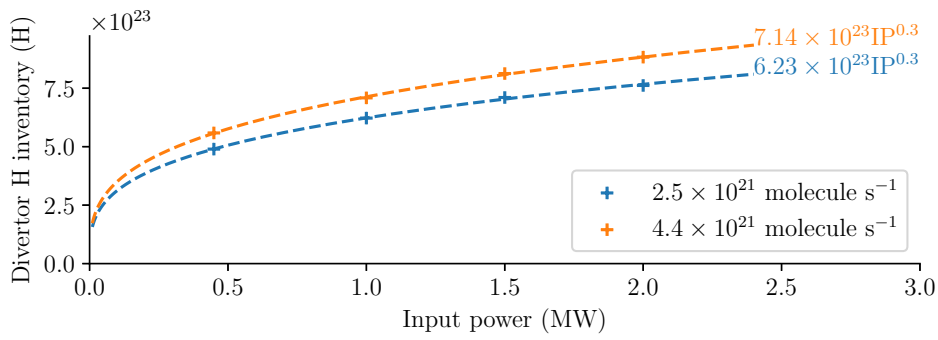


Figure 4.11: Evolution of the WEST divertor inventory as a function of input power for several puffing rates.

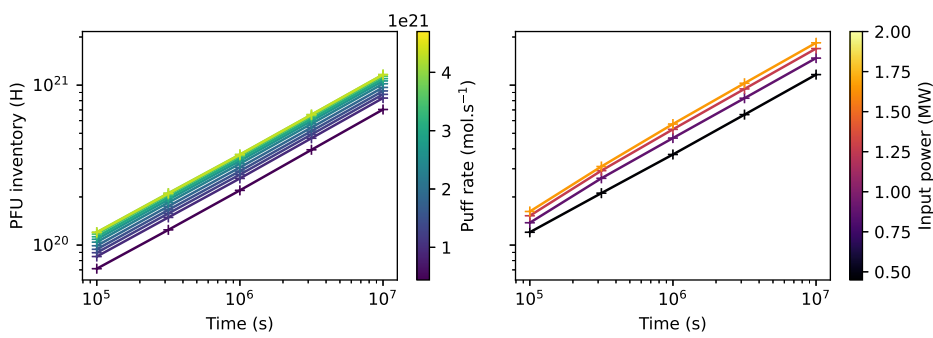


Figure 4.12: Temporal evolution of PFU inventories for different values of puffing rate (left) and input power (right).

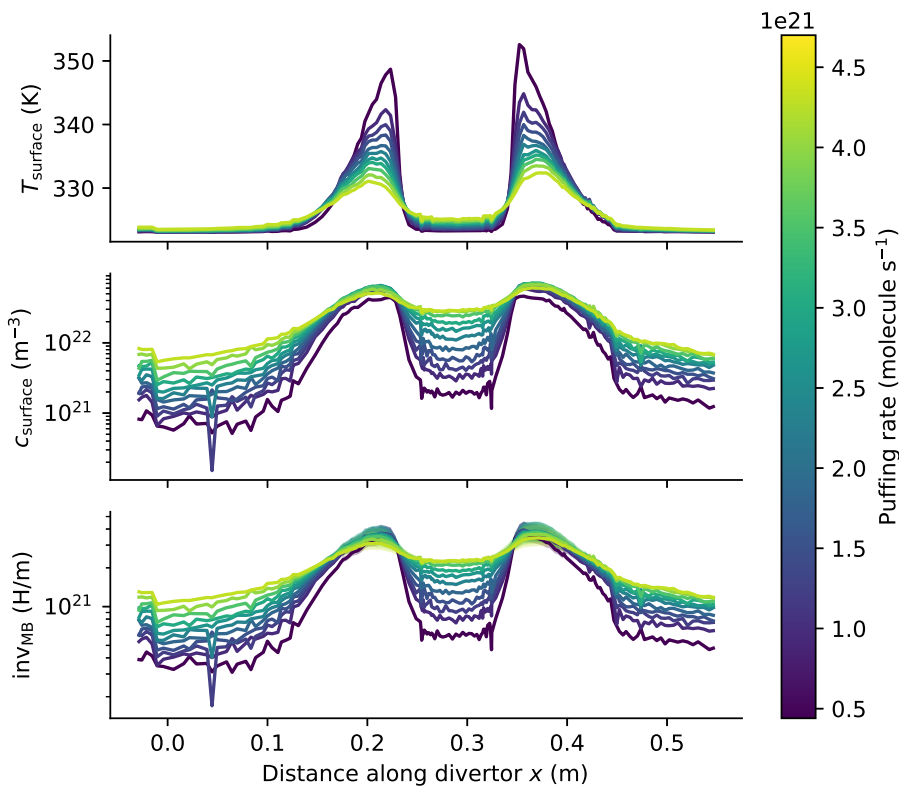


Figure 4.13: Distribution of surface temperature T_{surface} , surface concentration c_{surface} and inventory per unit thickness along the WEST divertor with a puffing rate varying from $4.4 \times 10^{20} \text{ s}^{-1}$ to $4.7 \times 10^{21} \text{ s}^{-1}$ with 0.45 MW of input power.

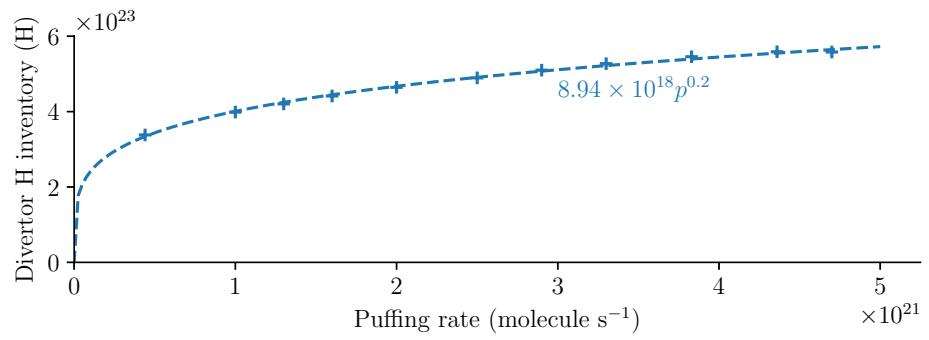
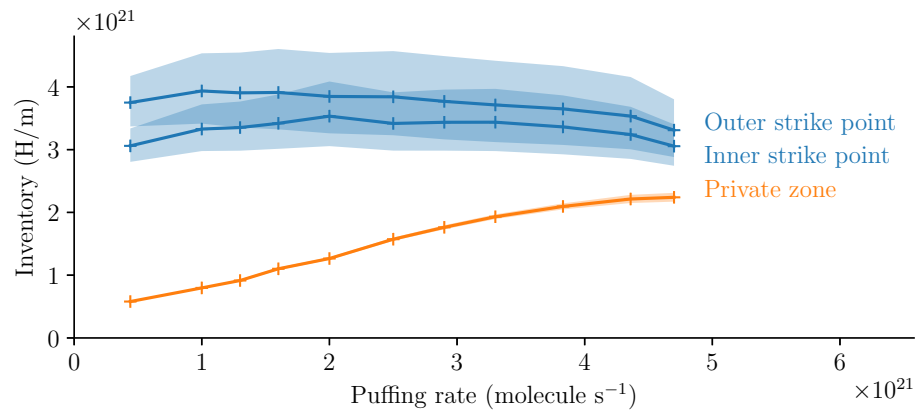


Figure 4.14: Evolution of the WEST divertor inventory as a function of puffing rate.



(a) Inventory per unit thickness after 10^7 s of exposure. The area corresponds to the 95% confidence interval.

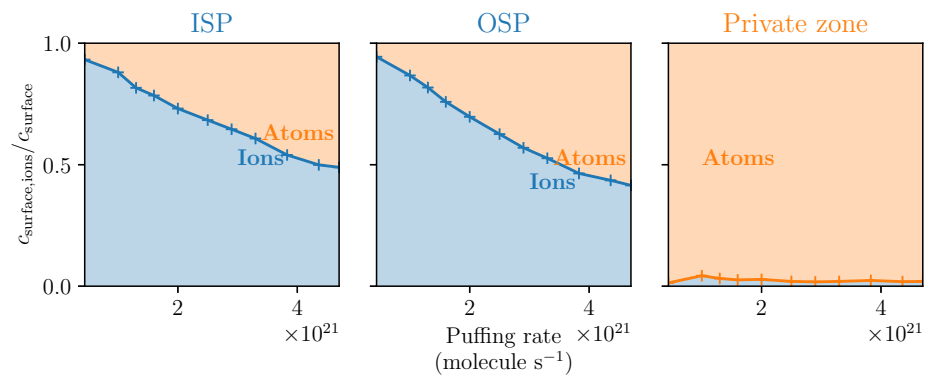


Figure 4.15: H retention at the strike points and in the private flux region as a function of puffing rate with 0.45 MW of input power.

(b) Contribution of ions to the surface concentration of H. ISP and OSP stand for Inner Strike Point and Outer Strike Point respectively.

4.4 Summary

The monoblock behaviour law proposed in Chapter 3 was used to estimate fuel retention in the divertors of WEST and ITER. The impact of key control parameters on the divertor inventory was studied (the input power, the puffing rate and the divertor neutral pressure).

It was shown that the inventory in WEST increases as the power 0.3 of the input power and as the power 0.2 of the puffing rate. The inventory in the ITER divertor was found to first increase with the neutral pressure up to 7 Pa then decrease, though the variation was smoother. The inventory in the outer vertical target of the ITER divertor is twice that of the inner vertical target. These results were in good agreement with the observations made in [26].

[26] Pitts et al. (2019)

However, it should be noted that both machines do not operate in the same regime. While WEST operates at low input power, ITER operates at high input power with a high recycling divertor. These differences in the operation regime can explain different trends.

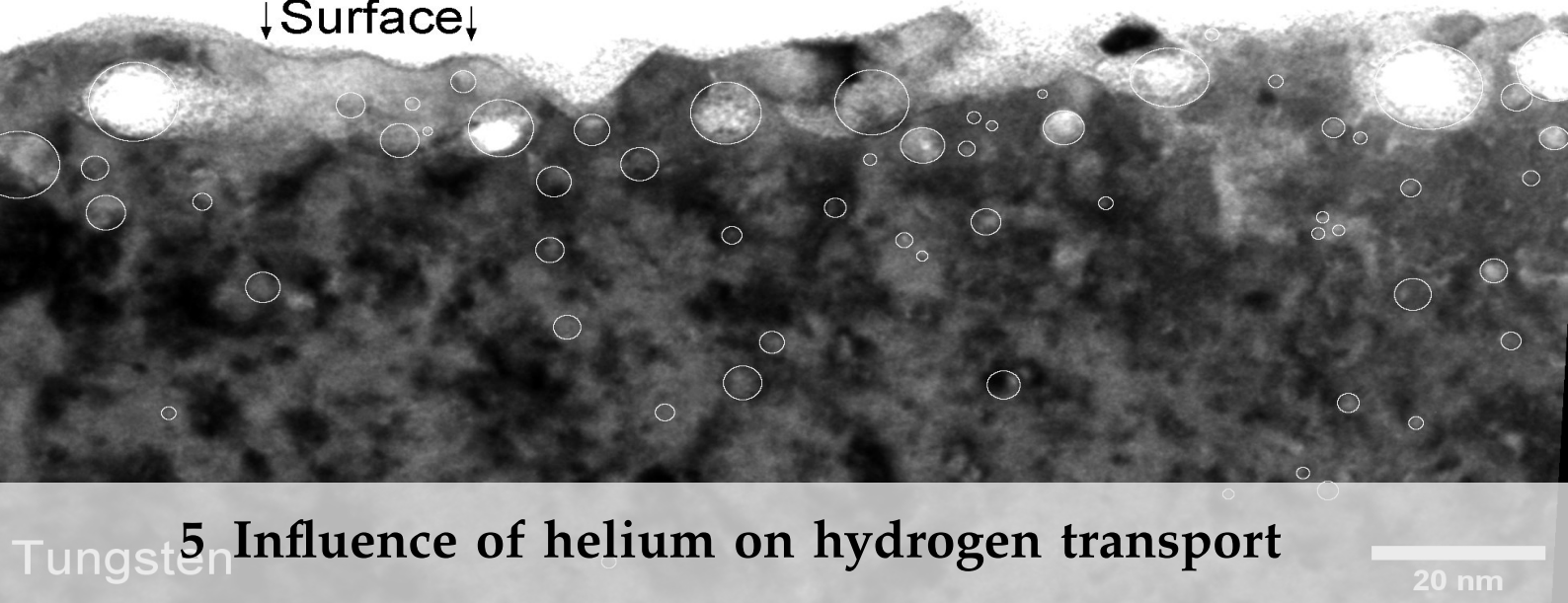
The maximum hydrogen inventory in the ITER divertor was approximately 14 g after 10^7 s of continuous plasma exposure (25 000 ITER discharges), which is well below the in-vessel safety limit of 700 g. Note that the total number of discharges in ITER will be approximately 23 300 [26]. Moreover, since the behaviour law is based on 2D monoblock simulations, this value is an upper estimate (see Section 3.2.2). 2D simulations are indeed conservative in terms of inventory (see Section 3.2.2).

The underlying monoblock model has also a few limitations, as detailed in Chapter 3. First, the set of trapping parameters that was used may not be relevant for every region of the divertor. These properties can however be experimentally estimated. The accuracy of the results could therefore be improved by running a new batch of FESTIM monoblock simulations with different trapping parameters like neutron-induced traps.

Then, this model does not take into account retention in Be co-deposited layers (i.e. Be particles eroded from the first wall redeposited in other locations of the vessel, trapping hydrogen). These are expected to be the main driver for H retention in ITER [228, 229]. However, this work is still relevant for full-tungsten environments like WEST or DEMO.

[228] De Temmerman et al. (2021)

[229] Schmid et al. (2015)



5 Influence of helium on hydrogen transport

Chapter 4 focussed on the estimation of the tritium inventory in the ITER divertor, taking into account only hydrogen implantation. However, the divertor of a tokamak will not only be exposed to hydrogen: it will also be bombarded by helium ions with a high enough energy to penetrate the tungsten lattice. Helium will also be generated from neutron transmutation and tritium decay.

This Chapter will therefore focus on determining the effect of helium on hydrogen transport and its impact on the conclusions made in Chapter 4.

It will first assess the different sources of helium in a tungsten divertor, which are the direct implantation of helium ions, the production of helium from tritium decay, and the production of helium from transmutation.

Then, a helium bubble growth model will be presented and applied to different exposure conditions. This model will be compared to published numerical results and experimental data.

Finally, based on the results of this new model, experiments investigating the effect of helium transport on hydrogen trapping will be reproduced. The final conclusion will determine if the results obtained in previous chapters are jeopardised.

5.1	Sources of helium . . .	85
5.2	Bubble growth model . . .	89
5.3	Verification & Validation	95
5.4	Bubble growth study	98
5.5	Influence on hydrogen transport .	108
5.6	Summary .	113

5.1 Sources of helium

As detailed in Section 1.4.1, helium can be produced in tungsten from neutron transmutation and from tritium decay. This section will focus on comparing these two indirect sources with direct helium implantation in monoblocks.

5.1.1 Neutron induced transmutation

In combination with the Paramak code [230] used for creating the monoblock geometry, a neutronics simulation was run to assess helium generation in a monoblock under neutron irradiation with the OpenMC code [231], a modern open-source Monte-Carlo neutron and photon transport code.

OpenMC simulates the transport of neutronics by modelling their paths from their birth until their deaths. Neutron interactions with matter (reflexion, absorption, fission...) are simulated using a probabilistic approach where each reaction has a corresponding cross-section (taken from the Evaluated Nuclear Data File (ENDF) [232]).

[230] Shimwell et al. (2021)

[231] Romano et al. (2015)

[232] Brown et al. (2018)

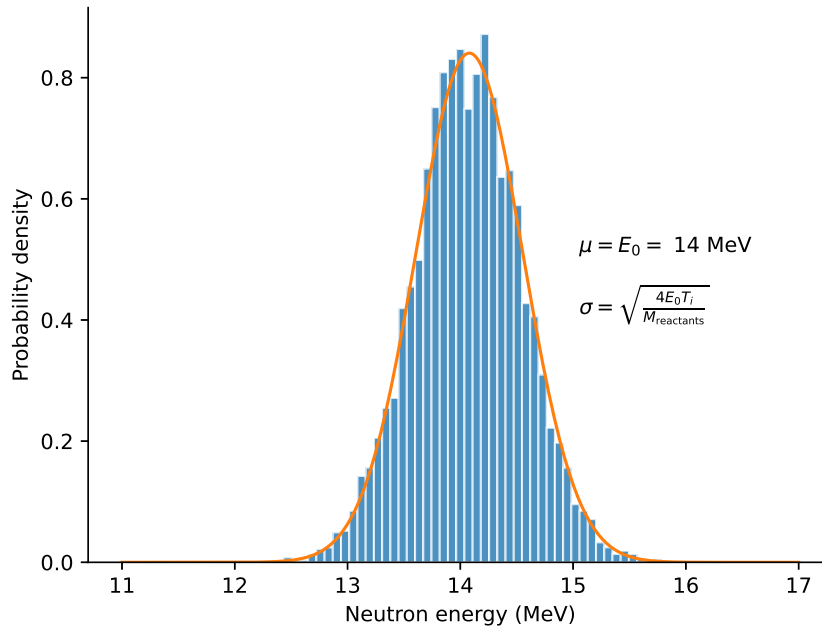


Figure 5.1: Muir neutron energy spectrum corresponding to a DT reaction sampled with 5000 particles.

In this simulation, a neutron source was placed above the monoblock and the total helium production was tallied via the $(n, X\alpha)$ reaction rate (MT reaction number 207). The neutron source corresponds to a 500 MW DT neutron source, which gives a neutron generation rate of 1.8×10^{20} neutrons s^{-1} (based on the energy produced by the DT fusion reaction). The neutrons energy follows a Muir energy spectrum [233] (see Figure 5.1). The probability density is a normal distribution with a standard deviation σ depending on the mass of the reactants $M_{\text{reactants}}$ and the plasma temperature T_i and the mean $\mu = E_0 = 14$ MeV is the neutron energy of the DT reaction:

[233] Ericsson (2019)

$$\sigma = \sqrt{\frac{4E_0T_i}{M_{\text{reactants}}}} \quad (5.1)$$

50 batches of 1 million neutrons were simulated in order to reduce the stochastic error inherent to Monte-Carlo methods.

The production of helium was found to be more important close to the top surface and to the neutron source (see Figure 5.2). It evolves as linearly with the distance from the top surface. The maximum generation rate is $\approx 7 \times 10^{18} \text{ m}^{-3} \text{ s}^{-1}$, which is well below the generation rate from direct implantation in the near surface. Figure 5.2c was obtained by averaging all the values by distance from the top surface. The error bars were computed by averaging the standard deviation provided by OpenMC.

Note that this is a conservative case as the monoblock simulated is right below the neutron source. Other monoblocks of the divertor will be tilted and shadowed by others and therefore will interact less with the neutrons.

5.1.2 Tritium decay

The generation of helium via tritium decay was computed from FESTIM simulations of hydrogen transport in monoblocks. For this case, a volumetric source was added to take the radioactive decay into account. The materials and trapping parameters can

be found in Chapter 3. The incident heat flux was set to 10 MW m^{-2} , the implanted particle flux to $1.61 \times 10^{22} \text{ m}^{-2} \text{ s}^{-1}$, the implantation range to $9.52 \times 10^{-10} \text{ m}$.

Equation 2.2 and Equation 2.3 can be written as:

$$\frac{\partial c_m}{\partial t} = \nabla \cdot (D \nabla c_m) - \sum \frac{\partial c_{t,i}}{\partial t} - \lambda_{\text{decay}} c_m \quad (5.2)$$

$$\frac{\partial c_{t,i}}{\partial t} = k_i \cdot c_m \cdot (n_i - c_{t,i}) - p_i \cdot c_{t,i} - \lambda_{\text{decay}} c_{t,i} \quad (5.3)$$

where λ_{decay} is the decay constant in s^{-1} . It is expressed from the tritium radioactive half-life $\tau_{1/2}$:

$$\lambda_{\text{decay}} = \frac{\ln 2}{\tau_{1/2}} \approx 1.77 \times 10^{-9} \text{ s}^{-1} \quad (5.4)$$

The generation rate of helium from tritium decay is directly proportional to the hydrogen (tritium) retention and can be expressed as $\lambda_{\text{decay}}(c_m + \sum c_{t,i})$. In order to remain conservative, it was computed at steady state.

The maximum generation rate of helium in the monoblock was found to be $6.5 \times 10^{12} \text{ m}^{-3} \text{ s}^{-1}$ (see Figure 5.3). This value assumes all the implanted hydrogen is tritium and should be halved to consider a 50%-50% DT mixture. This is order of magnitudes below the generation from direct implantation in the near surface region.

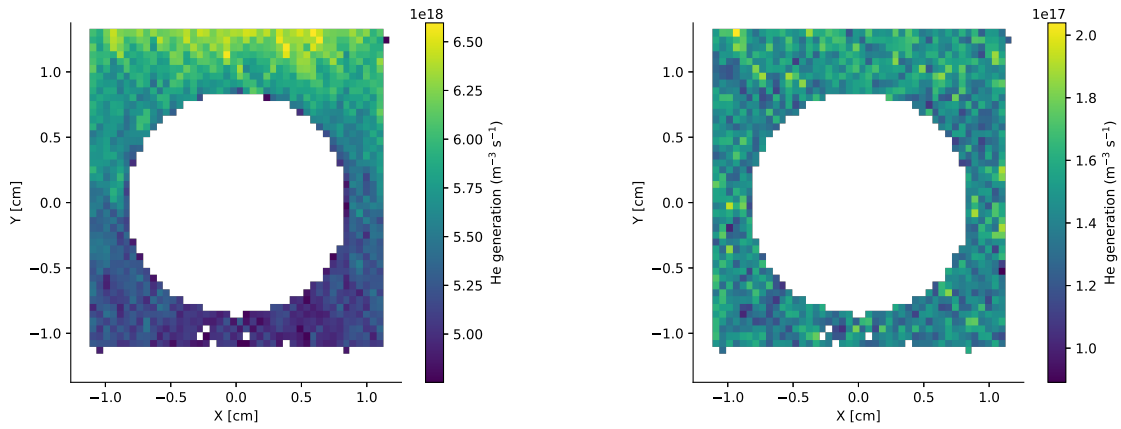
5.1.3 Comparison to direct implantation

The volumetric source of helium Γ due to direct implantation from the plasma can be calculated by:

$$\Gamma = \varphi_{\text{imp}} f(x) \quad (5.5)$$

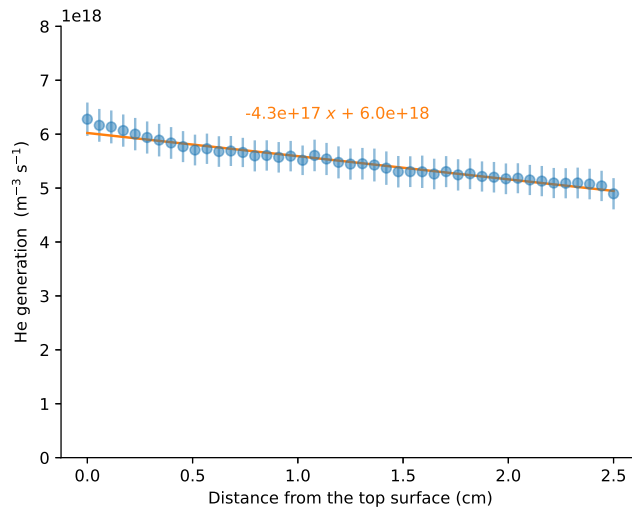
where $\varphi_{\text{imp}} = 1 \times 10^{23} \text{ m}^{-2} \text{ s}^{-1}$ is the implanted helium flux and $f(x)$ is a gaussian distribution centered on $R_p = 1.5 \text{ nm}$ and a width $\sigma = 1.0 \text{ nm}$, which correspond to typical implantation parameters for helium exposure in tokamaks.

When comparing the production of helium from indirect sources with the quantity helium implanted from the plasma Γ , it appears that the indirect sources are negligible in the exposed region (see Figure 5.4). Indirect helium production may become dominant in bulk regions - though may not necessarily be enough to produce helium bubbles.



(a) Helium generation (mean value).

(b) Helium generation (standard deviation).



(c) Distribution from the top surface. Errors bars correspond to the 95 % confidence interval.

Figure 5.2: Helium generation via transmutation in a monoblock (only tungsten is shown).

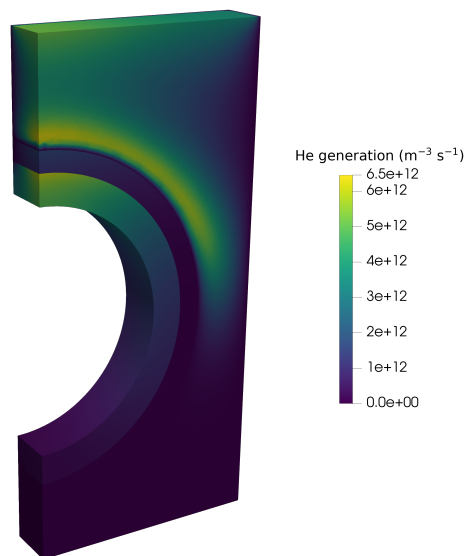


Figure 5.3: Steady state helium generation from tritium decay in a monoblock.

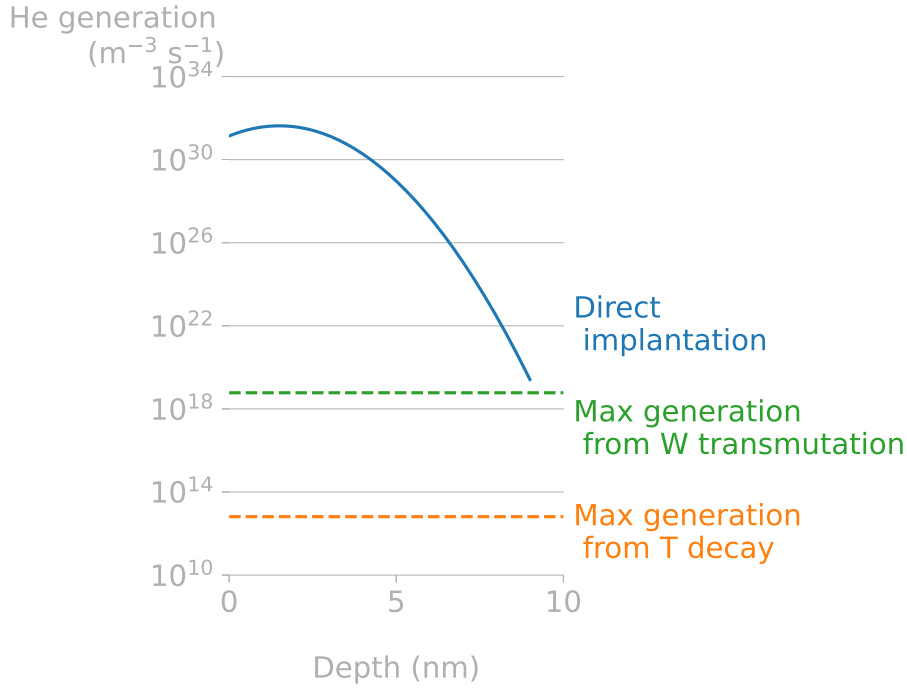


Figure 5.4: Comparison of the three sources of helium in a monoblock. The source from direct implantation was computed for an incident flux of $5 \times 10^{25} \text{ m}^{-2} \text{ s}^{-1}$ with a gaussian distribution (mean of 1 nm and standard deviation of 1.5 nm).

5.2 Bubble growth model

This Section describes the He transport model and the grouped approach employed to simplify it.

5.2.1 Helium clustering model

This model describes the evolution of the concentrations of pure interstitial He clusters (He_x) and mixed He-vacancies clusters ($\text{He}_x \text{V}_y$) that are formed by trap mutation events.

The spatio-temporal evolution of each species of size i is defined by:

$$\frac{\partial c_i}{\partial t} = \nabla \cdot (D_i \nabla c_i) + \Gamma_i + R_i \quad (5.6)$$

where $D = D_{0i} \cdot \exp(-E_{D_i}/(k_B \cdot T))$ is the thermally activated diffusion coefficient expressed in $\text{m}^2 \text{ s}^{-1}$. If a species i is assumed to be immobile, its diffusion coefficient D_i is zero. Γ_i is the external production rate of species i expressed in $\text{m}^{-3} \text{ s}^{-1}$. The term R_i is the coupling term due to reactions between species expressed in $\text{m}^{-3} \text{ s}^{-1}$.

A simple reaction between two species can be described as:



The forward rate constant $k_{A,B}^+$ is the clustering rate and is calculated using the theory of diffusion-limited reactions [234–236]:

$$k_{A,B}^+ = 4\pi(r_A + r_B)(D_A + D_B) \quad (5.8)$$

[234] Goldstein et al. (2007)

[235] Nichols (1978)

[236] Waite (1957)

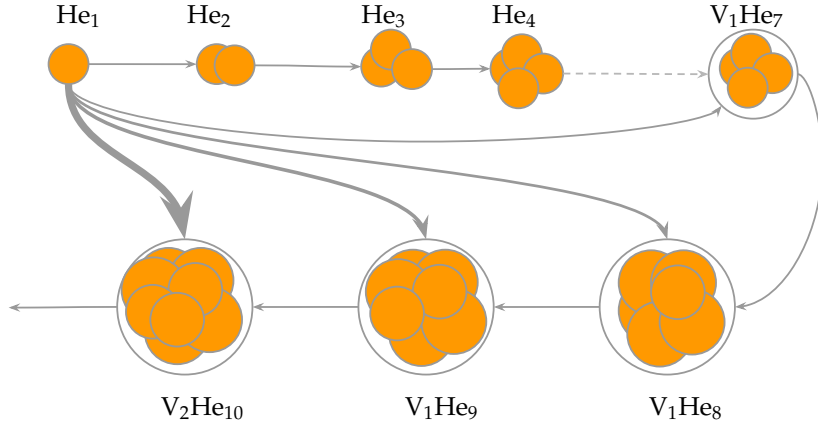


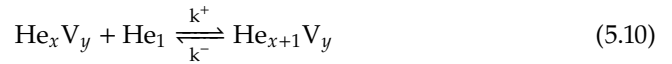
Figure 5.5: Representation of He clustering in solids. Dissociation is omitted for simplification purposes. The thickness of the grey arrows represents the magnitude of the reaction rate between mobile He₁ and other clusters at the same distance.

where r_A and r_B are the capture radii and D_A and D_B are the diffusion coefficients of species A and B respectively. The backward rate constant $k_{A,B}^-$ is the dissociation rate and is obtained using chemical equilibrium principles [234]:

$$k_{A,B}^- = \rho k_{A,B}^+ e^{\frac{-E_b}{k_B T}} \quad (5.9)$$

where $\rho = 6.3 \times 10^{28} \text{ m}^{-3}$ is the atomic density of W in m^{-3} and E_b is the binding energy for the equilibrium $AB \longrightarrow A + B$ in eV.

Considering only the absorption of He₁ by other clusters (see Figure 5.5):



The reaction term R_i is the coupling term between concentrations and is expressed as:

$$R_i = k_{i,i-1}^+ c_1 c_{i-1} - k_{i,1}^+ c_i c_1 + k_{i+1}^- c_{i+1} - k_i^- c_i \quad (5.11)$$

where c_i is the concentration of clusters of size i in m^{-3} . In Equation 5.11, the first term corresponds to the reactions producing clusters of size i . The second one corresponds to the ones reacting with clusters of size i . The third term accounts for bigger clusters dissociating. Finally, the last term corresponds to clusters of size i dissociating.

The system of equations can therefore be written as follows:

$$\frac{\partial c_1}{\partial t} = \nabla \cdot (D_1 \nabla c_1) + \Gamma + \sum_{i=2}^{\infty} k_i^- c_i - 2k_{1,1}^+ c_1^2 - \sum_{i=2}^{\infty} k_{1,i}^+ c_1 c_i \quad (5.12a)$$

$$\frac{\partial c_2}{\partial t} = \nabla \cdot (D_2 \nabla c_2) - k_{1,2}^+ c_1 c_2 + k_{1,1}^+ c_1^2 - k_2^- c_2 + k_3^- c_3 \quad (5.12b)$$

$$\vdots$$

$$\frac{\partial c_i}{\partial t} = -k_{1,i}^+ c_1 c_i + k_{1,i-1}^+ c_1 c_{i-1} - k_i^- c_i \quad (5.12c)$$

$$\frac{\partial c_{i+1}}{\partial t} = -k_{1,i+1}^+ c_1 c_{i+1} + k_{1,i}^+ c_1 c_i \quad (5.12d)$$

$$\vdots$$

5.2.2 Grouped approach

[88] Faney et al. (2014)

Extending this clustering model to clusters containing millions of helium extremely increases the computational cost. A grouped approach proposed by Faney et al. [88] for reducing the number of equations will therefore be employed. This technique consists in grouping clusters from an arbitrary size N in a single equation while explicitly accounting for smaller clusters. To do so, the dissociation of large clusters is neglected (i.e. $k_i^- = 0$ for $i > N$). This assumption is valid since the activation energy for trap mutation events is lower than that of He or vacancy emission [79]. Dissociation of large clusters by vacancy or He emission is therefore negligible. Moreover, clusters containing more than six He atoms are assumed to be immobile (i.e. $D_i = 0$ for $i > 6$). This assumption is motivated by DFT and MD results suggesting that the self-trapping energy is below the binding energy of one He atom in a pure He cluster for clusters containing more than five He atoms [79].

[79] Boisse et al. (2014)

For smaller clusters ($\text{He}_1, \text{He}_2, \dots, \text{He}_6$) the diffusion coefficient and the dissociation by He emission energy vary with the number of He atoms in the cluster (see Table 5.1).

Equation 5.12 can therefore be written as:

$$\frac{\partial c_1}{\partial t} = \nabla \cdot (D_1 \nabla c_1) + \Gamma + \sum_{i=2}^N k_i^- c_i - 2k_{1,1}^+ c_1^2 - \sum_{i=2}^N k_{1,i}^+ c_1 c_i - \sum_{i=N+1}^{\infty} k_{1,i}^+ c_1 c_i \quad (5.13a)$$

$$\frac{\partial c_2}{\partial t} = \nabla \cdot (D_2 \nabla c_2) - k_{1,2}^+ c_1 c_2 + k_{1,1}^+ c_1^2 - k_2^- c_2 + k_3^- c_3 \quad (5.13b)$$

$$\vdots$$

$$\sum_{i=N}^{\infty} \frac{\partial c_i}{\partial t} = k_{1,N}^+ c_1 c_N + \sum_{i=N+1}^{\infty} k_{1,i}^+ c_1 c_i - \sum_{i=N+1}^{\infty} k_{1,i}^+ c_1 c_i = k_{1,N}^+ c_1 c_N \quad (5.13c)$$

In order to simplify this set of equations, the following quantities are defined:

$$c_b = \sum_{i=N+1}^{\infty} c_i \quad : \text{bubbles concentration} \quad (5.14)$$

$$\langle i_b \rangle = \frac{1}{c_b} \sum_{i=N+1}^{\infty} i c_i \quad : \text{average He content in bubbles} \quad (5.15)$$

$$\langle r_b \rangle = \frac{1}{c_b} \sum_{i=N+1}^{\infty} r_i c_i \quad : \text{average radius in bubbles} \quad (5.16)$$

$$\langle k_b^+ \rangle = \frac{1}{c_b} \sum_{i=N+1}^{\infty} k_{1,i}^+ c_i \quad : \text{average clustering rate in bubbles} \quad (5.17)$$

Clusters with more than N He (c_b) will be referred as “bubbles” in the following.

Equation 5.13 therefore reads:

$$\frac{\partial c_1}{\partial t} = \nabla \cdot (D_1 \nabla c_1) + \Gamma + \sum_{i=2}^N k_i^- c_i - 2k_{1,1}^+ c_1^2 - \sum_{i=2}^N k_{1,i}^+ c_1 c_i - \langle k_b^+ \rangle c_1 c_b \quad (5.18a)$$

$$\frac{\partial c_2}{\partial t} = \nabla \cdot (D_2 \nabla c_2) - k_{1,2}^+ c_1 c_2 + k_{1,1}^+ c_1^2 - k_2^- c_2 + k_3^- c_3 \quad (5.18b)$$

⋮

$$\frac{\partial c_N}{\partial t} = -k_{1,N}^+ c_1 c_N + k_{1,N-1}^+ c_1 c_{N-1} - k_N^- c_N \quad (5.18c)$$

[89] Faney et al. (2015)

$$\frac{\partial c_b}{\partial t} = k_{1,N}^+ c_1 c_N \quad (5.18d)$$

$$(5.18e)$$

The radius of pure He clusters [89] given by:

$$r_{\text{He}_x} = r_{\text{He}_1} + \left(\frac{3}{4\pi} \frac{a_0^3}{10} x \right)^{1/3} - \left(\frac{3}{4\pi} \frac{a_0^3}{10} \right)^{1/3} \quad (5.19)$$

with $r_{\text{He}_1} = 0.3$ nm.

$\langle k_b^+ \rangle$ can be expressed as:

$$\langle k_b^+ \rangle = \frac{1}{c_b} \sum_{i=N+1}^{\infty} k_{1,i}^+ c_i \quad (5.20a)$$

$$= \frac{1}{c_b} 4\pi \sum_{i=N+1}^{\infty} c_i (r_1 + r_i) (D_1 + D_i) \quad (5.20b)$$

Assuming $D_i = 0$ for $i > N$:

$$\langle k_b^+ \rangle = \frac{1}{c_b} 4\pi D_1 \sum_{i=N+1}^{\infty} c_i (r_1 + r_i) \quad (5.21a)$$

$$= \frac{1}{c_b} 4\pi D_1 \left(\sum_{i=N+1}^{\infty} c_i r_1 + \sum_{i=N+1}^{\infty} c_i r_i \right) \quad (5.21b)$$

$$= \frac{1}{c_b} 4\pi D_1 \left(r_1 c_b + \sum_{i=N+1}^{\infty} c_i r_i \right) \quad (5.21c)$$

$$= 4\pi D_1 (r_1 + \langle r_b \rangle) \quad (5.21d)$$

For clusters containing both He and vacancies, the radius only depends on the number of vacancies m is given by [89]:

$$r_{\text{He}_i\text{V}_m} = r_{\text{He}_0\text{V}_1} + \left(\frac{3}{4\pi} \frac{a_0^3}{2} m \right)^{1/3} - \left(\frac{3}{4\pi} \frac{a_0^3}{2} \right)^{1/3} \quad (5.22)$$

with $a_0 = 0.318$ nm the lattice parameter and $r_{\text{He}_0\text{V}_1} = a_0 \sqrt{3}/4$.

The bubble radius $\langle r_b \rangle$ therefore reads:

$$\langle r_b \rangle = \frac{1}{c_b} \sum_{i=N+1}^{\infty} c_i r_{\text{He}_i\text{V}_m} \quad (5.23a)$$

$$= \frac{1}{c_b} \sum_{i=N+1}^{\infty} c_i \left(r_{\text{He}_0\text{V}_1} + \left(\frac{3}{4\pi} \frac{a_0^3}{2} m \right)^{1/3} - \left(\frac{3}{4\pi} \frac{a_0^3}{2} \right)^{1/3} \right) \quad (5.23b)$$

$$= r_{\text{He}_0\text{V}_1} + \left(\frac{3}{4\pi} \frac{a_0^3}{2} \right)^{1/3} \frac{1}{c_b} \sum_{i=N+1}^{\infty} c_i m^{1/3} - \left(\frac{3}{4\pi} \frac{a_0^3}{2} \right)^{1/3} \quad (5.23c)$$

The number of vacancies in bubbles m is assumed to be $i/4$ (i.e. four helium per vacancy). This assumption is motivated by MD computations showing that trap mutation events occur for every four additional helium in large vacancy-helium clusters. Moreover, theoretical models for He bubbles growth in metals suggest a similar trend [237].

[237] Hammond et al. (2020)

The average radius $\langle r_b \rangle$ therefore reads:

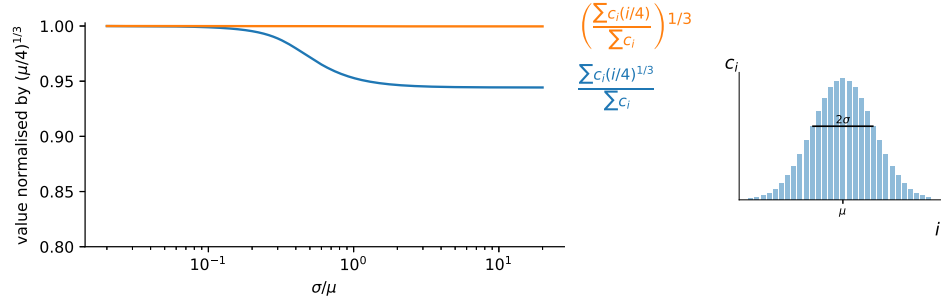
$$\langle r_b \rangle = r_{\text{He}_0\text{V}_1} + \left(\frac{3}{4\pi} \frac{a_0^3}{2} \right)^{1/3} \frac{1}{c_b} \sum_{i=N+1}^{\infty} c_i \left(\frac{i}{4} \right)^{1/3} - \left(\frac{3}{4\pi} \frac{a_0^3}{2} \right)^{1/3} \quad (5.24)$$

Assuming c_i follows a narrow gaussian distribution [89], $\frac{1}{c_b} \sum_{i=N+1}^{\infty} c_i \left(\frac{i}{4} \right)^{1/3} \approx \left(\frac{1}{c_b} \sum_{i=N+1}^{\infty} c_i \frac{i}{4} \right)^{1/3}$ (see Figure 5.6).

The final expression of the bubble mean radius is therefore:

$$\langle r_b \rangle = r_{\text{He}_0\text{V}_1} + \left(\frac{3}{4\pi} \frac{a_0^3}{2} \frac{\langle i_b \rangle}{4} \right)^{1/3} - \left(\frac{3}{4\pi} \frac{a_0^3}{2} \right)^{1/3} \quad (5.25)$$

Figure 5.6: Validity of the sum approximation in the computation of the bubble radius assuming c_i has a gaussian distribution centered on μ and with a standard deviation σ .



To solve for $\langle i_b \rangle$, is also useful to write the expression of the sum $\sum_{i=N+1}^{\infty} i \frac{\partial c_i}{\partial t}$:

$$\begin{aligned}
 \sum_{i=N+1}^{\infty} i \frac{\partial c_i}{\partial t} &= \sum_{i=N+1}^{\infty} i k_{1,i-1}^+ c_1 c_{i-1} - \sum_{i=N+1}^{\infty} i k_{1,i}^+ c_1 c_i \\
 &= (N+1) k_{1,N}^+ c_1 c_N + \sum_{i=N+2}^{\infty} i k_{1,i-1}^+ c_1 c_{i-1} - \sum_{i=N+1}^{\infty} i k_{1,i}^+ c_1 c_i \\
 &= (N+1) k_{1,N}^+ c_1 c_N + \sum_{i=N+1}^{\infty} (i+1) k_{1,i}^+ c_1 c_i - \sum_{i=N+1}^{\infty} i k_{1,i}^+ c_1 c_i \\
 &= (N+1) k_{1,N}^+ c_1 c_N + \sum_{i=N+1}^{\infty} (i+1) k_{1,i}^+ c_1 c_i - i k_{1,i}^+ c_1 c_i \\
 &= (N+1) k_{1,N}^+ c_1 c_N + \sum_{i=N+1}^{\infty} k_{1,i}^+ c_1 c_i \\
 \frac{\partial \langle i_b \rangle c_b}{\partial t} &= (N+1) k_{1,N}^+ c_1 c_N + \langle k_b^+ \rangle c_1 c_b \quad (5.26)
 \end{aligned}$$

The final form of the system of governing equations is obtained by adding Equation 5.26 to Equation 5.18:

$$\frac{\partial c_1}{\partial t} = \nabla \cdot (D_1 \nabla c_1) + \Gamma + \sum_{i=2}^N k_i^- c_i - 2k_{1,1}^+ c_1^2 - \sum_{i=2}^N k_{1,i}^+ c_1 c_i - \langle k_b^+ \rangle c_1 c_b \quad (5.27a)$$

$$\frac{\partial c_2}{\partial t} = \nabla \cdot (D_2 \nabla c_2) - k_{1,2}^+ c_1 c_2 + k_{1,1}^+ c_1^2 - k_2^- c_2 + k_3^- c_3 \quad (5.27b)$$

⋮

$$\frac{\partial c_N}{\partial t} = -k_{1,N}^+ c_1 c_N + k_{1,N-1}^+ c_1 c_{N-1} - k_N^- c_N \quad (5.27c)$$

$$\frac{\partial c_b}{\partial t} = k_{1,N}^+ c_1 c_N \quad (5.27d)$$

$$\frac{\partial (\langle i_b \rangle c_b)}{\partial t} = (N+1) k_{1,N}^+ c_1 c_N + \langle k_b^+ \rangle c_1 c_b \quad (5.27e)$$

[88] Faney et al. (2014)

The current implementation further simplifies Faney's model [88]:

- Interactions with self-interstitial atoms or pre-existing vacancies are not taken into account. In this work, the only dissociations are He emissions from small mobile clusters and trap mutation for large clusters. It was showed that this assumption did not have an impact on the results (see Figure 5.7).

Cluster	$D_0(\text{m}^2\text{s}^{-1})$	$E_D(\text{eV})$	$E_b(\text{eV})$
He ₁	2.95×10^{-8}	0.13	-
He ₂	3.24×10^{-8}	0.20	1.0
He ₃	2.26×10^{-8}	0.25	1.5
He ₄	1.68×10^{-8}	0.20	1.5
He ₅	5.20×10^{-9}	0.12	1.6
He ₆	1.20×10^{-9}	0.30	2.0

Table 5.1: Pure He clusters properties in W. Diffusion properties are taken from Faney et al. [89] and binding energies are taken from Becquart et al. [238].

- The only clusters explicitly computed are $\text{He}_{x \leq 6}$ (i.e. $N = 6$) whereas Faney's work explicitly accounted for clusters up to $\text{V}_{50}\text{He}_{250}$ and solved a bigger system of equations. The influence of this threshold N above which clusters are integrated in the quantity c_b is discussed in Section 5.4.2.

This He transport model was implemented in Python and solved using the finite element solving platform FEniCS [183].

[183] Alnæs et al. (2015)

5.3 Verification & Validation

5.3.1 Code comparison: Tendril case

The current implementation was compared to literature results [89]. Helium exposure in a tendril was simulated in 1D. The helium flux is $1 \times 10^{22} \text{m}^{-2} \text{s}^{-1}$ and the fluence was $5 \times 10^{25} \text{m}^{-2}$.

The domain size is 30 nm and the volumetric source term is described as follows:

$$\Gamma(x) = \varphi_{\text{imp}} f(x) \quad (5.28)$$

where $\varphi_{\text{imp}} = 1 \times 10^{22} \text{m}^{-2} \text{s}^{-1}$ is the implanted He flux and $f(x)$ is a Gaussian distribution with a mean value $\mu = R_p = 1.5 \text{nm}$ and a standard deviation $\sigma = 1 \text{nm}$ which corresponds to a 100 eV He implantation based on SRIM computations [173].

[173] Ziegler et al. (2010)

Mobile He clusters concentrations were set to zero at the tendril's surfaces ($x = 0 \text{nm}$ and $x = 30 \text{nm}$).

Concentration profiles computed by the current implementation showed good agreement with the ones obtained by Faney et al. [89] (see Figure 5.7). The discrepancies

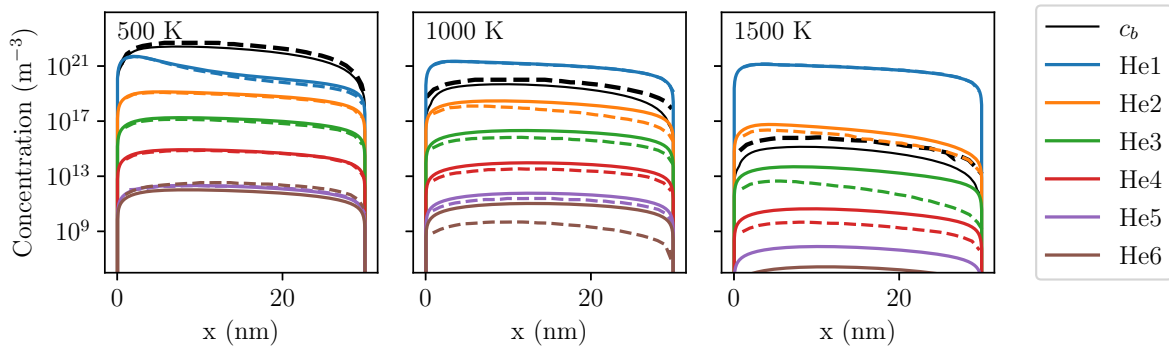


Figure 5.7: He clusters concentration profiles in the tendril at 500 K, 1000 K and 1500 K under 100 eV He exposure at $1 \times 10^{22} \text{m}^{-2} \text{s}^{-1}$ at a fluence of $5 \times 10^{25} \text{m}^{-2}$. Comparison between the current implementation (solid) and Faney's results [89] (dashed).

are likely due to a difference in the set of dissociation energies that have been used as these energies have an impact on the concentration profiles (see Figure 5.8). Indeed, at low temperature, where dissociation is not activated, the discrepancies were rather small whereas at high temperature, differences increased because dissociation became more dominant.

Moreover, increasing the temperature tended to inhibit bubble formation in the tendrils. This was explained by a greater increase in the dissociation rate and in losses at surfaces than the increase in the clustering rate. This observation is in agreement with MD results simulating He implantation in tendrils [239, 240]. The current implementation and the additional assumptions that were made are therefore valid.

[239] Wei et al. (2020)

[240] Wei et al. (2019)

5.3.2 Comparison with experiments

He implantation experiments were performed on W in the linear plasma device PSI-2 [241]. W was irradiated with 75 eV He at $2.3 \times 10^{22} \text{ m}^{-2} \text{ s}^{-1}$ and 1053 K for 13 s. A thin lamella for cross-sectional observations was prepared using the Focused Ion Beam (FIB) technique with a Dual Beam FIB (FEI Helios 600 NanoLab). Prior to FIB cutting, the surface of the sample was coated with a SiO layer for better contrast and then with a protective platinum layer to avoid damaging the surface during the lamella preparation. Cross-sectional observations of the He-implanted W were performed using TEM in a TEM FEI Titan 80-300 apparatus.

[241] Kreter et al. (2015)

A typical TEM image of the lamella is presented in Figure 5.9. Comparison of under- and over-focused TEM images allowed identification of the bubbles. Bubbles were observed up to 100 nm with larger bubbles closer to the surface and smaller bubbles deeper in the bulk. Open bubbles and holes at the surface were also observed suggesting bursting events occurred. This is in accordance with what was observed in the simulations (see Figure 5.12).

[97] Ialovega et al. (2020)

[131] Ialovega (2021)

[242] Schindelin et al. (2012)

A procedure was developed by Ialovega et al. [97, 131] to automate the bubble detection on TEM images using the ImageJ software [242]. The area of bubbles were computed as well as their diameter assuming a spherical shape for the bubbles. Bubble density and size as a function of depth was therefore computed using 12 pairs of under- and over-focused TEM images. The bubble density was found to range from $7 \times 10^{19} \text{ m}^{-3}$ to $2 \times 10^{20} \text{ m}^{-3}$ and the bubble radius ranged between 1 nm and 10 nm (see Figure 5.10). Although the resolution of the TEM is below 1 nm, the number of bubbles with radius below 2 nm is underestimated due to the limited contrast.

This experiment was simulated using the same exposure conditions. The simulated bubbles density c_b was found to be in accordance with the one measured experimentally. Some discrepancies were found at the near surface.

The bubble radius $\langle r_b \rangle$ is however overestimated by an order of magnitude compared to experimental measurements. This could imply that the current model linking the He content to the bubble radius is overestimated and that a more accurate one is needed. The model parametrisation could also have an impact on these results (see Figure 5.8). Bursting in over-pressurised bubbles close to the surface would also reduce the bubble size. Finally, it would be worth investigating this further to determine the impact of initial defects.

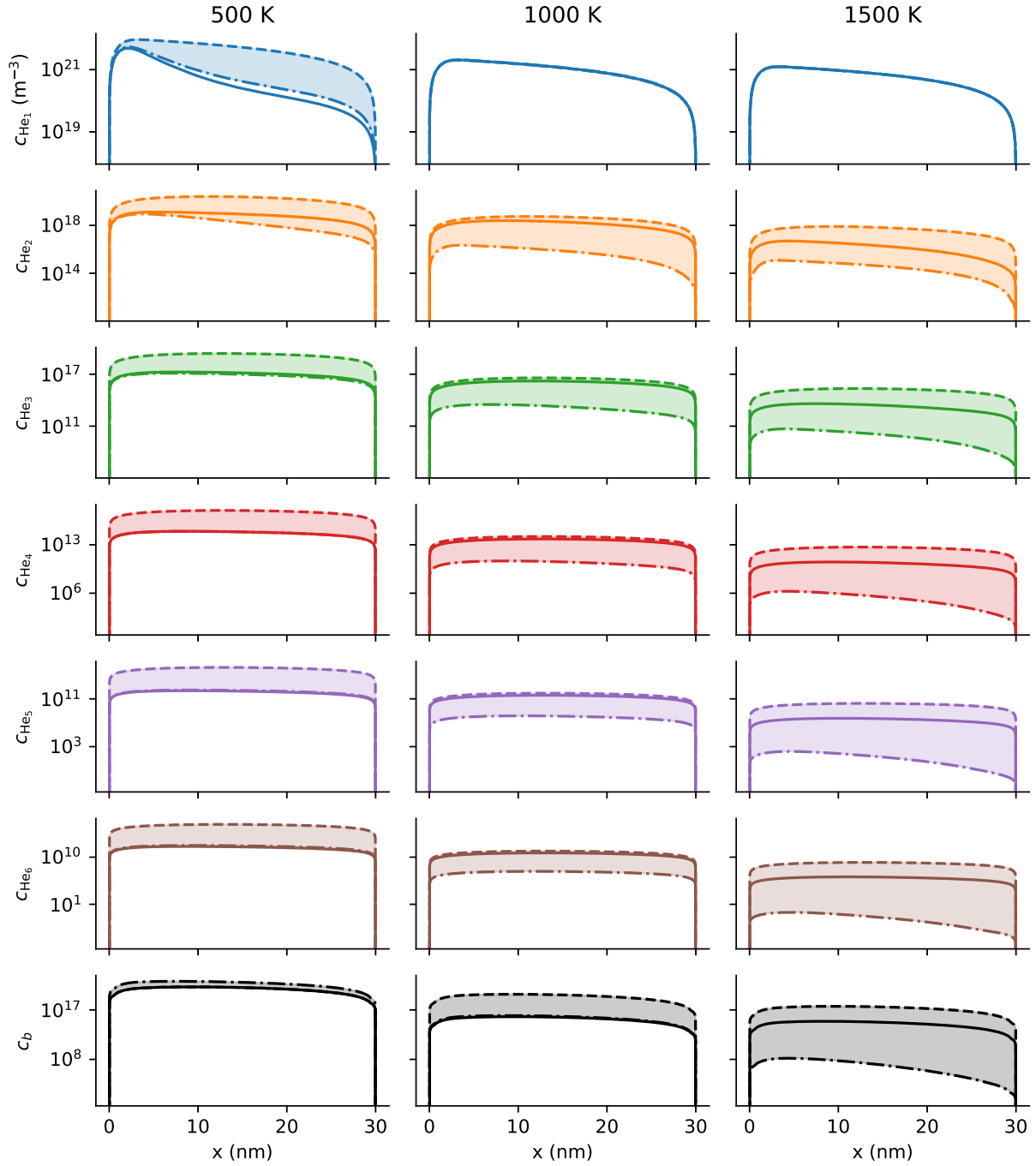


Figure 5.8: Helium clusters concentration profiles on the tendril case with dissociation energies varying from -0.5 eV (dash-point) to $+0.5$ eV (dash).

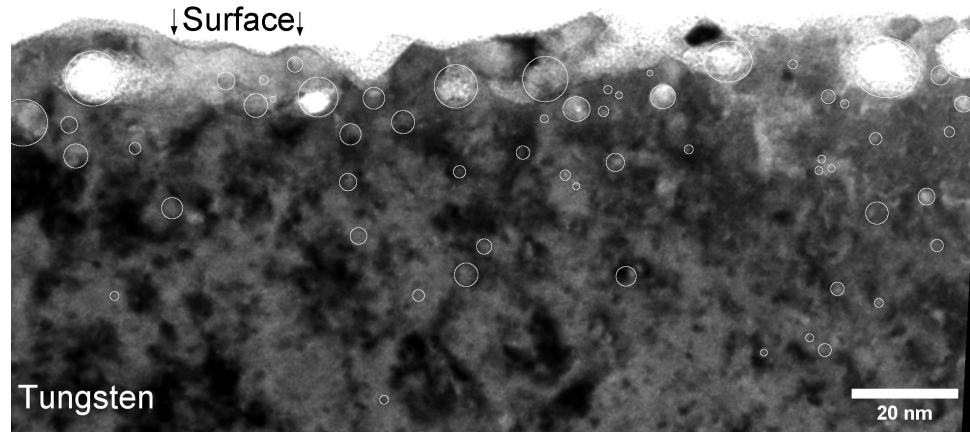


Figure 5.9: Transmission Electron Microscopy (TEM) images of W after exposure to 75 eV He at $2.3 \times 10^{22} \text{ m}^{-2} \text{ s}^{-1}$ and 1053 K for 13 s showing bubbles that have burst, large size bubbles at the near surface and small size bubbles in the bulk.

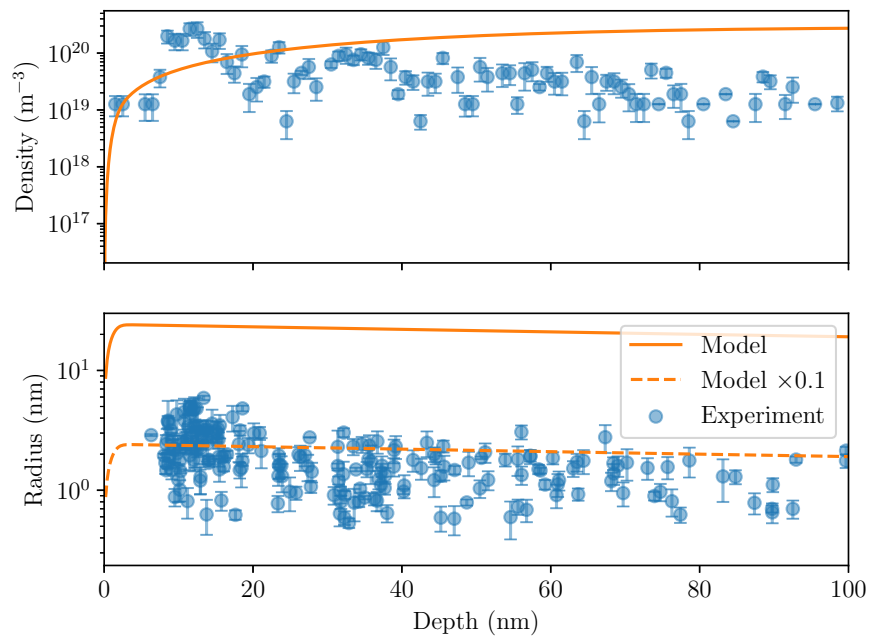


Figure 5.10: Comparison of experimental results with simulations for W implanted with 75 eV He at $2.3 \times 10^{22} \text{ m}^{-2} \text{ s}^{-1}$ and 1053 K for 13 s. Error bars correspond to the lowest and highest radius in the TEM image.

5.4 Bubble growth study

[89] Faney et al. (2015)

In this Section, the current implementation is first compared with the one from Faney [89] to ensure the additional assumptions do not produce different results. A standard half-slab case is then described and a parametric study is performed by varying the exposure conditions. Finally, the model is compared against experimental data.

5.4.1 Half-slab case

He transport was simulated in a 1D semi-infinite W slab. This case is the standard case describing the main quantities of interest of the parametric study performed in Section 5.4.2.

The domain size is 0.1 mm which is much greater than the penetration depth of He in the simulations. 100 eV He were implanted in the first 1.5 nm as in Section 5.3.1. The implanted flux was $1 \times 10^{22} \text{ m}^{-2} \text{ s}^{-1}$ and the temperature was 1000 K.

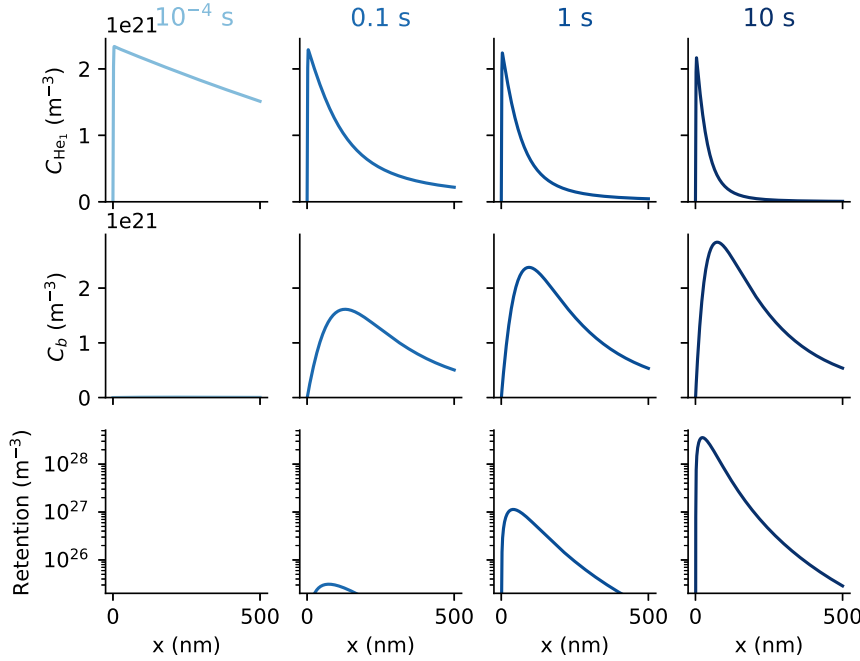


Figure 5.11: Concentration profiles of He₁ (left) and bubbles (right) in W exposed to 100 eV He at $10^{-22} \text{ m}^{-2} \text{ s}^{-1}$ and 1000 K.

At low fluences, He diffused quickly into the bulk (see Figure 5.11) and the bubbles' concentration c_b was found to be zero. As the fluence increased, bubbles started to appear and acted as strong sinks for mobile He. This led to a great decrease in the mobile He concentration profile.

It is worth noticing the maximum of c_b was not located at the maximum of c_{He_1} which is the implantation depth R_p . This was explained by the diffusion of small mobile clusters as shown by analytical models [243]. As He clusters, small mobile clusters diffuse deeper into the bulk until trap mutation occurs and bubbles nucleons (clusters with more than 6 He) are created. From that point, bubbles are formed relatively far from the surface. Because He is implanted in the first nanometres, c_{He_1} is maximum at $R_p = 1.5 \text{ nm}$ and interactions with bubbles are stronger in this region. This tends to draw the maximum location of c_b towards the surface.

[243] Krashennnikov et al. (2014)

The He content in bubbles $\langle i_b \rangle$ and the radius $\langle r_b \rangle$ were computed. After 10 s of implantation, bubbles located in the near surface contained up to 3×10^7 He. The maximum of $\langle r_b \rangle$ was found to be very close to the surface at approximately 2 nm (see Figure 5.12). This is explained by the high concentration of mobile He in this near surface region. Moreover, a bursting zone can be defined by the region where $\langle r_b \rangle$ is greater than the depth of the bubble. In this region, bubble of this size would have likely burst.

From this average He content in bubbles and from Equation 5.23 and Equation 5.19 expressing the clusters radii, the average radius $\langle r \rangle$ can be computed as:

$$\langle r \rangle = \frac{\sum_{i=1}^{\infty} c_i r_i}{\sum_{i=1}^{\infty} c_i} = \frac{\sum_{i=1}^N c_i r_i + c_b \langle r_b \rangle}{\sum_{i=1}^N c_i + c_b} \quad (5.29)$$

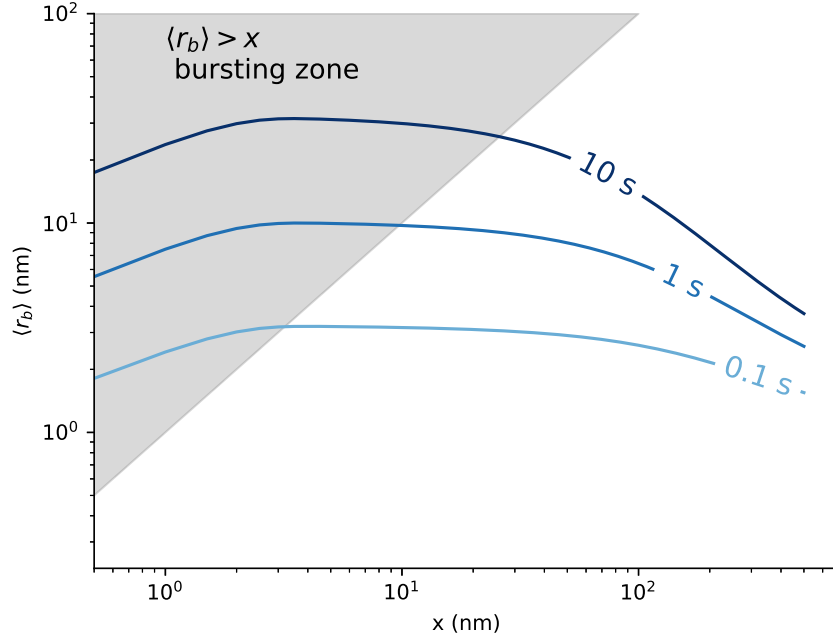


Figure 5.12: Profile of mean bubble radius $\langle r_b \rangle$ as a function of depth x in W exposed to 100 eV He at $10^{22} \text{ m}^{-2} \text{ s}^{-1}$ and 1000 K.

The average content of He in all clusters $\langle i \rangle$ is computed similarly:

$$\langle i \rangle = \frac{\sum_{i=1}^{\infty} c_i i}{\sum_{i=1}^{\infty} c_i} = \frac{\sum_{i=1}^N c_i i + c_b \langle i_b \rangle}{\sum_{i=1}^N c_i + c_b} \quad (5.30)$$

[89] Faney et al. (2015)

The values of these two quantities are similar to the ones obtained by Faney et al. [89]. After 100 s of exposure, the average radius 50 nm below the surface was above 10 nm (see Figure 5.13). Moreover, the location of the maximum of these quantities move towards the exposed surface.

The average radius $\langle r \rangle$ cannot be easily compared to experimental observations for it includes contributions from very small mobile He_x clusters which are not visible experimentally (only bubbles with a radius greater than 1-3 nm are observable depending on the observation technique).

5.4.2 Influence of exposure parameters on helium bubble growth

The impact of He flux and temperature T was studied on the case described in Section 5.4.1 in order to identify trends. Behaviour laws are identified and can be used to obtain information on He transport without needing to run any simulation.

In order to analyse the results, several quantities are computed. First the bubbles inventory is defined as:

$$I_{\text{bubbles}} = \int c_b dx \quad (5.31)$$

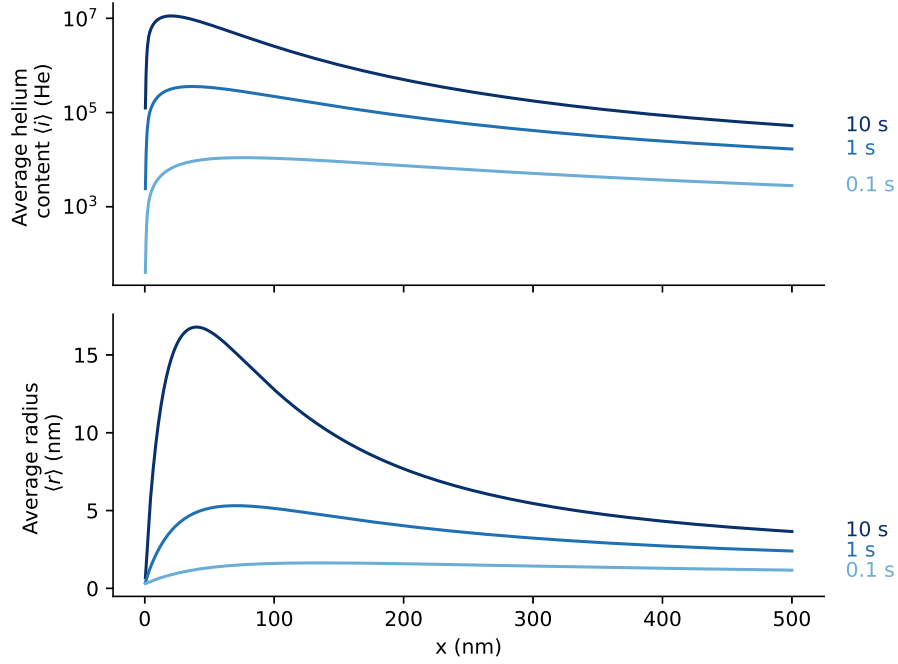


Figure 5.13: Average helium content $\langle i \rangle$ and average radius $\langle r \rangle$ in all clusters (mobile and bubbles) in W exposed to 100 eV He at $10^{22} \text{ m}^{-2} \text{ s}^{-1}$ and 1000 K.

The total helium inventory is calculated by:

$$I = \int \sum_{i=1}^N i c_i + \langle i_b \rangle c_b dx \approx \int \langle i_b \rangle c_b dx \quad (5.32)$$

The spatial mean helium content in bubbles can be computed as:

$$\langle \bar{i}_b \rangle = \frac{\int \langle i_b \rangle c_b dx}{\int c_b dx} \approx \frac{I}{I_{\text{bubbles}}} \quad (5.33)$$

The approximation made in Equation 5.32 and Equation 5.33 is valid as long as $\int \langle i_b \rangle c_b dx \gg \int \sum_{i=1}^N i c_i dx$ (i.e. the He inventory is dominated by that of the bubbles).

This is the case in these simulations because $N = 6$ (the influence of this parameter is discussed in Section 5.4.2).

Influence of N

In order to assess the impact of the parameter N in Equation 5.18, the evolution of the He inventory I , the mean He content in immobile clusters (different from $\langle \bar{i}_b \rangle$) and the bubbles inventory I_{bubbles} was computed with several values of N .

The flux of 100 eV He in this test case was $10^{20} \text{ m}^{-2} \text{ s}^{-1}$ and the temperature was 1000 K.

It was shown that varying N had no impact on these quantities whatsoever (see Figure 5.14). This highlights the very quick transition from nucleation regime to growth regime in this model.

The number of equations that need to be solved can therefore be minimised by setting the parameter N to its minimum ($N = 6$) without losing accuracy in the results. This minimum value corresponds to the number of mobile clusters which have to be explicitly simulated in order to account for all the diffusion mechanisms.

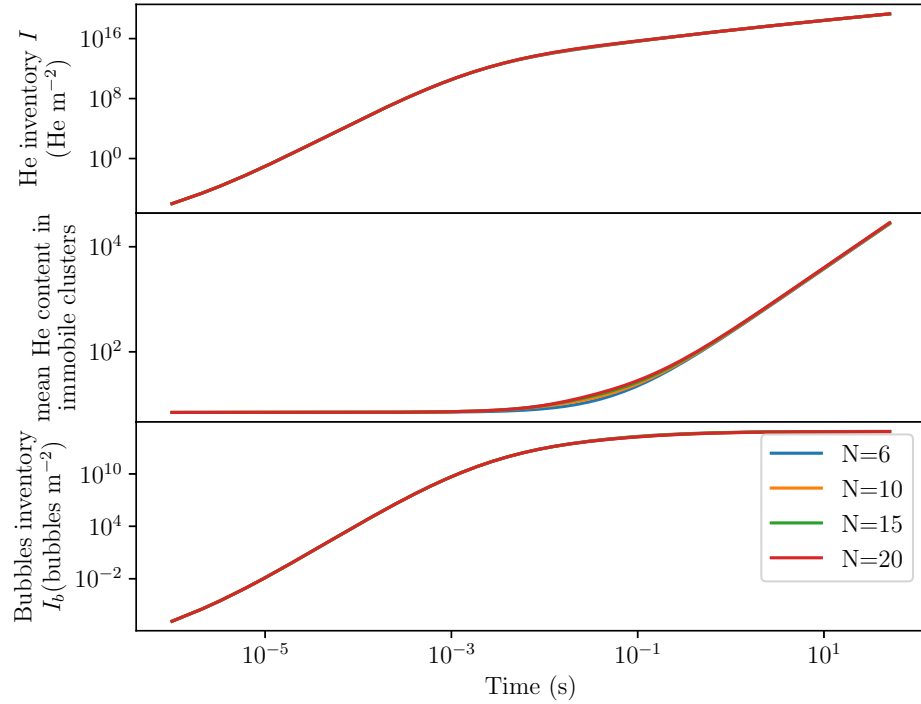


Figure 5.14: Comparison of several quantities of interest for several values of N in W exposed to 100 eV He at $10^{20} \text{ m}^{-2} \text{ s}^{-1}$ and 1000 K.

Parametric study

A parametric study was performed by varying the implanted flux φ_{imp} of 100 eV He between $1 \times 10^{17} \text{ m}^{-2} \text{ s}^{-1}$ and $5 \times 10^{21} \text{ m}^{-2} \text{ s}^{-1}$ and the sample temperature T between 100 K and 1200 K. The exposure time was 1 h.

More than 160 simulations were performed simulating 1 h of exposure. For each simulation, the quantities of interest described above were computed. A Gaussian regression process [208] was used to interpolate the data based on Bayesian inference as done in [244] (see Figure 5.15). The temporal evolution of these quantities was also assessed (see Figure 5.16).

After 1 h of exposure, the bubbles inventory I_{bubbles} shows a weak dependence on temperature at high temperature and a weak dependence on the implanted flux at low temperature (see Figure 5.15a). I_{bubbles} varies from $4 \times 10^{12} \text{ bubbles m}^{-2}$ at high temperature and low flux to $2 \times 10^{19} \text{ bubbles m}^{-2}$ at low temperature and high flux.

The He inventory I varies from $8 \times 10^{16} \text{ m}^{-2}$ at high temperature and low flux to 10^{25} m^{-2} at low temperature and high flux (see Figure 5.15b). For temperatures above 600 K, the temperature dependence is rather weak compared to the flux dependence.

For temperatures above 300 K, and after 1 h of exposure, the sample temperature does not impact the value of $\langle \bar{i}_b \rangle$ (see Figure 5.15c). The mean He content increases with the implanted flux as expected and varies between 10^3 He at low flux and $5 \times 10^8 \text{ He}$ at high flux.

[208] Bowman (2020)

[244] Delaporte-Mathurin et al. (2020)

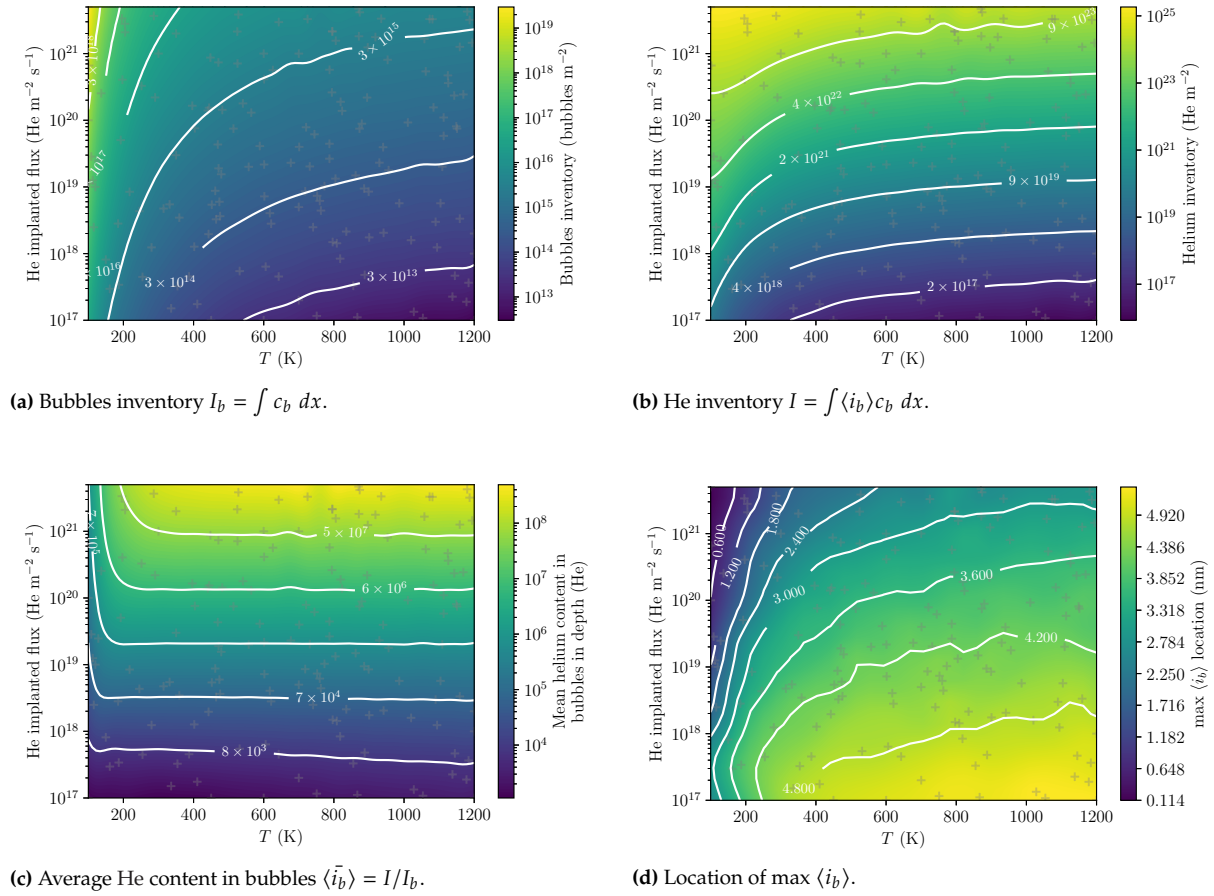


Figure 5.15: Evolution of quantities as a function of the implanted flux and temperature after 1 h of 100 eV He exposure. Grey crosses correspond to simulation points.

The position of the maximum of $\langle i_b \rangle$ tended to increase with temperature and decrease with implanted flux (see Figure 5.15d). After 1 h of exposure, it was found to be really close to the surface down to 0.1 nm at low temperatures and high fluxes. The validity of the model in this region of the parameter space is questionable considering that the bubble radius is greater than the thickness of the ligament between the edge of the bubble and the surface. Such a bubble would therefore have burst before reaching this size.

For each simulation point, the temporal evolution of the quantities described above has been computed. To better identify the time series on the φ_{imp}, T plane, lines have been coloured according to the parameter $c_{\text{He}_1, \text{ideal}}$ which is a function of both the implanted flux and the temperature (see Equation 5.34) expressed in m^{-3} .

$$c_{\text{He}_1, \text{ideal}} = \frac{\varphi_{\text{imp}} R_p}{D(T)} \quad (5.34)$$

where φ_{imp} is the implanted flux, D is the diffusion coefficient of mobile He_1 in W (see Table 5.1), $R_p = 1.5 \text{ nm}$ is the implantation depth and T is the temperature in K.

All these quantities showed a similar behaviour in time even though the kinetics were found to be different (see Figure 5.16). For instance, for each $(T, \varphi_{\text{imp}})$ couple, I_{bubbles} first increased as a power law of time before reaching a maximum (see Figure 5.16a). The total He inventory I increased with time and for each simulation point, but the

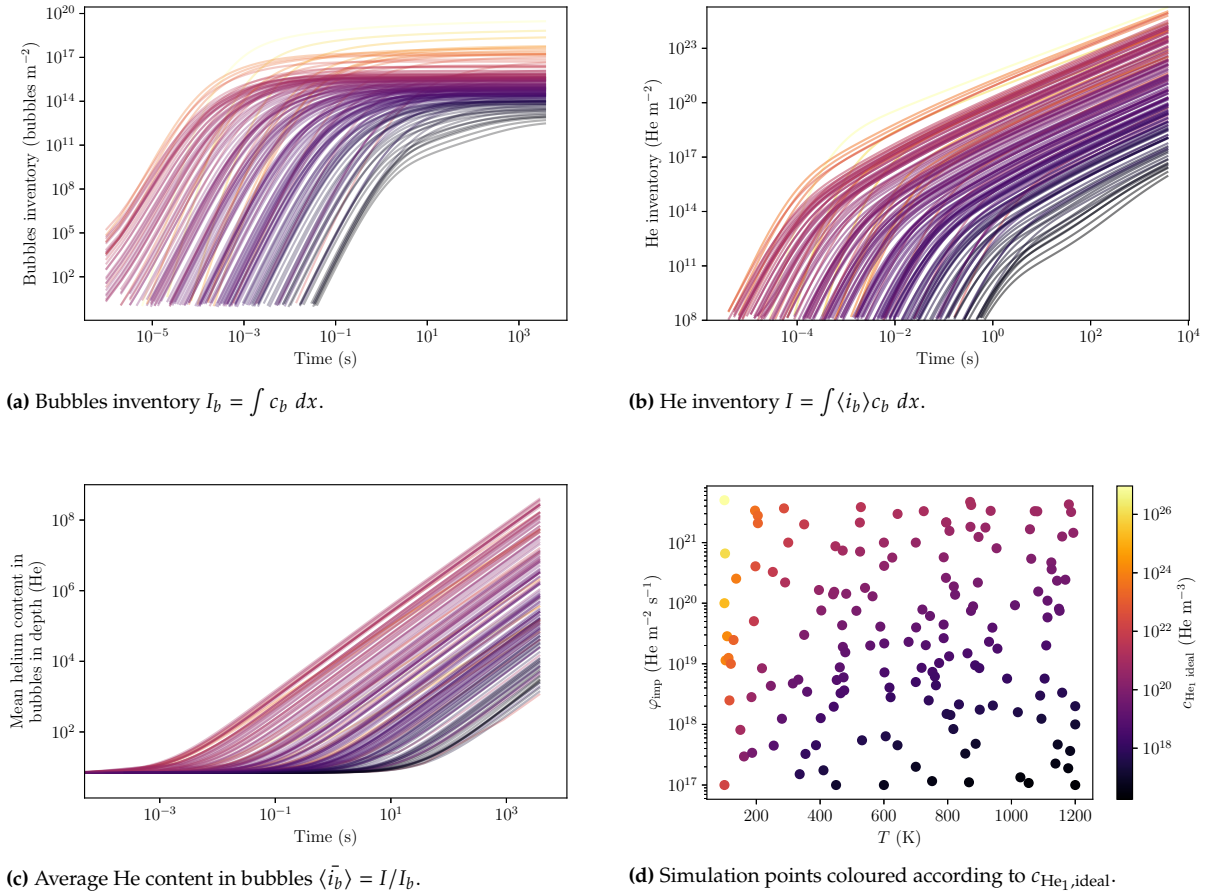


Figure 5.16: Temporal evolution of quantities in W exposed to 100 eV He at $10^{22} \text{ m}^{-2} \text{ s}^{-1}$ and 1000 K for temperatures varying from 120 K to 1200 K and implanted fluxes varying from $10^{17} \text{ m}^{-2} \text{ s}^{-1}$ to $10^{21} \text{ m}^{-2} \text{ s}^{-1}$. Each line corresponds to a simulation point (grey crosses on Figure 5.15a and points on Figure 5.16d). The lines are coloured according to the parameter $c_{\text{He}_1, \text{ideal}} = \varphi_{\text{imp}} R_p / D(T)$ with $R_p = 1.5 \text{ nm}$ and D the diffusion coefficient of He₁ in W.

growth rate decreased at long exposure times (see Figure 5.16b). This phenomenon is explained in details in Section 5.4.2. The depth of the maximum of $\langle i_b \rangle$ tended to decrease with time as it was observed in Section 5.4.1 (see Figure 5.16a).

Inventory evolution regimes

For every $(T, \varphi_{\text{imp}})$ couple, I_{bubbles} increased rapidly at low fluences until reaching a maximum at high fluences (see Figure 5.16a). On the other hand, the mean He content $\langle \bar{i}_b \rangle$ was constant at low fluences and increased at high fluences (see Figure 5.16c). The total He inventory I being the product of these two quantities, two different growth rates were observed (see Figure 5.16b and Figure 5.17).

This phenomenon can be attributed to two different regimes. The first regime is the nucleation regime where new bubbles nucleons are created (i.e. c_b and I_{bubbles} increase). In the nucleation regime, the bubble concentration c_b and the capture radius $\langle r_b \rangle$ are too low for the He content in bubbles $\langle i_b \rangle$ to increase significantly (i.e. $\langle \bar{i}_b \rangle$ is constant). The second regime is the bubble growth regime. In this regime, c_b is high enough for interactions between bubbles and mobile He to occur. Implanted interstitial He atoms (c_{He_1}) therefore interact preferably with bubbles rather than clustering with other interstitial He atoms. This means that no additional bubbles nucleons are created

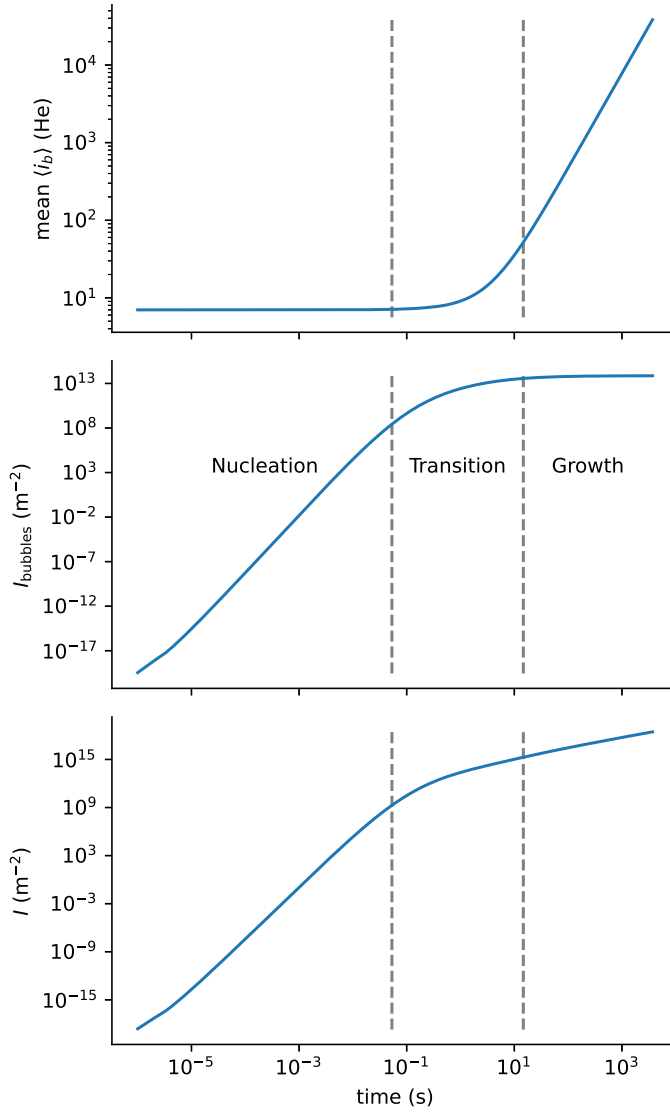


Figure 5.17: Temporal evolution of $\langle \bar{i}_b \rangle$, I_{bubbles} and I in W exposed to 100 eV He at $1.59 \times 10^{18} \text{ m}^{-2} \text{ s}^{-1}$ and 1020 K. The dashed grey vertical line represents the transition from nucleation regime to bubble growth regime.

(i.e. c_b reaches a maximum). Because interactions between bubbles and mobile He are strong, the term $\langle k_b^+ \rangle c_1 c_b$ in Equation 5.18 becomes significant and the He content increases (i.e. $\langle \bar{i}_b \rangle$ increases). This is illustrated by the thickness of the arrows in Figure 5.5.

These regimes can also be worked out analytically.

Nucleation regime When $c_N k_{1,N}^+ \gg \langle k_b^+ \rangle c_b$, Equation 5.27e can be simplified by:

$$\frac{\partial \langle i_b \rangle c_b}{\partial t} \approx (N+1) k_{1,N}^+ c_1 c_N = (N+1) \frac{\partial c_b}{\partial t} \quad (5.35)$$

By extending the temporal derivative, one can obtain:

$$c_b \frac{\partial \langle i_b \rangle}{\partial t} \approx (N+1) \frac{\partial c_b}{\partial t} - \langle i_b \rangle \frac{\partial c_b}{\partial t} \quad (5.36a)$$

$$\frac{\partial \langle i_b \rangle}{\partial t} \approx \frac{\partial c_b (N+1 - \langle i_b \rangle)}{\partial t c_b} \quad (5.36b)$$

Moreover, since $\langle i_b \rangle \approx N+1$, $\frac{\partial \langle i_b \rangle}{\partial t} \approx 0$. The bubble content $\langle i_b \rangle$ is therefore constant.

Growth regime When $c_N k_{1,N}^+ \ll \langle k_b^+ \rangle c_b$, Equation 5.27a can be simplified by:

$$\frac{\partial c_1}{\partial t} \approx \nabla \cdot (D_1 \nabla c_1) + \Gamma - \langle k_b^+ \rangle c_b c_1 \quad (5.37)$$

Moreover, $c_i \approx 0 \forall 2 \leq i \leq N$. This leads to $\frac{\partial c_b}{\partial t} \approx 0$.

Equation 5.27e can therefore be simplified:

$$\frac{\partial \langle i_b \rangle c_b}{\partial t} \approx \langle k_b^+ \rangle c_b c_1 \quad (5.38a)$$

$$c_b \frac{\partial \langle i_b \rangle}{\partial t} \approx \langle k_b^+ \rangle c_b c_1 \quad (5.38b)$$

The temporal evolution of the bubble content $\langle i_b \rangle$ can finally be written as:

$$\frac{\partial \langle i_b \rangle}{\partial t} \approx \langle k_b^+ \rangle c_1 \quad (5.39)$$

[243] Krasheninnikov
et al. (2014)

Dimensionless analysis

Following the adimensionalisation strategy proposed by Krasheninnikov et al. [243], the following dimensionless numbers are defined:

$$\hat{t} = t k_{1,1}^+ c_{\text{He}_1, \text{ideal}} \quad (5.40)$$

$$\hat{x} = \frac{x}{l_1} \quad (5.41)$$

$$\hat{c}_i = \frac{c_i}{c_{\text{He}_1, \text{ideal}}} \quad (5.42)$$

where l_1 is the characteristic length of the $\text{He}_1 + \text{He}_1 \rightarrow \text{He}_2$ reaction in m.

The dimensionless bubble inventory \hat{I}_{bubbles} can be computed as:

$$\hat{I}_{\text{bubbles}} = \int \hat{c}_b d\hat{x} \quad (5.43a)$$

$$= \frac{\int c_b dx}{c_{\text{He}_1, \text{ideal}} l_1} \quad (5.43b)$$

$$= \frac{I_{\text{bubbles}}}{c_{\text{He}_1, \text{ideal}} l_1} \quad (5.43c)$$

Similarly, the dimensionless helium inventory in bubbles \hat{I} can be expressed as:

$$\hat{I} = \frac{I}{c_{\text{He}_1, \text{ideal}} l_1} \quad (5.44)$$

By normalising the results obtained in Section 5.4.2, all simulation points seem to follow the same trend (see Figure 5.18). There are however some discrepancies, which are numerical artifacts.

The evolution of the dimensionless quantities can be fitted to obtain a law. The temporal evolution of $\langle \bar{i}_b \rangle$ is:

$$\langle \bar{i}_b \rangle = \frac{(N + 1)}{1 - e^{-\frac{100}{\hat{t}^{1.12}}}} \quad (5.45)$$

The temporal evolution of the bubble inventory \hat{I}_{bubbles} can be expressed as:

$$\hat{I}_{\text{bubbles}} = 10 \left(1 - e^{-\frac{\hat{t}}{10}}\right)^{6.5} \quad (5.46)$$

The limit of \hat{I}_{bubbles} when \hat{t} approaches infinity is 10.

The temporal evolution of the inventory \hat{I} is given by:

$$\hat{I} = \hat{I}_{\text{bubbles}} \langle \bar{i}_b \rangle \quad (5.47)$$

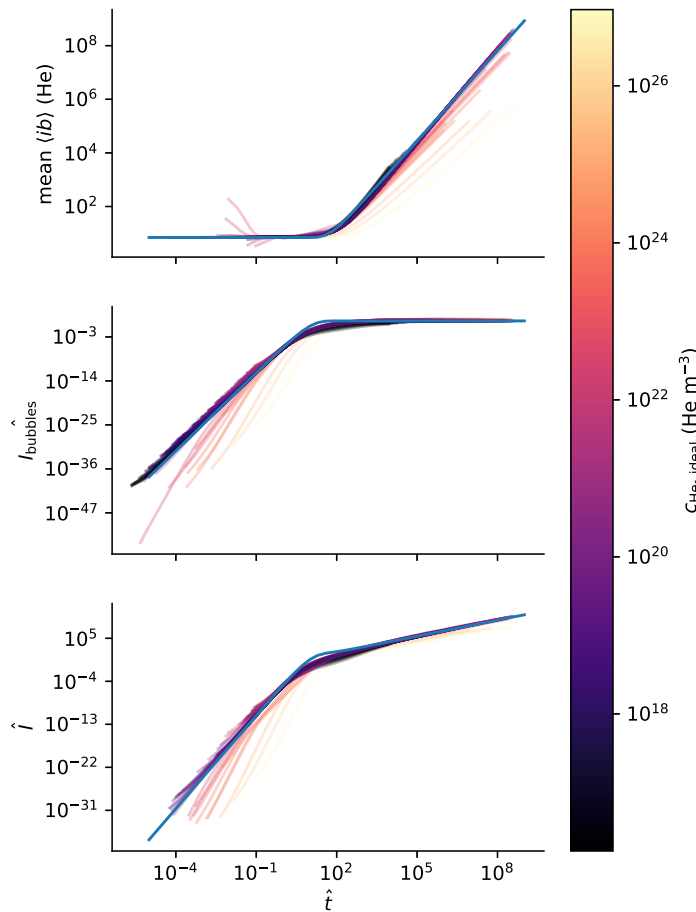


Figure 5.18: Evolution of $\langle \bar{i}_b \rangle$, \hat{I}_{bubbles} and \hat{I} as a function of \hat{t} for several $c_{\text{He}_1, \text{ideal}}$ values. The blue curves correspond to the fitted evolutions.

[243] Krasheninnikov et al. (2014)

These results are in accordance with the analytical analysis performed by Krasheninnikov et al. [243], where the authors predicted two different regimes whether $\hat{t} \ll 1$ or $\hat{t} \gg 1$. This is exactly what can be observed on Figure 5.18.

5.5 Influence on hydrogen transport

[97] Ialovega et al. (2020)

The focus of this Section is the coupled effects of He implantation and hydrogen transport. To this end, the experiment of Ialovega and co-workers [97] is reproduced with the He bubble model described in this Chapter coupled to FESTIM by converting a bubble density into trapping sites for hydrogen.

5.5.1 Experiment

A 100 μm thick tungsten sample was pre-damaged with 75 eV He at 1073 K. The He flux was $2.3 \times 10^{22} \text{ m}^{-2} \text{ s}^{-1}$ and the exposure time was 13 s. An initial cleaning TDS was performed up to 870 K.

Sequential deuterium loading and TDS were then repeated five times. 250 eV deuterium were implanted at room temperature with a flux of $1.7 \times 10^{16} \text{ m}^{-2} \text{ s}^{-1}$ and a fluence of $4.5 \times 10^{19} \text{ m}^{-2}$. The TDS phase ramps up to 1350 K (1250 K for the first TDS) at a rate of 1 K s^{-1} (see Figure 5.20).

The authors observed that the deuterium inventory after the first TDS was lower than after the following implantation/TDS cycles. They associated this increase to a modification of the near-surface microstructure. They also link the modification of the deuterium retention entirely with the variation of He bubbles density. Little mention was made of the influence of pre-existing defects and the pristine W (not exposed to He) TDS spectrum was only qualitatively comparable (authors communication).

5.5.2 Bubble growth simulation

The quantities c_b and $\langle r_b \rangle$ have been computed from the helium bubble model described in Section 5.2 (see Figure 5.19). The helium implantation distribution is a Gaussian with a mean value of 1.5 nm and a standard deviation of 0.8 nm corresponding to a 75 eV He exposure calculated with SRIM. The other parameters are unchanged.

5.5.3 FESTIM simulations

Four traps are simulated with FESTIM: traps 1-3 are pre-existing defects and trap 4 represents the traps induced by He bubbles. The detrapping energies and trap densities are set as free parameters, including the trap density n_b (see Table 5.2).

Considering deuterium is trapped on the surface of He bubbles, the bubble trap density n_b is given by:

$$n_b = f \cdot c_b \cdot \mathcal{A}(\langle r_b \rangle) \quad (5.48)$$

where f is a free parameter representing the number of trapping site per unit surface, $\mathcal{A} = 4\pi\langle r_b \rangle^2$ is the area in m^2 of a spherical bubble of radius $\langle r_b \rangle$, and c_b is the concentration of bubbles in m^{-3} .

[93] Frauenfelder (1969)

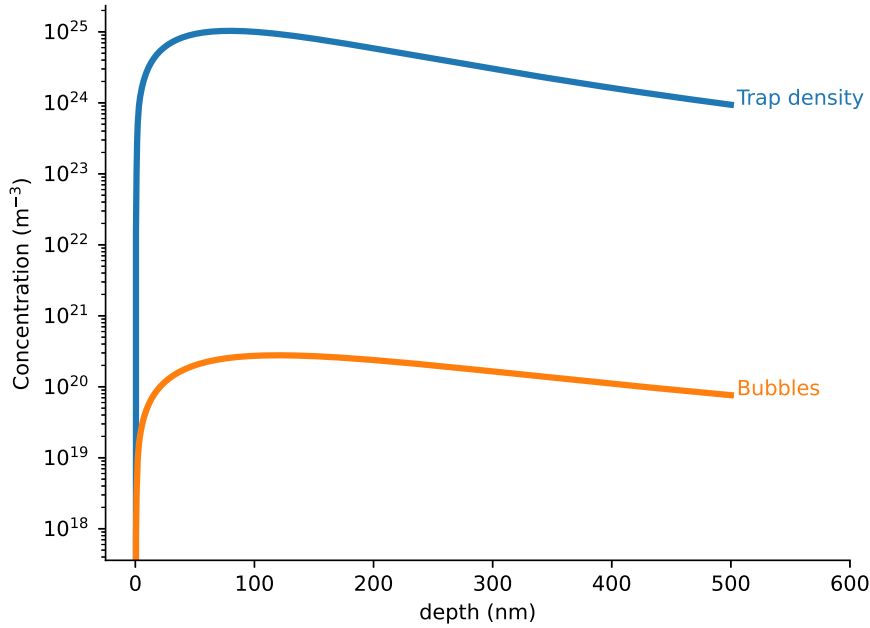


Figure 5.19: Spatial distribution of the bubbles density and the equivalent trap density (assuming $f = 3 \times 10^{18} \text{ m}^{-2}$).

	k_0 [$\text{m}^3 \text{ s}^{-1}$]	E_k [eV]	p_0 [s^{-1}]	E_p [eV]	n [m^{-3}]
Trap 1				free	free
Trap 2	9×10^{-17}	0.39	10^{13}	free	free
Trap 3				free	free
Trap bubbles				free	n_b

Table 5.2: Trap properties used to fit the TDS spectra. The density distribution n_b as well as detrapping energies E_p are assumed constant across TDS experiments.

The diffusion coefficient of deuterium ($\text{m}^2 \text{ s}^{-1}$) was set to $4.1 \times 10^{-7} \exp(-0.39/k_B T)$ [93]. The 250 eV deuterium implantation was represented by a Gaussian distribution with a mean implantation depth 10 nm and a standard deviation of 4.5 nm (calculated from SRIM [173]). Finally, an instantaneous recombination was assumed on the surfaces.

[173] Ziegler et al. (2010)

Using the parametric optimisation method presented in Section 2.5.2, the free parameters are identified.

5.5.4 Results

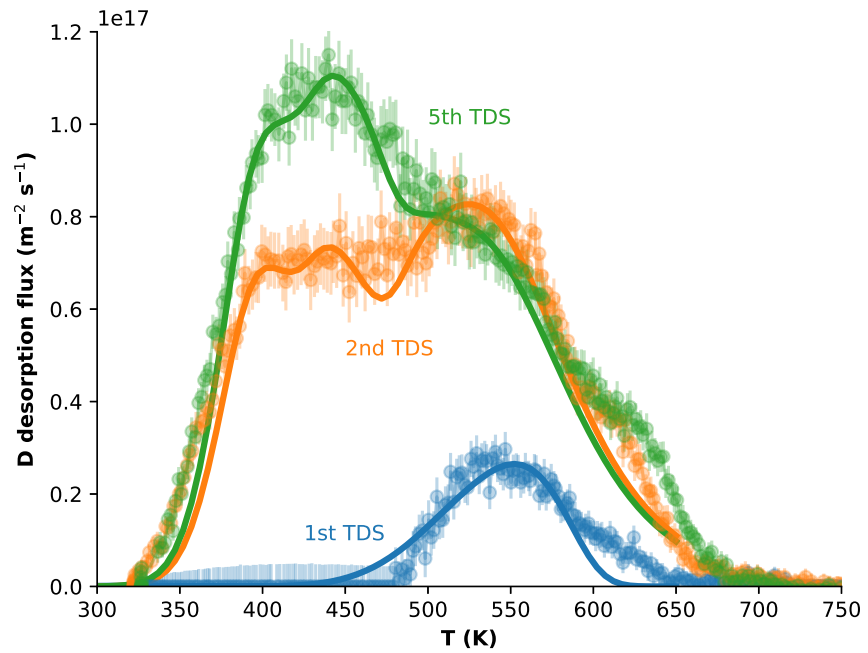
The properties obtained by the fitting procedure (see Table 5.3) fitted well the three TDS spectra (see Figure 5.20). As explained in [97], the last bump of desorption (around 600 K) is due to a temperature control issue and was therefore ignored in the fitting procedure. The detrapping energies of traps 1, 2 and 3 were found to be 1.08 eV, 1.20 eV and 1.38 eV respectively, whereas the trap attributed to He bubbles has a detrapping energy of 1.45 eV.

This would mean that if the TDS were run up to temperature around 1600 K, He_1V_1 clusters could dissociate resulting in additional free trapping sites for H and therefore different TDS spectra.

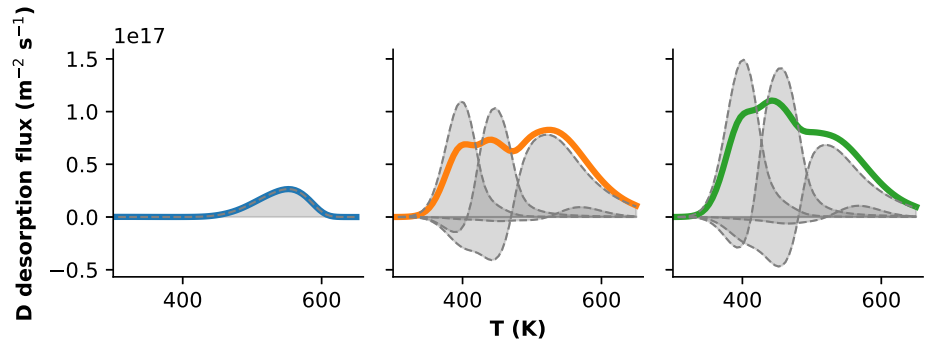
Table 5.3: Results of the fitting procedure. De-trapping energies E_p are given in eV, trap densities in at fr and f in m^{-2} .

	Trap 1		Trap 2		Trap 3		Trap bubbles	
	E_p	$n (\times 10^{-3})$	E_p	$n (\times 10^{-3})$	E_p	$n (\times 10^{-3})$	E_p	$f (\times 10^{18})$
1st TDS	-	0.00	-	0.00	-	0.00	1.42	3.00
2nd TDS	1.08	2.20	1.20	1.80	1.37	2.00	1.42	3.00
5th TDS	1.08	3.38	1.20	3.10	1.37	1.50	1.42	3.00

The H retention is not dominated by He-bubbles trapping but rather by pre-existing defects.



(a) Experimental TDS spectra fitted with FESTIM. Experimental points are taken from [97].



(b) Traps contribution to the TDS spectra.

Figure 5.20: Results of the TDS fitting procedure.

The densities of traps 1 and 2 increased from the 2nd to the 5th TDS (see Figure 5.21). However, the density of trap 3 decreased slightly (which is also visible on the TDS spectra shown in Figure 5.20). The processes at stake cannot yet be precisely described.

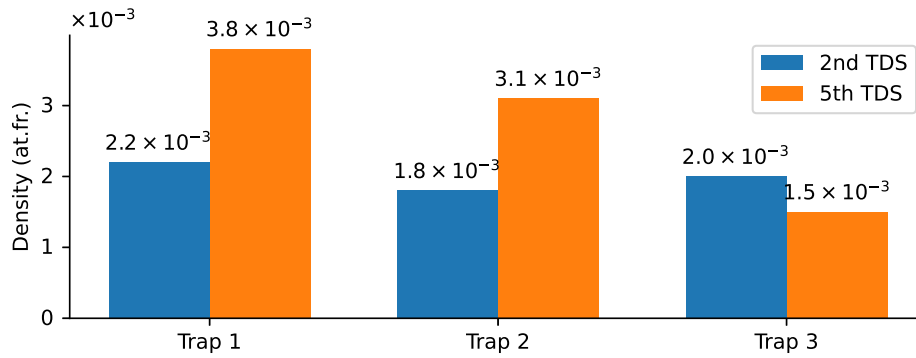


Figure 5.21: Evolution of the trap densities between the second and fifth TDS.

One possible interpretation of the results is:

- ▶ Initial state: the sample has some pre-existing defects
- ▶ He implantation: all pre-existing defects are saturated with He and bubbles are formed
- ▶ 1st D implantation: D can only be trapped around bubbles since defects are saturated with He
- ▶ 1st TDS (up to 1250 K): D is detrapped from bubbles (550 K peak), He dissociates from pre-existing defects
- ▶ 2nd D implantation: D is trapped around bubbles and in the non-saturated defects
- ▶ 2nd TDS (up to 1350 K): D is detrapped from bubbles (550 K peak) and from non-saturated defects (peaks 400K, 450K and 500K) + He trapped in deeper traps dissociate (because the TDS goes to higher temperatures)
- ▶ 3rd to 5th D implantations: D is trapped around bubbles and in pre-existing defects
- ▶ 3rd to 5th TDS: D is detrapped from bubbles and pre-existing defects (now more available than at the 2nd TDS)

This interpretation is represented (in a simplified way) on Figure 5.22.

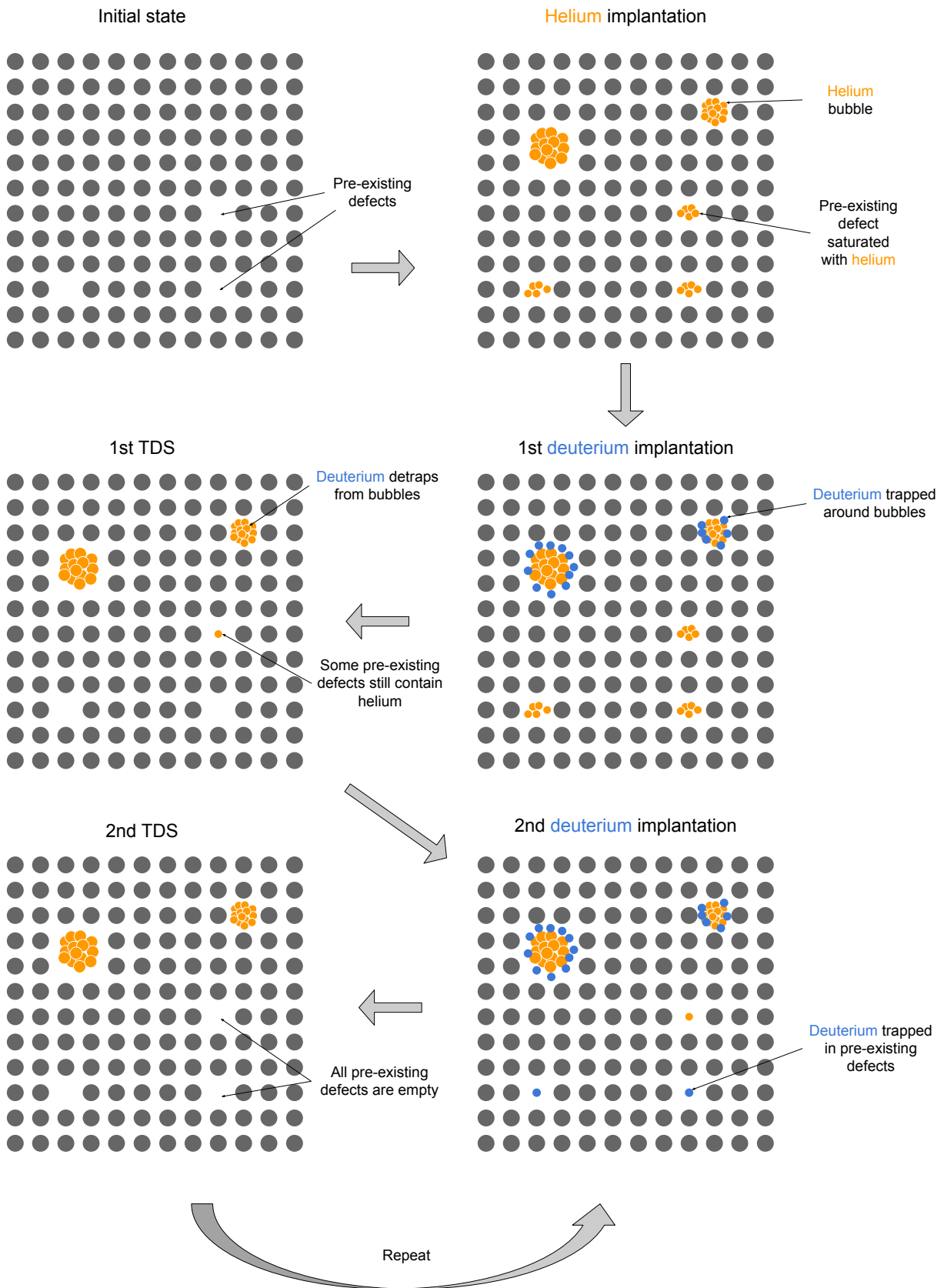


Figure 5.22: Schematic interpretation of the simulation results showing the several stages of the experiment (from He implantation to TDS cycles).

5.6 Summary

This Chapter investigated the influence of helium on hydrogen transport.

To do so, a cluster dynamics model was first developed to simulate the growth of helium bubbles in tungsten. This model was compared to existing numerical results and helium exposure experiments were reproduced. A parametric study was performed to investigate the impact of helium flux and temperature on the bubbles density and size. Finally, a dimensionless analysis was carried out to extract key parameters and identify two different bubble growth regimes.

Based on the results of the bubble growth model, the experiment of Ialovega and co-workers [97] was then reproduced with FESTIM and one possible explanation was given. Although fitting a TDS spectrum is not sufficient to draw strong conclusions, this work suggests that:

[97] Ialovega et al. (2020)

- ▶ Helium does not leave bubbles in significant quantities at these temperatures
- ▶ Helium occupies pre-existing defects avoiding hydrogen to get trapped
- ▶ Hydrogen retention is not dominated by helium-induced bubbles but rather by the saturation of pre-existing defects by helium

From these results, several experimental suggestions can be made. Running the TDS only up to 750 K would limit helium desorption from defects. Indeed, the authors [97] showed that there was no helium desorption below this temperature after the initial cleaning TDS. If helium does not desorb and remains in the pre-existing defects, the deuterium TDS spectra should not be affected and only the desorption from bubbles should be observed. This would confirm or infirm the interpretation of the results presented herein.

Moreover, if this interpretation was confirmed, it could have implications for hydrogen retention. Indeed, one could imagine reducing the tritium inventory of components by exposing them to helium first. Helium would saturate the existing defects, making it impossible for tritium to be trapped. However, having a helium inventory in components can also have negative consequences (see Section 1.4.2).

6 Conclusion

This Chapter will summarise the key findings of this research as well as the main contributions thereof. It will also review the limitations of the study and propose recommendations for future work.

Key findings

This study aimed to estimate the tritium inventory in the ITER tungsten divertor. One of the objectives was to evaluate the potential influence of helium exposure on this tritium inventory. The results indicate that, over the operation period of ITER, the divertor tritium inventory should remain well below the safety limit. Indeed, this component would not be the limiting factor and, if the limit is hit, it would likely be due to other causes (retention in co-deposited layers, other in-vessel components...). Moreover, the results suggest that the presence of helium could potentially reduce the tritium inventory by saturating the pre-existing defects in tungsten.

Contributions to the field

One of the main contribution of this research is the development of the FESTIM code: a hydrogen transport code that has been developed to answer the main questions of the study. The first article introducing FESTIM was published during the master project preceding this PhD research [178]. At the time of writing, FESTIM is used by a handful of researchers, engineers and students and applied on other cases. FESTIM was recently open-sourced and will hopefully greatly benefit the broader community.

The parametric optimisation method used in Chapter 2 now provides an efficient way of automatically fitting experimental data without manually tweaking parameters, saving precious time in the process. This method was published in a proceedings article [245].

The initial monoblock results shown in Chapter 3 were published in several articles [178, 245, 246]. The method of running parametric subcomponent simulations and then extract a behaviour law was nothing new. However, applying it to the estimation of the divertor inventory saved a significant amount of time compared to using the “brute force” approach of modelling the whole divertor at a time. This method was

published in 2020 [244] and can now be applied to other components like the breeding blanket, where the tritium inventory is also an issue.

The model developed to simulate the growth of helium bubbles in tungsten gives a rapid way of implementing and testing new physical models. This work was published in 2021 [247].

Finally, during this PhD research, several contributions were made to the open-source Paramak code and related neutronics tools [230].

Limitations

This study has physical limitations inherent to the assumptions that have been made. While some of these assumptions are conservative (i.e. represent a worst-case scenario) and do not jeopardise the key findings, others were made as a response to uncertainties. For instance, no desorption was assumed on the monoblocks gaps. The value of the recombination coefficient at the interface between the coolant and the monoblock also has a high uncertainty as it was measured in vacuum.

Many of the technical limitations of this research lie with the development issues of FESTIM. Since the code was built from scratch, features were added gradually. For instance, at the time the simulations in Section 3.3 were run, the surface concentration could not be inhomogeneous *and* directly dependent on the inhomogeneous surface temperature due to the heat flux. Therefore, the choice that was made was to impose a homogeneous surface temperature instead (and a homogeneous surface concentration). Even though the required feature was added a few months later, re-running all the FESTIM simulations was too much time-consuming given the time constraints.

Recommendations for future work

A more accurate behaviour law for the monoblock inventory can be obtained by redoing the parametric study. Instead of varying the surface concentration and temperature, one should vary the incident heat flux φ_{heat} as well as the product of the implantation range and implanted particle flux $\varphi_{\text{imp}} R_p$. Assuming the uncertainty regarding the recombination coefficient of tungsten is lifted, and recombination on gaps cannot be neglected, 3D simulations could also be run for the most exposed monoblocks. Hydrogen recombination from CuCrZr in contact with water should also be studied for this can reduce even more the tritium inventory while increasing the permeation flux to the coolant. Moreover, it would be extremely important to try and validate these results experimentally on a monoblock to scale. Monoblocks could for instance be exposed to hydrogen and then their hydrogen content could be measured from thermo-desorption techniques. These results could then be compared to FESTIM simulations.

To estimate the tritium inventory in the ITER vacuum vessel, studies should now focus on other components like the ITER first wall, the tritium breeding system, etc.

Regarding the influence of helium on hydrogen transport, future work could involve experimental studies investigating the simultaneous exposure of hydrogen and helium in tungsten to confirm, or infirm the suggested results of this research. For example, re-running the experiments presented in Section 5.5.1 but running the TDS only up to 750 K could help deconvolute the phenomena at stake. If the results interpretations made in Chapter 5 were to be confirmed, running this experiment with different

helium fluences/fluxes would produce different bubble densities/size distribution and could help identifying a more general expression for the trap density per unit surface around bubbles.

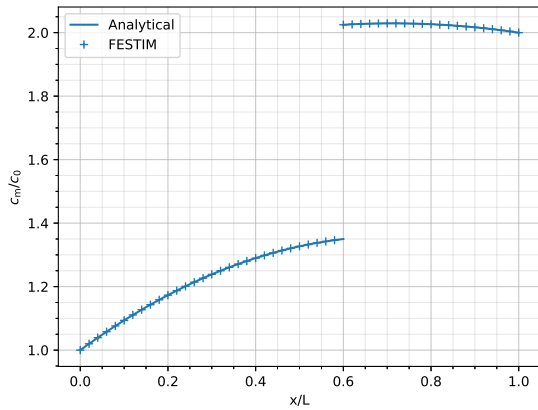
APPENDIX

A

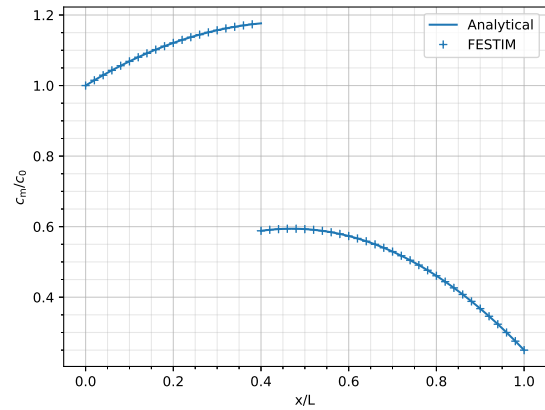
FESTIM verification

A.1 Conservation of chemical potential (MES)

This verification case aims at checking the FESTIM code is correctly solving the governing Equation 1.34, Equation 2.2 and Equation 2.19.



(a) Case 1: $\alpha = 2$, $\beta = 1.5$, $\gamma = 0.6$, $\tilde{c}_L = 2$, $\tilde{f} = 1$.



(b) Case 2: $\alpha = 1.5$, $\beta = 0.5$, $\gamma = 0.4$, $\tilde{c}_L = 0.25$, $\tilde{f} = 2$.

Figure A.1: Concentration profiles simulated by FESTIM against analytical solutions.

The uni-dimensional test case considered in this Section was made of two subdomains Ω_1 and Ω_2 and is described as follows:

$$\Omega = [0, L] = \Omega_1 \cup \Omega_2 \quad (\text{A.1a})$$

$$\Omega_1 = [0, x_{\text{int}}] \quad (\text{A.1b})$$

$$\Omega_2 = [x_{\text{int}}, L] \quad (\text{A.1c})$$

$$D = \begin{cases} D_1, & \text{in } \Omega_1 \\ D_2, & \text{in } \Omega_2 \end{cases} \quad (\text{A.1d})$$

$$S = \begin{cases} S_1, & \text{in } \Omega_1 \\ S_2, & \text{in } \Omega_2 \end{cases} \quad (\text{A.1e})$$

The following dimensionless quantities are introduced:

$$\tilde{c}_m = c_m/c_0 \quad (\text{A.2a})$$

$$\tilde{x} = x/L \quad (\text{A.2b})$$

$$\tilde{f} = f \frac{L^2}{D_{\text{eq}}c_0} \quad (\text{A.2c})$$

$$\alpha = D_2/D_1 \quad (\text{A.2d})$$

$$\beta = S_2/S_1 \quad (\text{A.2e})$$

$$\gamma = x_{\text{int}}/L \quad (\text{A.2f})$$

$$(\text{A.2g})$$

where $D_{\text{eq}} = (D_1D_2)^{1/2}$.

By integrating Equation 2.2 and assuming steady-state (i.e. $\partial c/\partial t = 0$), one can obtain the following dimensionless form:

$$\tilde{c}_m = \begin{cases} -\frac{1}{2}\alpha^{1/2}\tilde{f}\tilde{x}^2 + a_1\tilde{x} + b_1, & \text{in } \Omega_1 \\ -\frac{1}{2}\alpha^{-1/2}\tilde{f}\tilde{x}^2 + a_2\tilde{x} + b_2, & \text{in } \Omega_2 \end{cases} \quad (\text{A.3})$$

where a_1, b_1, a_2, b_2 are the unknowns of the problem to be determined. The boundary conditions and the equilibrium law at the interface are defined as:

$$\tilde{c}_m(\tilde{x} = 0) = 1 \quad (\text{A.4a})$$

$$\tilde{c}_m(\tilde{x} = 1) = \tilde{c}_L \quad (\text{A.4b})$$

$$\tilde{c}_m^-(\tilde{x} = \gamma) = \beta \tilde{c}_m^+(\tilde{x} = \gamma) \quad (\text{A.4c})$$

$$\nabla \tilde{c}_m^-(\tilde{x} = \gamma) = \alpha \nabla \tilde{c}_m^+(\tilde{x} = \gamma) \quad (\text{A.4d})$$

Equation A.3 can be solved with these constraints and coefficients describing \tilde{c}_m therefore read:

$$\begin{aligned} a_1 &= a_0 \alpha^{1/2} \\ b_1 &= 1 \\ a_2 &= a_0 \alpha^{-1/2} \\ b_2 &= \tilde{c}_L + \frac{1}{2}\alpha^{-1/2}\tilde{f} - a_2 \\ a_0 &= \frac{2\alpha^{1/2}(\tilde{c}_L - \beta) + \tilde{f}(\gamma^2(\alpha\beta - 1) + 1)}{1 - \gamma + \alpha\beta\gamma} \end{aligned} \quad (\text{A.5})$$

It is worth noting that when $\beta = 1$ (i.e. $S_1 = S_2 = S$) the solution becomes independent of S and $c_m^-(x_{\text{int}}) = c_m^+(x_{\text{int}})$. Moreover, when $\alpha = 1$ (i.e. $D_1 = D_2 = D$), then $a_1 = a_2 = a_0$ which is the solution for steady-state diffusion in a mono-material.

The solution computed by FESTIM was found to be in very good agreement with the analytical solution for several test cases (see Figure A.1).

However, this method does not exercise all the terms in the governing Equation 2.19. For instance, this analytical solution is only uni-dimensional, steady state is assumed and material properties are constant within the materials. Having an exact solution from an analytical resolution for a general problem (multidimensional, transient, heterogeneous material properties, etc...) is often complex. In order to exercise all these

terms, the Method of Manufactured Solutions (MMS) will therefore be employed for it offers a good alternative to unravel these complexities.

A.2 Conservation of chemical potential (MMS)

This verification case aims at checking the FESTIM code is correctly solving the governing Equation 1.34, Equation 2.2 and Equation 2.19.

The domain Ω for this test problem is a unit square composed of two subdomains Ω_1 and Ω_2 (see Equation A.6).

$$\Omega = [0, 1] \times [0, 1] \quad (\text{A.6a})$$

$$\Omega_1 = [0, x_{\text{int}}] \times [0, 1] \quad (\text{A.6b})$$

$$\Omega_2 = [x_{\text{int}}, 1] \times [0, 1] \quad (\text{A.6c})$$

$$(\text{A.6d})$$

In order to unravel the complexity of an analytical resolution of the direct problem, a manufactured solution c_m was constructed (see Equation A.7) and the problem was solved backwards.

$$c_M = \begin{cases} c_{M1}, & \text{on } \Omega_1 \\ \frac{S_2}{S_1} \cdot c_{M1}, & \text{on } \Omega_2 \end{cases} \quad (\text{A.7})$$

where $c_{M1} = 2 + \cos(2\pi x) \cdot \cos(2\pi y) + t$

It is worth noting that, when choosing a manufactured solution, one must ensure it satisfies all the governing equations (especially Equation 1.34). In our case, c_M ensures the flux conservation at the interface and the continuity of the quantity c_m/S .

Properties are assumed time and space dependent in order to test every portion of the code (see Equation A.8).

$$D_1(x, y, t) = D_{10} \exp(-E_{D1}/(k_B \cdot T(x, y, t))) \quad (\text{A.8a})$$

$$D_2(x, y, t) = D_{20} \exp(-E_{D2}/(k_B \cdot T(x, y, t))) \quad (\text{A.8b})$$

$$S_1(x, y, t) = S_{10} \exp(-E_{S1}/(k_B \cdot T(x, y, t))) \quad (\text{A.8c})$$

$$S_2(x, y, t) = S_{20} \exp(-E_{S2}/(k_B \cdot T(x, y, t))) \quad (\text{A.8d})$$

$$T(x, y, t) = 500 + 30 \cos(2\pi x) \cos(2\pi y) \cos(2\pi t) \quad (\text{A.8e})$$

with $k_B = 8.617 \times 10^{-5} \text{ eV K}^{-1}$ the Boltzmann constant, $D_{10} = 1$, $E_{D1} = 0.1$, $D_{20} = 2$, $E_{D2} = 0.2$, $S_{10} = 1$, $E_{S1} = 0.1$, $S_{20} = 2$ and $E_{S2} = 0.2$. The temperature T varies around 500 K so that, given the activation energies, properties do not approach zero.

By injecting the manufactured solution c_M into the governing Equation 2.2, the source term can be expressed as:

$$\begin{aligned} f(x, y, t) &= \frac{\partial c_M}{\partial t} - \vec{\nabla} \cdot (D(x, y) \vec{\nabla} c_M) \\ &= \begin{cases} \frac{\partial c_{M1}}{\partial t} - \vec{\nabla} \cdot (D_1(x, y) \vec{\nabla} c_{M1}), & \text{on } \Omega_1 \\ \frac{\partial c_{M2}}{\partial t} - \vec{\nabla} \cdot (D_2(x, y) \vec{\nabla} c_{M2}), & \text{on } \Omega_2 \end{cases} \end{aligned} \quad (\text{A.9})$$

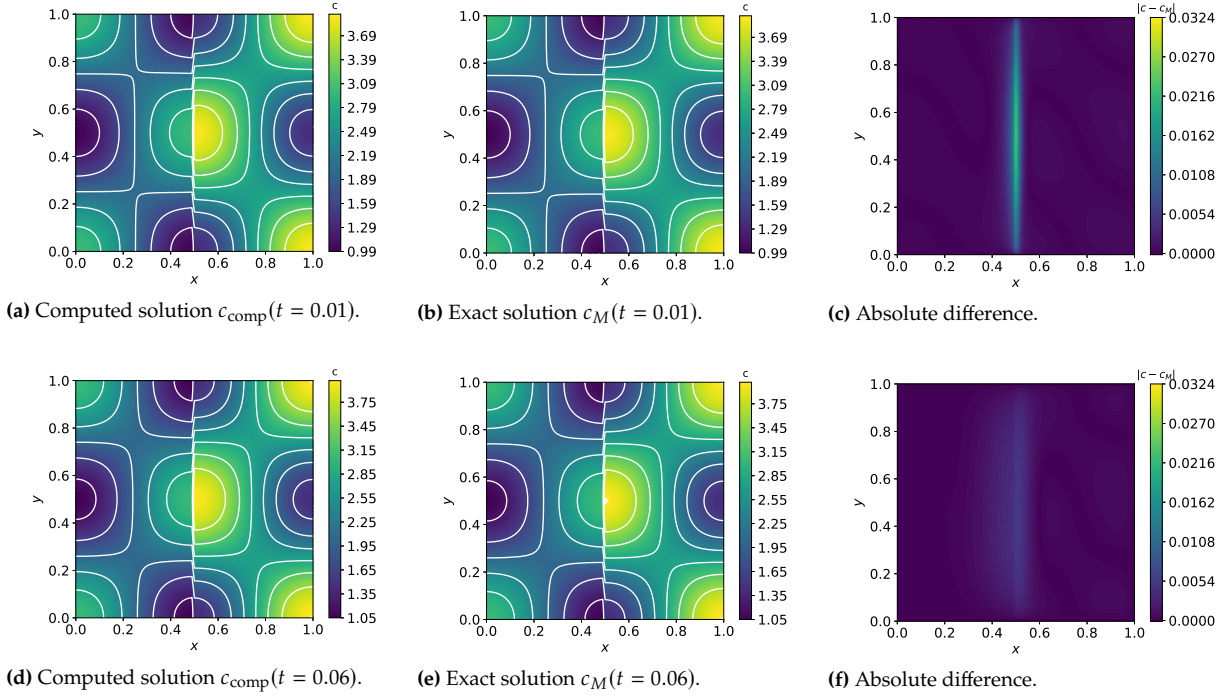


Figure A.2: Comparison of concentration fields simulated by FESTIM with manufactured solutions.

The source term f was then fed into FESTIM alongside with the initial and boundary conditions described below:

$$c_m(x, y, t) = c_M(x, y, t), \text{ on } \partial\Omega \quad (\text{A.10a})$$

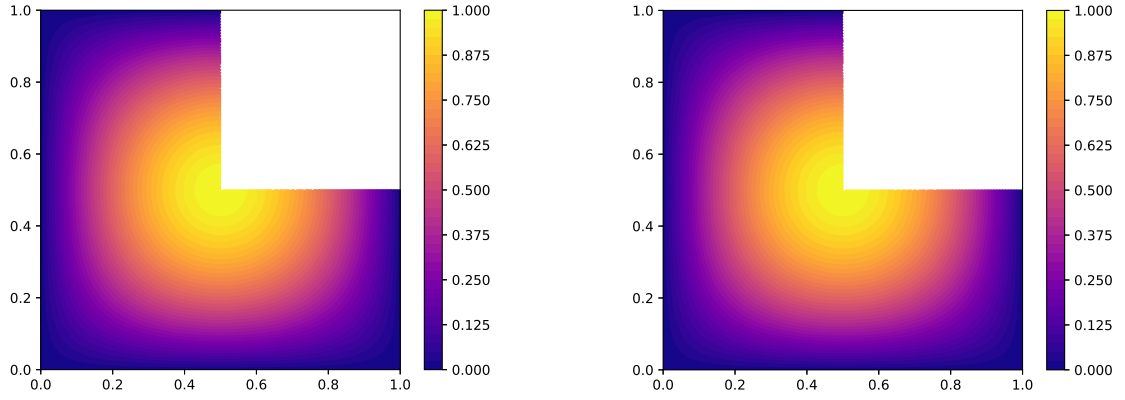
$$c_m(x, y, t = 0) = c_M(x, y, t = 0), \text{ on } \Omega \quad (\text{A.10b})$$

The computed solution c_{comp} can then be compared with the manufactured solution c_M in order to quantitatively measure the numerical error. After running the MMS process, the computed solution and the manufactured solution were in very good agreement at several arbitrarily chosen times of simulation (see Figure A.2). The absolute difference between the manufactured solution and the computed one was found to be zero on the boundary and maximum at the interface between the two materials. This is explained by the Dirichlet boundary conditions enforcing the computed solution on the boundary. This difference decreases by increasing the mesh refinement and decreasing the stepsize. Nonetheless, the error was found to remain orders of magnitude lower than the actual solution.

A.3 Heat transfer (MMS)

The heat transfer module in FESTIM can also be verified using the method of manufactured solutions.

Let us select the following test problem on an elbow domain $\Omega = [0, 1] \times [0, 0.5] \cup [0, 0.5] \times [0.5, 1]$ with the manufactured solution $T_D(x, y) = \sin(\omega\pi x) \sin(\omega\pi y)$.

(a) Computed temperature $N = 64$.

(b) Exact temperature.

Figure A.3: Verification of the heat transfer module in FESTIM.

$$\nabla \cdot \lambda \nabla T = -f \quad (\text{A.11})$$

$$T = T_D \text{ on } y \in [0, 1] \quad (\text{A.12})$$

$$-\lambda \nabla T \cdot \mathbf{n} = -\lambda \nabla T_D \cdot \mathbf{n} \text{ on other surfaces} \quad (\text{A.13})$$

$$\lambda(x, y) = 2 + T_D^2 \quad (\text{A.14})$$

$$(\text{A.15})$$

The source term f is therefore:

$$f = 2\pi^2 \omega^2 f_0 \sin(\pi \omega x) \sin(\pi \omega y) \quad (\text{A.16})$$

$$f_0 = (3f_1 f_2 - f_1 - f_2 + 2) \quad (\text{A.17})$$

$$f_1 = \sin^2(\pi \omega x) \quad (\text{A.18})$$

$$f_2 = \sin^2(\pi \omega y) \quad (\text{A.19})$$

$$(\text{A.20})$$

The computed FESTIM solution is extremely similar to the exact solution (see Figure A.3). It is also possible to compute the L2-error for several number of cell divisions in the x and y directions N to ensure the error decreases as a power law of N . Moreover, the L2-error should be proportional to h^{d+1} where $h = 1/N$ and d is the polynomial degree of the elements [248]. This was verified for P1 and P3 elements and a super-convergence rate was observed for the P2 elements (see Figure A.4).

[248] Vu-Huu et al. (2021)

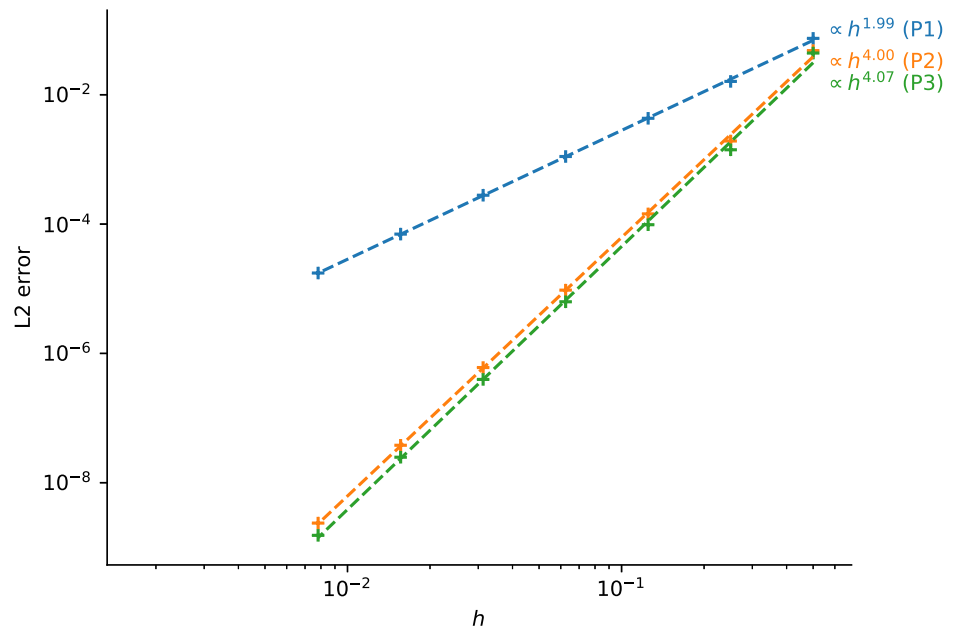


Figure A.4: Evolution of the L2 error on T showing the convergence rates for the 2D heat transfer case.

B

Interface transient model

A kinetic model of trapping/detrapping at the interface between two materials based on the idealised energy diagram shown in Figure B.1 is presented. On this diagram, $E_{\text{diff},k}$ is the barrier for the diffusion of H from interstitial site to interstitial site, $E_{k \rightarrow i}$ is the trapping energy from material k to the interface, $E_{i \rightarrow k}$ is the detrapping energy from the interface to the interface and $E_{S,k}$ is the solution energy of H in material k . In this model, H is split into three populations: the concentrations of mobile H in materials 1 & 2 (c_1 and c_2 respectively) expressed in m^{-3} and the concentration of H trapped at the interface c_i (in m^{-2}). The interface coverage is defined as: $\theta_i = \frac{c_i}{n_i}$ where

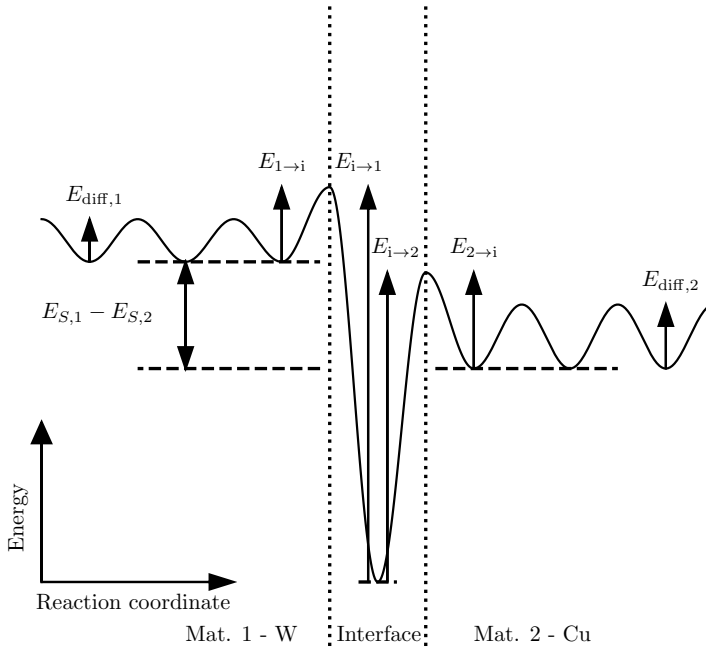


Figure B.1: Idealised potential energy diagram describing the interactions of H at the interface between two materials. In this case, $E_{S,1} > E_{S,2}$ (consistent with a W/Cu interface Table 3.1).

n_i is the sites' concentration on the interface (in m^{-2}). The interface is considered as a 2D defect (like a surface), hence the unit of c_i and n_i is m^{-2} . In this model, 2 types of reactions are considered at the interface:

- ▶ the trapping from material k to the interface: $\text{H}_k \rightarrow \text{H}_i$.
- ▶ the detrapping from the interface to material k : $\text{H}_i \rightarrow \text{H}_k$.

The rate (s^{-1}) of each reaction $x \rightarrow y$ is written with an Arrhenius law:

$$v_{x \rightarrow y}(T) = v_0^{x \rightarrow y} \exp\left(-\frac{E_{x \rightarrow y}}{k_B T}\right) \quad (\text{B.1})$$

with $v_0^{x \rightarrow y}$ (s^{-1}) the pre-exponential factor, $E_{x \rightarrow y}$ (eV) the energy barrier for the reaction $x \rightarrow y$, k_B ($eV K^{-1}$) the Boltzmann constant and T (K) the temperature.

The jump from interstitial site to interstitial site in material k is assumed to be described by the Fick's law on diffusion characterised by the diffusion coefficient of H in material k $D_{k \in \{1,2\}}$ ($m^2 s^{-1}$). Thus, the flux balance at the interface gives:

$$\lambda_1 \left(\frac{\partial c_1}{\partial t} \right)_{x_i} = v_{i \rightarrow 1} c_i - \lambda_1 c_1 (1 - \theta_i) v_{1 \rightarrow i} - D_1 \left(\frac{\partial c_1}{\partial x} \right)_{x_i} \quad (B.2)$$

$$\frac{dc_i}{dt} = \lambda_1 c_1 (1 - \theta_i) v_{1 \rightarrow i} - v_{i \rightarrow 1} c_i + \lambda_2 c_2 (1 - \theta_i) v_{2 \rightarrow i} - v_{i \rightarrow 2} c_i \quad (B.3)$$

$$\lambda_2 \left(\frac{\partial c_2}{\partial t} \right)_{x_i} = v_{i \rightarrow 2} c_i - \lambda_2 c_2 (1 - \theta_i) v_{2 \rightarrow i} + D_2 \left(\frac{\partial c_2}{\partial x} \right)_{x_i} \quad (B.4)$$

where $\lambda_{k \in \{1,2\}}$ (m) is the distance between two interstitial sites in material k (such that $\lambda_k c_k(x_i)$ represent the areal density of interstitial H at the depth x_i which interacts with the interface). In Equation B.2 and Equation B.4, the first term on the right-hand side corresponds to the detrapping from the interface to material k , the second term correspond to the trapping to the interface and the last term corresponds to the diffusion that carries away particles from the interface region (it is important to note that the signs of these fluxes are different). At steady-state, when the time derivatives are null and the diffusive flux can be neglected (i.e. when the diffusion depth is long compared to λ_k), one gets:

$$\frac{c_2}{c_1} = \frac{\lambda_1 v_{i \rightarrow 2}(T) v_{1 \rightarrow i}(T)}{\lambda_2 v_{2 \rightarrow i}(T) v_{i \rightarrow 1}(T)} = \frac{S_2(T)}{S_1(T)} \quad (B.5)$$

with $S_k(T)$ ($m^{-3} Pa^{-0.5}$) the solubility of H in material k . The condition to have such steady-state is:

$$E_{S,1} - E_{S,2} = E_{i \rightarrow 1} - E_{i \rightarrow 2} - E_{1 \rightarrow i} + E_{2 \rightarrow i} \quad (B.6)$$

The simple kinetic presented here allows us to see how fast the equilibrium given by Equation 1.34 is reached. For the test case, we further simplify the model by considering that the concentration of interstitial H in material 1 c_1 is constant (i.e. $\partial c_1 / \partial t = 0$). The diffusive fluxes are neglected in Equation B.4 in order to solve a 0D problem. The system of equation is solved with the SciPy package [195] which uses the odepack library [249].

A W/Cu interface is simulated at 475 K. All parameters in the model have been constrained so that it corresponds to the steady state condition in Equation B.6 in the case of a W/Cu interface considering for both W and Cu, $E_{k \rightarrow i} = E_{diff,k}$ with $k=Cu$ or W. The values of λ for W and Cu are 110 pm and 65 pm respectively. The concentration of H in W is set to $c_1 = 10^{18} m^{-3}$. The concentration of trapping site at the interface is set to $n_i = 10^{19} m^{-2}$. All pre-exponential factors are set to $10^{13} s^{-1}$. The only free parameter left is $E_{i \rightarrow 2}$ and a parametric study is performed (see Figure B.2).

The ratio c_2/c_1 steady state value is approximately 10^5 (see Figure B.2(a)). The ratio θ_i/θ_i^{eq} does not depend on the value of the detrapping energy (see Figure B.2(b)). τ_1 and τ_2 are defined as the time at which c_i and c_2 have reached 95% of their equilibrium

value. In this case, both τ_1 and τ_2 remain below 10^3 s (see Figure B.2(c)). The interface is saturated with H for $E_{i \rightarrow, 2}/(k_B T) > 25$ (see Figure B.2(d)).

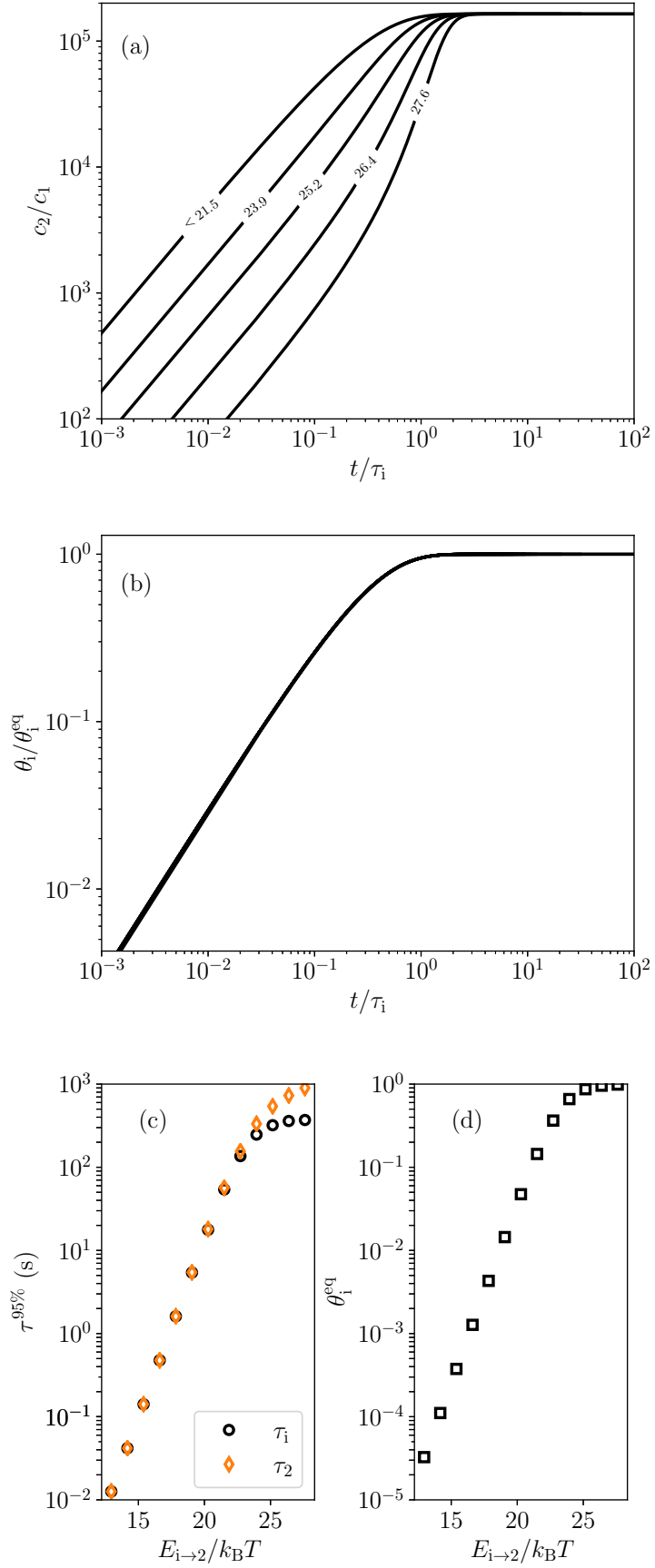


Figure B.2: (a) Evolution of the ratio c_2/c_1 with normalised time t/τ_1 for different values of $E_{i \rightarrow 2}/k_B T$. (b) Evolution of the ratio θ_i/θ_i^{eq} with normalised time t/τ_1 (independent of $E_{i \rightarrow 2}/k_B T$). (c) Evolution of the time to reach 95% of the steady-state concentration, τ_1 and τ_2 as a function of $E_{i \rightarrow 2}/k_B T$. (d) Evolution of θ_i^{eq} as a function of $E_{i \rightarrow 2}/k_B T$. The temperature in the simulation is 475 K, the concentration in the material 1 (W) is $c_1 = 10^{18} \text{ m}^{-3}$ and the concentration of trapping site at the interface is $n_i = 10^{19} \text{ m}^{-2}$.

C

DEMO monoblocks

So far, only 2D monoblocks simulations were run, assuming an infinite thickness (or assuming no desorption from the poloidal gaps). The goal of this section is to assess the influence of 3D edge effects on the monoblocks simulation results. It will be shown that the error induced by 2D assumption decreases for thick monoblocks.

C.1 Methodology

The DEMO monoblock geometry differs slightly from the ITER geometry (see Figure C.1) but the general concept is the same, meaning the observations made in this Section are also valid for the ITER geometry.

The boundary conditions for the steady state heat transfer problem are the same as for the 2D case (see Equation C.1). The boundary conditions for the transient H transport problem are similar (see Equation C.2). A non-homogeneous mobile concentration is assumed at the plasma exposed surface to simulate an implanted source of particles (see Section 2.2.2). Depending on the simulation case (with or without desorption on the gaps), the other external surfaces (except the cooling surfaces) will either be insulated or an instantaneous recombination will be assumed.

$$-\lambda \nabla T \cdot \mathbf{n} = \varphi_{\text{heat}} \quad \text{on } \Gamma_{\text{top}} \quad (\text{C.1a})$$

$$-\lambda \nabla T \cdot \mathbf{n} = -h \cdot (T_{\text{coolant}} - T) \quad \text{on } \Gamma_{\text{coolant}} \quad (\text{C.1b})$$

where $\varphi_{\text{heat}} = 10 \text{ MW}$, $h = 7 \times 10^4 \text{ W m}^{-2} \text{ K}^{-1}$ is the heat exchange coefficient and $T_{\text{coolant}} = 323 \text{ K}$ is the coolant temperature.

$$c_m = \frac{\varphi_{\text{imp}} R_p}{D} \quad \text{on } \Gamma_{\text{top}} \quad (\text{C.2a})$$

$$-D \nabla c_m \cdot \mathbf{n} = K_{\text{CuCrZr}} \cdot c_m^2 \quad \text{on } \Gamma_{\text{coolant}} \quad (\text{C.2b})$$

$$c_m = 0 \quad \text{on } \Gamma_{\text{toroidal}} \text{ and } \Gamma_{\text{pipe}} \quad (\text{C.2c})$$

$$c_m = 0 \quad \text{or} \quad -D \nabla c_m \cdot \mathbf{n} = 0 \quad \text{on } \Gamma_{\text{poloidal}} \quad (\text{C.2d})$$

where $\varphi_{\text{imp}} = 1.6 \times 10^{22} \text{ H m}^{-2} \text{ s}^{-1}$ is the implanted particle flux, $R_p = 1 \times 10^{-9} \text{ m}$ is the particle implantation depth, $K_{\text{CuCrZr}} = 2.9 \times 10^{-14} \exp -1.92/(k_B T)$ is the H recombination coefficient in CuCrZr expressed in $\text{m}^4 \text{ s}^{-1}$.

Two intrinsic traps were set in W, one trap in the Cu interlayer and two traps in the CuCrZr cooling pipe (see Table C.1).

Transient simulations up to 10^7 s were run.

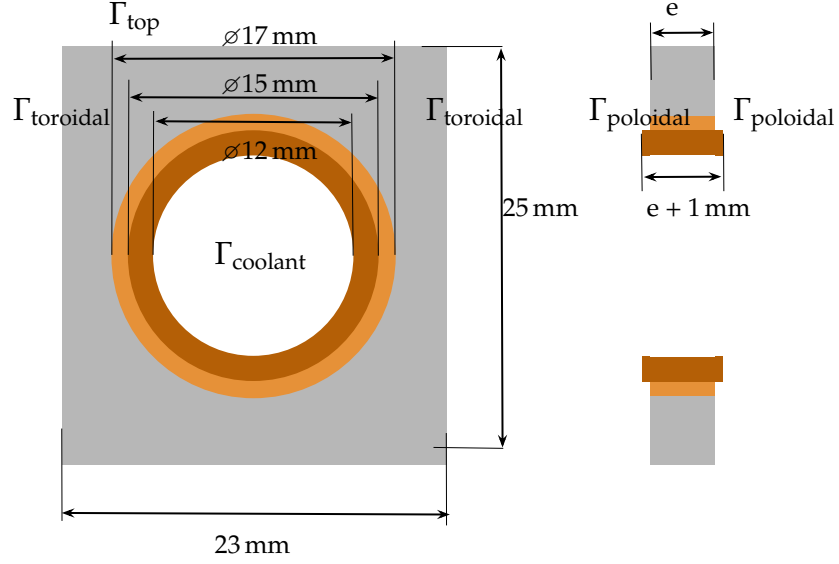


Figure C.1: 3D geometry of the DEMO monoblock used for the simulations showing W armour ■, Cu interlayer ■, CuCrZr alloy cooling pipe ■.

Table C.1: Traps properties used in the 3D DEMO monoblocks simulations.

	Material	$k_0(\text{m}^3 \text{s}^{-1})$	$E_k(\text{eV})$	$p_0(\text{s}^{-1})$	$E_p(\text{eV})$	$n_i(\text{at fr})$
Trap 1	W	8.96×10^{-17}	0.39	1×10^{13}	0.87	1.0×10^{-3}
Trap 2	W	8.96×10^{-17}	0.39	1×10^{13}	1.00	4.0×10^{-4}
Trap 3	Cu	6.0×10^{-17}	0.39	8.0×10^{13}	0.50	5.0×10^{-5}
Trap 4	CuCrZr	1.2×10^{-16}	0.42	8.0×10^{13}	0.85	5.0×10^{-5}

C.2 Standard case

FESTIM simulations were run with and without desorption on the gaps.

The temperature field obtained was very similar to the 2D case (see Figure C.2) with a top surface temperature of approximately 1200 K.

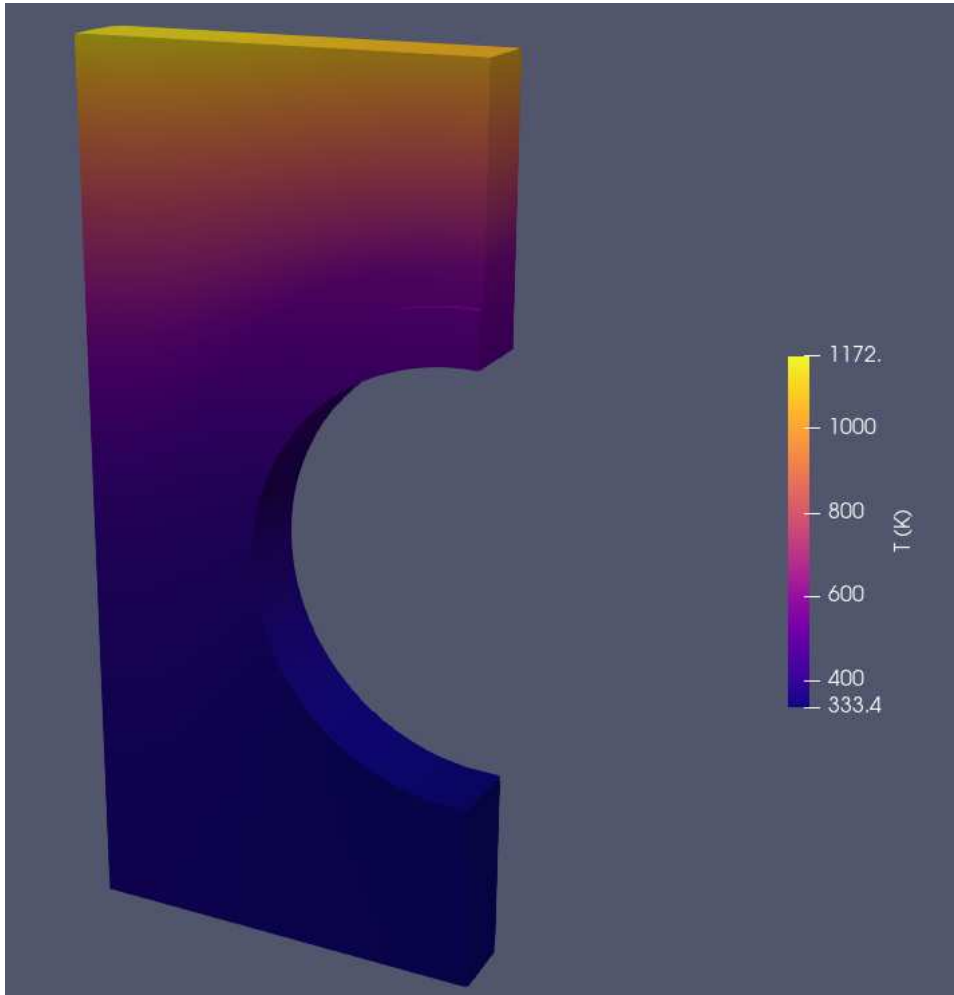


Figure C.2: Temperature field of the 3D DEMO monoblock.

As expected, a higher retention was observed in the case without desorption (see Figure C.3). This is explained by the surface losses.

The total H inventory in the monoblock was also between one and three orders of magnitude lower in the case with desorption (see Figure C.4). This difference increased with the exposure time. Moreover, the steady state was reached way earlier for the case with desorption whereas the inventory kept increasing after 10^7 s for the insulated case. This means that not taking desorption from the gaps into account in 2D simulations is a conservative assumption in terms of H inventory. The simulations performed in Section 3.3 then overestimate the monoblock H inventory.

These 3D simulations are however essential to estimate the outgassing fluxes from the poloidal gaps. The particle flux at the poloidal gap is six times higher than the flux at the toroidal gap (see Figure C.5). The permeation flux to the coolant is five to six orders of magnitude lower than the fluxes at the gaps. The particle fluxes at the gaps (poloidal and toroidal) were approximately 10^{12} H s^{-1} whereas the flux towards the cooling channel was below 10^7 H s^{-1} . The values of the outgassing fluxes from both the gaps are orders of magnitude lower than that of the retrodesorbed flux (i.e. the flux

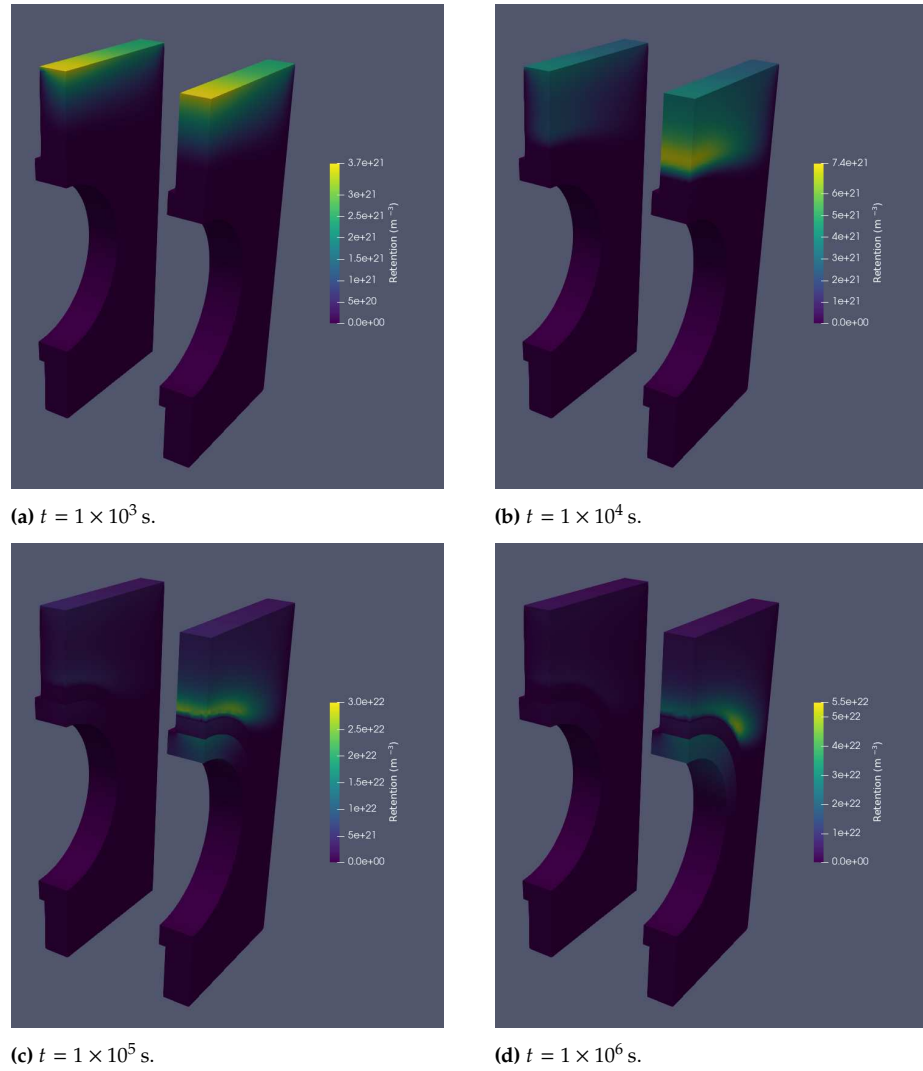


Figure C.3: Retention fields of the DEMO monoblock with (left) or without (right) recombination on the poloidal gaps (standard case). Note the colour bars are different.

of implanted particles that diffuse back to the exposed surface). This means 3D edge effects will not affect previous results regarding the outgassing to the vessel. They will however impact the value of the contamination flux towards the coolant as assuming an instantaneous recombination on the gaps will lead to way less particles reaching the cooling surface and therefore a lower flux.

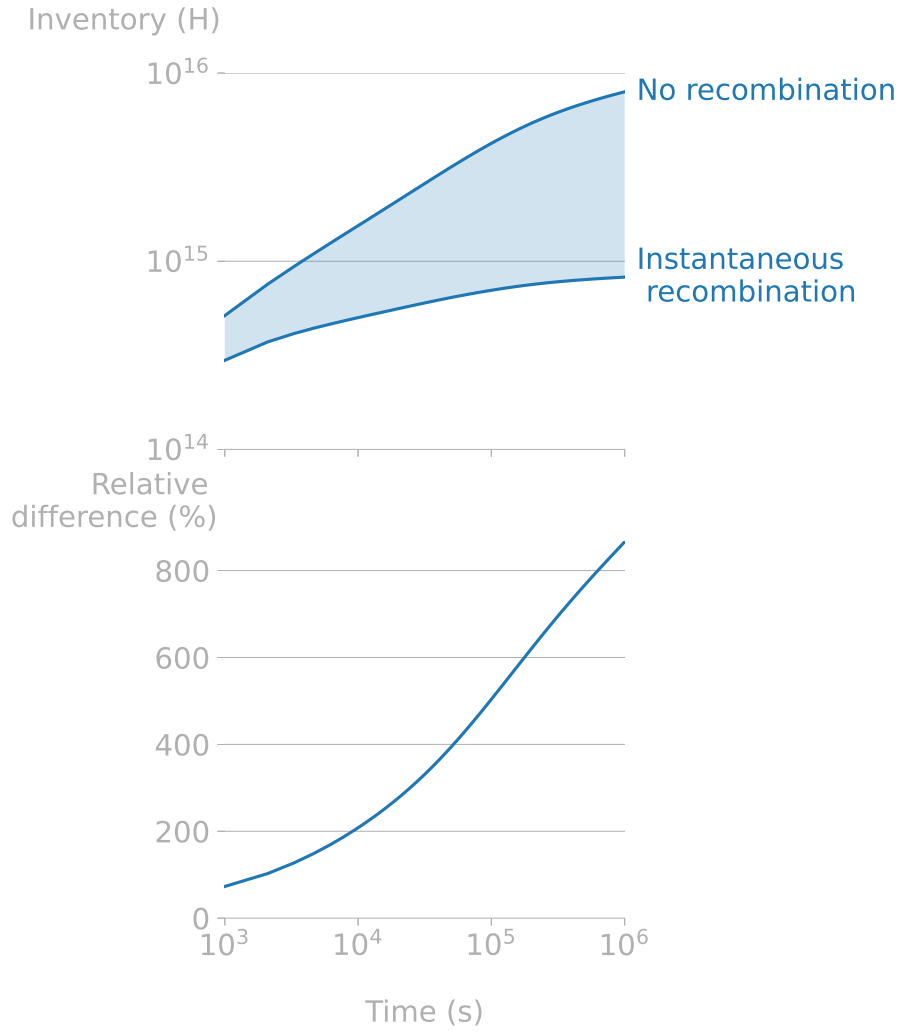


Figure C.4: Temporal evolution of the monoblock inventory (standard case).

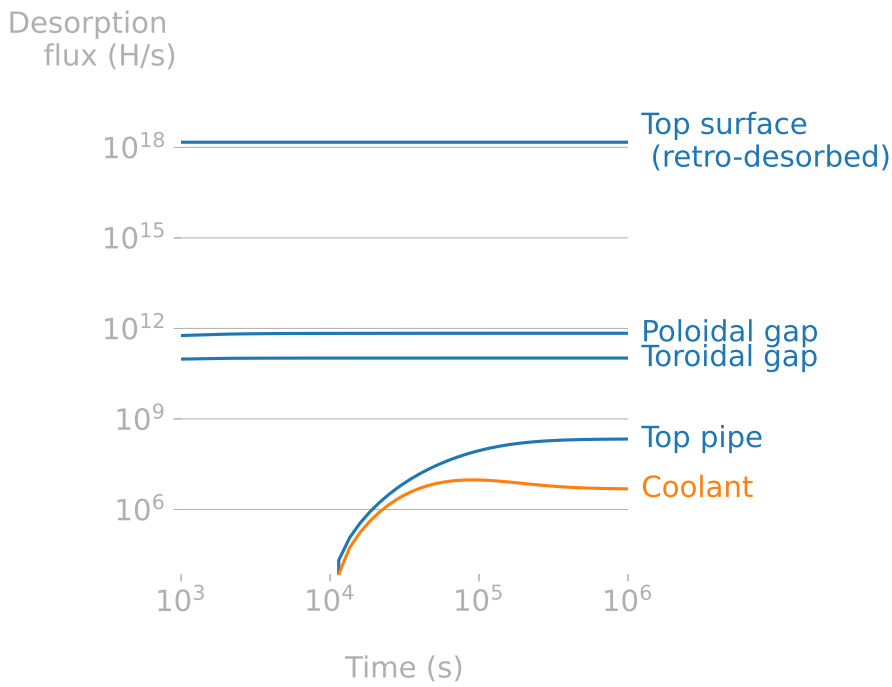


Figure C.5: Temporal evolution of outgassing fluxes for the standard case with desorption from the poloidal gaps. Blue lines correspond to the fluxes towards the vacuum vessel, the orange line is the flux towards the coolant.

C.3 Influence of the monoblock thickness

Several simulations were run with monoblock thicknesses varying from 4 mm to 14 mm.

As the thickness increases, the inventory per unit thickness increases for the case with instantaneous recombination on the poloidal gap (see Figure C.4). It remains constant for the case with no recombination since it is equivalent to a 2D case (the decrease observed at low thicknesses is due to the impact of the CuCrZr pipe between monoblocks as shown on Figure C.1). The relative difference between the cases with or without recombination on the poloidal gap decreases as the thickness increases (see Figure C.6). After 1×10^6 s of exposure, for a thickness of 4 mm the relative difference is 200% and drops at 30% for 14 mm. This result was expected as the edge effects become negligible at large thicknesses.

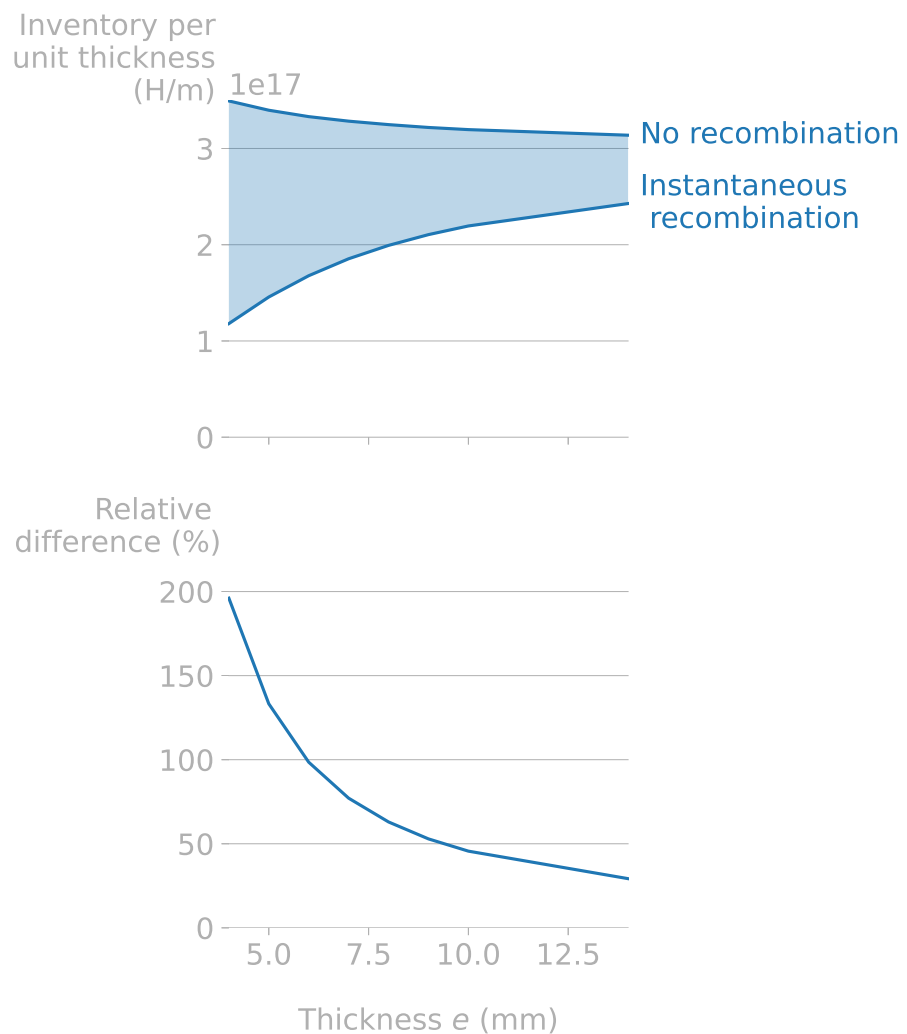


Figure C.6: Evolution of the inventory with or without recombination at the poloidal gap for several monoblock thicknesses at $t = 1 \times 10^6$ s.

The permeation flux towards the cooling channel per unit thickness globally increases with the monoblock thickness (see Figure C.7). It is always higher in the case without recombination on the gaps. Similarly to the inventory, the relative difference between the cases with or without recombination on the poloidal gap decreases with the thickness.

Finally, the extrusion of the CuCrZr pipe between monoblocks has an impact on

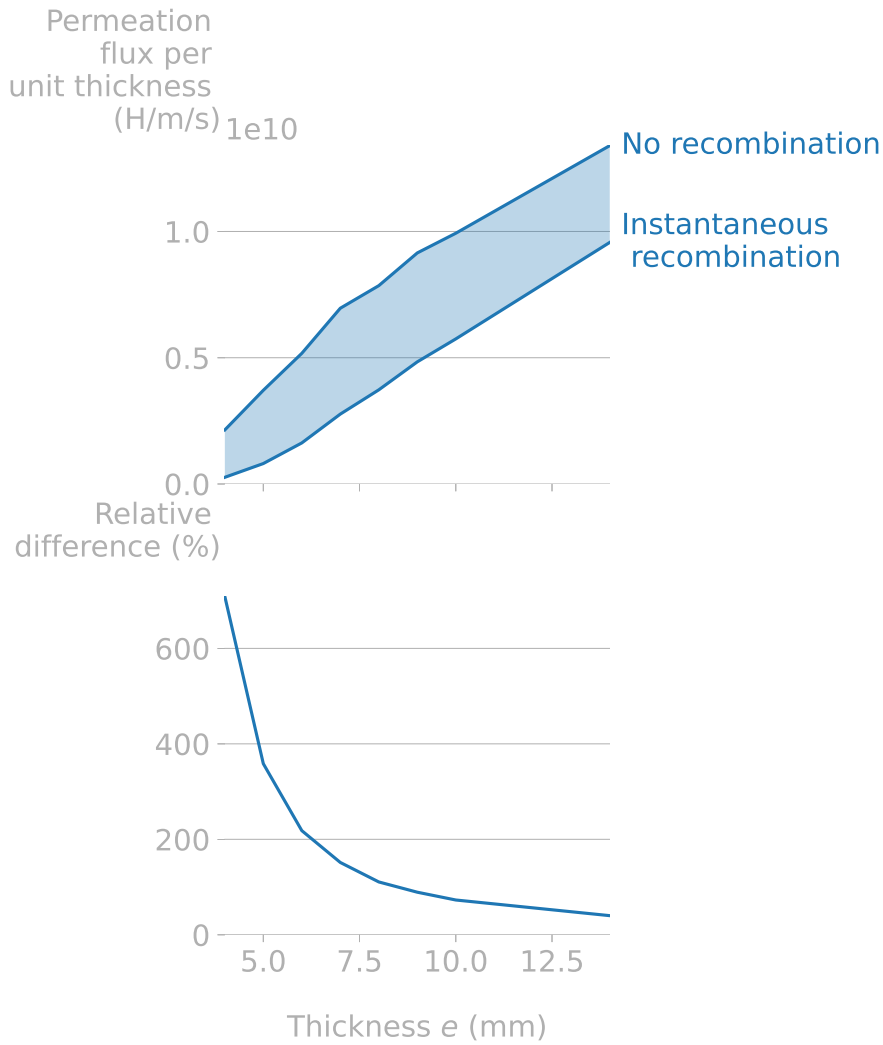


Figure C.7: Evolution of the permeation flux to the coolant with or without recombination at the poloidal gap for several monoblock thicknesses at $t = 1 \times 10^6$ s.

the permeation flux and the inventory. Without this extrusion, the case without recombination on the poloidal gap corresponds to a pure 2D case and the inventory is independent of the thickness (see Figure C.8).

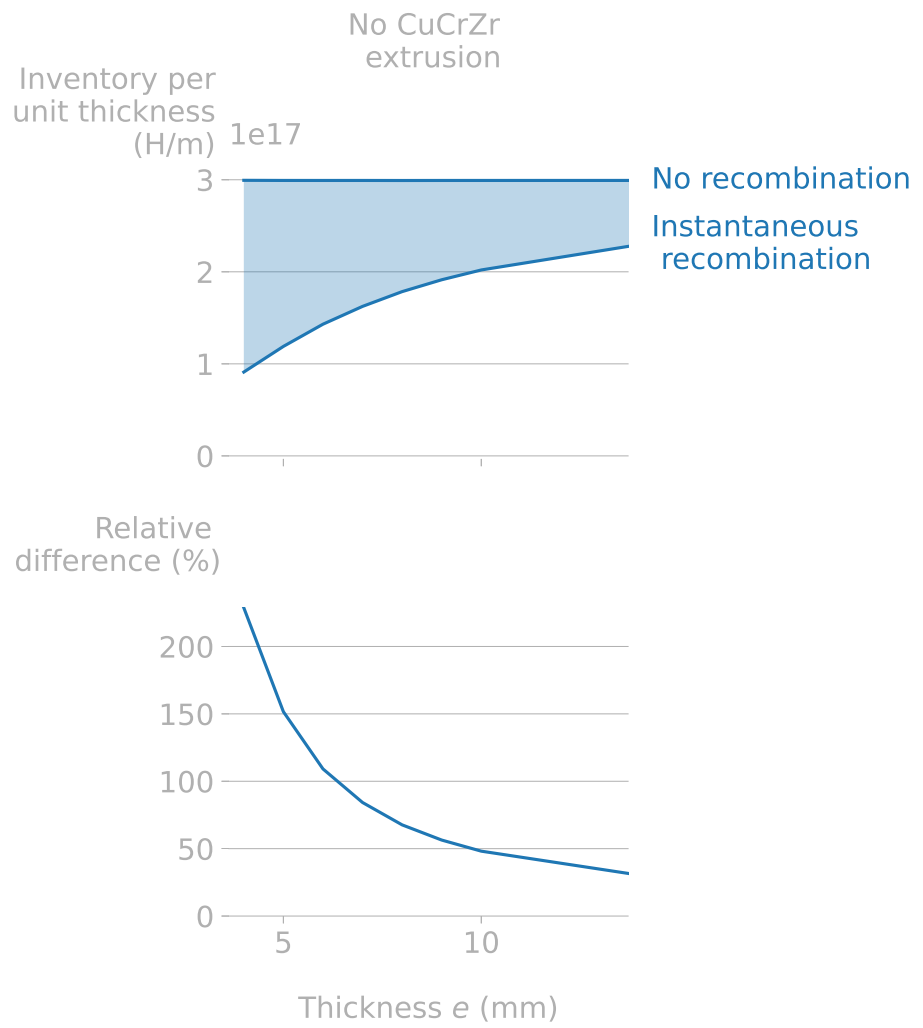


Figure C.8: Evolution of the permeation flux with or without recombination at the poloidal gap for several monoblock thicknesses without Cu-CrZr extrusion at $t = 1 \times 10^6$ s.

Bibliography

Here are the references in citation order.

- [1] Pierre Friedlingstein et al. 'Global Carbon Budget 2021'. English. In: *Earth System Science Data Discussions* (Nov. 2021). Publisher: Copernicus GmbH, pp. 1–191. doi: [10.5194/essd-2021-386](https://doi.org/10.5194/essd-2021-386) (cited on page v).
- [2] Anthony J. Webster. 'Fusion: Power for the future'. en. In: *Physics Education* 38.2 (Mar. 2003). Publisher: IOP Publishing, pp. 135–142. doi: [10.1088/0031-9120/38/2/305](https://doi.org/10.1088/0031-9120/38/2/305) (cited on page v).
- [3] Alf Köhn-Seemann and Julien Hillairet. *alfkoehn/fusion_plots: Second release of the fusion plot package (new plots added)*. June 2021. doi: [10.5281/zenodo.4946068](https://doi.org/10.5281/zenodo.4946068). URL: <https://zenodo.org/record/4946068> (cited on page 1).
- [4] Garry McCracken and Peter Stott, eds. *Fusion (Second Edition)*. en. Boston: Academic Press, Jan. 2013 (cited on pages 2–4).
- [5] R.A. Forrest et al. *FENDL-3 Library - Summary Documentation*. Tech. rep. INDC(NDS)-0628 INIS Reference Number: 44045168. International Atomic Energy Agency (IAEA), 2012, p. 26 (cited on pages 2, 3).
- [6] A. B. Zylstra et al. 'Burning plasma achieved in inertial fusion'. en. In: *Nature* 601.7894 (Jan. 2022), pp. 542–548. doi: [10.1038/s41586-021-04281-w](https://doi.org/10.1038/s41586-021-04281-w) (cited on page 5).
- [7] J.-L. Miquel, C. Lion, and P. Vivini. 'The Laser Mega-Joule : LMJ & PETAL status and Program Overview'. en. In: *Journal of Physics: Conference Series* 688 (Mar. 2016). Publisher: IOP Publishing, p. 012067. doi: [10.1088/1742-6596/688/1/012067](https://doi.org/10.1088/1742-6596/688/1/012067) (cited on page 5).
- [8] J. Mailloux et al. 'Overview of JET results for optimising ITER operation'. en. In: *Nuclear Fusion* 62.4 (Apr. 2022). Publisher: IOP Publishing, p. 042026. doi: [10.1088/1741-4326/ac47b4](https://doi.org/10.1088/1741-4326/ac47b4) (cited on page 6).
- [9] T. Casper et al. 'Development of the ITER baseline inductive scenario'. en. In: *Nuclear Fusion* 54.1 (Dec. 2013). Publisher: IOP Publishing, p. 013005. doi: [10.1088/0029-5515/54/1/013005](https://doi.org/10.1088/0029-5515/54/1/013005) (cited on page 6).
- [10] G. Federici et al. 'Overview of EU DEMO design and R&D activities'. en. In: *Fusion Engineering and Design*. Proceedings of the 11th International Symposium on Fusion Nuclear Technology-11 (ISFNT-11) Barcelona, Spain, 15-20 September, 2013 89.7 (Oct. 2014), pp. 882–889. doi: [10.1016/j.fusengdes.2014.01.070](https://doi.org/10.1016/j.fusengdes.2014.01.070) (cited on page 6).
- [11] B. N. Sorbom et al. 'ARC: A compact, high-field, fusion nuclear science facility and demonstration power plant with demountable magnets'. en. In: *Fusion Engineering and Design* 100 (Nov. 2015), pp. 378–405. doi: [10.1016/j.fusengdes.2015.07.008](https://doi.org/10.1016/j.fusengdes.2015.07.008) (cited on page 6).
- [12] A. J. Creely et al. 'Overview of the SPARC tokamak'. en. In: *Journal of Plasma Physics* 86.5 (Oct. 2020). Publisher: Cambridge University Press. doi: [10.1017/S0022377820001257](https://doi.org/10.1017/S0022377820001257) (cited on page 6).
- [13] Howard Wilson et al. 'STEP—on the pathway to fusion commercialization'. In: Dec. 2020. doi: [10.1088/978-0-7503-2719-0ch8](https://doi.org/10.1088/978-0-7503-2719-0ch8) (cited on page 6).
- [14] Rémi Delaporte-Mathurin and Nicolas Aloueva. *RemDelaporteMathurin/fusion-world: Patch 0.4.1*. June 2022. doi: [10.5281/ZENODO.6624244](https://doi.org/10.5281/ZENODO.6624244). URL: <https://zenodo.org/record/6624244> (cited on pages 6, 7).
- [15] Darya Ivanova. 'Plasma-Facing Components in Tokamaks : Material Modification and Fuel Retention'. eng. In: (2012). Publisher: KTH Royal Institute of Technology (cited on page 6).
- [16] G. M. McCracken. 'A review of the experimental evidence for arcing and sputtering in tokamaks'. en. In: *Journal of Nuclear Materials* 93-94 (Oct. 1980), pp. 3–16. doi: [10.1016/0022-3115\(80\)90299-8](https://doi.org/10.1016/0022-3115(80)90299-8) (cited on page 6).

- [17] S. Van den Kerkhof et al. 'Impact of ELM mitigation on the ITER monoblock thermal behavior and the tungsten recrystallization depth'. en. In: *Nuclear Materials and Energy* 27 (June 2021), p. 101009. doi: [10.1016/j.nme.2021.101009](https://doi.org/10.1016/j.nme.2021.101009) (cited on page 6).
- [18] Jochen Linke et al. 'Challenges for plasma-facing components in nuclear fusion'. en. In: *Matter and Radiation at Extremes* 4.5 (Sept. 2019), p. 056201. doi: [10.1063/1.5090100](https://doi.org/10.1063/1.5090100) (cited on page 7).
- [19] G. Federici et al. 'Plasma-material interactions in current tokamaks and their implications for next step fusion reactors'. en. In: *Nuclear Fusion* 41.12 (Dec. 2001). Publisher: IOP Publishing, pp. 1967–2137. doi: [10.1088/0029-5515/41/12/218](https://doi.org/10.1088/0029-5515/41/12/218) (cited on page 7).
- [20] K. Sugiyama et al. 'Measurement of Tritium Surface Distribution on TFTR Bumper Limiter Tiles'. en. In: *Physica Scripta* 2004.T108 (Jan. 2004). Publisher: IOP Publishing, p. 68. doi: [10.1238/Physica.Topical.108a00068](https://doi.org/10.1238/Physica.Topical.108a00068) (cited on page 7).
- [21] E. Pajuste et al. 'Tritium in plasma-facing components of JET with the ITER-Like-Wall'. en. In: *Physica Scripta* 96.12 (Nov. 2021). Publisher: IOP Publishing, p. 124050. doi: [10.1088/1402-4896/ac29db](https://doi.org/10.1088/1402-4896/ac29db) (cited on page 7).
- [22] E. Havlíčková et al. 'The effect of the Super-X divertor of MAST Upgrade on impurity radiation as modelled by SOLPS'. en. In: *Journal of Nuclear Materials. PLASMA-SURFACE INTERACTIONS* 21 463 (Aug. 2015), pp. 1209–1213. doi: [10.1016/j.jnucmat.2014.10.073](https://doi.org/10.1016/j.jnucmat.2014.10.073) (cited on page 8).
- [23] P. Rodriguez-Fernandez et al. 'Overview of the SPARC physics basis towards the exploration of burning-plasma regimes in high-field, compact tokamaks'. en. In: *Nuclear Fusion* 62.4 (Mar. 2022). Publisher: IOP Publishing, p. 042003. doi: [10.1088/1741-4326/ac1654](https://doi.org/10.1088/1741-4326/ac1654) (cited on page 8).
- [24] A. Q. Kuang et al. 'Divertor heat flux challenge and mitigation in SPARC'. en. In: *Journal of Plasma Physics* 86.5 (Oct. 2020). Publisher: Cambridge University Press. doi: [10.1017/S0022377820001117](https://doi.org/10.1017/S0022377820001117) (cited on page 8).
- [25] D. D. Ryutov and V. A. Soukhanovskii. 'The snowflake divertor'. en. In: *Physics of Plasmas* 22.11 (Nov. 2015), p. 110901. doi: [10.1063/1.4935115](https://doi.org/10.1063/1.4935115) (cited on page 8).
- [26] R. A. Pitts et al. 'Physics basis for the first ITER tungsten divertor'. en. In: *Nuclear Materials and Energy* 20 (Aug. 2019), p. 100696. doi: [10.1016/j.nme.2019.100696](https://doi.org/10.1016/j.nme.2019.100696) (cited on pages 9, 72, 75, 76, 83).
- [27] Z. Vizvary et al. 'European DEMO first wall shaping and limiters design and analysis status'. en. In: *Fusion Engineering and Design* 158 (Sept. 2020), p. 111676. doi: [10.1016/j.fusengdes.2020.111676](https://doi.org/10.1016/j.fusengdes.2020.111676) (cited on page 8).
- [28] Yan Huang, Mark S. Tillack, and Nasr M. Ghoniem. 'Tungsten monoblock concepts for the FNSF first wall and divertor'. In: 2016 (cited on page 8).
- [29] T. Hirai et al. 'Use of tungsten material for the ITER divertor'. en. In: *Nuclear Materials and Energy* 9 (Dec. 2016), pp. 616–622. doi: [10.1016/j.nme.2016.07.003](https://doi.org/10.1016/j.nme.2016.07.003) (cited on pages 8, 58).
- [30] F. Dompetail et al. 'The design and optimisation of a monoblock divertor target for DEMO using thermal break interlayer'. en. In: *Fusion Engineering and Design* 154 (May 2020), p. 111497. doi: [10.1016/j.fusengdes.2020.111497](https://doi.org/10.1016/j.fusengdes.2020.111497) (cited on page 8).
- [31] J. H. You et al. 'European divertor target concepts for DEMO: Design rationales and high heat flux performance'. en. In: *Nuclear Materials and Energy* 16 (Aug. 2018), pp. 1–11. doi: [10.1016/j.nme.2018.05.012](https://doi.org/10.1016/j.nme.2018.05.012) (cited on page 8).
- [32] Laurent Guerrini et al. 'Fabrication of ITER Divertor Cassette Body prototypes'. en. In: *Fusion Engineering and Design* 162 (Jan. 2021), p. 112054. doi: [10.1016/j.fusengdes.2020.112054](https://doi.org/10.1016/j.fusengdes.2020.112054) (cited on page 10).
- [33] A. Durif et al. 'Impact of tungsten recrystallization on ITER-like components for lifetime estimation'. In: *Fusion Engineering and Design* 138 (Jan. 2019), pp. 247–253. doi: [10.1016/j.fusengdes.2018.11.003](https://doi.org/10.1016/j.fusengdes.2018.11.003) (cited on page 8).
- [34] Alan Durif. 'Modélisation de la durée de vie de composants face au plasma dans les réacteurs à fusion thermonucléaire'. These de doctorat. Lyon, Dec. 2019 (cited on pages 8, 10).

- [35] Eliseo Visca et al. 'Manufacturing and testing of ITER-like divertor plasma facing mock-ups for DEMO'. en. In: *Fusion Engineering and Design* 136 (Nov. 2018), pp. 1593–1596. doi: [10.1016/j.fusengdes.2018.05.064](https://doi.org/10.1016/j.fusengdes.2018.05.064) (cited on pages 8, 10).
- [36] K. C. Jordan, B. C. Blanke, and W. A. Dudley. 'Half-life of tritium'. en. In: *Journal of Inorganic and Nuclear Chemistry* 29.9 (Sept. 1967), pp. 2129–2131. doi: [10.1016/0022-1902\(67\)80265-3](https://doi.org/10.1016/0022-1902(67)80265-3) (cited on page 11).
- [37] Muyi Ni et al. 'Tritium supply assessment for ITER and DEMOnstration power plant'. en. In: *Fusion Engineering and Design*. Proceedings of the 27th Symposium On Fusion Technology (SOFT-27); Liège, Belgium, September 24-28, 2012 88.9 (Oct. 2013), pp. 2422–2426. doi: [10.1016/j.fusengdes.2013.05.043](https://doi.org/10.1016/j.fusengdes.2013.05.043) (cited on page 11).
- [38] M. Glugla et al. 'The ITER tritium systems'. en. In: *Fusion Engineering and Design*. Proceedings of the 24th Symposium on Fusion Technology 82.5 (Oct. 2007), pp. 472–487. doi: [10.1016/j.fusengdes.2007.02.025](https://doi.org/10.1016/j.fusengdes.2007.02.025) (cited on page 11).
- [39] Jonathan Shimwell et al. 'Multiphysics analysis with CAD-based parametric breeding blanket creation for rapid design iteration'. en. In: *Nuclear Fusion* 59.4 (Mar. 2019), p. 046019. doi: [10.1088/1741-4326/ab0016](https://doi.org/10.1088/1741-4326/ab0016) (cited on pages 11–13, 66).
- [40] J. Aubert et al. 'Design and preliminary analyses of the new Water Cooled Lithium Lead TBM for ITER'. en. In: *Fusion Engineering and Design* 160 (Nov. 2020), p. 111921. doi: [10.1016/j.fusengdes.2020.111921](https://doi.org/10.1016/j.fusengdes.2020.111921) (cited on page 12).
- [41] A. Del Nevo et al. 'Recent progress in developing a feasible and integrated conceptual design of the WCLL BB in EUROfusion project'. en. In: *Fusion Engineering and Design*. SI:SOFT-30 146 (Sept. 2019), pp. 1805–1809. doi: [10.1016/j.fusengdes.2019.03.040](https://doi.org/10.1016/j.fusengdes.2019.03.040) (cited on page 12).
- [42] Francisco A. Hernández et al. 'Overview of the HCPB Research Activities in EUROfusion'. In: *IEEE Transactions on Plasma Science* 46.6 (June 2018). Conference Name: IEEE Transactions on Plasma Science, pp. 2247–2261. doi: [10.1109/TPS.2018.2830813](https://doi.org/10.1109/TPS.2018.2830813) (cited on page 12).
- [43] F. Hernández et al. 'A new HCPB breeding blanket for the EU DEMO: Evolution, rationale and preliminary performances'. en. In: *Fusion Engineering and Design*. Proceedings of the 29th Symposium on Fusion Technology (SOFT-29) Prague, Czech Republic, September 5-9, 2016 124 (Nov. 2017), pp. 882–886. doi: [10.1016/j.fusengdes.2017.02.008](https://doi.org/10.1016/j.fusengdes.2017.02.008) (cited on page 12).
- [44] Pavel Pereslavytsev et al. 'Neutronic analyses for the optimization of the advanced HCPB breeder blanket design for DEMO'. en. In: *Fusion Engineering and Design*. Proceedings of the 29th Symposium on Fusion Technology (SOFT-29) Prague, Czech Republic, September 5-9, 2016 124 (Nov. 2017), pp. 910–914. doi: [10.1016/j.fusengdes.2017.01.028](https://doi.org/10.1016/j.fusengdes.2017.01.028) (cited on page 12).
- [45] Julien Aubert et al. 'Status of the EU DEMO HCLL breeding blanket design development'. en. In: *Fusion Engineering and Design*. Special Issue: Proceedings of the 13th International Symposium on Fusion Nuclear Technology (ISFNT-13) 136 (Nov. 2018), pp. 1428–1432. doi: [10.1016/j.fusengdes.2018.04.133](https://doi.org/10.1016/j.fusengdes.2018.04.133) (cited on page 12).
- [46] Jean-Charles Jaboulay et al. 'Nuclear analysis of the HCLL blanket for the European DEMO'. en. In: *Fusion Engineering and Design*. Proceedings of the 29th Symposium on Fusion Technology (SOFT-29) Prague, Czech Republic, September 5-9, 2016 124 (Nov. 2017), pp. 896–900. doi: [10.1016/j.fusengdes.2017.01.050](https://doi.org/10.1016/j.fusengdes.2017.01.050) (cited on page 12).
- [47] F. R. Ugorri et al. 'Tritium transport modeling at system level for the EUROfusion dual coolant lithium-lead breeding blanket'. en. In: *Nuclear Fusion* 57.11 (Aug. 2017). Publisher: IOP Publishing, p. 116045. doi: [10.1088/1741-4326/aa7f9d](https://doi.org/10.1088/1741-4326/aa7f9d) (cited on page 12).
- [48] I. Palermo et al. 'Neutronic design studies of a conceptual DCLL fusion reactor for a DEMO and a commercial power plant'. en. In: *Nuclear Fusion* 56.1 (Nov. 2015). Publisher: IOP Publishing, p. 016001. doi: [10.1088/0029-5515/56/1/016001](https://doi.org/10.1088/0029-5515/56/1/016001) (cited on page 12).
- [49] G. Federici et al. 'An overview of the EU breeding blanket design strategy as an integral part of the DEMO design effort'. en. In: *Fusion Engineering and Design* 141 (Apr. 2019), pp. 30–42. doi: [10.1016/j.fusengdes.2019.01.141](https://doi.org/10.1016/j.fusengdes.2019.01.141) (cited on page 12).

- [50] Mohamed Abdou et al. 'Blanket/first wall challenges and required R&D on the pathway to DEMO'. en. In: *Fusion Engineering and Design* 100 (Nov. 2015), pp. 2–43. doi: [10.1016/j.fusengdes.2015.07.021](https://doi.org/10.1016/j.fusengdes.2015.07.021) (cited on page 12).
- [51] Mohamed Abdou et al. 'Physics and technology considerations for the deuterium–tritium fuel cycle and conditions for tritium fuel self sufficiency'. en. In: *Nuclear Fusion* 61.1 (Nov. 2020). Publisher: IOP Publishing, p. 013001. doi: [10.1088/1741-4326/abbf35](https://doi.org/10.1088/1741-4326/abbf35) (cited on page 12).
- [52] Marco Utili et al. 'Design of the Test Section for the Experimental Validation of Antipermeation and Corrosion Barriers for WCLL BB'. en. In: *Applied Sciences* 12.3 (Jan. 2022). Number: 3 Publisher: Multidisciplinary Digital Publishing Institute, p. 1624. doi: [10.3390/app12031624](https://doi.org/10.3390/app12031624) (cited on page 13).
- [53] Bryn Bridges et al. *Review of risks from tritium, Subgroup on Tritium internal dosimetry of the Advisory Group on Ionising Radiation. Report of the independent Advisory Group on Ionising Radiation*. Nov. 2007 (cited on page 13).
- [54] Augustin Janssens. 'Emerging Issues on Tritium and Low Energy Beta Emitters'. en. In: (Nov. 2007), p. 100 (cited on page 13).
- [55] Neil Hyatt. *Radioactive wastes from fusion energy: preliminary position paper*. en. Tech. rep. 3735. Nov. 2021 (cited on page 13).
- [56] T. Honda et al. 'Analyses of loss of vacuum accident (LOVA) in ITER'. en. In: *Fusion Engineering and Design* 47.4 (Jan. 2000), pp. 361–375. doi: [10.1016/S0920-3796\(99\)00067-8](https://doi.org/10.1016/S0920-3796(99)00067-8) (cited on page 13).
- [57] Joachim Roth et al. 'Tritium inventory in ITER plasma-facing materials and tritium removal procedures'. en. In: *Plasma Physics and Controlled Fusion* 50.10 (Aug. 2008). Publisher: IOP Publishing, p. 103001. doi: [10.1088/0741-3335/50/10/103001](https://doi.org/10.1088/0741-3335/50/10/103001) (cited on page 13).
- [58] G. De Temmerman et al. 'Efficiency of thermal outgassing for tritium retention measurement and removal in ITER'. In: *Nuclear Materials and Energy*. Proceedings of the 22nd International Conference on Plasma Surface Interactions 2016, 22nd PSI 12 (Aug. 2017), pp. 267–272. doi: [10.1016/j.nme.2016.10.016](https://doi.org/10.1016/j.nme.2016.10.016) (cited on page 13).
- [59] R. Arredondo et al. 'Preliminary estimates of tritium permeation and retention in the first wall of DEMO due to ion bombardment'. en. In: *Nuclear Materials and Energy* 28 (Sept. 2021), p. 101039. doi: [10.1016/j.nme.2021.101039](https://doi.org/10.1016/j.nme.2021.101039) (cited on page 13).
- [60] M. Shimada and R. J. Pawelko. 'Tritium permeability measurement in hydrogen-tritium system'. en. In: *Fusion Engineering and Design* 129 (Apr. 2018), pp. 134–139. doi: [10.1016/j.fusengdes.2018.02.033](https://doi.org/10.1016/j.fusengdes.2018.02.033) (cited on page 13).
- [61] Karine Liger. 'Overview of the TRANSAT (TRANSversal Actions for Tritium) project'. en. In: *Fusion Engineering and Design* (2018), p. 5 (cited on page 13).
- [62] X. Lefebvre et al. 'Preliminary results from a detritiation facility dedicated to soft housekeeping waste'. en. In: *Fusion Engineering and Design*. Tenth International Symposium on Fusion Nuclear Technology (ISFNT-10) 87.7 (Aug. 2012), pp. 1040–1044. doi: [10.1016/j.fusengdes.2012.02.076](https://doi.org/10.1016/j.fusengdes.2012.02.076) (cited on page 13).
- [63] R. A. Causey, R. A. Karnesky, and C. San Marchi. '4.16 - Tritium Barriers and Tritium Diffusion in Fusion Reactors'. en. In: *Comprehensive Nuclear Materials*. Ed. by Rudy J. M. Konings. Oxford: Elsevier, Jan. 2012, pp. 511–549. doi: [10.1016/B978-0-08-056033-5.00116-6](https://doi.org/10.1016/B978-0-08-056033-5.00116-6) (cited on page 13).
- [64] Marco Utili et al. 'Development of anti-permeation and corrosion barrier coatings for the WCLL breeding blanket of the European DEMO'. en. In: *Fusion Engineering and Design* 170 (Sept. 2021), p. 112453. doi: [10.1016/j.fusengdes.2021.112453](https://doi.org/10.1016/j.fusengdes.2021.112453) (cited on page 13).
- [65] J. Denis et al. 'Dynamic modelling of local fuel inventory and desorption in the whole tokamak vacuum vessel for auto-consistent plasma-wall interaction simulations'. en. In: *Nuclear Materials and Energy* 19 (May 2019), pp. 550–557. doi: [10.1016/j.nme.2019.03.019](https://doi.org/10.1016/j.nme.2019.03.019) (cited on page 14).
- [66] Rion A Causey. 'Hydrogen isotope retention and recycling in fusion reactor plasma-facing components'. In: *Journal of Nuclear Materials* 300.2 (Feb. 2002), pp. 91–117. doi: [10.1016/S0022-3115\(01\)00732-2](https://doi.org/10.1016/S0022-3115(01)00732-2) (cited on pages 14, 24).

- [67] M. Shimada and B. J. Merrill. 'Tritium decay helium-3 effects in tungsten'. en. In: *Nuclear Materials and Energy*. Proceedings of the 22nd International Conference on Plasma Surface Interactions 2016, 22nd PSI 12 (Aug. 2017), pp. 699–702. doi: [10.1016/j.nme.2016.11.006](https://doi.org/10.1016/j.nme.2016.11.006) (cited on pages 14, 15).
- [68] G.F. Knoll. *Radiation detection and measurement, 2nd ed.* INIS Reference Number: 20080161. United States: John Wiley and Sons Inc, 1989 (cited on page 14).
- [69] Jonathan Shimwell and Rémi Delaporte-Mathurin. *XSPLOT - Neutron cross section plotter for isotopes*. original-date: 2021-05-27T18:08:21Z. Aug. 2021. URL: <https://github.com/openmc-data-storage/isotope-xs-plotter> (cited on page 15).
- [70] James Dark et al. 'Influence of hydrogen trapping on WCLL breeding blanket performances'. en. In: *Nuclear Fusion* 61.11 (Oct. 2021). Publisher: IOP Publishing, p. 116076. doi: [10.1088/1741-4326/ac28b0](https://doi.org/10.1088/1741-4326/ac28b0) (cited on pages 15, 22, 40).
- [71] Y. Watanabe et al. 'Status of JENDL High Energy File'. en. In: *Journal of the Korean Physical Society* 59.2 (Aug. 2011). Publisher: The Korean Physical Society, pp. 1040–1045. doi: [10.3938/jkps.59.1040](https://doi.org/10.3938/jkps.59.1040) (cited on page 15).
- [72] M. R. Gilbert et al. 'Neutron-induced dpa, transmutations, gas production, and helium embrittlement of fusion materials'. en. In: *Journal of Nuclear Materials*. FIFTEENTH INTERNATIONAL CONFERENCE ON FUSION REACTOR MATERIALS 442.1, Supplement 1 (Nov. 2013), S755–S760. doi: [10.1016/j.jnucmat.2013.03.085](https://doi.org/10.1016/j.jnucmat.2013.03.085) (cited on page 15).
- [73] M. R. Gilbert et al. 'An integrated model for materials in a fusion power plant: transmutation, gas production, and helium embrittlement under neutron irradiation'. en. In: *Nuclear Fusion* 52.8 (Aug. 2012). Publisher: IOP Publishing, p. 083019. doi: [10.1088/0029-5515/52/8/083019](https://doi.org/10.1088/0029-5515/52/8/083019) (cited on page 15).
- [74] Enrique Martínez et al. 'Thermal gradient effect on helium and self-interstitial transport in tungsten'. In: *Journal of Applied Physics* 130.21 (Dec. 2021). Publisher: American Institute of Physics, p. 215904. doi: [10.1063/5.0071935](https://doi.org/10.1063/5.0071935) (cited on page 16).
- [75] E. A. Hodille et al. 'Estimation of the tritium retention in ITER tungsten divertor target using macroscopic rate equations simulations'. en. In: *Physica Scripta* T170 (Oct. 2017), p. 014033. doi: [10.1088/1402-4896/aa8787](https://doi.org/10.1088/1402-4896/aa8787) (cited on pages 16, 67).
- [76] Glen R. Longhurst. 'The soret effect and its implications for fusion reactors'. en. In: *Journal of Nuclear Materials* 131.1 (Mar. 1985), pp. 61–69. doi: [10.1016/0022-3115\(85\)90425-8](https://doi.org/10.1016/0022-3115(85)90425-8) (cited on page 16).
- [77] Sofiane Benannoune et al. 'Multidimensional finite-element simulations of the diffusion and trapping of hydrogen in plasma-facing components including thermal expansion'. en. In: *Physica Scripta* T171 (Jan. 2020), p. 014011. doi: [10.1088/1402-4896/ab4335](https://doi.org/10.1088/1402-4896/ab4335) (cited on pages 16, 18, 28, 29).
- [78] J. Boisse, C. Domain, and C. S. Becquart. 'Modelling self trapping and trap mutation in tungsten using DFT and Molecular Dynamics with an empirical potential based on DFT'. en. In: *Journal of Nuclear Materials*. Proceedings of the 16th International Conference on Fusion Reactor Materials (ICFRM-16) 455.1 (Dec. 2014), pp. 10–15. doi: [10.1016/j.jnucmat.2014.02.031](https://doi.org/10.1016/j.jnucmat.2014.02.031) (cited on pages 16, 22).
- [79] J. Boisse et al. 'Modeling of the self trapping of helium and the trap mutation in tungsten using DFT and empirical potentials based on DFT'. en. In: *Journal of Materials Research* 29.20 (Oct. 2014). Publisher: Cambridge University Press, pp. 2374–2386. doi: [10.1557/jmr.2014.258](https://doi.org/10.1557/jmr.2014.258) (cited on pages 16, 91).
- [80] Stephen T. Lam et al. 'Modeling LiF and FLiBe Molten Salts with Robust Neural Network Interatomic Potential'. en. In: *ACS Applied Materials & Interfaces* 13.21 (June 2021), pp. 24582–24592. doi: [10.1021/acscami.1c00604](https://doi.org/10.1021/acscami.1c00604) (cited on page 16).
- [81] Jörg Behler. 'Constructing high-dimensional neural network potentials: A tutorial review'. en. In: *International Journal of Quantum Chemistry* 115.16 (Aug. 2015), pp. 1032–1050. doi: [10.1002/qua.24890](https://doi.org/10.1002/qua.24890) (cited on page 16).
- [82] Thibault Faney. 'Numerical Simulations of Tungsten under Helium Irradiation'. PhD thesis. UC Berkeley, 2013 (cited on pages 16, 17).

- [83] A. Einstein. 'Über die von der molekularkinetischen Theorie der Wärme geforderte Bewegung von in ruhenden Flüssigkeiten suspendierten Teilchen'. en. In: *Annalen der Physik* 322.8 (1905). [_eprint: https://onlinelibrary.wiley.com/doi/pdf/10.1002/andp.19053220806](https://onlinelibrary.wiley.com/doi/pdf/10.1002/andp.19053220806), pp. 549–560. doi: [10.1002/andp.19053220806](https://doi.org/10.1002/andp.19053220806) (cited on page 16).
- [84] Li-Fang Wang et al. 'Molecular dynamics studies of hydrogen diffusion in tungsten at elevated temperature: Concentration dependence and defect effects'. en. In: *International Journal of Hydrogen Energy* 45.1 (Jan. 2020), pp. 822–834. doi: [10.1016/j.ijhydene.2019.10.151](https://doi.org/10.1016/j.ijhydene.2019.10.151) (cited on page 16).
- [85] X. W. Zhou et al. 'Molecular Dynamics Simulations of Hydrogen Diffusion in Aluminum'. en. In: *The Journal of Physical Chemistry C* 120.14 (Apr. 2016), pp. 7500–7509. doi: [10.1021/acs.jpcc.6b01802](https://doi.org/10.1021/acs.jpcc.6b01802) (cited on page 16).
- [86] D. Kato et al. 'Super-saturated hydrogen effects on radiation damages in tungsten under the high-flux divertor plasma irradiation'. en. In: *Nuclear Fusion* 55.8 (July 2015), p. 083019. doi: [10.1088/0029-5515/55/8/083019](https://doi.org/10.1088/0029-5515/55/8/083019) (cited on page 16).
- [87] Yi-Nan Liu et al. 'Hydrogen diffusion in tungsten: A molecular dynamics study'. en. In: *Journal of Nuclear Materials*. Proceedings of the 16th International Conference on Fusion Reactor Materials (ICFRM-16) 455.1 (Dec. 2014), pp. 676–680. doi: [10.1016/j.jnucmat.2014.09.003](https://doi.org/10.1016/j.jnucmat.2014.09.003) (cited on page 16).
- [88] T. Faney and B. D. Wirth. 'Spatially dependent cluster dynamics modeling of microstructure evolution in low energy helium irradiated tungsten'. en. In: *Modelling and Simulation in Materials Science and Engineering* 22.6 (Aug. 2014), p. 065010. doi: [10.1088/0965-0393/22/6/065010](https://doi.org/10.1088/0965-0393/22/6/065010) (cited on pages 16, 23, 91, 94).
- [89] T. Faney, S. I. Krasheninnikov, and B. D. Wirth. 'Spatially dependent cluster dynamics model of He plasma surface interaction in tungsten for fusion relevant conditions'. en. In: *Nuclear Fusion* 55.1 (2015), p. 013014. doi: [10.1088/0029-5515/55/1/013014](https://doi.org/10.1088/0029-5515/55/1/013014) (cited on pages 16, 18, 23, 92, 93, 95, 98, 100).
- [90] Faiza Sefta. 'Surface Response of Tungsten to Helium and Hydrogen Plasma Flux as a Function of Temperature and Incident Kinetic Energy'. en. PhD thesis. UC Berkeley, 2013 (cited on pages 16, 23, 25).
- [91] Danny Perez et al. 'The mobility of small vacancy/helium complexes in tungsten and its impact on retention in fusion-relevant conditions'. eng. In: *Scientific Reports* 7.1 (2017), p. 2522. doi: [10.1038/s41598-017-02428-2](https://doi.org/10.1038/s41598-017-02428-2) (cited on pages 16, 22).
- [92] G. Holzner et al. 'Solute diffusion of hydrogen isotopes in tungsten—a gas loading experiment'. en. In: *Physica Scripta* T171 (Jan. 2020). Publisher: IOP Publishing, p. 014034. doi: [10.1088/1402-4896/ab4b42](https://doi.org/10.1088/1402-4896/ab4b42) (cited on page 17).
- [93] R. Frauenfelder. 'Solution and Diffusion of Hydrogen in Tungsten'. In: *Journal of Vacuum Science and Technology* 6.3 (May 1969), pp. 388–397. doi: [10.1116/1.1492699](https://doi.org/10.1116/1.1492699) (cited on pages 17, 57, 58, 108, 109).
- [94] R. A. Anderl, D. F. Holland, and G. R. Longhurst. 'Hydrogen transport behavior of metal coatings for plasma-facing components'. en. In: *Journal of Nuclear Materials* 176-177 (Dec. 1990), pp. 683–689. doi: [10.1016/0022-3115\(90\)90127-9](https://doi.org/10.1016/0022-3115(90)90127-9) (cited on page 17).
- [95] R. A. Anderl et al. 'Deuterium Transport and Trapping in Polycrystalline Tungsten'. In: *Fusion Technology* 21.2P2 (Mar. 1992), pp. 745–752. doi: [10.13182/FST92-A29837](https://doi.org/10.13182/FST92-A29837) (cited on pages 17, 55).
- [96] Rémi Delaporte-Mathurin and Jhdark. *RemDelaporteMathurin/h-transport-materials: Release 0.4.0*. June 2022. doi: [10.5281/ZENODO.6627157](https://doi.org/10.5281/ZENODO.6627157). URL: <https://zenodo.org/record/6627157> (cited on pages 18, 21).
- [97] Mykola Ialovega et al. 'Hydrogen trapping in tungsten: impact of helium irradiation and thermal cycling'. en. In: *Physica Scripta* T171 (Jan. 2020). Publisher: IOP Publishing, p. 014066. doi: [10.1088/1402-4896/ab68bd](https://doi.org/10.1088/1402-4896/ab68bd) (cited on pages 19, 23, 28, 96, 108–110, 113).
- [98] Jie Hou et al. 'Predictive model of hydrogen trapping and bubbling in nanovoids in bcc metals'. en. In: *Nature Materials* 18.8 (Aug. 2019), pp. 833–839. doi: [10.1038/s41563-019-0422-4](https://doi.org/10.1038/s41563-019-0422-4) (cited on page 18).
- [99] A. De Backer et al. 'Hydrogen accumulation around dislocation loops and edge dislocations: from atomistic to mesoscopic scales in BCC tungsten'. en. In: *Physica Scripta* T170 (Nov. 2017), p. 014073. doi: [10.1088/1402-4896/aa9400](https://doi.org/10.1088/1402-4896/aa9400) (cited on page 18).

- [100] A. De Backer et al. 'Multiscale modelling of the interaction of hydrogen with interstitial defects and dislocations in BCC tungsten'. en. In: *Nuclear Fusion* 58.1 (Nov. 2017), p. 016006. doi: [10.1088/1741-4326/aa8e0c](https://doi.org/10.1088/1741-4326/aa8e0c) (cited on page 18).
- [101] N. Fernandez, Y. Ferro, and D. Kato. 'Hydrogen diffusion and vacancies formation in tungsten: Density Functional Theory calculations and statistical models'. In: *Acta Materialia* 94 (Aug. 2015), pp. 307–318. doi: [10.1016/j.actamat.2015.04.052](https://doi.org/10.1016/j.actamat.2015.04.052) (cited on pages 18, 57, 58).
- [102] Guang-Hong Lu, Hong-Bo Zhou, and Charlotte S. Becquart. 'A review of modelling and simulation of hydrogen behaviour in tungsten at different scales'. en. In: *Nuclear Fusion* 54.8 (July 2014), p. 086001. doi: [10.1088/0029-5515/54/8/086001](https://doi.org/10.1088/0029-5515/54/8/086001) (cited on page 18).
- [103] K. Heinola et al. 'Hydrogen interaction with point defects in tungsten'. In: *Physical Review B* 82.9 (Sept. 2010). Publisher: American Physical Society, p. 094102. doi: [10.1103/PhysRevB.82.094102](https://doi.org/10.1103/PhysRevB.82.094102) (cited on page 18).
- [104] Hong-Bo Zhou et al. 'Investigating behaviours of hydrogen in a tungsten grain boundary by first principles: from dissolution and diffusion to a trapping mechanism'. en. In: *Nuclear Fusion* 50.2 (Jan. 2010). Publisher: IOP Publishing, p. 025016. doi: [10.1088/0029-5515/50/2/025016](https://doi.org/10.1088/0029-5515/50/2/025016) (cited on page 18).
- [105] Etienne Hodille. 'Study and modeling of the deuterium trapping in ITER relevant materials'. en. PhD thesis. Aix-Marseille, Nov. 2016 (cited on pages 20, 29, 34).
- [106] O. V Ogorodnikova, J Roth, and M Mayer. 'Deuterium retention in tungsten in dependence of the surface conditions'. In: *Journal of Nuclear Materials. Plasma-Surface Interactions in Controlled Fusion Devices* 15 313-316 (Mar. 2003), pp. 469–477. doi: [10.1016/S0022-3115\(02\)01375-2](https://doi.org/10.1016/S0022-3115(02)01375-2) (cited on pages 18, 47, 49, 50).
- [107] Etienne Augustin Hodille et al. 'Modelling tritium adsorption and desorption from tungsten dust particles with a surface kinetic model'. en. In: *Nuclear Fusion* (2021). doi: [10.1088/1741-4326/ac0f37](https://doi.org/10.1088/1741-4326/ac0f37) (cited on page 19).
- [108] K. Heinola and T. Ahlgren. 'First-principles study of H on the reconstructed W(100) surface'. In: *Physical Review B* 81.7 (Feb. 2010). Publisher: American Physical Society, p. 073409. doi: [10.1103/PhysRevB.81.073409](https://doi.org/10.1103/PhysRevB.81.073409) (cited on page 19).
- [109] P. Alnot, A. Cassuto, and D. A. King. 'Adsorption and desorption kinetics with no precursor trapping: Hydrogen and deuterium on W {100}'. en. In: *Surface Science* 215.1 (May 1989), pp. 29–46. doi: [10.1016/0039-6028\(89\)90697-3](https://doi.org/10.1016/0039-6028(89)90697-3) (cited on page 19).
- [110] P. W. Tamm and L. D. Schmidt. 'Interaction of H₂ with (100)W. II. Condensation'. In: *The Journal of Chemical Physics* 52.3 (Feb. 1970). Publisher: American Institute of Physics, pp. 1150–1160. doi: [10.1063/1.1673110](https://doi.org/10.1063/1.1673110) (cited on page 19).
- [111] A. Dunand et al. 'Surface oxygen versus native oxide on tungsten: contrasting effects on deuterium retention and release'. en. In: *Nuclear Fusion* 62.5 (Mar. 2022). Publisher: IOP Publishing, p. 054002. doi: [10.1088/1741-4326/ac583a](https://doi.org/10.1088/1741-4326/ac583a) (cited on page 19).
- [112] J. E Whitten and R Gomer. 'The coadsorption of H and O on the W(110) plane'. en. In: *Surface Science* 409.1 (June 1998), pp. 16–26. doi: [10.1016/S0039-6028\(98\)00188-5](https://doi.org/10.1016/S0039-6028(98)00188-5) (cited on page 19).
- [113] Donald F. Johnson and Emily A. Carter. 'Hydrogen in tungsten: Absorption, diffusion, vacancy trapping, and decohesion'. en. In: *Journal of Materials Research* 25.2 (Feb. 2010), pp. 315–327. doi: [10.1557/JMR.2010.0036](https://doi.org/10.1557/JMR.2010.0036) (cited on page 19).
- [114] A. Nojima and K. Yamashita. 'A theoretical study of hydrogen adsorption and diffusion on a W(110) surface'. en. In: *Surface Science* 601.14 (July 2007), pp. 3003–3011. doi: [10.1016/j.susc.2007.05.019](https://doi.org/10.1016/j.susc.2007.05.019) (cited on page 19).
- [115] M. Ajmalghan et al. 'Surface coverage dependent mechanisms for the absorption and desorption of hydrogen from the W(110) and W(111) surfaces: a density functional theory investigation'. en. In: *Nuclear Fusion* 59.10 (Aug. 2019). Publisher: IOP Publishing, p. 106022. doi: [10.1088/1741-4326/ab33e7](https://doi.org/10.1088/1741-4326/ab33e7) (cited on page 19).

- [116] Alfons H. M. Krom and Ad Bakker. 'Hydrogen trapping models in steel'. en. In: *Metallurgical and Materials Transactions B* 31.6 (Dec. 2000), pp. 1475–1482. doi: [10.1007/s11663-000-0032-0](https://doi.org/10.1007/s11663-000-0032-0) (cited on page 20).
- [117] Ali Y. Hamid et al. 'Molecular dynamics simulations of helium clustering and bubble growth under tungsten surfaces'. en. In: *Computational Materials Science* 163 (June 2019), pp. 141–147. doi: [10.1016/j.commatsci.2019.03.008](https://doi.org/10.1016/j.commatsci.2019.03.008) (cited on pages 22, 23).
- [118] Karl D. Hammond et al. 'Large-scale atomistic simulations of low-energy helium implantation into tungsten single crystals'. In: *Acta Materialia* 144 (Feb. 2018), pp. 561–578. doi: [10.1016/j.actamat.2017.09.061](https://doi.org/10.1016/j.actamat.2017.09.061) (cited on page 22).
- [119] Charlotte S. Becquart and Christophe Domain. 'A density functional theory assessment of the clustering behaviour of He and H in tungsten'. en. In: *Journal of Nuclear Materials. Fusion Reactor Materials* 386-388 (Apr. 2009), pp. 109–111. doi: [10.1016/j.jnucmat.2008.12.085](https://doi.org/10.1016/j.jnucmat.2008.12.085) (cited on page 22).
- [120] A. Y. Dunn et al. 'A rate theory study of helium bubble formation and retention in Cu–Nb nanocomposites'. en. In: *Journal of Nuclear Materials* 435.1 (Apr. 2013), pp. 141–152. doi: [10.1016/j.jnucmat.2012.12.041](https://doi.org/10.1016/j.jnucmat.2012.12.041) (cited on page 22).
- [121] K. O. E. Henriksson, K. Nordlund, and J. Keinonen. 'Molecular dynamics simulations of helium cluster formation in tungsten'. en. In: *Nuclear Instruments and Methods in Physics Research Section B: Beam Interactions with Materials and Atoms* 244.2 (Mar. 2006), pp. 377–391. doi: [10.1016/j.nimb.2005.10.020](https://doi.org/10.1016/j.nimb.2005.10.020) (cited on page 22).
- [122] K. O. E. Henriksson et al. 'Difference in formation of hydrogen and helium clusters in tungsten'. en. In: *Applied Physics Letters* 87.16 (Oct. 2005), p. 163113. doi: [10.1063/1.2103390](https://doi.org/10.1063/1.2103390) (cited on page 22).
- [123] A. De Backer et al. 'Modeling of helium bubble nucleation and growth in austenitic stainless steels using an Object Kinetic Monte Carlo method'. en. In: *Nuclear Instruments and Methods in Physics Research Section B: Beam Interactions with Materials and Atoms. Proceedings of the 12th International Conference on Computer Simulation of Radiation Effects in Solids*, Alacant, Spain, 8-13 June, 2014 352 (June 2015), pp. 107–114. doi: [10.1016/j.nimb.2014.11.110](https://doi.org/10.1016/j.nimb.2014.11.110) (cited on page 22).
- [124] Sophie Blondel et al. 'Modeling Helium Segregation to the Surfaces of Plasma-Exposed Tungsten as a Function of Temperature and Surface Orientation'. In: *Fusion Science and Technology* 71.1 (Jan. 2017), pp. 22–35. doi: [10.13182/FST16-112](https://doi.org/10.13182/FST16-112) (cited on page 22).
- [125] Lin Hu et al. 'Interactions of mobile helium clusters with surfaces and grain boundaries of plasma-exposed tungsten'. In: *Journal of Applied Physics* 115.17 (May 2014), p. 173512. doi: [10.1063/1.4874675](https://doi.org/10.1063/1.4874675) (cited on page 22).
- [126] Lin Hu et al. 'Dynamics of small mobile helium clusters near tungsten surfaces'. en. In: *Surface Science* 626 (Aug. 2014), pp. L21–L25. doi: [10.1016/j.susc.2014.03.020](https://doi.org/10.1016/j.susc.2014.03.020) (cited on page 22).
- [127] K. Morishita. 'Nucleation path of helium bubbles in metals during irradiation'. In: *Philosophical Magazine* 87.7 (Mar. 2007), pp. 1139–1158. doi: [10.1080/14786430601096910](https://doi.org/10.1080/14786430601096910) (cited on page 22).
- [128] J. B. Condon and T. Schober. 'Hydrogen bubbles in metals'. In: *Journal of Nuclear Materials* 207 (Dec. 1993), pp. 1–24. doi: [10.1016/0022-3115\(93\)90244-5](https://doi.org/10.1016/0022-3115(93)90244-5) (cited on page 22).
- [129] Karl D. Hammond et al. 'Helium flux effects on bubble growth and surface morphology in plasma-facing tungsten from large-scale molecular dynamics simulations'. en. In: *Nuclear Fusion* 59.6 (May 2019), p. 066035. doi: [10.1088/1741-4326/ab12f6](https://doi.org/10.1088/1741-4326/ab12f6) (cited on pages 23, 25).
- [130] Wei Zhang et al. 'Simulation of migration and coalescence of helium bubbles in nickel'. en. In: *Journal of Nuclear Materials* 518 (May 2019), pp. 48–53. doi: [10.1016/j.jnucmat.2019.02.023](https://doi.org/10.1016/j.jnucmat.2019.02.023) (cited on page 23).
- [131] Mykola Ialovega. 'Surface Conditions of Tungsten Components: Impact on Hydrogen Inventory'. These de doctorat. Aix-Marseille, Feb. 2021 (cited on pages 23, 96).
- [132] N. C. Pyper et al. 'Excited helium under high pressures in the bulk and in nanobubbles'. In: *Philosophical Magazine Letters* 97.8 (Aug. 2017). Publisher: Taylor & Francis_eprint: <https://doi.org/10.1080/09500839.2017.1347724>, pp. 295–303. doi: [10.1080/09500839.2017.1347724](https://doi.org/10.1080/09500839.2017.1347724) (cited on page 23).

- [133] W. Q. Chen et al. 'Irradiation hardening induced by blistering in tungsten due to low-energy high flux hydrogen plasma exposure'. en. In: *Journal of Nuclear Materials* 522 (Aug. 2019), pp. 11–18. doi: [10.1016/j.jnucmat.2019.05.004](https://doi.org/10.1016/j.jnucmat.2019.05.004) (cited on page 24).
- [134] M. J. Baldwin and R. P. Doerner. 'Formation of helium induced nanostructure 'fuzz' on various tungsten grades'. en. In: *Journal of Nuclear Materials* 404.3 (Sept. 2010), pp. 165–173. doi: [10.1016/j.jnucmat.2010.06.034](https://doi.org/10.1016/j.jnucmat.2010.06.034) (cited on pages 24, 26).
- [135] A. A. Haasz, M. Poon, and J. W. Davis. 'The effect of ion damage on deuterium trapping in tungsten'. en. In: *Journal of Nuclear Materials* 266-269 (Mar. 1999), pp. 520–525. doi: [10.1016/S0022-3115\(98\)00586-8](https://doi.org/10.1016/S0022-3115(98)00586-8) (cited on page 24).
- [136] Y. Ueda et al. 'Hydrogen blister formation and cracking behavior for various tungsten materials'. en. In: *Journal of Nuclear Materials*. PSI-16 337-339 (Mar. 2005), pp. 1010–1014. doi: [10.1016/j.jnucmat.2004.10.077](https://doi.org/10.1016/j.jnucmat.2004.10.077) (cited on page 24).
- [137] Wenmin Wang et al. 'Blister formation of tungsten due to ion bombardment'. en. In: *Journal of Nuclear Materials* 299.2 (Nov. 2001), pp. 124–131. doi: [10.1016/S0022-3115\(01\)00679-1](https://doi.org/10.1016/S0022-3115(01)00679-1) (cited on page 24).
- [138] T. Shimada et al. 'Blister formation in tungsten by hydrogen and carbon mixed ion beam irradiation'. en. In: *Journal of Nuclear Materials*. Plasma-Surface Interactions in Controlled Fusion Devices 15 313-316 (Mar. 2003), pp. 204–208. doi: [10.1016/S0022-3115\(02\)01447-2](https://doi.org/10.1016/S0022-3115(02)01447-2) (cited on page 24).
- [139] Yulu Zhou et al. 'The growth and release of helium bubbles near tungsten surface studied with molecular dynamics simulations'. en. In: *Nuclear Instruments and Methods in Physics Research Section B: Beam Interactions with Materials and Atoms* 455 (Sept. 2019), pp. 66–73. doi: [10.1016/j.nimb.2019.06.023](https://doi.org/10.1016/j.nimb.2019.06.023) (cited on page 25).
- [140] Faiza Sefta, Niklas Juslin, and Brian D. Wirth. 'Helium bubble bursting in tungsten'. In: *Journal of Applied Physics* 114.24 (Dec. 2013), p. 243518. doi: [10.1063/1.4860315](https://doi.org/10.1063/1.4860315) (cited on page 25).
- [141] Sophie Blondel et al. 'Continuum-scale modeling of helium bubble bursting under plasma-exposed tungsten surfaces'. en. In: *Nuclear Fusion* 58.12 (Nov. 2018), p. 126034. doi: [10.1088/1741-4326/aae8ef](https://doi.org/10.1088/1741-4326/aae8ef) (cited on pages 25, 29).
- [142] G. M. Wright et al. 'Tungsten nano-tendrils growth in the Alcator C-Mod divertor'. en. In: *Nuclear Fusion* 52.4 (Mar. 2012), p. 042003. doi: [10.1088/0029-5515/52/4/042003](https://doi.org/10.1088/0029-5515/52/4/042003) (cited on pages 25, 26).
- [143] C. Grisolia et al. 'Tritium absorption and desorption in ITER relevant materials: comparative study of tungsten dust and massive samples'. en. In: *Journal of Nuclear Materials*. PLASMA-SURFACE INTERACTIONS 21 463 (Aug. 2015), pp. 885–888. doi: [10.1016/j.jnucmat.2014.10.089](https://doi.org/10.1016/j.jnucmat.2014.10.089) (cited on page 26).
- [144] D. Nishijima et al. 'Sputtering properties of tungsten 'fuzzy' surfaces'. en. In: *Journal of Nuclear Materials*. Proceedings of the 19th International Conference on Plasma-Surface Interactions in Controlled Fusion 415.1, Supplement (Aug. 2011), S96–S99. doi: [10.1016/j.jnucmat.2010.12.017](https://doi.org/10.1016/j.jnucmat.2010.12.017) (cited on page 26).
- [145] M. J. Baldwin et al. 'The effects of high fluence mixed-species (deuterium, helium, beryllium) plasma interactions with tungsten'. en. In: *Journal of Nuclear Materials*. Proceedings of the 18th International Conference on Plasma-Surface Interactions in Controlled Fusion Device 390-391 (June 2009), pp. 886–890. doi: [10.1016/j.jnucmat.2009.01.247](https://doi.org/10.1016/j.jnucmat.2009.01.247) (cited on page 26).
- [146] M. J. Baldwin and R. P. Doerner. 'Helium induced nanoscopic morphology on tungsten under fusion relevant plasma conditions'. en. In: *Nuclear Fusion* 48.3 (Jan. 2008), p. 035001. doi: [10.1088/0029-5515/48/3/035001](https://doi.org/10.1088/0029-5515/48/3/035001) (cited on page 26).
- [147] K. B. Woller, D. G. Whyte, and G. M. Wright. 'Dynamic measurement of the helium concentration of evolving tungsten nanostructures using Elastic Recoil Detection during plasma exposure'. en. In: *Journal of Nuclear Materials*. PLASMA-SURFACE INTERACTIONS 21 463 (Aug. 2015), pp. 289–293. doi: [10.1016/j.jnucmat.2014.11.126](https://doi.org/10.1016/j.jnucmat.2014.11.126) (cited on page 26).
- [148] Karl D. Hammond. 'Helium, hydrogen, and fuzz in plasma-facing materials'. en. In: *Materials Research Express* 4.10 (Oct. 2017), p. 104002. doi: [10.1088/2053-1591/aa8c22](https://doi.org/10.1088/2053-1591/aa8c22) (cited on page 26).

- [149] M. Wirtz et al. 'Influence of helium induced nanostructures on the thermal shock performance of tungsten'. In: *Nuclear Materials and Energy* 9 (Dec. 2016), pp. 177–180. doi: [10.1016/j.nme.2016.07.002](https://doi.org/10.1016/j.nme.2016.07.002) (cited on pages 26, 27).
- [150] Shuichi Takamura et al. 'Formation of Nanostructured Tungsten with Arborescent Shape due to Helium Plasma Irradiation'. In: *Plasma and Fusion Research* 1 (2006), pp. 051–051. doi: [10.1585/pfr.1.051](https://doi.org/10.1585/pfr.1.051) (cited on page 26).
- [151] Patrick McCarthy et al. 'Enhanced fuzzy tungsten growth in the presence of tungsten deposition'. en. In: *Nuclear Fusion* 60.2 (Jan. 2020), p. 026012. doi: [10.1088/1741-4326/ab6060](https://doi.org/10.1088/1741-4326/ab6060) (cited on page 27).
- [152] Chunjie Niu et al. 'Effect of temperature on the growth and surface bursting of He nano-bubbles in W under fusion-relevant He ion irradiations'. en. In: *Fusion Engineering and Design* 163 (Feb. 2021), p. 112159. doi: [10.1016/j.fusengdes.2020.112159](https://doi.org/10.1016/j.fusengdes.2020.112159) (cited on page 27).
- [153] Gregory De Temmerman et al. 'Nanostructuring of molybdenum and tungsten surfaces by low-energy helium ions'. en. In: *Journal of Vacuum Science & Technology A: Vacuum, Surfaces, and Films* 30.4 (July 2012), p. 041306. doi: [10.1116/1.4731196](https://doi.org/10.1116/1.4731196) (cited on page 27).
- [154] Nathan Lemahieu et al. 'H/He irradiation on tungsten exposed to ELM-like thermal shocks'. en. In: *Fusion Engineering and Design*. Proceedings of the 12th International Symposium on Fusion Nuclear Technology-12 (ISFNT-12) 109-111 (Nov. 2016), pp. 169–174. doi: [10.1016/j.fusengdes.2016.03.035](https://doi.org/10.1016/j.fusengdes.2016.03.035) (cited on page 27).
- [155] Shuang Cui et al. 'Thermal conductivity reduction of tungsten plasma facing material due to helium plasma irradiation in PISCES using the improved 3-omega method'. In: *Journal of Nuclear Materials* 486 (Apr. 2017), pp. 267–273. doi: [10.1016/j.jnucmat.2017.01.023](https://doi.org/10.1016/j.jnucmat.2017.01.023) (cited on page 27).
- [156] L. Buzi et al. 'Response of tungsten surfaces to helium and hydrogen plasma exposure under ITER relevant steady state and repetitive transient conditions'. en. In: *Nuclear Fusion* 57.12 (Sept. 2017), p. 126009. doi: [10.1088/1741-4326/aa81e4](https://doi.org/10.1088/1741-4326/aa81e4) (cited on page 27).
- [157] K Tokunaga et al. 'Synergistic effects of high heat loading and helium irradiation of tungsten'. en. In: *Journal of Nuclear Materials*. Proceedings of the 11th International Conference on Fusion Reactor Materials (ICFRM-11) 329-333 (Aug. 2004), pp. 757–760. doi: [10.1016/j.jnucmat.2004.04.178](https://doi.org/10.1016/j.jnucmat.2004.04.178) (cited on page 27).
- [158] H. T. Lee et al. 'Hydrogen and helium trapping in tungsten under simultaneous irradiations'. en. In: *Journal of Nuclear Materials*. Plasma-Surface Interactions-17 363-365 (June 2007), pp. 898–903. doi: [10.1016/j.jnucmat.2007.01.111](https://doi.org/10.1016/j.jnucmat.2007.01.111) (cited on pages 27, 28).
- [159] Z. J. Bergstrom, M. A. Cusentino, and B. D. Wirth. 'A Molecular Dynamics Study of Subsurface Hydrogen-Helium Bubbles in Tungsten'. In: *Fusion Science and Technology* 71.1 (Jan. 2017), pp. 122–135. doi: [10.13182/FST16-121](https://doi.org/10.13182/FST16-121) (cited on page 28).
- [160] Y. Ueda et al. 'Simultaneous irradiation effects of hydrogen and helium ions on tungsten'. en. In: *Journal of Nuclear Materials*. Fusion Reactor Materials 386-388 (Apr. 2009), pp. 725–728. doi: [10.1016/j.jnucmat.2008.12.300](https://doi.org/10.1016/j.jnucmat.2008.12.300) (cited on page 28).
- [161] M. Miyamoto et al. 'Microscopic damage of tungsten exposed to deuterium–helium mixture plasma in PISCES and its impacts on retention property'. en. In: *Journal of Nuclear Materials*. Proceedings of the 19th International Conference on Plasma-Surface Interactions in Controlled Fusion 415.1, Supplement (Aug. 2011), S657–S660. doi: [10.1016/j.jnucmat.2011.01.008](https://doi.org/10.1016/j.jnucmat.2011.01.008) (cited on page 28).
- [162] S. Markelj, T. Schwarz-Selinger, and A. Založnik. 'Hydrogen isotope accumulation in the helium implantation zone in tungsten'. en. In: *Nuclear Fusion* 57.6 (Apr. 2017), p. 064002. doi: [10.1088/1741-4326/aa6b27](https://doi.org/10.1088/1741-4326/aa6b27) (cited on page 28).
- [163] Luigi Candido et al. 'An integrated hydrogen isotopes transport model for the TRIEX-II facility'. en. In: *Fusion Engineering and Design* 155 (June 2020), p. 111585. doi: [10.1016/j.fusengdes.2020.111585](https://doi.org/10.1016/j.fusengdes.2020.111585) (cited on pages 28, 29).
- [164] Stephen Dixon. *aurora-multiphysics/achlys: Isotope self-diffusion*. Dec. 2021. doi: [10.5281/zenodo.6412090](https://doi.org/10.5281/zenodo.6412090). URL: <https://zenodo.org/record/6412090> (cited on pages 28, 29).

- [165] Glen R. Longhurst. *TMAP7 User Manual*. English. Tech. rep. INEEL/EXT-04-02352. Idaho National Laboratory (INL), Dec. 2008. doi: [10.2172/952013](https://doi.org/10.2172/952013) (cited on pages 29, 51, 53).
- [166] Chaofeng Sang et al. 'Modelling of hydrogen isotope inventory in mixed materials including porous deposited layers in fusion devices'. en. In: *Nuclear Fusion* 52.4 (Mar. 2012), p. 043003. doi: [10.1088/0029-5515/52/4/043003](https://doi.org/10.1088/0029-5515/52/4/043003) (cited on page 29).
- [167] D. Matveev et al. 'Reaction-diffusion modeling of hydrogen transport and surface effects in application to single-crystalline Be'. en. In: *Nuclear Instruments and Methods in Physics Research Section B: Beam Interactions with Materials and Atoms* 430 (Sept. 2018), pp. 23–30. doi: [10.1016/j.nimb.2018.05.037](https://doi.org/10.1016/j.nimb.2018.05.037) (cited on page 29).
- [168] K. Schmid, U. von Toussaint, and T. Schwarz-Selinger. 'Transport of hydrogen in metals with occupancy dependent trap energies'. In: *Journal of Applied Physics* 116.13 (Oct. 2014). Publisher: American Institute of Physics, p. 134901. doi: [10.1063/1.4896580](https://doi.org/10.1063/1.4896580) (cited on page 29).
- [169] A McNabb and P K. Foster. 'A new analysis of the diffusion of hydrogen in iron and ferritic steels'. In: *Transactions of the Metallurgical Society of AIME* 227 (1963), pp. 618–627 (cited on page 31).
- [170] F. Waelbroeck et al. *Influence of bulk and surface phenomena on the hydrogen permeation through metals*. Tech. rep. Juel-1966 INIS Reference Number: 16053332. Germany, 1984, p. 201 (cited on page 32).
- [171] Klaus Schmid and Mikhail Zibrov. 'On the use of recombination rate coefficients in hydrogen transport calculations'. en. In: *Nuclear Fusion* (2021). doi: [10.1088/1741-4326/ac07b2](https://doi.org/10.1088/1741-4326/ac07b2) (cited on page 32).
- [172] M. A. Pick and K. Sonnenberg. 'A model for atomic hydrogen-metal interactions — application to recycling, recombination and permeation'. en. In: *Journal of Nuclear Materials* 131.2 (Apr. 1985), pp. 208–220. doi: [10.1016/0022-3115\(85\)90459-3](https://doi.org/10.1016/0022-3115(85)90459-3) (cited on page 32).
- [173] James F. Ziegler, M. D. Ziegler, and J. P. Biersack. 'SRIM – The stopping and range of ions in matter (2010)'. In: *Nuclear Instruments and Methods in Physics Research Section B: Beam Interactions with Materials and Atoms*. 19th International Conference on Ion Beam Analysis 268.11 (June 2010), pp. 1818–1823. doi: [10.1016/j.nimb.2010.02.091](https://doi.org/10.1016/j.nimb.2010.02.091) (cited on pages 33, 74, 95, 109).
- [174] M. Shimada and C. N. Taylor. 'Improved tritium retention modeling with reaction-diffusion code TMAP and bulk depth profiling capability'. en. In: *Nuclear Materials and Energy* 19 (May 2019), pp. 273–278. doi: [10.1016/j.nme.2019.03.008](https://doi.org/10.1016/j.nme.2019.03.008) (cited on page 33).
- [175] K. Schmid. 'Diffusion-trapping modelling of hydrogen recycling in tungsten under ELM-like heat loads'. en. In: *Physica Scripta* T167 (Jan. 2016). Publisher: IOP Publishing, p. 014025. doi: [10.1088/0031-8949/T167/1/014025](https://doi.org/10.1088/0031-8949/T167/1/014025) (cited on pages 33, 69).
- [176] Michael Smith. *ABAQUS/Standard User's Manual, Version 6.9*. English. 2009 (cited on page 35).
- [177] D. R. Poirier and G. H. Geiger. 'Correlations and Data for Heat Transfer Coefficients'. en. In: *Transport Phenomena in Materials Processing*. Ed. by D. R. Poirier and G. H. Geiger. Cham: Springer International Publishing, 2016, pp. 247–279. doi: [10.1007/978-3-319-48090-9_8](https://doi.org/10.1007/978-3-319-48090-9_8) (cited on page 36).
- [178] Rémi Delaporte-Mathurin et al. 'Finite element analysis of hydrogen retention in ITER plasma facing components using FESTIM'. en. In: *Nuclear Materials and Energy* 21 (Dec. 2019), p. 100709. doi: [10.1016/j.nme.2019.100709](https://doi.org/10.1016/j.nme.2019.100709) (cited on pages 36, 47, 67, 115).
- [179] Daniel Arndt et al. 'The deal.II finite element library: Design, features, and insights'. en. In: *Computers & Mathematics with Applications*. Development and Application of Open-source Software for Problems with Numerical PDEs 81 (Jan. 2021), pp. 407–422. doi: [10.1016/j.camwa.2020.02.022](https://doi.org/10.1016/j.camwa.2020.02.022) (cited on page 36).
- [180] Tzanio Kolev and Veselin Dobrev. *Modular Finite Element Methods (MFEM)*. Language: en. 2010. doi: [10.11578/DC.20171025.1248](https://doi.org/10.11578/DC.20171025.1248). URL: <https://www.osti.gov/doecode/biblio/35738> (cited on page 36).
- [181] Cody J. Permann et al. 'MOOSE: Enabling massively parallel multiphysics simulation'. en. In: *SoftwareX* 11 (Jan. 2020), p. 100430. doi: [10.1016/j.softx.2020.100430](https://doi.org/10.1016/j.softx.2020.100430) (cited on page 36).
- [182] F. Hecht. 'New development in freefem++'. en. In: *Journal of Numerical Mathematics* 20.3-4 (Jan. 2012). doi: [10.1515/jnum-2012-0013](https://doi.org/10.1515/jnum-2012-0013) (cited on page 36).

- [183] Martin Alnæs et al. 'The FEniCS Project Version 1.5'. en. In: *Archive of Numerical Software* 3.100 (Dec. 2015). doi: [10.11588/ans.2015.100.20553](https://doi.org/10.11588/ans.2015.100.20553) (cited on pages 36, 95).
- [184] Anders Logg, Kent-Andre Mardal, and Garth Wells. *Automated Solution of Differential Equations by the Finite Element Method*. en. 1st ed. 2012 (cited on page 36).
- [185] James Paul Ahrens, Berk Geveci, and Charles Chi Wang Law. 'ParaView: An End-User Tool for Large-Data Visualization'. In: *The Visualization Handbook*. 2005. doi: [10.1016/B978-012387582-2/50038-1](https://doi.org/10.1016/B978-012387582-2/50038-1) (cited on page 40).
- [186] John D. Hunter. 'Matplotlib: A 2D Graphics Environment'. In: *Computing in Science Engineering* 9.3 (May 2007). Conference Name: Computing in Science Engineering, pp. 90–95. doi: [10.1109/MCSE.2007.55](https://doi.org/10.1109/MCSE.2007.55) (cited on page 40).
- [187] Charles R. Harris et al. 'Array programming with NumPy'. en. In: *Nature* 585.7825 (Sept. 2020). Bandiera_abtest: a Cc_license_type: cc_by Cg_type: Nature Research Journals Number: 7825 Primary_atype: Reviews Publisher: Nature Publishing Group Subject_term: Computational neuroscience;Computational science;Computer science;Software;Solar physics Subject_term_id: computational-neuroscience;computational-science;computer-science;software;solar-physics, pp. 357–362. doi: [10.1038/s41586-020-2649-2](https://doi.org/10.1038/s41586-020-2649-2) (cited on page 40).
- [188] *Periodic Table of the Finite Elements*. URL: <https://www-users.cse.umn.edu/~arnold/femtable/> (cited on page 40).
- [189] B. D. Dudson et al. 'Verification of BOUT++ by the method of manufactured solutions'. In: *Physics of Plasmas* 23.6 (June 2016), p. 062303. doi: [10.1063/1.4953429](https://doi.org/10.1063/1.4953429) (cited on pages 41, 42).
- [190] Patrick J. Roache. 'Code Verification by the Method of Manufactured Solutions'. en. In: *Journal of Fluids Engineering* 124.1 (Mar. 2002), pp. 4–10. doi: [10.1115/1.1436090](https://doi.org/10.1115/1.1436090) (cited on pages 41, 42).
- [191] Glen R. Longhurst and James Ambrosek. 'Verification and Validation of the Tritium Transport Code TMAP7'. In: *Fusion Science and Technology* 48.1 (Aug. 2005), pp. 468–471. doi: [10.13182/FST05-A967](https://doi.org/10.13182/FST05-A967) (cited on pages 41, 42).
- [192] J. H. Yu et al. 'Deuterium retention in re-solidified tungsten and beryllium'. In: *Nuclear Materials and Energy* 18 (Jan. 2019), pp. 297–306. doi: [10.1016/j.nme.2019.01.011](https://doi.org/10.1016/j.nme.2019.01.011) (cited on page 46).
- [193] E. A. Hodille et al. 'Macroscopic rate equation modeling of trapping/detrapping of hydrogen isotopes in tungsten materials'. In: *Journal of Nuclear Materials* 467 (Dec. 2015), pp. 424–431. doi: [10.1016/j.jnucmat.2015.06.041](https://doi.org/10.1016/j.jnucmat.2015.06.041) (cited on pages 46, 49, 55, 58).
- [194] Andreas Drexler et al. 'Model-based interpretation of thermal desorption spectra of Fe-C-Ti alloys'. en. In: *Journal of Alloys and Compounds* 789 (June 2019), pp. 647–657. doi: [10.1016/j.jallcom.2019.03.102](https://doi.org/10.1016/j.jallcom.2019.03.102) (cited on page 47).
- [195] Pauli Virtanen et al. 'SciPy 1.0: fundamental algorithms for scientific computing in Python'. en. In: *Nature Methods* 17.3 (Mar. 2020). Number: 3 Publisher: Nature Publishing Group, pp. 261–272. doi: [10.1038/s41592-019-0686-2](https://doi.org/10.1038/s41592-019-0686-2) (cited on pages 47, 128).
- [196] Jorge Nocedal and S. Wright. *Numerical Optimization*. en. 2nd ed. Springer Series in Operations Research and Financial Engineering. New York: Springer-Verlag, 2006 (cited on page 47).
- [197] Caitlin Hurley et al. 'Numerical modeling of thermal desorption mass spectroscopy (TDS) for the study of hydrogen diffusion and trapping interactions in metals'. en. In: *International Journal of Hydrogen Energy* 40.8 (Mar. 2015), pp. 3402–3414. doi: [10.1016/j.ijhydene.2015.01.001](https://doi.org/10.1016/j.ijhydene.2015.01.001) (cited on page 50).
- [198] R. A. Anderl et al. 'Deuterium transport in Cu, CuCrZr, and Cu/Be'. In: *Journal of Nuclear Materials* 266-269 (Mar. 1999), pp. 761–765. doi: [10.1016/S0022-3115\(98\)00878-2](https://doi.org/10.1016/S0022-3115(98)00878-2) (cited on pages 52, 56, 68).
- [199] O. V. Ogorodnikova. 'Recombination coefficient of hydrogen on tungsten surface'. en. In: *Journal of Nuclear Materials* 522 (Aug. 2019), pp. 74–79. doi: [10.1016/j.jnucmat.2019.05.017](https://doi.org/10.1016/j.jnucmat.2019.05.017) (cited on pages 55, 69).
- [200] F. Reiter, K. S. Forcey, and G. Gervasini. *A compilation of tritium : Material interaction parameters in fusion reactor materials*. en. Publications Office of the European Union, July 1996 (cited on pages 57, 58).

- [201] E Serra and A Perujo. 'Hydrogen and deuterium transport and inventory parameters in a Cu-0.65Cr-0.08Zr alloy for fusion reactor applications'. en. In: *Journal of Nuclear Materials* 258-263 (Oct. 1998), pp. 1028-1032. doi: [10.1016/S0022-3115\(98\)00276-1](https://doi.org/10.1016/S0022-3115(98)00276-1) (cited on pages 57, 58).
- [202] A. Aiello et al. 'Hydrogen Isotopes Permeability in Eurofer 97 Martensitic Steel'. In: *Fusion Science and Technology* 41.3P2 (May 2002), pp. 872-876. doi: [10.13182/FST41-872](https://doi.org/10.13182/FST41-872) (cited on page 57).
- [203] T.J. Dolan and R.A. Anderl. *Assessment of database for interaction of tritium with ITER plasma facing materials*. en. Tech. rep. EGG-FSP-11348, 10191406. Sept. 1994, EGG-FSP-11348, 10191406. doi: [10.2172/10191406](https://doi.org/10.2172/10191406) (cited on page 58).
- [204] J.B. Lister, A. Portone, and Y. Gribov. 'Plasma control in ITER'. In: *IEEE Control Systems Magazine* 26.2 (Apr. 2006). Conference Name: IEEE Control Systems Magazine, pp. 79-91. doi: [10.1109/MCS.2006.1615274](https://doi.org/10.1109/MCS.2006.1615274) (cited on page 62).
- [205] Etienne Augustin Hodille et al. 'Modelling of hydrogen isotopes trapping, diffusion and permeation in divertor monoblocks under ITER-like conditions'. en. In: *Nuclear Fusion* (2021). doi: [10.1088/1741-4326/ac2abc](https://doi.org/10.1088/1741-4326/ac2abc) (cited on page 64).
- [206] S. Benannoune et al. 'Numerical simulation by finite element modelling of diffusion and transient hydrogen trapping processes in plasma facing components'. In: *Nuclear Materials and Energy* 19 (May 2019), pp. 42-46. doi: [10.1016/j.nme.2019.01.023](https://doi.org/10.1016/j.nme.2019.01.023) (cited on page 66).
- [207] C. E Rasmussen and C. K. I. Williams. *Gaussian Processes for Machine Learning*. 2006 (cited on page 66).
- [208] Chris Bowman. *C-bowman/inference-tools: 0.5.3 release*. Apr. 2020. doi: [10.5281/zenodo.3757497](https://doi.org/10.5281/zenodo.3757497). URL: <https://zenodo.org/record/3757497#.XueCdUUzaUm> (cited on pages 66, 68, 102).
- [209] S. Brezinsek et al. 'Beryllium migration in JET ITER-like wall plasmas'. en. In: *Nuclear Fusion* 55.6 (May 2015). Publisher: IOP Publishing, p. 063021. doi: [10.1088/0029-5515/55/6/063021](https://doi.org/10.1088/0029-5515/55/6/063021) (cited on page 67).
- [210] K. Heinola et al. 'Fuel retention in JET ITER-Like Wall from post-mortem analysis'. en. In: *Journal of Nuclear Materials*. PLASMA-SURFACE INTERACTIONS 21 463 (Aug. 2015), pp. 961-965. doi: [10.1016/j.jnucmat.2014.12.098](https://doi.org/10.1016/j.jnucmat.2014.12.098) (cited on page 67).
- [211] C. Björkas and K. Nordlund. 'Variables affecting simulated Be sputtering yields'. en. In: *Journal of Nuclear Materials* 439.1 (Aug. 2013), pp. 174-179. doi: [10.1016/j.jnucmat.2013.04.036](https://doi.org/10.1016/j.jnucmat.2013.04.036) (cited on page 67).
- [212] Alice Hu and Ahmed Hassanein. 'Predicting hydrogen isotope inventory in plasma-facing components during normal and abnormal operations in fusion devices'. en. In: *Journal of Nuclear Materials* 465 (Oct. 2015), pp. 582-589. doi: [10.1016/j.jnucmat.2015.06.048](https://doi.org/10.1016/j.jnucmat.2015.06.048) (cited on page 68).
- [213] M. H. J. 't Hoen et al. 'Strongly Reduced Penetration of Atomic Deuterium in Radiation-Damaged Tungsten'. In: *Physical Review Letters* 111.22 (Nov. 2013). Publisher: American Physical Society, p. 225001. doi: [10.1103/PhysRevLett.111.225001](https://doi.org/10.1103/PhysRevLett.111.225001) (cited on page 69).
- [214] E. A. Hodille et al. 'Retention and release of hydrogen isotopes in tungsten plasma-facing components: the role of grain boundaries and the native oxide layer from a joint experiment-simulation integrated approach'. en. In: *Nuclear Fusion* 57.7 (May 2017). Publisher: IOP Publishing, p. 076019. doi: [10.1088/1741-4326/aa6d24](https://doi.org/10.1088/1741-4326/aa6d24) (cited on page 69).
- [215] Anže Založnik et al. 'Deuterium atom loading of self-damaged tungsten at different sample temperatures'. en. In: *Journal of Nuclear Materials* 496 (Dec. 2017), pp. 1-8. doi: [10.1016/j.jnucmat.2017.09.003](https://doi.org/10.1016/j.jnucmat.2017.09.003) (cited on page 69).
- [216] Matic Pečovnik et al. 'Influence of grain size on deuterium transport and retention in self-damaged tungsten'. en. In: *Journal of Nuclear Materials* 513 (Jan. 2019), pp. 198-208. doi: [10.1016/j.jnucmat.2018.10.026](https://doi.org/10.1016/j.jnucmat.2018.10.026) (cited on page 69).
- [217] Jerome Guterl, R. D. Smirnov, and P. Snyder. 'Effects of surface processes on hydrogen outgassing from metal in desorption experiments'. en. In: *Nuclear Fusion* 59.9 (Aug. 2019). Publisher: IOP Publishing, p. 096042. doi: [10.1088/1741-4326/ab280a](https://doi.org/10.1088/1741-4326/ab280a) (cited on page 69).

- [218] H. Bufferand et al. 'Three-dimensional modelling of edge multi-component plasma taking into account realistic wall geometry'. en. In: *Nuclear Materials and Energy* 18 (Jan. 2019), pp. 82–86. doi: [10.1016/j.nme.2018.11.025](https://doi.org/10.1016/j.nme.2018.11.025) (cited on page 71).
- [219] E. Kaveeva et al. 'SOLPS-ITER modelling of ITER edge plasma with drifts and currents'. en. In: *Nuclear Fusion* 60.4 (Mar. 2020). Publisher: IOP Publishing, p. 046019. doi: [10.1088/1741-4326/ab73c1](https://doi.org/10.1088/1741-4326/ab73c1) (cited on pages 71, 72).
- [220] S. J. Zweben. *Effect of Deuterium Gas Puff On The Edge Plasma In NSTX*. en. Tech. rep. PPPL-4999, 1129011. Feb. 2014, PPPL-4999, 1129011. doi: [10.2172/1129011](https://doi.org/10.2172/1129011) (cited on page 71).
- [221] W. Zhang et al. 'Scrape-off layer density tailoring with local gas puffing to maximize ICRF power coupling in ITER'. en. In: *Nuclear Materials and Energy* 19 (May 2019), pp. 364–371. doi: [10.1016/j.nme.2018.12.025](https://doi.org/10.1016/j.nme.2018.12.025) (cited on page 71).
- [222] H. Bufferand et al. 'Numerical modelling for divertor design of the WEST device with a focus on plasma-wall interactions'. en. In: *Nuclear Fusion* 55.5 (May 2015), p. 053025. doi: [10.1088/0029-5515/55/5/053025](https://doi.org/10.1088/0029-5515/55/5/053025) (cited on page 71).
- [223] G. Ciralo et al. 'First modeling of strongly radiating WEST plasmas with SOLEDGE-EIRENE'. en. In: *Nuclear Materials and Energy* 20 (Aug. 2019), p. 100685. doi: [10.1016/j.nme.2019.100685](https://doi.org/10.1016/j.nme.2019.100685) (cited on page 72).
- [224] F. Imbeaux et al. 'Design and first applications of the ITER integrated modelling & analysis suite'. en. In: *Nuclear Fusion* 55.12 (Oct. 2015). Publisher: IOP Publishing, p. 123006. doi: [10.1088/0029-5515/55/12/123006](https://doi.org/10.1088/0029-5515/55/12/123006) (cited on page 73).
- [225] Jae-Sun Park, Xavier Bonnin, and Richard Pitts. 'Assessment of ITER divertor performance during early operation phases'. en. In: *Nuclear Fusion* 61.1 (Dec. 2020). Publisher: IOP Publishing, p. 016021. doi: [10.1088/1741-4326/abc1ce](https://doi.org/10.1088/1741-4326/abc1ce) (cited on pages 73, 74).
- [226] Rémi Delaporte-Mathurin et al. *IRFM/divHretention source code Github repository* <https://github.com/IRFM/divHretention>. original-date: 2021-02-02T15:25:50Z. June 2021. URL: <https://github.com/IRFM/divHretention> (cited on page 74).
- [227] Remi Delaporte-Mathurin. *divHretention: Tool to estimate H retention in tokamak divertors, v0.1.3 PyPi distribution*. URL: <https://pypi.org/project/divHretention/> (cited on page 74).
- [228] Gregory De Temmerman et al. 'Data on erosion and hydrogen fuel retention in Beryllium plasma-facing materials'. en. In: *Nuclear Materials and Energy* 27 (June 2021), p. 100994. doi: [10.1016/j.nme.2021.100994](https://doi.org/10.1016/j.nme.2021.100994) (cited on page 83).
- [229] K. Schmid et al. 'WALLDYN simulations of global impurity migration in JET and extrapolations to ITER'. en. In: *Nuclear Fusion* 55.5 (May 2015), p. 053015. doi: [10.1088/0029-5515/55/5/053015](https://doi.org/10.1088/0029-5515/55/5/053015) (cited on page 83).
- [230] Jonathan Shimwell et al. 'The Paramak: automated parametric geometry construction for fusion reactor designs'. en. In: *F1000Research* 10 (Jan. 2021), p. 27. doi: [10.12688/f1000research.28224.1](https://doi.org/10.12688/f1000research.28224.1) (cited on pages 85, 116).
- [231] Paul K. Romano et al. 'OpenMC: A state-of-the-art Monte Carlo code for research and development'. en. In: *Annals of Nuclear Energy. Joint International Conference on Supercomputing in Nuclear Applications and Monte Carlo 2013, SNA + MC 2013. Pluri- and Trans-disciplinarity, Towards New Modeling and Numerical Simulation Paradigms* 82 (Aug. 2015), pp. 90–97. doi: [10.1016/j.anucene.2014.07.048](https://doi.org/10.1016/j.anucene.2014.07.048) (cited on page 85).
- [232] D. A. Brown et al. 'ENDF/B-VIII.0: The 8th Major Release of the Nuclear Reaction Data Library with CIELO-project Cross Sections, New Standards and Thermal Scattering Data'. en. In: *Nuclear Data Sheets. Special Issue on Nuclear Reaction Data* 148 (Feb. 2018), pp. 1–142. doi: [10.1016/j.nds.2018.02.001](https://doi.org/10.1016/j.nds.2018.02.001) (cited on page 85).
- [233] Göran Ericsson. 'Advanced Neutron Spectroscopy in Fusion Research'. en. In: *Journal of Fusion Energy* 38.3 (Aug. 2019), pp. 330–355. doi: [10.1007/s10894-019-00213-9](https://doi.org/10.1007/s10894-019-00213-9) (cited on page 86).

- [234] Byron Goldstein, Harold Levine, and David Torney. 'Diffusion Limited Reactions'. In: *SIAM Journal on Applied Mathematics* 67.4 (2007). Publisher: Society for Industrial and Applied Mathematics, pp. 1147–1165 (cited on pages 89, 90).
- [235] F. A. Nichols. 'On the estimation of sink-absorption terms in reaction-rate-theory analysis of radiation damage'. en. In: *Journal of Nuclear Materials* 75.1 (July 1978), pp. 32–41. doi: [10.1016/0022-3115\(78\)90026-0](https://doi.org/10.1016/0022-3115(78)90026-0) (cited on page 89).
- [236] T. R. Waite. 'Theoretical Treatment of the Kinetics of Diffusion-Limited Reactions'. In: *Physical Review* 107.2 (July 1957). Publisher: American Physical Society, pp. 463–470. doi: [10.1103/PhysRev.107.463](https://doi.org/10.1103/PhysRev.107.463) (cited on page 89).
- [237] Karl D. Hammond, Dimitrios Maroudas, and Brian D. Wirth. 'Theoretical Model of Helium Bubble Growth and Density in Plasma-Facing Metals'. en. In: *Scientific Reports* 10.1 (Feb. 2020). Number: 1 Publisher: Nature Publishing Group, p. 2192. doi: [10.1038/s41598-020-58581-8](https://doi.org/10.1038/s41598-020-58581-8) (cited on page 93).
- [238] C. S. Becquart et al. 'Microstructural evolution of irradiated tungsten: Ab initio parameterisation of an OKMC model'. en. In: *Journal of Nuclear Materials* 403.1 (Aug. 2010), pp. 75–88. doi: [10.1016/j.jnucmat.2010.06.003](https://doi.org/10.1016/j.jnucmat.2010.06.003) (cited on page 95).
- [239] Guo Wei et al. 'A better nanochannel tungsten film in releasing helium atoms'. en. In: *Journal of Nuclear Materials* 532 (Apr. 2020), p. 152044. doi: [10.1016/j.jnucmat.2020.152044](https://doi.org/10.1016/j.jnucmat.2020.152044) (cited on page 96).
- [240] Guo Wei et al. 'Understanding the release of helium atoms from nanochannel tungsten: a molecular dynamics simulation'. en. In: *Nuclear Fusion* 59.7 (June 2019). Publisher: IOP Publishing, p. 076020. doi: [10.1088/1741-4326/ab14c7](https://doi.org/10.1088/1741-4326/ab14c7) (cited on page 96).
- [241] A. Kreter et al. 'Linear Plasma Device PSI-2 for Plasma-Material Interaction Studies'. In: *Fusion Science and Technology* 68.1 (July 2015). Publisher: Taylor & Francis _eprint: <https://doi.org/10.13182/FST14-906>, pp. 8–14. doi: [10.13182/FST14-906](https://doi.org/10.13182/FST14-906) (cited on page 96).
- [242] Johannes Schindelin et al. 'Fiji: an open-source platform for biological-image analysis'. en. In: *Nature Methods* 9.7 (July 2012). Bandiera_abtest: a Cg_type: Nature Research Journals Number: 7 Primary_atype: Reviews Publisher: Nature Publishing Group Subject_term: Imaging;Software Subject_term_id: imaging;software, pp. 676–682. doi: [10.1038/nmeth.2019](https://doi.org/10.1038/nmeth.2019) (cited on page 96).
- [243] S. I. Krasheninnikov, T. Faney, and B. D. Wirth. 'On helium cluster dynamics in tungsten plasma facing components of fusion devices'. en. In: *Nuclear Fusion* 54.7 (May 2014), p. 073019. doi: [10.1088/0029-5515/54/7/073019](https://doi.org/10.1088/0029-5515/54/7/073019) (cited on pages 99, 106, 108).
- [244] Rémi Delaporte-Mathurin et al. 'Parametric study of hydrogenic inventory in the ITER divertor based on machine learning'. en. In: *Scientific Reports* 10.1 (Oct. 2020). Number: 1 Publisher: Nature Publishing Group, p. 17798. doi: [10.1038/s41598-020-74844-w](https://doi.org/10.1038/s41598-020-74844-w) (cited on pages 102, 116).
- [245] Rémi Delaporte-Mathurin et al. 'Parametric optimisation based on TDS experiments for rapid and efficient identification of hydrogen transport materials properties'. en. In: *Nuclear Materials and Energy* (Mar. 2021), p. 100984. doi: [10.1016/j.nme.2021.100984](https://doi.org/10.1016/j.nme.2021.100984) (cited on page 115).
- [246] Rémi Delaporte-Mathurin et al. 'Influence of interface conditions on hydrogen transport studies'. en. In: *Nuclear Fusion* 61.3 (2021), p. 036038. doi: [10.1088/1741-4326/abd95f](https://doi.org/10.1088/1741-4326/abd95f) (cited on page 115).
- [247] Rémi Delaporte-Mathurin et al. 'Influence of exposure conditions on helium transport and bubble growth in tungsten'. en. In: *Scientific Reports* 11.1 (July 2021), p. 14681. doi: [10.1038/s41598-021-93542-9](https://doi.org/10.1038/s41598-021-93542-9) (cited on page 116).
- [248] T Vu-Huu et al. 'The convergence rate of a polygonal finite element for Stokes flows on different mesh families'. en. In: *Journal of Physics: Conference Series* 1777.1 (Feb. 2021), p. 012065. doi: [10.1088/1742-6596/1777/1/012065](https://doi.org/10.1088/1742-6596/1777/1/012065) (cited on page 125).
- [249] Alan C. Hindmarch. 'ODEPACK, A Systematized Collection of ODE Solvers'. In: *Scientific Computing* (1982), pp. 55–64 (cited on page 128).

